LBL-30077

Lawrence Berkeley Laboratory
UNIVERSITY OF CALIFORNIA

CHEMICAL BIODYNAMICS DIVISION

Structural Studies of Manganese and Halide in the Photosynthetic Oxygen Evolving Complex

V.J. DeRose
(Ph.D. Thesis)

October 1990

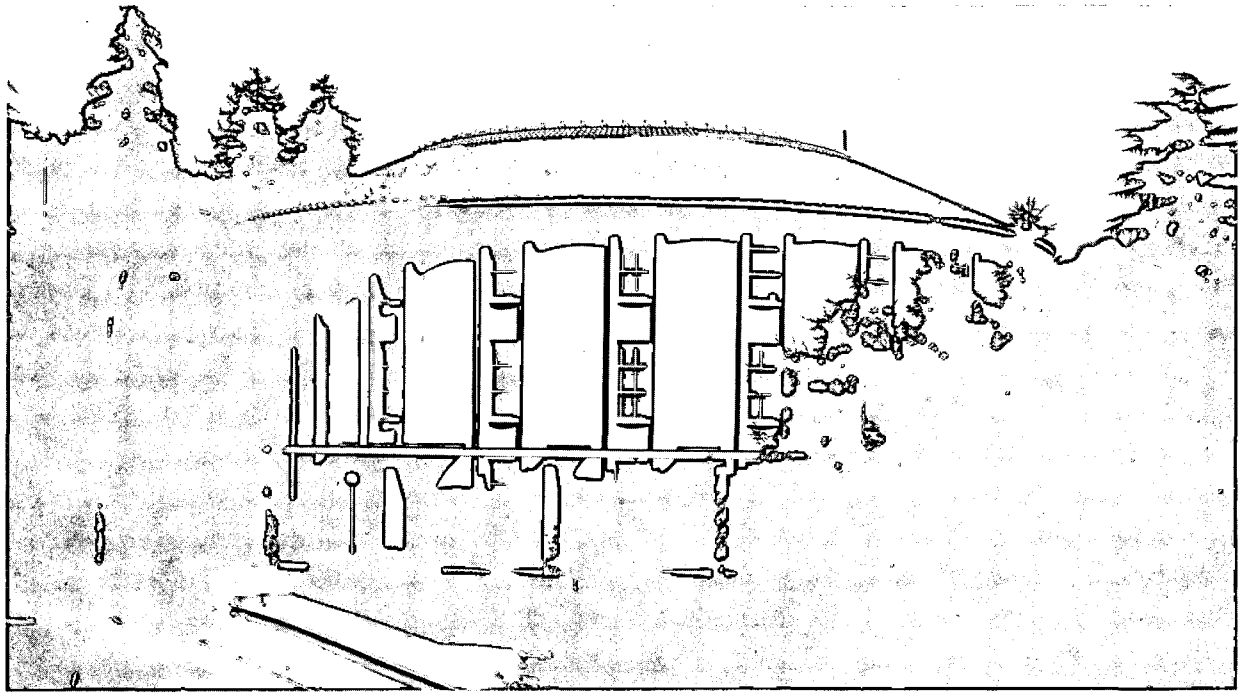

LOAN COPY
Circulates
for 2 weeks
Bldg. 50 Library.
LBL-30077
Copy 2

Prepared for the U.S. Department of Energy under Contract Number DE-AC03-76SF00098

Structural Studies of Manganese and Halide in the Photosynthetic Oxygen Evolving Complex

Victoria Jeanne DeRose

Ph.D. Thesis

October, 1990

Lawrence Berkeley Laboratory
University of California
Berkeley, California 94720

This work was supported by the U.S. Department of Energy
under contract number DE-AC03-76SF00098

Structural Studies of Manganese and Halide in the Photosynthetic Oxygen Evolving Complex

by Victoria Jeanne DeRose

Abstract

Electron paramagnetic resonance (EPR) and X-ray absorption spectroscopy (XAS) were used as probes of the manganese atoms of the oxygen evolving complex (OEC). Spectroscopic investigations of halide-substituted preparations were used to obtain information concerning the structural relationship between halide and the manganese complex. Electron spin echo spectroscopy (ESE) provided information about the amino acid ligands to the manganese atoms.

XAS studies at liquid helium temperatures allowed the observation of a scatterer at >3 Å from the absorbing manganese. Extended X-ray absorption fine structure (EXAFS) data taken on preparations from both spinach and the thermophilic cyanobacterium *Synechococcus* sp. fit to nearly identical parameters. By comparison with model compounds the scatterer at >3 Å fits well to a single manganese-manganese distance per the four manganese in the OEC cluster. A structural model for the OEC which includes this new manganese-manganese distance is discussed.

The correlation between fluoride inhibition of oxygen evolution activity and enhancement of the g=4 EPR signal which arises from the OEC in the S_2 state was ascertained. A distinct narrowing of the g=4 EPR signal in the presence of fluoride was confirmed. The narrowing of the EPR signal is interpreted as being due to fluoride binding to the manganese. EXAFS analysis of fluoride-inhibited preparations showed subtle differences from the control samples. A damping of the scattering due to manganese at 2.7 Å was observed in data from the fluoride-treated preparations poised in the S_2 state.

EXAFS of bromide-substituted PSII preparations from *Synechococcus* showed no change relative to EXAFS of chloride-containing samples. The substructure observed by high resolution EPR of the S_2-state multiline signal also

shows no change in the presence of bromide. These results argue strongly against the presence of a halide ligand bridging the manganese in the OEC, but do not exclude a single terminal halide ligand.

ESE spectroscopy of ^{15}N-containing preparations from *Synechococcus* identify nuclear envelope modulation due to nitrogen near the manganese of the OEC. The modulation frequency is consistent with its arising from an amino acid ligand such as a histidine.

I dedicate this thesis
to my loving parents.

Acknowledgements

I have been fortunate to meet and work with many people in the last several years. I am very happy to be able to acknowledge them.

I thank Professor Kenneth Sauer for providing an atmosphere of scientific freedom tempered with constructive criticism. The independence which he fosters allowed me to be exposed to a number of diverse techniques. I appreciate and have benefited from his priorities of clear oral and written communication. I also sincerely thank him for continued support as I developed in this atmosphere.

I thank Dr. Mel Klein for his enthusiasm and his confidence. I appreciate his interest in technical details as well as in the larger problems, and the manner in which he shares the depths of his knowledge while respecting every new proposal, regardless of its ignorant background. His appreciation and enjoyment of the work that we do is fun as well as inspiring.

I am grateful to Dr. William Armstrong for his many comments and suggestions while reading this thesis.

Dr. Ann McDermott and Dr. Vittal Yachandra were my practical research advisors, and I am forever grateful for their encouragement, advice, and scientific training as well as for their friendship. Ann and Vittal introduced the spectroscopy of PSII in *Synechococcus* to the laboratory, and were coworkers on the ^{15}N-substitution project. Ann started me on the bromide-replacement project. Both Ann and Vittal introduced me to the joys of X-ray absorption spectroscopy.

Aside from scientific guidance, the enthusiasm that Vittal provides was essential to my work. In addition, his social and political commentary provided new depths to my education, as well as to my enjoyment in the lab. I thank him for all of his help and companionship.

I feel lucky to have worked with Ann, as the experience has provided me an example of spirit and creativity which I look to for inspiration. I thank her for the timely interest which she took in my graduate career.

Dr. David Britt designed, built and operated the electron spin echo spectrometer used in the ^{15}N-substitution project. I thank him for introducing me to this subject, as well as for inspiring me with the diversity of his knowledge and interests.

I thank Ishita Mukerji for her friendship. Working with her was one of the most enjoyable experiences I have had in science. I also believe that I have drunk more coffee with her than with anyone else in my life.

X-ray absorption spectroscopy is an ongoing group project in this laboratory. Vittal, Ishita, and Sir Matthew Latimer make up the present group, and all of the data presented in this thesis was collected through their collaboration. Collectively they worked through the challenges of a new cryostat and X-ray detection system, and provided for amazingly fruitful data collection. Dr. David Goodin wrote the programs used in the data analysis. It is not possible to overstate the importance of these versatile programs, which we use for display and analysis of EPR spectra as well. Dr. James Cole and Dr. Jean-Luc Zimmermann began the work on fluoride-inhibited PSII. I also thank Jim for teaching me about EPR. I thank Jean-Luc for helpful discussions and his continued collaboration on the X-ray project, as well as for many entertaining discussions concerning the comparison between France to the United States. I thank Dr. Peter Sandusky for some important suggestions regarding halide and PSII. Conversations with Dr. Warren Beck are always stimulating, and I appreciate his input as well on halide and PSII. Dr. Ron Guiles was instrumental in developing the X-ray project as well as in obtaining the many model compounds that we now use. Melissa Grush and Wenchuan Liang also assisted in X-ray data collection. Gary Smith in this laboratory has provided for an impressive array of computational abilities.

I thank Dr. Britt Hedman and Robert Mayer of SSRL for their immense technical help with the liquid helium cryostat. I also thank Dr. Britton Chance for the use of the Ge detector, and Dr. Syed Khalid of the NSLS for his patient assistance on beamline X9A. Dr. Steve Cramer must be acknowledged for the all-important use of his cryostat and on occasion for his Ge detector.

I appreciate the many past and present members of the Sauer-Klein group who have made the laboratory an interesting and enjoyable place. It would take far too long to list them all, so please excuse any missing members. I thank Dr. Steve Worland for patiently teaching me how to isolate membrane proteins I enjoyed many scientific, exercise and food-related activities with Dr. Trish Maxson. I am happy to have known Dr. Dr. Sarah Tabbutt. Matthew, Yvonne, Mary, Martin, Dennis, Wen and Melissa currently provide for an interesting social atmosphere. I thank Dr. Sandra Laursen for her companionship while she was here, and for her suppport from afar. I also thank Dr. Josef Zwanziger for inspiring me while at Chicago to continue in science, and for his continued friendship.

I would like to acknowledge the many people I have met outside of the laboratory. I thank Rick Murray for reminding me that life is too short to waste time on small things, and for introducing me to a bunch of geologists whose company I have enjoyed greatly. My current housemates Elise and Elizabeth are models of support and I appreciate their friendship. I am very lucky to have Paul at my side. It is impossible to overemphasize the importance of his encouragement and support. I thank Max for simply being Max.

Finally, I am blessed with parents who are forever accepting, loving, and full of humor. Without their unending encouragement I would not be writing a thesis.

This work was supported by a grant from the National Science Foundation (DMB 88-04526) and by the Director, Division of Energy Biosciences, Office of Basic Energy Sciences, Office of Energy Research of the Department of Energy under contract DE-AC03-76SF00098. Research was carried out in part at the National Synchrotron Light Source, Brookhaven National Laboratory, which is supported by the U.S. Department of Energy, Division of Materials Sciences and Division of Chemical Sciences. Beamline X9A is supported by the National Biostructures Research Resource (NIH-RR01633). Synchrotron radiation facilities were also provided by the Stanford Synchrotron Radiation Laboratory, which is supported by the U.S. Department of Energy, Office of Basic Energy Sciences and the NIH Biotechnology Program, Division of Research Resources.

Table of Contents

Chapter 1
Introduction

Importance of photosynthetic water oxidation 1
Cyanobacteria 2
The reaction center 3
The polypeptide composition of photosystem II 5
Oxygen evolution and the Kok cycle 7
Manganese and the oxygen evolving complex 7
Chloride and calcium in photosystem II 10
Goals of this work 11

Chapter 2
Materials and Methods

Preparation of oxygen-evolving photosystem II particles from *Synechococcus* sp.
Growth of *Synechococcus* sp. 12
Growth of *Synechococcus* sp. in bromide media 14
Growth of *Synechococcus* sp. in $^{14}NO_3^-$ and $^{15}NO_3^-$ 14
Preparation of PSII from *Synechococcus* sp. 18
Photosystem II preparations from spinach 21
Oxygen evolution 22
X-ray absorption spectroscopy
Synchrotron radiation sources 23
X-ray fluorescence detection 30
Data analysis 38

Chapter 3

The Structure of Manganese in the Oxygen Evolving Complex from Spinach and *Synechococcus* sp.: New Information from X-ray Absorption Spectroscopy at Low Temperatures

Materials and Methods 41

Results

Low temperature EXAFS of PSII in the S_1 state 41

Fits to peak III and comparison with model compounds 48

Comparison of the EXAFS from the S_1 and S_2 states 62

Discussion 62

Chapter 4

The Effect of Fluoride Inhibition on the Oxygen Evolving Complex: EPR and EXAFS Studies

Introduction 75

Materials and Methods 78

Results

Relation between the fluoride-induced inhibition of oxygen evolution and formation of the g=4 EPR signal 80

Properties of the g=4 EPR signal produced by inhibition with fluoride 83

X-ray absorption spectroscopy of fluoride-inhibited PSII samples 92

Discussion 107

Chapter 5

X-ray Absorption and Electron Paramagnetic Resonance Experiments on Bromide-Substituted PSII preparations from *Synechococcus* sp.

Introduction 122

Materials and Methods 126

Results 127

Chloride activation of oxygen evolution in PSII preparations

from *Synechococcus* sp. 127
EPR studies of bromide-substituted PSII particles from *Synechococcus* 133
X-ray absorption experiments on bromide-substituted PSII particles from *Synechococcus* 143
Discussion 153

Chapter 6

Continuous Wave EPR and Electron Spin Echo Spectroscopy Studies of ^{14}N- and ^{15}N-containing Photosystem II Preparations from *Synechococcus* sp.

Introduction 157
Materials and Methods 159
Results
Continuous wave EPR of the multiline signal from ^{14}N- and ^{15}N-grown *Synechococcus* 160
ESEEM of ^{15}N- and ^{14}N-grown *Synechococcus* PSII 165
Nitrogen modulation in dark-adapted samples 165
Discussion 172

Chapter 7

Summary and Suggested Future Work

Structure of the oxygen evolving complex 179
Amino acid ligands 181
Cofactor arrangement 181
Mechanisms for water oxidation 182
Future work
Halide ligation to the manganese 186
The broad g=2 EPR signal from fluoride-inhibited PSII preparations 192
The dark "multiline" signal from bromide-grown *Synechococcus* preparations 192

References 194

Abbreviations

BBY	Photosystem II-enriched membrane preparation (Berthold et al., 1981)
Bipy	2,2'-bipyridine
Chl	chlorophyll
Cyt	cytochrome
DCBQ	2,6-dichloro-*p*-benzoquinone
DMSO	dimethyl sulfoxide
EDTA	ethylenediamine tetraacetic acid
EPR	electron paramagnetic resonance
ESE, ESEEM	electron spin echo, electron spin echo envelope modulation
EXAFS	extended X-ray absorption fine structure
Hepes	4-(2-hydroxyethyl)-1-piperazineethanesulfonic acid
HIm	imidazole
MES	4-morpholineethanesulfonic acid
NADP	nicotinamide adenine dinucleotide phosphate
NSLS	National Synchrotron Light Source
OEC	oxygen evolving complex
PMSF	phenylmethyl sulfonyl fluoride
PPBQ	phenyl-*p*-benzoquinone
PSII	photosystem II
pyr	pyridine
SSRL	Stanford Synchrotron Radiation Laboratory
tacn	1,4,7-triazacyclononane
Tiron	4,5-dihydroxy-1,3-benzene-disulfonic acid
Tris	tris (hydroxymethyl) aminoethane
XANES, XAS	X-ray absorption near edge structure, X-ray absorption spectroscopy

Chapter 1

Introduction

Importance of photosynthetic water oxidation

It is estimated that the light-driven cleavage of water to molecular oxygen in photosynthetic organisms produces ~10^{17} g O_2 per year [Johnson, 1970]. The total supply of oxygen in the atmosphere which is now left after two billion years of photosynthetic oxygen evolution is estimated at 10^{21} g O_2. Most of the oxygen created by photosynthetic organisms is recombined in oxidative respiration and combustion, and in oxidizing products of both man-made and geologic processes such as carbon monoxide, nitric oxide and sulfur dioxide; the remainder is responsible for maintaining an oxidizing atmosphere and a protective ozone layer. Nonbiological photodissociation of water followed by escape of hydrogen gas takes place in the outer atmosphere at an estimated oxygen production rate of only 10^{11} g O_2 per year [Johnson, 1970], which is two orders of magnitude lower than what would be necessary to oxidize a year's worth of anthropogenic sulfur dioxide emissions, or about the same as the yearly sulfur dioxide emission from the active Kilauea volcano in Hawaii [Gerlach & Graeber, 1985]. Photosynthetic oxygen evolution clearly plays an irreplaceable role in maintaining a life-supporting atmosphere.

Every molecule of water is the potential source of two reducing equivalents which are stored in reduced carbon compounds and later retrieved by nonphotosynthetic organisms. This overall reaction can be represented as:

$$H_2O + CO_2 \Rightarrow (CH_2O) + O_2$$

Reduced carbon compounds form the basis of the food chain as well as fuel resources in the form of oil deposits. It is worthy of note that the modern rate of depletion of these fuel resources, at ~10^{16} g C per year, is three orders of magnitude greater than the estimated yearly rate of return to the fossil reservoir [Johnson, 1970].

Sunlight is the source of energy in biological water oxidation. In isolated photosynthetic membranes, four photons of $\leq$680 nm wavelength are required to oxidize two molecules of H_2O and release one molecule of O_2. This corresponds to ~ 700 kJ of photon energy used to drive a reaction with an overall energy requirement of ~570 kJ [Sauer, 1986]. If these were the only factors in the reaction, this would correspond to

~80% efficiency of solar energy conversion. In practice, the overall efficiency of initial energy conversion in the biological photochemical "reaction center" is likely closer to 30%, which is still twice that attained with artificial photochemical devices [Norris & Schiffer, 1990; see also Fahrenbruch & Bube, 1983].

It is clear from the above considerations that an understanding on the molecular level of the mechanism of photosynthetic water oxidation has importance for practical as well as philosophical reasons.

Cyanobacteria

The development of cyanobacteria is widely held responsible for the generation of an oxygenic atmosphere beginning around 3 billion years ago [Brock, 1973]. Cyanobacteria now exist in a multitude of aqueous environments, including fresh water lakes, the oceans, and thermal hot springs. They are prokaryotic organisms which are mainly photoautotrophic, although some photoheterotrophic organisms have been found which will grow in the light using a carbon source other than CO_2 [Stanier, 1973]. The narrow range of carbon sources which are usable by photoheterotrophic cyanobacteria includes sucrose, fructose, and one or two disaccharides. Very few chemoheterotrophs, which grow in the dark with added organic compounds, have been found among the cyanobacteria. Taxonomically cyanobacteria are divided into genus based on the cell shape (rods or spheres) and the presence of structures such as gas vacuoles. *Synechococcus* sp., the cyanobacterium used in the work presented in this thesis, is a thermophilic rod-shaped unicellular cyanobacterium which has not been further classified.

The cyanobacteria have a cell wall and cytoplasmic membrane, and an additional thylakoid membrane structure in which the proteins involved in photosynthetic reactions are embedded. The thylakoid has a double membrane which encloses an intrathylakoid space or lumen. In cyanobacteria, the light-harvesting complexes known as phycobilisomes are found perched on the outer (stromal) sides of the thylakoid membrane. The remarkable structure and functionality of phycobilisomes has been reviewed [Bryant, 1986]. Phycobilisomes funnel light energy into photosystem I and photosystem II, which each have additional associated, chlorophyll-containing light harvesting proteins which presumably fine tune the transferred energy to meet the primary photoreactants.

The photosynthetic apparatus in higher plants is housed in the chloroplast organelle. While the components in the membrane are very similar to those in

cyanobacteria (for review, see Bryant (1986)), the membrane structure is different between the organisms. In chloroplasts, photosystem II components are predominantly found in stacked or grana regions of the thylakoid membrane, whereas photosystem I is found in unstacked regions. There is no evidence for such a separation between photosystems in cyanobacteria.

The first photo*chemical* event in each photosystem is the photooxidation of a "primary donor" molecule. The strong oxidizing potential of the oxidized primary donor in photosystem II is used for the oxidation of water. The reduced acceptor is a quinone molecule which accepts two electrons and two protons to become an electron carrier to the rest of the electron transport chain (Figure 1.1). The potential of the oxidized primary donor in photosystem I is less positive, and the unique reducing power of the terminal electron acceptors, iron-sulfur centers A, B, and X, is coupled to the reduction of NADP to NADPH via soluble ferredoxins. Powered by the two photosystems, a reducing equivalent is transferred from water to NADPH over a potential range of 1 V. This results not only in a stored reducing equivalent, but also in creating a potential gradient across the thylakoid membrane which is coupled to the formation of ATP by ATPase.

The reaction center

In 1988 the Nobel prize was presented to Drs. Hartmut Michel, Johann Deisenhofer, and Robert Huber for deriving the first X-ray crystallographic structure of a photochemical reaction center. The complex, isolated from the photosynthetic bacterium *R. viridis*, consists of four polypeptides in which are arranged the photochemical cofactors. The combination of this three dimensional structure with the wealth of information which had been derived spectroscopically has resulted in a relatively complete picture of the first photochemical events in this photosystem [reviewed in Huber, 1989]. The first molecule to perform chemistry upon absorbing light, the primary reactant, is a pair of bacteriochlorophyll molecules arranged with suitable orbital overlap such that the formation of an excited singlet state following energy transfer results in the transfer of an electron to a secondary electron acceptor, leaving an unpaired electron or "hole" behind. Fast electron transfer from the secondary acceptor, which is another bacteriochlorophyll molecule, through a bacteriopheophytin molecule and finally to a quinone, occurs within 200 ps. This charge separated state is stabilized in that the reduction of the photooxidized donor by a cytochrome c species is faster (270 ps) than

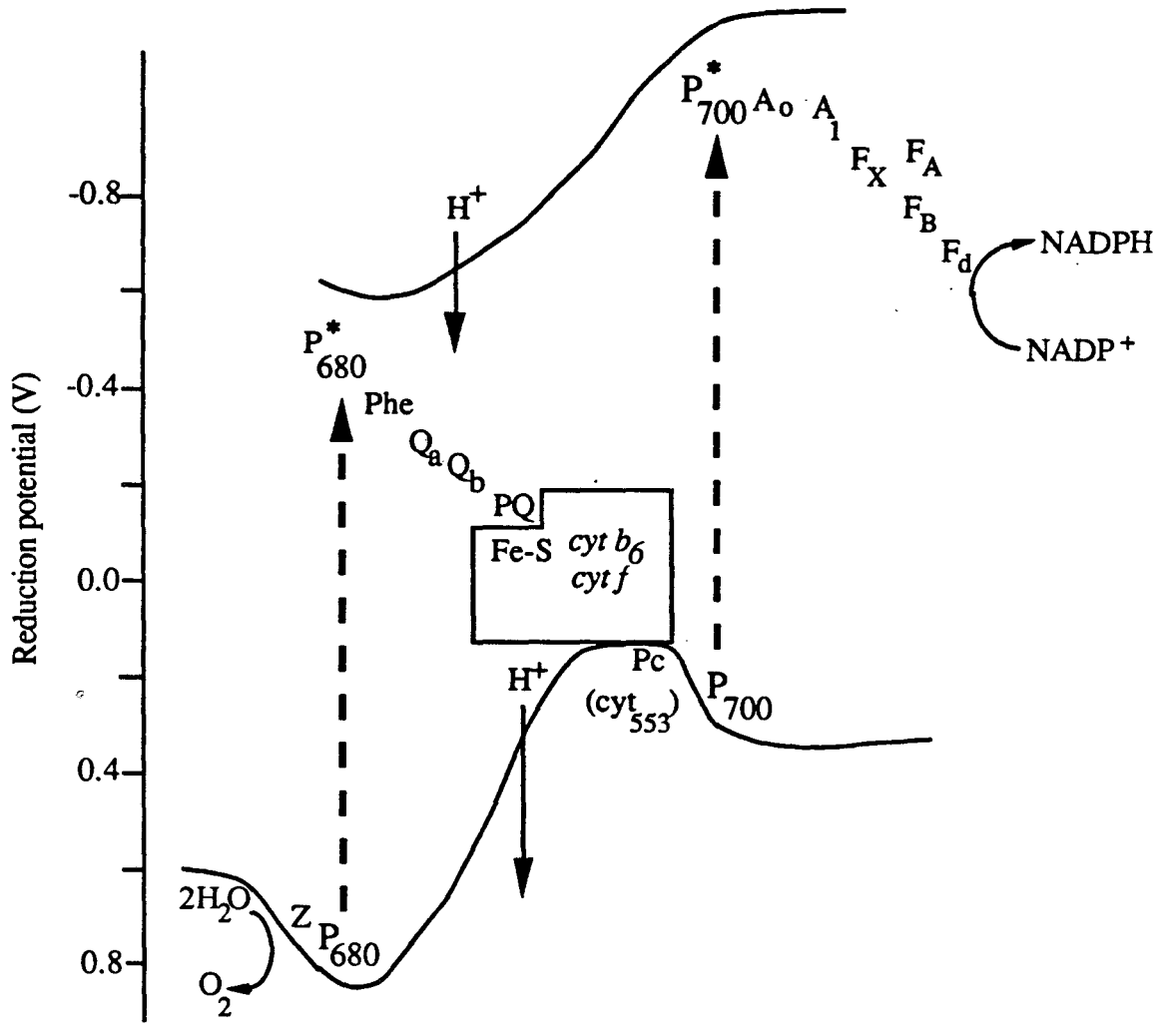

Figure 1.1 The Photosynthetic Z-Scheme

Electron transport components are arranged vertically as a function of midpoint potential and horizontally in the direction of electron transfer [adapted from Blankenship & Prince (1985)]. Dotted lines indicate an absorbed quantum of energy; solid lines indicate membrane boundaries.

charge recombination between the reduced quinone and the oxidized donor (~1 ms).

Huber (1989) suggests that the role of the protein matrix, in addition to arranging these cofactors as "closely spaced aromatic macrocycles with matched redox potentials," is to provide a hydrophobic environment which facilitates electron transfer. Such a role becomes clear when the amino acid sequences of proteins from different photosynthetic species are compared. Photosynthetic bacteria such as *R. viridis* contain only one photosystem, which performs cyclic electron transfer coupled to a proton gradient and formation of ATP. The D_1 and D_2 polypeptides, which contain the photosystem II photoreactants of cyanobacteria and higher plants, have ~25% homology on the amino acid level with the sequences of the L and M subunits of the *R. viridis* reaction center. The folding pattern for the D_1 and D_2 polypeptides derived from hydropathy plots predicts them to adopt the same intramembrane multi-helical arrangement as the L and M subunits [Trebst, 1986; Barber, 1987]. Many of the amino acid residues responsible for binding the cofactors are fully conserved between the different photosynthetic organisms [Michel & Deisenhofer, 1988].

The polypeptide composition of photosystem II

A schematic of the polypeptide compositions of oxygen-evolving photosystem II preparations from both cyanobacteria and higher plants is shown in Figure 1.2. The only differences between the organisms lie in two extrinsic polypeptides, the 17 and 24 kD polypeptides, which are found in higher plants but not in cyanobacteria. The light-harvesting polypeptides of 47 and 43 kD contain chlorophyll a. The D_1 and D_2 polypeptides are predicted to have 5 transmembrane helices each. Regions near the carboxy termini of the polypeptides on the lumenal side of the membrane are found to be highly conserved amongst oxygen-evolving organisms, but lacking or not conserved amongst non-oxygen-evolving photosynthetic bacteria. These regions are predicted to form a binding site for the oxygen evolving complex [Michel & Deisenhofer, 1988]. The 33 kD extrinsic polypeptide can be removed from photosystem II preparations in high ionic strength. Its removal results in destabilization of the oxygen evolving complex. The 17 and 24 kD polypeptides found in higher plants can also be removed in high ionic strength, which results in an increased requirement in the oxygen evolving complex for the cofactors Ca^{+2} and Cl^-. Finally, cytochrome b_{559} consists of two membrane-spanning subunits [Tae et al., 1988] with a single heme group bridged between them [Miyazaki et al., 1989]. The physiological role for the cytochrome is not

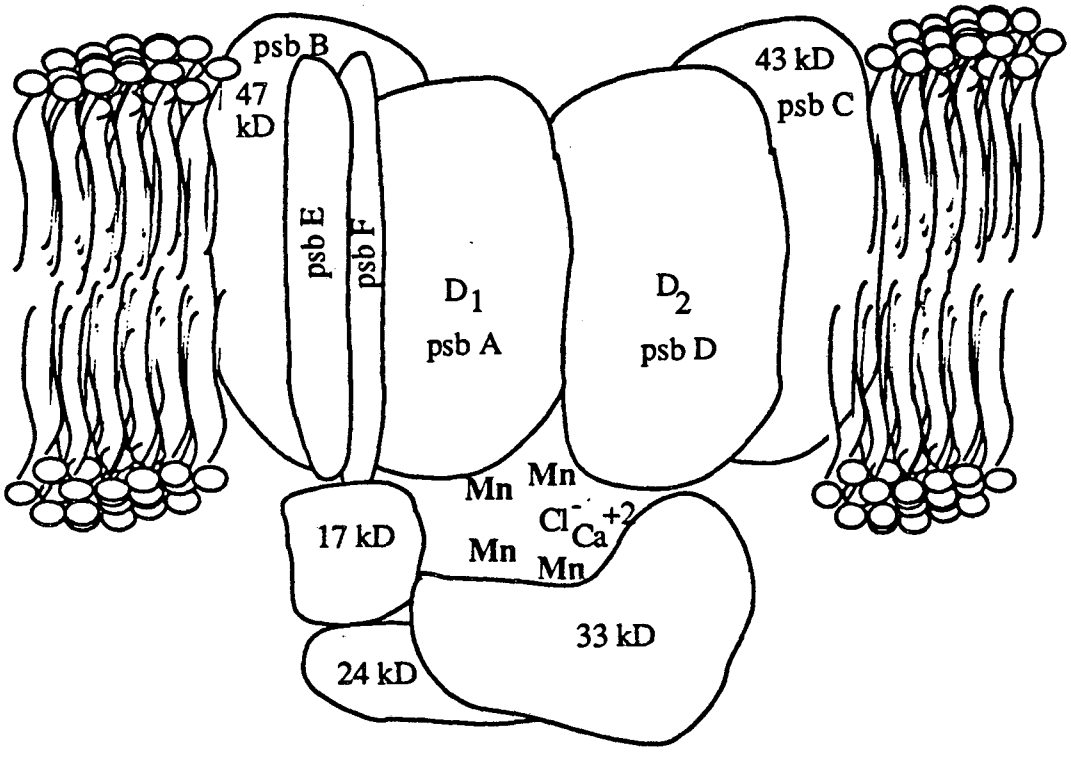

Figure 1.2 Polypeptide composition of oxygen evolving complex preparations.

yet known, although a role in protecting the reaction center against photooxidation has been suggested (Thompson & Brudvig, 1988).

Oxygen evolution and the Kok cycle

The connection between the four-electron chemistry of water oxidation and the one-electron chemistry of the reaction center in photosystem II was elucidated by Joliot and Kok (1969, 1970). It was found that a series of brief (10 μs), saturating flashes of light trained on chloroplasts resulted in a pattern of oxygen yield. The maximum oxygen yield appeared after the third flash and every fourth flash thereafter [Joliot et al., 1969]. This result was interpreted to give the S-state model for oxygen evolution. In this model, the oxygen evolving complex can attain five possible oxidation states, S_0-S_4 [Kok et al., 1970]. In the dark, the complex relaxes predominantly to the S_1 state. Each flash of light advances the complex by one oxidation, or S-state. Oxygen is released in S_4, relaxing the complex to the S_0 state in the dark. The S-state "clock" is shown in Figure 1.3.

The development of the S-state clock implied that the mechanism of water oxidation involved several steps. Intermediates predicted to arise during such a mechanism include hydroxyl radicals, hydrogen peroxide and the superoxide anion [Renger, 1987]. These species are highly reactive and pose the danger of oxidative degradation of biomolecules. A template for the water oxidation reaction was therefore suggested which could stabilize the intermediates of the reaction by participating as a redox intermediate.

Manganese and the oxygen evolving complex

Manganese has long been associated with photosynthetic water oxidation. Four manganese are isolated per photosystem II [Cheniae & Martin, 1970; Yocum et al., 1981; Ohno et al., 1986]. Spectroscopic signals have been sought from manganese as the complex is advanced through the S states. Electron paramagnetic resonance, ultraviolet absorption spectroscopy, and X-ray absorption spectroscopy have all been brought to bear on this problem [reviewed in Babock, 1987; Pecoraro, 1988; Sauer et al., 1990]. Results from X-ray absorption edge spectroscopy indicate that manganese increases in oxidation state as the S-state of the complex is advanced from S_0 to S_2 [Goodin et al., 1984; Yachandra et al., 1987; Guiles et al., 1990b]. Advance to S_3 does

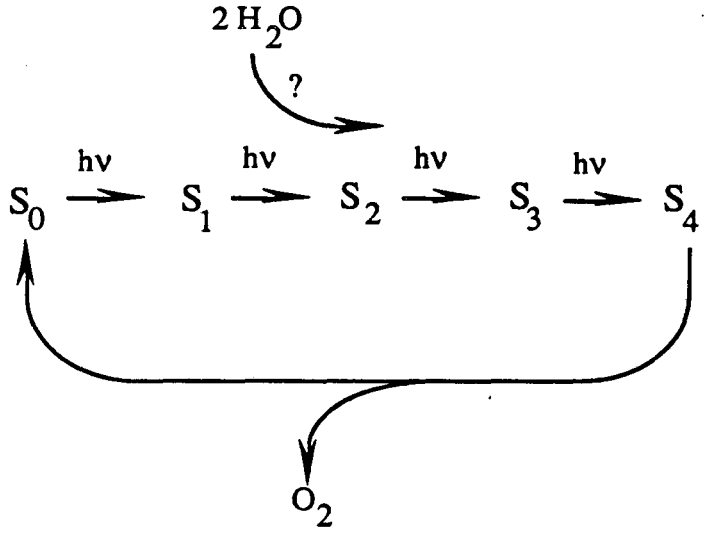

Figure 1.3 The S-state model of oxygen evolution [Kok et al., 1970].

not result in a shift of the x-ray edge to higher energies, interpreted to mean that manganese is not oxidized at this step [Guiles et al., 1990a].

The first EPR signal associated with manganese from the oxygen evolving complex was seen in chloroplasts which had been illuminated and then quenched to low temperature [Dismukes & Siderer, 1981]. The complex "multiline" EPR signal from the S_2 state of the oxygen evolving complex consists of $\geq$ 18 Mn hyperfine lines, separated by approximately 80 G, from at least two exchange-coupled Mn nuclei. The signal is very similar to that from the model compond di-μ-oxo bridged Mn(III)Mn(IV)$(bipy)_2$. The EPR spectra from Mn(III)Mn(IV) binuclear complexes contains only 16 lines, however. The construction of detailed spin hamiltonians for exchange-coupled Mn nuclei allowed successful simulations of the EPR signal from the Mn(III)Mn(IV) model compound [Cooper et al., 1978], but the more complicated multiline EPR signal from the oxygen evolving complex has not yet been simulated. A second EPR signal from the S_2 state is found at g=4 and has also been assigned to Mn [Cole et al., 1987; Kim et al., 1990]. The appearance of these signals is affected by a variety of treatments, which will be summarized later. No conventional EPR signals have been detected from the S_1 or S_3 states of untreated photosystem II preparations, but a signal observed using parallel polarization EPR has been assigned to an even spin system in the S_1 state [Dexheimer et al., 1990].

Extended X-ray absorption fine structure (EXAFS) spectroscopy gives a radial distribution function of nearest neighbors to the manganese. Results from EXAFS indicate minimal units of di-μ-oxo-bridged structures, with Mn-Mn distances of 2.7 Å, which remain substantially unchanged upon advance from S_1 through S_3 [Yachandra et al., 1987; McDermott et al., 1988; Guiles et al., 1990a]. A feature at ca. 3.3 Å which potentially results from another Mn-Mn interaction has recently been detected in low-temperature EXAFS of spinach core preparations and in spinach chloroplasts [Penner-Hahn et al., 1990; George et al., 1989]. The Mn-Mn distances and coordination numbers have prompted proposals of a number of structures for the oxygen evolving complex including dinuclear, trinuclear, and tetranuclear manganese centers.

Most of the above mentioned experiments have given identical results for oxygen evolution preparations from both spinach and cyanobacteria. Two notable exceptions in the similarity between the two organisms are that the g=4 EPR signal has not been detected in cyanobacterial preparations, and the X-ray absorption edge appears 0.5-1.0 eV lower in cyanobacterial preparations [McDermott et al., 1988]. The EXAFS and the multiline EPR signals appear to be very similar between the two organisms. Studies on

the cyanobacterial preparation in S_0 and S_3 have not been undertaken, nor has the parallel-mode EPR signal been sought in cyanobacteria.

Chloride and calcium in photosystem II

Light-induced oxygen evolution activity in both plants and cyanobacteria requires both calcium and chloride. The chloride requirement has long been known [Warburg & Lüttgens, 1946]. The requirement for calcium was discovered more recently [Ghanotakis et al., 1984]. Both ions have been found to have profound effects on the spectroscopic signals from the oxygen evolving complex.

In cyanobacteria, a single tightly bound calcium is found per PSII [Ohno et al., 1986], and a nonspecific divalent cation requirement for oxygen evolution has been observed. Calcium binding in higher plants appears to be well protected by the extrinsic 24 kD polypeptide. Lack of calcium, and replacement of calcium with strontium, have both been found to strongly affect the multiline EPR signals of spinach preparations [Boussac et al., 1989; Sivaraja & Dismukes, 1989]. Without calcium the complex does not advance beyond S_3, and a new EPR signal which is reported to arise from the S_3 state of calcium-depleted preparations has been found. Evidence that calcium and chloride activate in sequence has been reported [Waggoner & Yocum, 1990].

A chloride requirement for oxygen evolution has been detected in cyanobacteria [McSwain et al., 1976; Stewart et al., 1985]. More extensive studies on the specific effects of chloride and other anions have been carried out in preparations from spinach. These are summarized in greater detail in the introductions to Chapters 4 and 5, and thoroughly reviewed by Critchley (1985) and Babcock (1987). Broadly, two effects of chloride have been studied. One is the specific effect of chloride and other anions on the EPR signals and other spectroscopic signatures of the oxygen evolving complex. For example, chloride or bromide are necessary for advance from S_2 to S_3, and for formation of the multiline EPR signal [Theg et al., 1984; Ono et al., 1986, 1987; Yachandra et al., 1986]. A second effect of halide is the protective influence that chloride and other anions exert with respect to loss of manganese and the extrinsic polypeptides [Homann, 1988b; Wydryznski et al., 1990]. With regard to separating the protective and the specific functions of halide, the reversibility of the experiment is important; many of the effects of chloride-depletion have been shown to be reversible upon the re-addition of chloride.

The specific effects that halide has on the oxygen evolving complex have prompted at least two suggested types of action for halide. One is that halide binds as a ligand to manganese, protecting a water or hydroxide-binding site [Wydrzynski & Sauer,

1980; Sandusky & Yocum, 1986]. Alternatively, halide could bind in a protein-formed pocket near the oxygen evolving complex [Coleman & Govindjee, 1988] or bridge a water ligand and a positively charged amino acid [Homann, 1988b]. At present, no direct evidence exists for either alternative.

Goals of this work

The goal of the work presented in this thesis is to gain spectroscopic evidence for or against halide ligation to the manganese in the oxygen evolving complex. Results from EPR and EXAFS spectroscopy of fluoride-inhibited preparations from spinach are described in Chapter 4, and in Chapter 5 the EXAFS of bromide-substituted samples from *Synechococcus* are presented. Chapters 3 and 6 contain general information about the structure of the oxygen evolving complex. The EXAFS of spinach and *Synechococcus* PSII preparations, performed at liquid helium temperatures, are compared in Chapter 3. Such a characterization is important, because the other EXAFS studies depend on the ability to detect and analyze small changes in the spectra. In Chapter 6, an electron spin echo spectroscopy study of ^{15}N-labelled PSII preparations from *Synechococcus* is reported. In this experiment, the single unidentified nuclear envelope modulation frequency in the multiline EPR spectrum from the oxygen evolving complex is shown to be due to nitrogen.

Chapter 2

Materials and Methods

In this chapter the methods of protein preparation, X-ray absorption spectroscopy data collection, and X-ray absorption fine structure (EXAFS) data analysis are described.

Preparation of oxygen-evolving Photosystem II particles from *Synechococcus* sp.

The techniques of growing *Synechococcus* and preparing Photosystem II (PSII) particles are extensions of procedures developed previously in this laboratory (McDermott et al., 1988). The procedure outlined here was optimized for yield of PSII and specific activity of PSII as judged by oxygen evolution assays and yield of the multiline EPR signal. These improvements, which result in approximately doubling the specific activity reported by McDermott et al. (1988), were necessary to perform the electron spin echo experiments described in Chapter 6 and the X-ray absorption experiments described in Chapters 3 and 5. Two modifications of the preparation, the growth on bromide salts to replace chloride in the oxygen-evolving complex, and the growth on limiting amounts of nitrate as the sole nitrogen source, are also described.

Growth of Synechococcus sp.

The source of the thermophilic bacteria *Synechococcus* sp. was a continuous culture originally supplied to this laboratory by Dr. Akihiko Yamigishi (Yamagishi & Katoh, 1983). For large-scale preparation, *Synechococcus* was grown in 10-liter volumes. The standard growth media, which was modified from Dyer & Gafford (1961), is in Table 2.1. The salt compositions were chosen to isolate the added chloride. It was found that copper contamination in the final PSII preparation gave rise to a large g=2.1 EPR signal which interferes with EPR and ESE measurements, and so copper was removed from the growth medium. In the absence of copper, cytochrome c_{553} is induced to replace plastocyanin (Bryant, 1986).

Synechococcus sp. grows at 55 °C, and sterile technique is not necessary as the cultures show no contamination other than a yellow bacterium which does not interfere with the PSII preparation. The general growth procedure is to prepare 10 l of media and allow it to warm to ~40 °C in a 20 l aquarium tank using a submersible heater (Jäger) before inoculating with cyanobacteria. A bubbling stone lies at the bottom of the

Table 2.1

Growth media for *Synechococcus* sp.[a]

Stock Solutions	g/l	mM[b]
Major (x100[c])		
KH_2PO_4	25	1.8
$K_2HPO_4 \cdot 3H_2O$	32.8	1.4
$NaNO_3$	50	5.9
KNO_3	50	5.0
	pH to 7.5 with NaOH	
Minor (x200)		
H_3BO_3	6.8	0.55
EDTA(Na_2)	6	0.16
$(NH_4)_6Mo_7O_{24} \cdot 4H_2O$	4.4	0.18
$MnSO_4 \cdot H_2O$	0.7	0.020
$ZnSO_4 \cdot 7H_2O$	0.132	0.0025
$Co(NO_3)_2 \cdot 6H_2O$	0.003	0.000055
	(0.3 ml of 10mg/ml solution)	
Mg^{+2} (x1000)		
$MgSO_4 \cdot 7H_2O$	150	0.61
Ca^{+2} (x1000)		
$Ca(NO_3)_2 \cdot 2H_2O$	128	0.55
Fe^{+3} (x1000)		
$Fe_2(SO_4)_3 \cdot H_2O$	24	0.059
Halide (x500)		
NaCl	75	3.0
or NaBr	130	

(a) Growth medium is modified from Dyer & Gafford (1961)

(b) Final concentration in mixed media.

(c) i.e., dilute by 100 to prepare growth media.

aquarium to supply a mixture of 5% CO_2/95% N_2 and to mix the media. It is important to monitor the pH after inoculation, because the pH of the media can decrease rapidly before the added bacteria reach log phase growth. The ratio of PSII/PSI in isolated thylakoids increases as illumination is increased during growth. For the first 12 hr the tank is protected from light. Between 12-30 hr light is supplied by a single incandescent bulb (~500 μE/(m^2-sec)), from 30-50 hr the intensity is increased to ~900 μE/(m^2-sec) with 2 additional incandescent bulbs, and for the last 12 hrs ~900 μE/(m^2-sec) is added from two fluorescent lights. Figure 2.1 is a growth curve from *Synechococcus* grown in this way. It was found that the greatest total oxygen evolution activity (specific activity x mg Chl) was obtained in thylakoids harvested at ~72 hr after inoculation.

Growth of Synechococcus sp. in bromide media.

To substitute bromide for chloride in the PSII particles, *Synechococcus* was grown and PSII particles were isolated in media in which bromide replaced chloride. The media were the same as in Table 2.1 for growth and Table 2.3 for PSII isolation, except that NaBr and $CaBr_2$ replaced NaCl and $CaCl_2$. Precautions were taken to minimize contamination from chloride. Since chloride is a common contaminant in glass, plastic containers were used when possible. The growth tank was soaked with 0.5 M NaBr at 55 °C for two days prior to use. Chemicals were chosen which contained a minimal amount of chloride contamination. From the listed contaminations in the chemicals used, the final growth media contained approximately 10 μM Cl^-. It was found that cyanobacteria could not grow beyond three cycles of inoculation/growth, as described above, in a media prepared in this way without the addition of NaCl or NaBr. This indicates that this contaminating chloride level is insufficient for sustained growth. The preparations used for spectroscopy were from cyanobacteria harvested after at least 5 cycles of inoculation/growth, as described above, in media containing 3 mM Br^-. The total yields of oxygen evolution activity as well as the specific activies were unchanged in samples prepared in the presence of Br^- instead of Cl^-.

Growth of Synechococcus sp. in $^{14}NO_3^-$ and $^{15}NO_3^-$

To substitute ^{15}N for ^{14}N in the OEC from *Synechococcus*, the growth medium was altered to make KNO_3 the sole source of nitrogen. This growth medium is described in Table 2.2. $K^{15}NO_3$ (99%) was obtained from Cambridge Isotopes. To minimize the cost of the isotope replacement experiments, the concentration of added N was reduced from 11 to 4 mM. This did not affect the yield of PSII prepared from a 10 l culture, but the cyanobacteria took longer to grow to maximum density (sometimes

Figure 2.1 Typical growth curve for *Synechococcus* sp. The relative concentration of cells during growth was monitored by counting the number of cells (in an arbitrary volume) under a light microscope. Each point represents the average and standard deviation of 5-6 cell count determinations per time interval. The results from two separate batches of *Synechococcus* are shown. The vertical arrow indicates the typical period for cell harvesting, at 72 hours after inoculation. Growth conditions are discussed in the text.

Figure 2.1 Growth curve for *Synechococcus* sp.

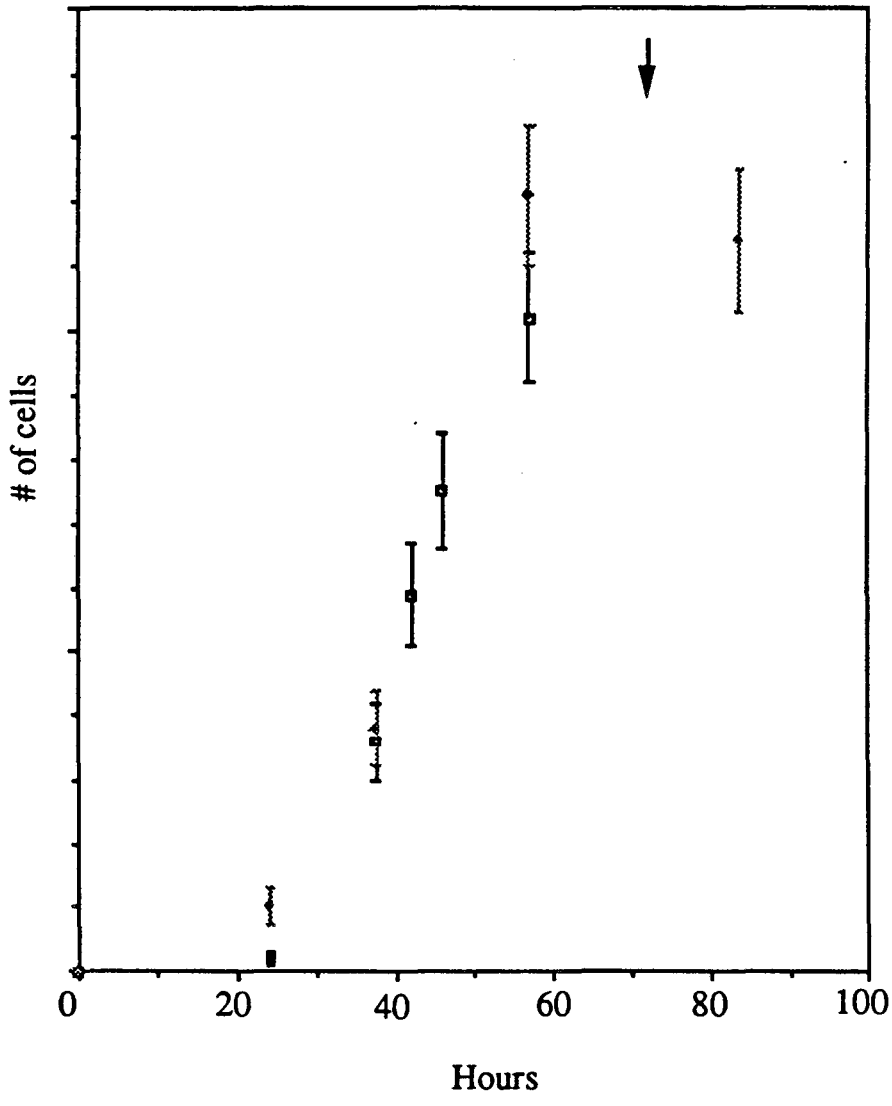

Table 2.2

NO_3^--based growth medium for *Synechococcus* sp.

Major (x 1)[a]	g/10 l	mM[b]
KNO_3	4.0	4.0
KH_2PO_4	6.8	5.0
$Na_2HPO_4 \cdot 7H_2O$	8.0	3.0
Stock solutions		
Minor (x 200)	g/l	
H_3BO_3	6.8	0.55
$Na_2MoO_4 \cdot 2H_2O$	3.6	0.018
$MnCl_2 \cdot 4H_2O$	0.8	0.020
$ZnSO_4 \cdot 7H_2O$	0.132	0.0025
$CoSO_4 \cdot 7H_2O$	0.003	0.000055
	(0.3 ml of 10 mg/ml solution)	
Mg^{+2} (x 1000)[c]		
$MgSO_4 \cdot 7H_2O$	150	0.61
Ca^{+2} (x 1000)		
$CaCl_2 \cdot 2H_2O$	80	0.55
Fe^{+3} (x 1000)		
$FeCl_3 \cdot 6H_2O$	16	0.06

(a) These components were mixed first in 1 l H_2O. The pH was adjusted to ~7 with NaOH. The mixture was added to the final growth medium, and that was adjusted to pH ~8. Since this growth medium is not buffered, it is important to check the pH often during growth.
(b) Final concentration in mixed media.
(c) Since this is the major source of sulfur it should not be substituted for a different magnesium salt.

several days instead of 72 hr). For ^{15}N labelling, bacteria were grown first on $^{14}NO_3^-$-based media through two generations. Bacteria "trained" on NO_3^- were then used to inoculate a 250 ml volume of $^{15}NO_3^-$-based medium. The final 10 l culture of $^{15}NO_3^-$-based was inoculated with the yield from this small volume.

Preparation of PSII from Synechococcus sp.

The yields discussed here were typical for bacteria grown and harvested as above. The necessary buffers are listed in Table 2.3.

Cells were harvested at 8000 x g in a Sorvall GSA rotor (6 min, 6000 rpm) or Sorvall HG swinging bucket rotor (6-10 min, 4500 rpm). Cells were resuspended in Medium 1 to 500 ml and pelleted at 6000 rpm for 20 min. During this and succeeding resuspensions, care was taken to avoid an orange-yellow edge of the pellet which was sometimes present and was due to contaminating bacteria. A very hard, waxy bottom of the pellet was also left behind, as it was due to dead cells. Cells were resuspended and homogenized with a tissue homogenizer into 100 ml of Medium 2. The cell walls were broken with 100 mg lysozyme by incubating for 30 min in a 37-42°C water bath. During this incubation cells were kept dark and were stirred gently. After incubation cells were pelleted at 15000 xg (Sorvall SS34 rotor, 18000 rpm, 15 min) and resuspended and homogenized into 80 ml of Medium 3. After this step all procedures were performed on ice and under dim light to minimize degredation of the oxygen-evolving complex. The cells were broken in a pre-chilled French pressure cell at 5000 psi. Each 40 ml volume was passed twice through the French press. To degrade DNA, which otherwise can pellet with the thylakoid membranes, the broken cell mixture was incubated for 30 min on ice with 1-10 μg of DNAase (Sigma). Mg^{+2}, a cofactor of DNAase, was added to a final concentration of 5 mM. As before, cells were kept in the dark and were stirred during the incubation. After the incubation EDTA was added to a concentration of 10 mM in order to chelate nonspecific Mn^{+2}, and the cell walls and unbroken cells were pelleted at 10000 x g (10K rpm, 15 min, SS34 rotor). The supernatant was poured off into ultracentrifuge tubes, and the thylakoid membranes were pelleted at 100,000 x g (1 hr, 50K rpm, 60 Ti rotor, 4°C). The supernatant of this and subsequent thylakoid wash steps was brilliant blue and contained most of the phycobiliproteins from the cyanobacteria. The thylakoid membranes were resuspended using a homogenizer into 100 ml of Medium 4 and pelleted as before. Medium 4 contains 0.5 M sucrose which is an effective cryoprotectant for these membranes. The preparation can be resuspended in Medium 4 and stored at -80°C for several months

Table 2.3

Buffers for PSII preparation from *Synechococcus* sp.

Medium #1	Medium #2
50 mM Hepes, pH 7.5	0.4 M Mannitol
10 mM NaCl	5 mM EDTA
~1 mM PMSF[a]	50 mM Hepes, pH 7.5
	1 mM PMSF

Medium #3	Medium #4
50 mM MES pH 6.5	0.5 M Sucrose
10 mM NaCl	50 mM MES pH 6.5
1 mM PMSF	5 mM $CaCl_2$
	1 mM PMSF

(a) It is sufficient to add a very small amount of solid PMSF (a protease inhibitor) directly to the solution. Alternatively, PMSF is added from a stock solution in ethanol.

with a loss of only ~5 % of the specific oxygen evolution activity.

Thylakoids isolated in this way typically had oxygen evolution activities of 350-450 μmole O_2/(mg Chl-hr). The typical yield of chlorophyll at this stage from a 10-liter culture was 70-90 mg Chl.

PSII was separated from PSI in the thylakoid membrane by specific extraction with detergent. The thylakoids were first washed 2-3 times to remove phycobilisomes by resuspending in Medium 4 and then pelleting the membranes as described above. The thylakoids were then resuspended to 1 mg/ml Chl in Medium 4. It is especially important to homogenize well during this resuspension. The detergent extraction was performed at room temperature, and it was important to bring the centrifuge rotors to room temperature as well to avoid cooling the preparation. Because the concentration of detergent which is optimal to solubilize PSII selectively from PSI is sensitive to a difference of 0.05%, and differs between preparations, a "pre-extraction" curve was important. Four 1 ml aliquots of the 1 mg/ml Chl thylakoid preparation are used. β-octyl gluoside was added from a freshly prepared solution of 10% (w/v) in water to a final concentration of 0.60, 0.65, 0.70, and 0.75% (w/v). The aliquots were mixed and then immediately centrifuged for 30 min at 300000xg (50,000 rpm in a 50.3 Ti rotor) at 24 °C. After centrifugation the supernatants of the aliquots were drawn off immediately and were kept on ice during the oxygen evolution assays. Both oxygen evolution and Chl concentration were determined for each aliquot. It was important to mix each supernatant before these measurements. The detergent concentration that gave the optimal specific activity was chosen for the bulk extraction. In most, but not all, cases extraction with 0.65% β-octyl gluocoside resulted in the highest specific activity.

The bulk extraction was performed in the same way. The 1 mg/ml Chl thylakoid suspension was brought to room temperature before the detergent was added. After adding the β-octyl glucoside, the solution was mixed briefly and immediately centrifuged for 1 hr at 24 °C (50K rpm, 60 Ti rotor). The supernatant was poured off and immediately diluted to twice the original volume with Medium 4. The PSII particles were pelleted from this supernatant by centrifugation for 4 hr at 300000xg (50K rpm, 60 Ti rotor) at 4°C. The pellets were collected, resuspended in Medium 4, and pelleted for 2 hr using the same conditions.

The PSII particles havd a typical oxygen evolution activity of 3500-4500 μmole O_2/mg Chl-hr. Usually 80% of the total activity present in the thylakoids (specific activity x mg Chl) was extracted.

For ESE and EPR measurements, 1 mM EDTA was included in this and subsequent steps. This was important to suppress a small signal from Mn^{+2} which interfered with the measurements. For EPR/ESE samples, the PSII particles were usually resuspended once more in Medium 4 without sucrose and pelleted as above for 1-2 hrs. To make very concentrated EPR samples, the pellets were scraped from the centrifuge tubes and placed in siliconized depression plates typically used for protein crystallization. A few drops of Medium 4 + 50% glycerol (v/v) were added and a small paintbrush used to thoroughly mix the suspension. The mixture was drawn directly into the barrel of a 1 ml Hamilton disposable syringe. A long (10 inch) needle was attached to the syringe and the PSII suspension was dispelled evenly into the EPR tubes. Between 4 and 5 EPR samples, 0.3 ml volume each and about 4 mgs Chl/ml, could be made from a PSII preparation starting with one 10 l culture

For X-ray absorption measurements, EDTA was not added to the PSII particle wash steps. In this way, adventitious Mn^{+2} was more likely to be EPR-observable. After being pelleted in Medium 4, the PSII particles were resuspended in Medium 4 minus sucrose and pelleted as above for 4-8 hr. The pellets, which were then very hard, were scraped from the centrifuge tubes and placed in siliconized depression plates. One or two drops of glycerol were thoroughly mixed into the pellets with a small spatula. The suspension was packed tightly into Lucite sample holders and the top of each sample was made as smooth as possible with the edge of the spatula. Typically 3-4 X-ray spectroscopy samples, approximately 0.120 ml volume and 10 mg Chl/ml, could be made from one 10 l culture of *Synechococcus*.

The EPR and X-ray spectroscopy samples were prepared under a dim green safety light in the cold room (4 °C). Samples were dark-adapted (incubated in total darkness) for 1 hr before being frozen at 77 K. Samples were poised in the S_2 state using low temperature illumination. Samples were immersed in a methanol/solid CO_2 bath and allowed to equilibrate for 3-5 min. The samples were then illuminated for 5-10 min with a 400 W tungsten lamp thermally isolated from the sample by a 5 cm water filter containing 5% aqueous $CuSO_4$. The amplitude of the multiline EPR signal was monitored as a function of illumination time. Typically the amplitude of the multiline signal did not increase after 5 min illumination time.

Photosystem II preparations from spinach

Photosystem II-enriched membranes were prepared from spinach leaves using a modified version of the preparation described by Berthold et al. (1981) as communicated by Dr. Jean-Luc Zimmermann. Washed, de-veined leaves from 4-6 bunches of spinach

were ground in a Waring blender for ~10 sec in 800 ml Medium A [0.4 M NaCl, 4 mM $MgCl_2$, 1 mM EDTA, 5 mM sodium ascorbate, 2 mg/ml bovine serum albumin (BSA) (Sigma), 50 mM Hepes, pH 7.5]. The sodium ascorbate and BSA were added to Medium A shortly before the grinding procedure. The ground mixture was strained in two steps through 4 and then 16 layers of cheesecloth and immediately centrifuged (Sorvall GS3 or GSA rotor, 6000 rpm, 6 min, 4°C). The grinding step and subsequent steps were performed in the cold room (4°C) and as quickly as possible to minimize proteolytic degradation. All subsequent steps were performed under dim light and on ice. The pelleted chloroplasts were resuspended into 320 mls of Medium B [150 mM NaCl, 8 mM $MgCl_2$, 50 mM Hepes pH 7.5] and centrifuged again as above. The broken chloroplasts were then resuspended into Medium C [15 mM NaCl, 5 mM $MgCl_2$, 50 mM Mes pH 6] to a chlorophyll concentration of < 2 mg Chl/ml. Triton X-100 detergent pre-dissolved in Medium C was added such that the final mixture was 2 mg Chl/ml and 25 mg Triton/mg Chl. Typically 100-150 mg Chl were obtained from 4-6 bunches of spinach. This mixture was incubated with gentle stirring and in complete darkness for 20 min. The solubilized PSI membranes were then separated from the PSII-enriched membranes by centrifuging the mixture (Sorvall SS34 rotor, 18000 rpm, 30 min). The pelleted PSII membranes were resuspended in Medium D [0.4 M sucrose, 5 mM $CaCl_2$, 5 mM $MgCl_2$, 50 mM Mes pH 6.0] and subjected to low speed centrifugation (2000 rpm, 2 min) to remove excess starch. It is important to resuspend the membranes well for this step. After the low speed centrifugation the supernatant was poured off the resulting grey pellet, and PSII membranes were then pelleted by centrifugation of the supernatant (18000 rpm, 30 min).

The pelleted membranes were either stored in Medium D at -80°C for future use, or subjected to various treatments (as described, for example, in Chapter 4). For larger preparations (i.e., 8 bunches of spinach) the volumes of Media A and B were doubled. Typically, 70-130 mg Chl of PSII were obtained from 4-8 bunches of spinach, with specific activities of ~600 μmole O_2(mg Chl-hr)$^{-1}$. Samples were poised in the S_1 and S_2 states as described above.

Oxygen evolution

Oxygen evolution activity measurements were performed using a Clark-type oxygen electrode (Yellow Springs Instruments, Ohio). The contents of the electrode cuvette were stirred continuously with a small magnetic stir bar. The cuvette was maintained at 24 °C through a water jacket attached to a circulating temperature control bath. Illumination was provided by a slide projector lamp. A 360 nm cutoff filter was

used to exclude UV light from the cuvette. A spherical flask containing water was in place before the electrode cuvette to both focus the light and to act as a heat filter. DCBQ was used as an electron acceptor. DCBQ was added from a stock solution in DMSO to a final concentration of 2 mM. Chlorophyll assays were performed using acetone extracts in the method of Arnon (1949). Chlorophyll concentrations used for oxygen evolution assays were ~10 μg/ml for PSII preparations from *Synechococcus* and ~50 μg/ml for PSII membranes from spinach.

X-ray Absorption Spectroscopy.

The data presented in Chapters 3, 4 and 5 were collected on beamlines X9A and X19A at the National Synchrotron Light Source (NSLS) at Brookhaven National Laboratory, and beamlines 6-2 and 4-2 at Stanford Synchrotron Radiation Laboratory (SSRL). The synchrotron laboratory at SSRL has been described (Guiles, 1988; McDermott, 1987). In this section some characteristics of the NSLS and of the beamlines used there are described. In addition, aspects of the use of a new multi-element solid state detector and low temperature liquid helium cryostat are discussed.

Synchrotron radiation sources

Synchrotron radiation is high-intensity radiation produced by electrons travelling at relativistic speeds. At these speeds, when electrons are accelerated into an arc they emit radiation tangental to the arc and directed towards their direction of motion. This synchrotron radiation has several properties which make it a powerful source for spectroscopy (see Winick, 1987; Kim, 1986). The radiation is highly collimated, with a very small vertical rise angle, and is polarized in the plane of the electron orbit. The emission is broad band, with energies ranging between the infrared and hard X-rays.

Electron storage rings use a combination of bending magnets and "insertion devices," which have many magnetic poles in a short length, to produce synchrotron radiation. The intensity and wavelength output of different synchrotron facilities depend on their operating energies E, the operating currents I, and the strength of the magnetic fields in the bending and insertion device magnets. The wavelengths available from electrons travelling with kinetic and potential energy E (maintained in the storage rings by the input of radiofrequencies) which are bent by a magnetic field B are limited by a "cutoff" value, E_c:

$$E_c[\text{keV}] = 0.665\ E^2[\text{GeV}^2]\ B[\text{T}]$$

The photon flux (in (photons/sec/mrad/0.1 % bandwitdth)) available from the same bending magnet depends on the current I (Kim, 1986):

$$\frac{\delta F}{\delta \theta} \approx E\,I$$

A wiggler insertion device generally operates at a higher magnetic field than a bending magnet, and also increases the intensity of radiation by a factor equal to about twice the number of magnet poles. In Figure 2.2 is plotted the photon flux available from the bending magnets at SSRL, which operates with electron energies at 3.0 GeV, from the NSLS, which operates with electron energies at 2.5 GeV, and from the Advanced Light Source (ALS, under construction), which will operate at 1.5 GeV. This plot combines the operating energies of the rings with the average currents of operation (40 mA for SSRL, 100 mA for the NSLS, 400 mA (expected) for the ALS). Also plotted are the photon fluxes available from the 54 - pole wiggler insertion devices on beamline VI-2 at SSRL, and the (expected) 13.6T wiggler for the ALS. The number of poles for the ALS wiggler device has not yet been decided. For X-ray absorption experiments of transition metals (5-10 keV), it can be seen that these sources differ by two orders of magnitude in flux. As will be discussed later, although the beamline components in general attenuate the intensity incident on the sample, it is the count rates available for the solid-state X-ray fluorescence detectors which limit the amount of usable flux for our experiments. The operating conditions at the NSLS provide fluorescence counts that are still above this limiting count rate. The advantage of the higher intensities available from the insertion devices at SSRL is that more methods to increase the ratio of signal to scatter, which generally also decrease the intensity of the beam, can be used to optimize the experiment.

The components in the beamline generally determine the ratio of fundamental to harmonic content and the energy resolution in the beam that arrives at the sample. Because the higher energy harmonics have a greater scattering cross section, their presence both worsens the ratio of signal to scatter that arrives at the fluorescence detector and decreases the linearity between detector components. Figure 2.3a is a diagram of typical beamline components. In general, a pair of slits controls the intensity incident to the monochromator. A focussing mirror may be either before or after the monochromator. X-ray mirrors are metal plated and have cutoff energies due absorption by the metal plating. They can be used either to focus intensity to a small spot size, or at

Figure 2.2 Relative photon fluxes from some synchrotron sources. The calculated photon flux as a function of energy is plotted for several sources of synchrotron radiation. The National Synchrotron Light Source (NSLS) at Brookhaven National Laboratory, Stanford Synchrotron Radiation Laboratory (SSRL) at the Stanford Linear Accelerator site, and Advanced Light Source (ALS), under construction at Lawrence Berkeley Laboratory, are represented. The curves were adapted from Atwood et al., 1986 (SSRL); Lawrence Berkeley Laboratory PUB-643, 1988 (ALS); Gmür et al., 1989 (NSLS).

Figure 2.2
Relative Photon Fluxes of some Synchrotron Sources

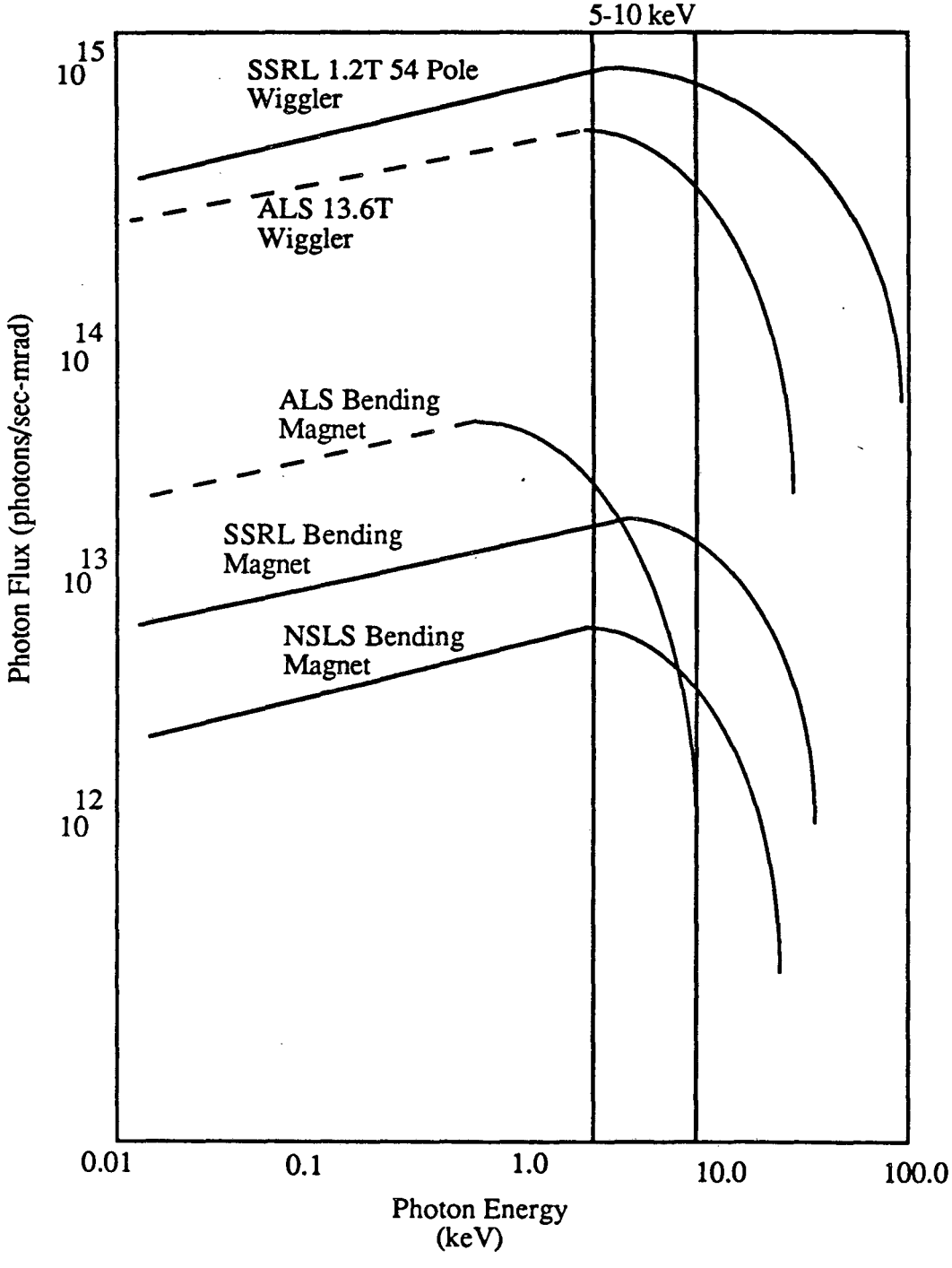

glancing angles to reject harmonics. The monochromator is a pair of channel-cut Si crystals, and the wavelength of X-ray is tuned by Bragg diffraction from the crystal planes. Another pair of slits controls the size of the beam entering the experimental area.

The choice of crystal cut is important. Each face has a characteristic separation **d** between lattice planes which determines the resolution of the monochromator, the "glitch" spectrum (characteristic wavelengths at which other crystal planes interfere with the outgoing wavelength), and the flux attenuation of the monochromator. As **d** decreases, both the energy resolution and flux attenuation increase. X-ray absorption fine structure (EXAFS) and X-ray absorption near-edge structure (XANES) experiments have different requirements for energy resolution and flux. XANES experiments are designed to measure differences as small as 1 eV, which places stringent conditions on the energy resolution. EXAFS experiments require less energy resolution (the EXAFS oscillations are on the order of several eV) and so resolution can be sacrificed for greater throughput.

Unfortunately, the crystals with the greatest throughput (Si<111>) have many glitches in the Mn EXAFS region (6.4-7.2 KeV). Our recent experiences with Si<111> crystals have indicated that the use of a "leveling" system available on beamline X19A at the NSLS has made it possible to use Si<111> crystals to acquire EXAFS data which are not affected by the crystal glitches. This leveler monitors the intensity before and after the monochromator, and adjusts a piezoelectric transducer voltage applied to one crystal of the monochromator to keep these intensities at a constant ratio. The effect of the applied voltage on the crystal is to pull it slightly from parallel alignment, a process known as "detuning." As the crystals are detuned the effect of the crystal glitch is minimized. The leveler operates point by point as the X-ray energy is scanned, which slightly increases the time spent per data point. Without such a glitch rejection scheme, Si<400> crystals with a focussed beam to counteract the intensity loss through the crystals are good for EXAFS. These crystals have no glitches in the Mn EXAFS region. Alternatively, one orientation (set 220-2 at SSRL) of Si<220> crystals has only one glitch at 6540 eV and two small glitches near 7100 eV. The other orientation has several glitches between 6500-7100 eV, so it is necessary to get a spectrum from the set of Si<220> crystals before use.

For XANES experiments, energy resolution is more important than throughput. The focussing mirror tends to degrade the resolution, so it is not used. We found that Si<400> crystals, while having the best energy resolution, were prone to crystal heating effects which changed the lattice spacing and affected the energy calibration. Si<111> crystals did not give good energy resolution. With Si<220> crystals we attained very

Figure 2.3 Experimental arrangement for X-ray fluorescence detection. In Figure 2.3a, the typical components present in X-ray beamlines are shown. The components are described in the text. The mirror and levelling system are not present in all beamlines. In Figure 2.3b, the experimental arrangement for fluorescence detection is shown.

Figure 2.3a
Beamline components

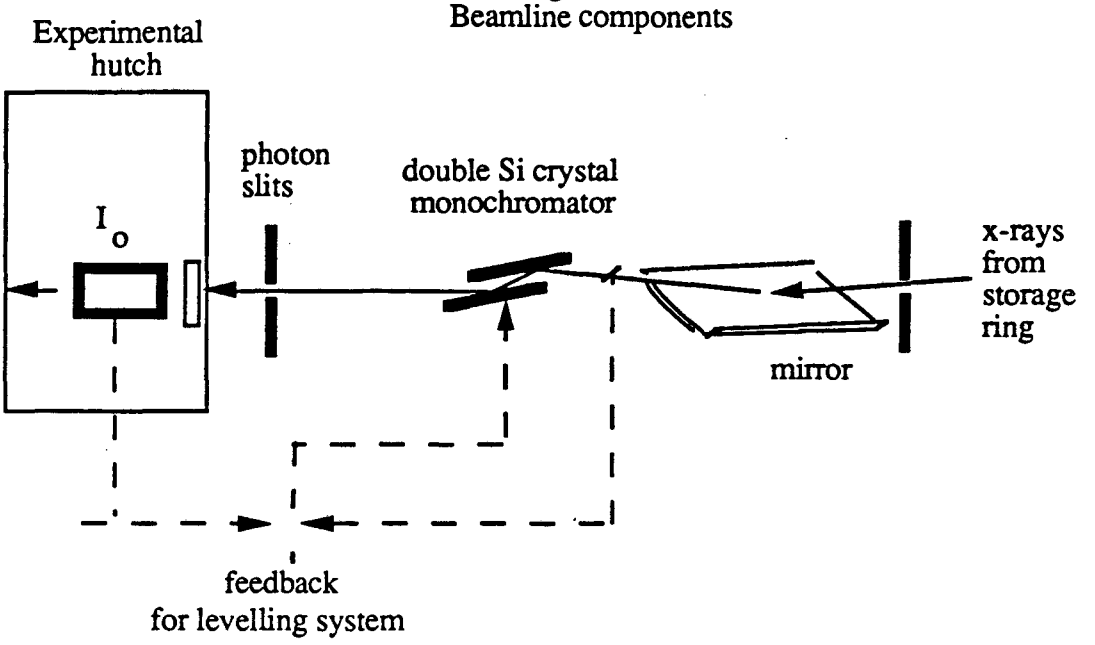

Figure 2.3b
Fluorescence Detection

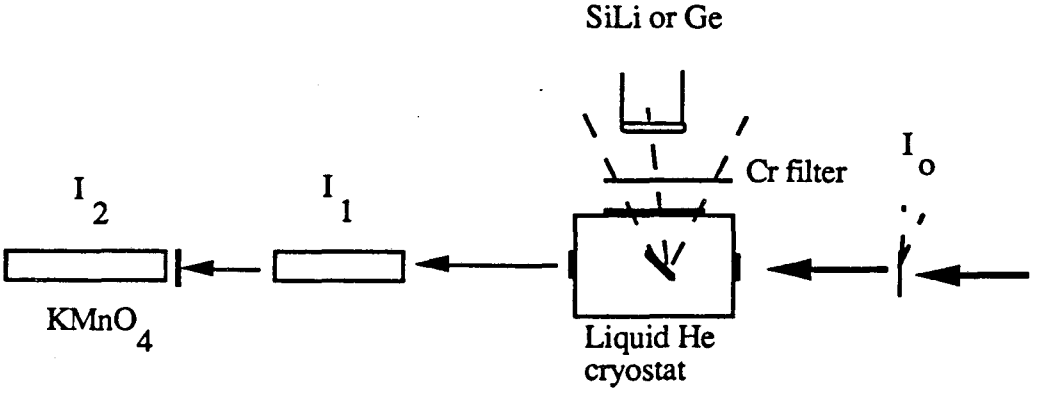

good energy resolution (1.5 eV at 6543 eV), and they were used for the data described in this thesis.

X-ray Fluorescence Detection.

Figure 2.3b is a diagram of the detection scheme forX-ray fluorescence and absorption. In our experiment, a small percentage of the incoming X-rays are scattered by a piece of kapton, and are detected by a photomultiplier tube. The intensity after the sample is measured with an ionization chamber purged with N_2. A sample of $KMnO_4$ is taped to the face of a second ionization chamber and provides energy calibration.

The sample temperature is kept at 10K in a liquid helium cryostat (Oxford Systems, Oxford, England). The cryostat has small (1.5 cm diameter) entrance and exit ports, and larger (5 cm diameter) side ports to collect a large solid angle of fluorescence. The sample is attached to a rod which is removable from the cryostat. The orientation of the sample can be adjusted with respect to the incoming X-rays. Cold helium is circulated through a jacket around a copper heat exchanger which is in contact with the sample space. The sample space can be flushed with helium gas, or kept under vacuum ($\sim 10^{-3}$ torr). This cryostat maintains temperature stability at 10 K of $\pm$ 0.5 K over several hours with a liquid helium flow of approximately 0.5-1.0 l/hr.

Samples are placed in lucite holders of approximately 2.5 x 0.5 x 0.2 cm. The sample holders are hollowed out (2.3 x 0.4 cm) and hold ~120 µl. Mylar tape holds the sample on one side, and the other side is directly exposed to the X-ray source. The width of the holders was chosen in part to fit in the sample receiver of the Air Products liquid helium cryostat used in EPR studies. In this way, both EPR and X-ray spectroscopy can be performed on the same sample. The samples fit onto an aluminum holder which is held on the end of the Oxford cryostat sample rod. The manipulations of loading and unloading the protein samples from the aluminum holder were performed under liquid nitrogen, and under dim green light.

Fluorescence from the sample is detected at right angles from the incoming beam. This is to minimize the effect of scatter, which is maximal at 0° and 180° from the direction of the incoming X-rays, whereas fluorescence is emitted isotropically. For X-ray absorption of an element with atomic number Z, one method of reducing scattered radiation at the detector is to use a filter made of the element with atomic number (Z-1) [Stern & Heald, 1979]. Energy greater than the fluorescence from element Z is absorbed by the filter. The fluorescence yield of the filter is typically approximately 20%, making this a good method of reducing unwanted photons. The filter also attenuates the yield of the Mn fluorescence; thus, there is a balance between the increase

in signal to noise and the decrease in the number of counts that reach the detector. For some of the experiments reported here, a Cr filter was used.

For most of the experiments in this thesis, a 13-element Ge solid-state detector (Canberra Instruments, New Jersey; generous loans from Dr. Steven P. Cramer and Dr. Britton Chance) was used. The layout of the 13 elements is in Figure 2.4. The central element of the detector receives the highest ratio of fluorescence to scatter, whereas the outer detector elements receive many more scatter counts. In Figure 2.4, the shading of the elements indicates the relative values of the quantity $F/T^{1/2}$, where F is the number of counts due to fluorescence and T is the number of total counts. The shading indicates the average of this value for several experiments. In some experiments a single element silicon-lithium drifted solid state detector (United Scientific) was used. Both detectors have a single element area of ~1.8 cm^2, and have similar associated electronics.The electronic components are diagrammed in Figure 2.5.

The detector element consists of a semi-conductor wafer which is biased by 1 kV. X-ray photons incident on the element create pulses of current with area proportional to the energy of the X-rays. The current pulses are sent to a shaping amplifier, which puts out uniform width pulses with voltage proportional to the x-ray energy. These pulses are sent to a discriminator (single channel analyzer) which is windowed with an upper and lower voltage to choose only pulses at the energy of interest. The discriminator is triggered by the "fast out" of the shaping amplifier. An oscilloscope or multichannel analyzer is used to monitor the pulses coming out of the shaping amplifier and out of the discriminator. The output of the shaping amplifier is sketched in Figure 2.6 as a histogram of counts separated in energy. The K_α and K_β fluorescence from the Cr filter and the Mn sample are shown, as well as the peak due to scatter which will increase in energy as the scan progresses. The K_α peak is selected for by the discriminator.

For fluorescence experiments of dilute samples, the noise level is represented by the statistical fluctuation in the total number of counts that reach the detector, or $T^{1/2}$. Thus, the signal to noise ratio is best represented by the quantity $F/T^{1/2}$, where F is the number of counts due to Mn fluorescence and T is the total number of counts. The experimental set up is designed to maximize this quantity, which is determined by measuring the counts above (N_a) and below (N_b) the Mn absorption edge energy and calculating $(N_a - N_b)/(N_a)^2$. For a typical spinach PSII sample, the output of the shaping amplifier had a $F/T^{1/2}$ value of 5, whereas the discriminator windows could usually be set to attain a signal to noise of 25-30. An additional factor in choosing aspects of the experiment, such as whether or not to use the Cr filter, is the flatness of

Figure 2.4 Diagram showing arrangement of 13 elements on solid state detector face. The elements are approximately 1.5 cm in diameter. Each element is shaded to indicate the ratio $F/T^{1/2}$ for fluorescence data collected from a typical PSII sample. On each element face, each concentric circle represents a unit of $F/T^{1/2}$. Elements are numbered as seen when facing the detector. Data were not collected from element 5, because it had been damaged.

Figure 2.4
Face of 13-element Ge detector

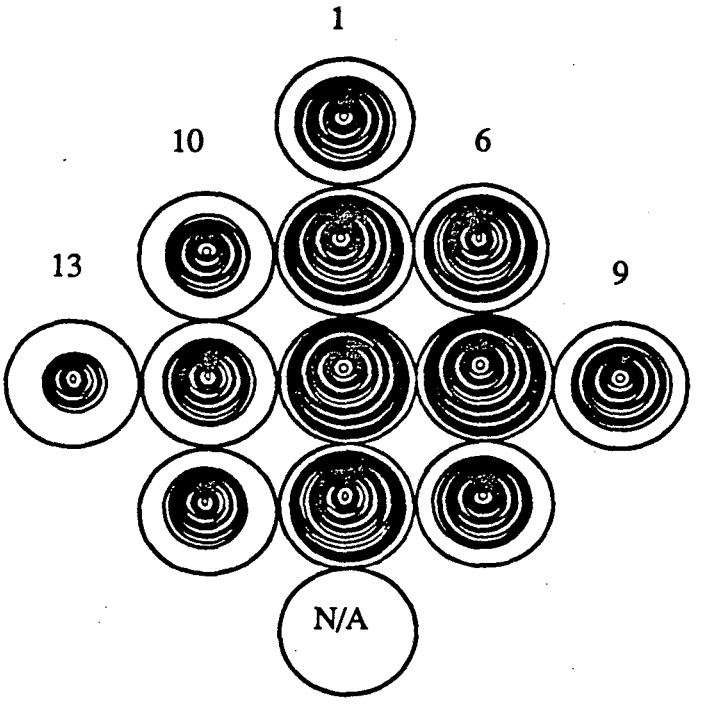

Figure 2.5. Electronic components for X-ray fluorescence detectors. The components used to shape and analyze the output from the detector preamplifier are shown. The components are described in the text. A Princeton shaping amplifier and delay gate generator are used with the single element United Scientific detector, whereas the Canberra Ge detector and amplifier do not require a separate delay gate.

Figure 2.5
Electronic components for energy-resolving x-ray fluorescence detectors

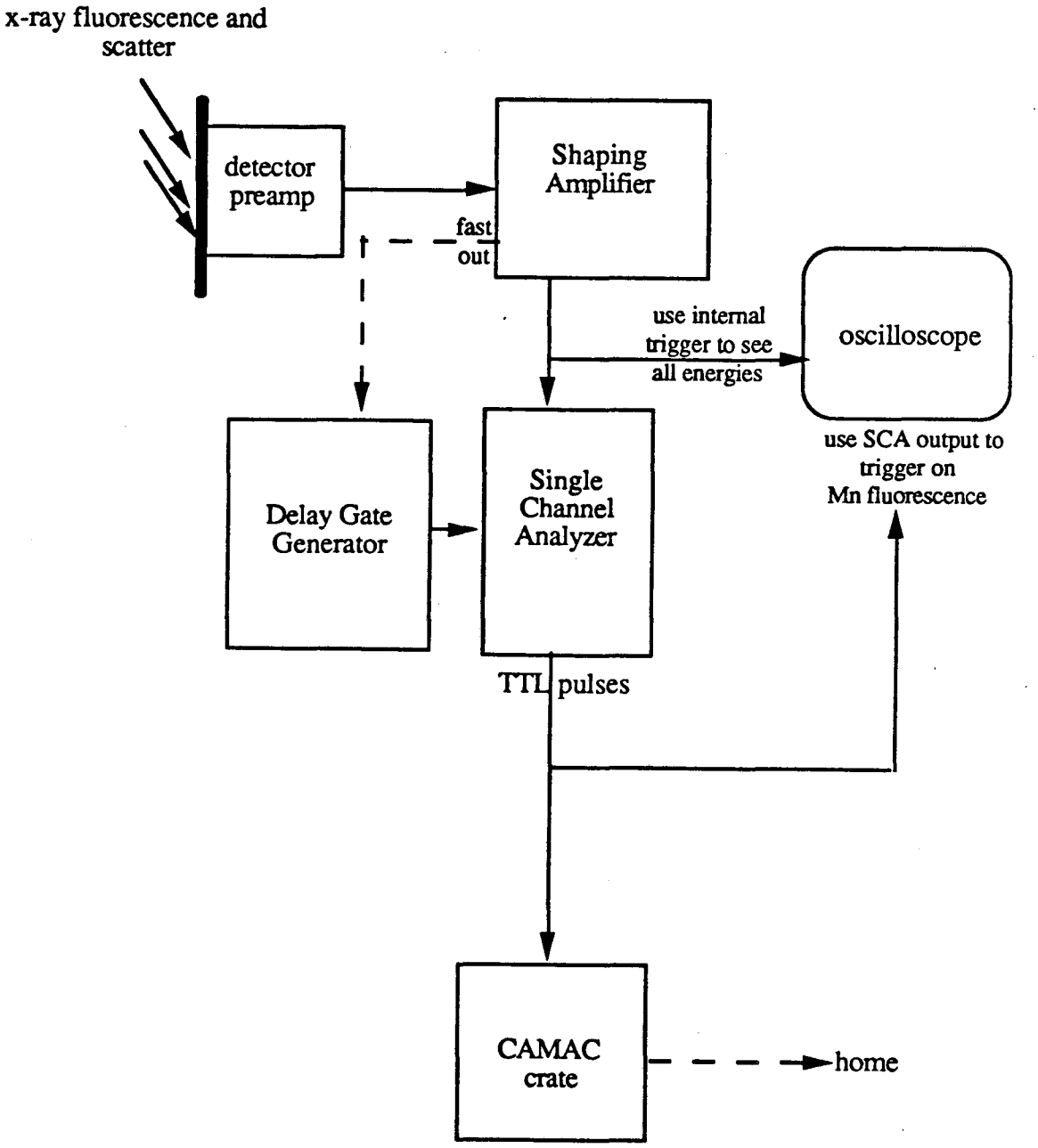

Figure 2.6. Histogram of X-ray photons as a function of energy. In the upper part of the figure, peaks from the sources of x-ray photons in a typical Mn K-edge fluorescence experiment are depicted as a function of energy. The relative amplitudes of the Cr fluorescence and scatter peaks will depend on the conditions of the experiment. The (idealized) settings for the single channel analyzer, used to discriminate against scatter and Cr fluorescence counts, are depicted. In the lower part of the figure, the width of the Mn K_α peak for a typical experiment is shown. This trace was adapted from a peak height analysis of discriminator window settings for the central element (#3 in Figure 2.5) of the Ge detector. A Cr filter was not used in this experiment.

Figure 2.6

Energy-resolved X-ray photons from solid-state detector

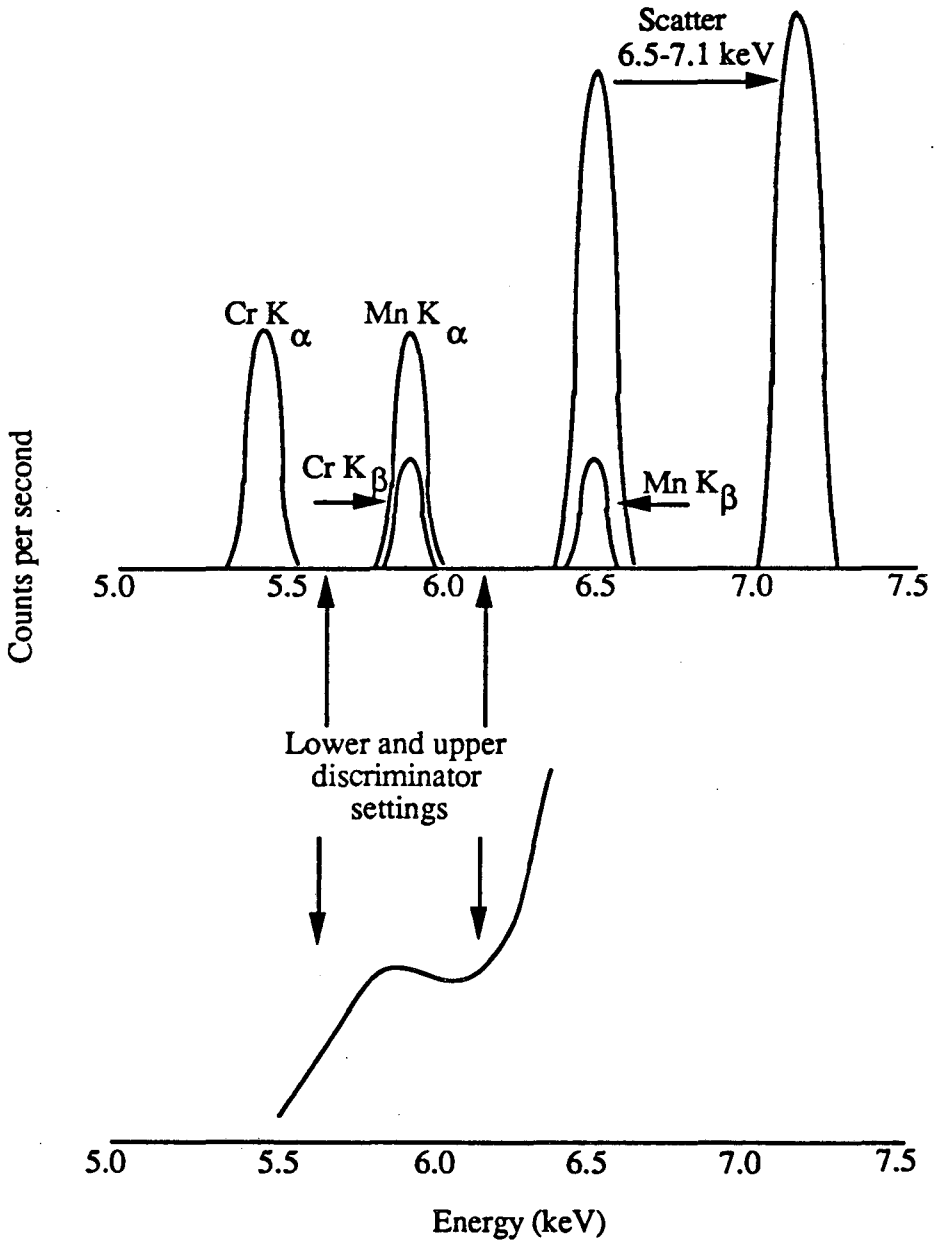

the background before the absorption edge. The shape of the background is dependent on the amount of scatter as well as the characteristics of the discriminator window, and can be difficult to model in the data analysis. This makes it desirable to attain a flat background.

In the optimization of the experimental set up, the linearity of the electronic components plays a large role. The shaping amplifier has a characteristic time constant t_c which determines the count rate at which it becomes saturated (count rates above $\sim 1/(10t_c)$ may be saturating). The Princeton shaping amplifier used with the single element SiLi detector has a 2μs shaping time constant, and puts out triangular shaped pulses. The Canberra spectroscopy amplifier model 2020 was also set with a 2 μs time constant, and outputs a gaussian shaped pulse. The height of the triangular shaped pulse from the Princeton shaping amplifier is read faster by the discriminator, but the amplifier becomes saturated at count rates far below those for the discriminator. Both amplifiers are predicted to saturate at about 50,000 cps and have been determined empirically to saturate at around 40,000 cps. For this reason, the experiment was always optimized to the best value of $F/T^{1/2}$ at 40,000 total counts per second.

Data Analysis

The analysis programs for EXAFS and XANES data were described in detail by Goodin (1984) and Guiles (1989). Two additions to these descriptions of the data analysis are the weighting of data from the multi-element fluorescence detector, and the use of new "curved wave" phase and amplitude functions in simulating the *k*-space data.

As shown in Figure 2.4, the different elements of the multi-element Ge detector receive very different ratios of signal to scatter. Several schemes to weight the data from the different channels before adding them together were empirically tested. For the data used in this thesis it was determined that weighting the channels by their relative signal to noise values ($F/T^{1/2}$) gave the highest ratio of amplitudes of the Fourier transform peaks at low apparent R (<3 Å, due to heavy atom scatterers) and high apparent R (>6 Å, amplitude of high frequency noise contributions). It is of note that others (Cramer and Scott, 1981) suggest weighting data from multi-element detectors by F/T. For our data, weighting the fluorescence channels by F/T gave higher levels of background noise than weighting the channels by $F/T^{1/2}$. This could change with relative amounts of scatter in separate data sets, however, and probably should be re-investigated for data sets of very different quality.

For EXAFS experiments, the added data were treated as described (Goodin, 1984; Yachandra et al., 1987). Briefly, a linear fit to the points before the X-ray

absorption edge is subtracted from the added energy-space data, and the data are normalized to an absorption amplitude of unity. The edge absorption amplitude is calculated as the intersection between a second-order polynomial fit to the data after the edge and a line drawn through the point of maximum amplitude in the absorption edge. After normalization the maximum amplitude in the absorption edge is consistently 1.3 for Mn samples from the oxygen-evolving complex. The data are divided by the absorption due to a free atom (tabulated by McMaster et al., 1969). Then another second-order polynomial fit to the data above the edge is subtracted from the data. This is the subtraction of the absorbance due to scatter and other elements in the sample, which combine to give a low-frequency background. The data are converted from a function of energy E to a function of photoelectron wave vector k as $k = [2m_e/h^2(E-E_0)]^{1/2}$, where E_0 is the threshold energy for photoionization. This leaves the EXAFS oscillations $\chi(k)$, which are described, as a function of photoelectron wave vector k, for a given atom i with backscattering neighbors j at a distance r_j:

$$\chi(k) = \frac{\Delta\mu}{\mu} = \sum_j \frac{N_j}{kr_j^2} |f_j(k,\pi)| \sin[2kr_j + \psi_j(k)]\, e^{-2\sigma_j^2 k^2}\, e^{-2r_j/\lambda_j(k)} \qquad (2\text{-}1)$$

The backscattering amplitude f_j is a function of the atomic number of the backscattering element. The phase shift ψ_j includes the phase shift from the central atom absorber as well as from the backscattering element. The Debye-Waller factor σ describes the attenuating effect due to thermal vibrations, and an additional damping term λ_j accounts for inelastic losses from the backscattering atom. In practice, contributions from σ and λ_j are combined, leading to a strong correlation between the number of backscattering atoms N_j and the damping term σ.

The Fourier transform of equation (2-1) with respect to k gives peaks at distance $(r_j + \psi_j/2)$ which is denoted R'. A window function can be applied to the Fourier transform to remove the effects of high frequency noise. Fourier filtered k-space data is the back-transform of the Fourier transform following the application of a window function. Simulations using equation (2-1) of the Fourier filtered k-space data are used to discriminate between different models of the structure around the central atom (Teo, 1986). The input for the simulations in general consists of N_j, r_j, σ_j, and the term ΔE_0 which allows for differences between the true threshold energy and the one arbitrarily chosen in the conversion from energy to k-space.

The phase and amplitude functions for backscattering atoms have been calculated (Teo & Lee, 1979) using a simplifying assumption that the outgoing photoelectron resembles a plane wave at the backscattering atom. Recently, new phase and amplitude factors have been calculated using a more realistic, "curved wave" approximation (McKale, 1988). Unlike the old values, these new calculated values have a functional dependence on r_j as well as k. The "curved wave" approximated values were tabulated by McKale (1988) for distances between the central absorbing atom and backscattering atoms of 1.5 and 4.0 Å, and are currently used in the EXAFS simulation routines.

Chapter 3

The Structure of Manganese in the Oxygen Evolving Complex from Spinach and *Synechococcus* sp.: New Information from X-ray Absorption Spectroscopy at Low Temperatures

In this chapter the results of Mn X-ray absorption spectroscopy performed at liquid helium temperatures (10 K) on PSII preparations from spinach and *Synechococcus* sp. are presented. The goal of these experiments is to characterize the structure of the oxygen evolving complex as deduced from the EXAFS of these preparations at low temperature. Previous X-ray absorption spectroscopy on these preparations has been performed at 180 K (Yachandra et al., 1987; McDermott et al., 1988). The principal effect of the lower temperature is expected to be a reduced contribution from vibrational disorder. This reduced disorder should enhance the information available from atoms at longer (>3 Å) distances from the Mn.

Materials and Methods

PSII oxygen evolving preparations from spinach and *Synechococcus* sp. were isolated and poised in the S_1 and S_2 states as described in Chapter 2.

X-ray absorption spectroscopy on photosystem II samples was performed on NSLS beamline X19A using a Si<111> monochromator and Ge solid state detector as described in Chapter 2. Sample temperatures were maintained at 10 K using a liquid helium cryostat as described. Some model compound data were taken at SSRL on beamlines IV-2 and VI-2 using an array of photomultiplier tubes for fluorescence detection and a nitrogen boil-off cryostat (as in Yachandra et al., 1987). EXAFS analysis was performed as described in Chapter 2. Theoretical parameters derived from curved wave functions (McKale et al., 1988) were used for phase and amplitude functions in the fitting procedures.

Results

Low temperature EXAFS of PSII in the S_1 state. The Mn EXAFS data from a *Synechococcus* PSII preparation poised in the S_1 state are presented in Figures 3.1 and

Figure 3.1 *k*-space Mn EXAFS data from a PSII preparation from *Synechococcus* sp. The data shown are weighted by k^3. The average of 12 scans, 5 seconds per scan per point, is shown. Data collection was performed at a sample temperature of 10 K. A single crystal glitch was removed in energy space, corresponding to k~9 $Å^{-1}$. The dotted line is a Fourier filtered data set containing peaks I-III shown in Figure 3.2.

Figure 3.2 Fourier transform of Mn EXAFS data from a PSII preparation from *Synechococcus* sp. The Fourier transform is of the data from Figure 3.1, with no apodization window applied. Three main peaks are identified.

Figure 3.1
k-space EXAFS of a PSII preparation from
Synechococcus sp

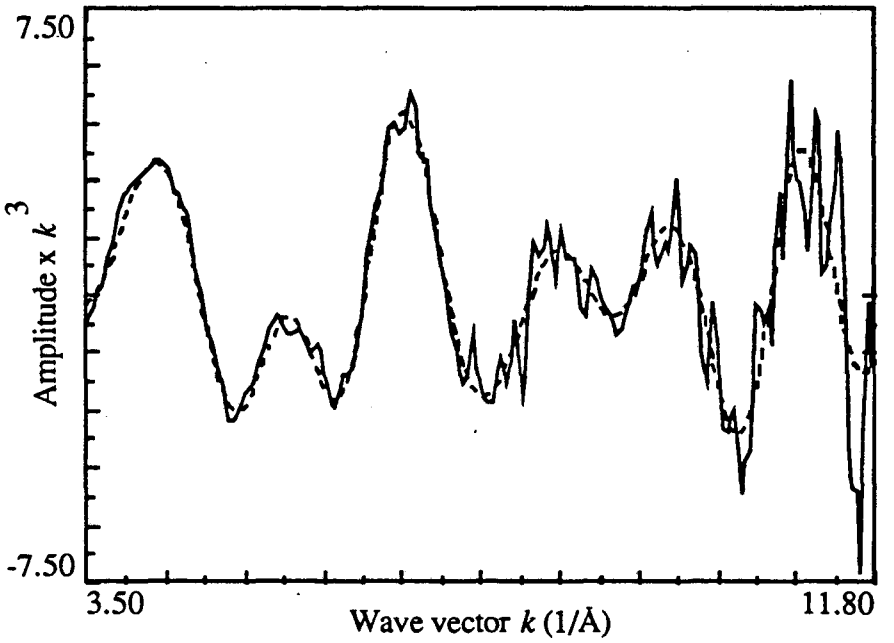

Figure 3.2 Fourier transform of EXAFS data from *Synechococcus* sp.

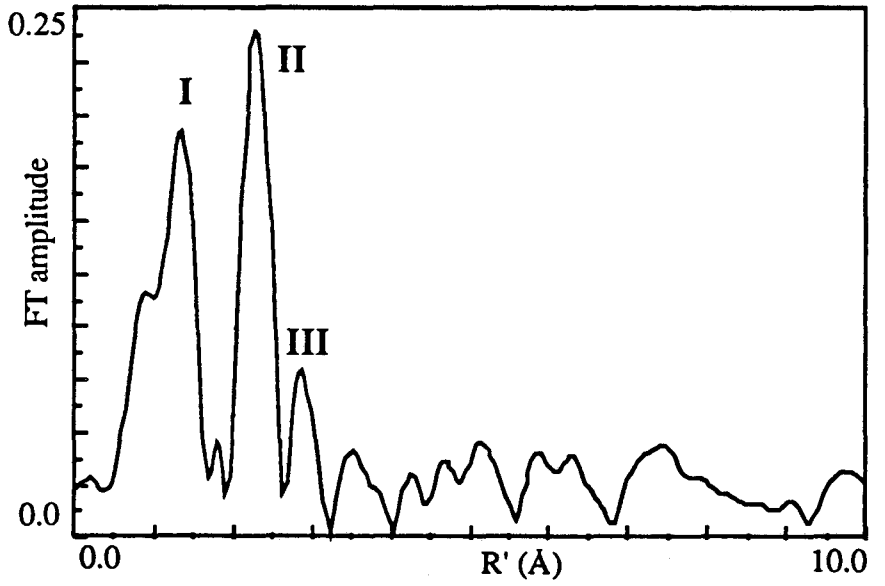

3.2. The k^3-weighted k-space trace in Figure 3.1 has very good signal to noise. The Fourier transform of this data in Figure 3.2 shows three main peaks, labelled I - III. Peaks I and II show little change from data taken at 180 K [McDermott et al., 1988]. Peak III, however, was not reliably observed in data taken at the higher temperature [Guiles et al., 1990a]. In addition, the small peak *between* peaks I and II is often observed in the data taken at low temperatures on the S_1 preparations.

Fourier filtering is employed to remove high frequency noise from the k-space data. Analytical fitting to the k-space data is performed on Fourier filtered data sets. The dashed line plotted over the data in Figure 3.1 is an example of Fourier filtered k-space data. The Fourier filtering was performed by applying a square windowing function of 0 Å $\leq$ R' $\leq$ 4 Å to the Fourier transform shown in Figure 3.2. The dashed line in Figure 3.1 is the back-transformation of the windowed Fourier transform. It is clear that the Fourier filtered data closely follow the original data.

To simplify the fitting procedure it is possible to isolate the Fourier transform peaks before back-transformation. In Figure 3.3 the k-space data which result from back-transformation of isolated peaks (I and II) are plotted over the original data. The isolated back transformed data from peaks (I and II) do not follow the original data as well as the full back-transform from all three peaks that is shown in Figure 3.2, which emphasizes the importance of peak III in this low temperature data.

Curve-fitting procedures were performed on isolated peaks (I and II). Further isolation, i.e. of only peak I, was avoided. Although peaks I and II are well separated, the windowing function can introduce artifacts (i.e., Zhang et al., 1989) or information contained between the Fourier transform peaks can be lost. In addition, the question of the number of adjustable parameters that can be used in a fit favors a multi-shell isolate. The number of degrees of freedom for a given windowed k-space transform is generally given as $N_f=(2/\pi)(\Delta k)(\Delta R)$, where Δk is the range of k-space used for the Fourier transform and ΔR is the width of the window function. For a single Fourier transform peak of ΔR~1 Å and for Δk of 8.5 Å, N_f is only 5. For peaks I and II, ΔR~3 Å and Δk~8.5 Å. This gives N_f of 16. This means that a fit to the isolated peaks (I and II) k-space data can include 4 independent shells of scatterers with 4 unknowns (R, N, σ and ΔE) without being overdetermined. The isolated single peak data are slightly overdetermined with fit to two independent shells of scatterers. In general, including an additional shell of scatterers to a fit is considered "justified" if it reduces the fit error by ~50%. The fit error is the sum of residuals between the simulated fit and the actual data.

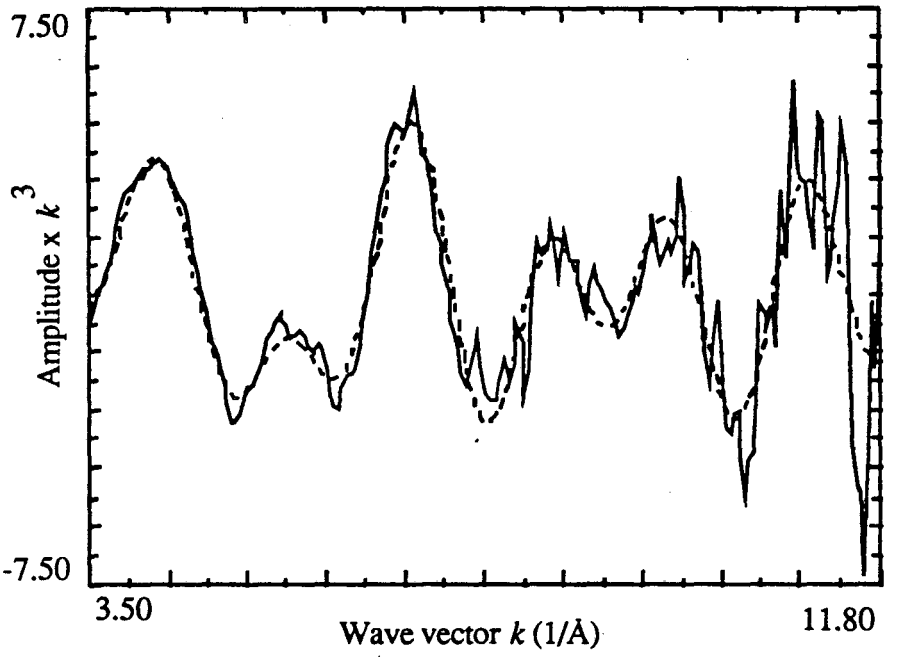

Figure 3.3 Plot of the back-transformed Fourier isolate of peaks I and II. The EXAFS data are described in Figure 3.2. A square window function was applied to peaks I and II (R'=0-3 Å) and the data were back-transformed to *k*-space. The isolated *k*-space data (dotted line) is plotted over the original *k*-space data.

A representative fit to the *k*-space data of peaks I and II is shown in Figure 3.4. The fit parameters are tabulated in Figure 3.4 and Table 3.2. The *Synechococcus* S_1 data were fit to a shell of O (or N) atoms at R=1.8 Å from the Mn, and a shell of Mn (or Fe) at 2.7 Å. The addition of an O or N shell at R=1.9-2.0 Å decreases the calculated fitting error by a factor of 2. Further shells (i.e., Cl) cannot be justified as their addition does not substantially lower the fitting error. These results are in general agreement with parameters obtained from data taken at 180 K [McDermott et al., 1988].

The low frequency background present in EXAFS data is known to interfere with short metal-ligand distances derived from curve-fitting techniques. The low frequency background is evident as a peak at R(apparent)<1 Å in the Fourier transforms of raw data. In the Fourier transform shown in Figure 3.2 the low frequency background has been removed using two steps; a second-order polynomial fit to the last 200 eV of the data was subtracted in energy space, and a four-domain spline fit from k=1 - 11.9 $Å^{-1}$ to the k^3 space data was subtracted in k^3 space. To check for background effects in the first shell fit parameters, the fit results reported in Figure 3.4 were compared with fits to data in which a different background removal method was used. The subtraction of a two-domain spline fit to the energy space data was chosen as an alternative method of background removal [Penner-Hahn et al., 1990]. The parameters for the fit of peaks I and II from data treated with this alternate background removal method are within the errors reported for the parameters in Figure 3.4. This indicates that the results from the data fitting procedure are independent of the method used for background removal.

The low temperature EXAFS data of the PSII preparation from spinach are very similar to those from *Synechococcus* (data not shown). The best fit parameters for the spinach S_1 data do not differ significantly from those for *Synechococcus,* and are listed in Table 3.2.

Fits to peak III and comparison with model compounds. The *k*-space oscillations due to the isolated peak III (from the *Synechococcus* data) and the corresponding fit are shown in Figure 3.5. This peak fits well to Mn (or Fe) at a distance of 3.3 Å. The addition of a C shell at 3 Å decreases the calculated fitting error by a factor of 2. The data can also be fit with two shells of C at 3.0 and 3.3 Å (not shown), but the calculated fitting error is twice that of the Mn, C fit. For this reason the (C, C) fit to peak III is considered less favorable than a fit to (Mn, C).

Figure 3.4. Analytical fit of isolated peaks I and II. The *Synechococcus* S_1 state Fourier filtered *k*-space data from isolated peaks (I and II) described in Figure 3.3 (solid line) are fit as described in the text. The fit shown (dotted line) is representative of the quality, as judged by fit error, of this type of analysis. The fit error is the least squares sum of the point-by-point deviations between the fit and the data. The parameters for this and other, equally good fits, are given in Table 3.2.

Figure 3.4
Representative fit of isolated peaks I and II

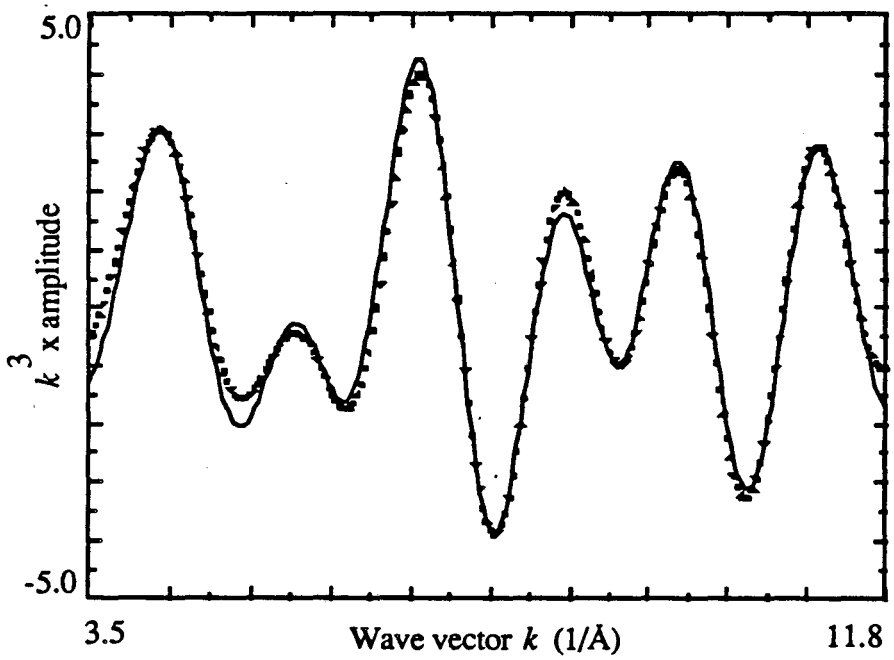

Typical Fit Parameters:

Atom	R(Å)	N	σ^2(Å^2)
O	1.82	2.2	.002
O	1.91	5.0	.012
Mn	2.73	1.2	.005

Fit Error = 16

Figure 3.5 Fit to isolated peak III. A window function was applied to peak III of the Fourier transform of *Synechococccus* S_1 data, shown in Figure 3.2. The back-transformed *k*-space data (solid line) is fit well to a Mn scatterer at 3.3 Å (dotted line). Parameters for fits which give similar fit errors are discussed in the text.

Figure 3.5
Typical fit to isolated peak III

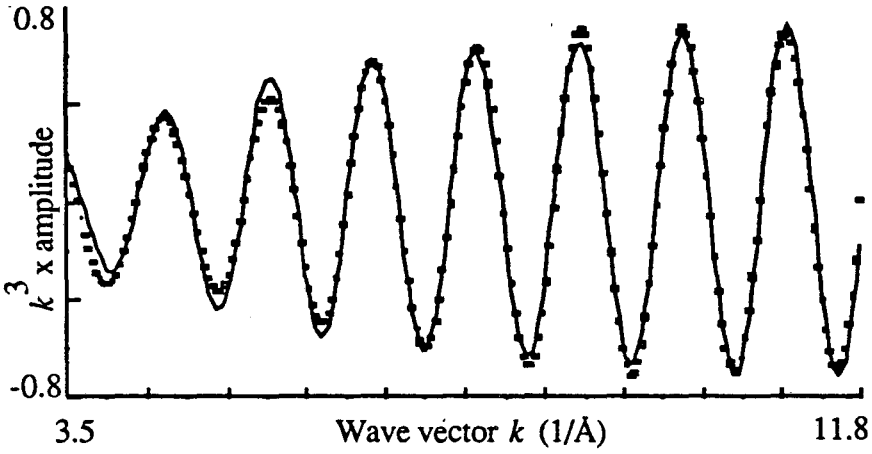

Typical Fit Parameters:

Atom	R(Å)	N	σ^2(Å)^2
Mn	3.28	0.45	.002
C	3.22	1.3	.013

Fit error = 0.3

Five model compounds (generously provided by the research groups of Drs. G. Christou, K. Wieghardt, and J.-J. Girerd) which contain Mn-Mn distances at ~3.3 Å were also studied. The parameters obtained from fits to model compound data are necessary to determine the range of reasonable values for the Debye Waller and ΔE_0 variables in fits of systems whose structure is not known. The structures of the model compounds are shown schematically in Figure 3.6. Three of the compounds contain Mn-Mn distances of both ~2.8 and ~3.3 Å. All of the compounds have a mixed O,N terminal ligand environment. Two compounds also contain Cl as terminal ligands.

An example of low temperature enhancement of long-distance interactions is evident in the Fourier transforms of EXAFS data for the "asymmetric tetramer" [Mn_4O_3 core], shown in Figure 3.7. This compound contains three Mn-Mn vectors at 2.8 Å and three Mn-Mn vectors at 3.3 Å. In addition, there are several Mn-Cl interactions. Figure 3.7a is the Fourier transform of data collected at 180 K. There is no evidence of Mn-Mn distances beyond 2.8 Å in this Fourier transform. The Fourier transform of data collected at 10 K (Figure 3.7b), however, shows a peak at R(apparent)=3 Å. The appearance of this peak at lower temperature is due to the decreased vibrational disorder at lower temperature between atoms at distances $\geq$3 Å. The larger amplitude of the first peak in the Fourier transform of Figure 3.7b is probably due to the influence of the terminal Cl atoms (R=2.2 Å), whose vibrational disorder is also expected to decrease at lower temperatures.

The Fourier transforms of the "butterfly" complex [Mn_4O_2 core] and the "asymmetric trimer" [Mn_3O_4 core] are shown in Figure 3.8. Both of these complexes contain more Mn-Mn vectors at 3.3 Å than at 2.8 Å. In these data the third peak is much more pronounced relative to the second peak (note that the "butterfly" data were taken at 180K). In Figure 3.9c the Fourier transform of the "symmetric trimer" [Mn_3O core] is shown. This compound contains Mn-Mn vectors of only 3.3 Å . Figure 3.8d is the Fourier transform of a "dimer" [Mn_2O core] compound. The lower amplitudes of the peaks in the Fourier transform of this dimer compound reflect both the fewer number of 3.3 Å distance vectors and the large disorder of the triazocyclononane (tacn) ligands [Wieghardt et al., 1988].

The results of fits to the isolated 3rd peaks for these model compounds are depicted in Figure 3.9 (a-d) and Table 3.3. The following method was used in fitting each compound. For each model, a series of fits was attempted: a single Mn shell, a single C shell, Mn + Mn, C + C, and Mn + C. An additional shell was considered

Figure 3.6 Model compounds containing Mn-Mn distances of ≥ 3 Å. For simplicity only bridging oxygen ligands and chloride ligands are shown.
(a) Asymmetric tetramer: $[Mn(III)_3Mn(IV)O_3Cl_4(pyr)_3(CH_3CO_2)_3]$ [Li et al., 1988].
(b) Asymmetric trimer: $[Mn(IV)_3O_4Cl_2(bipy)_4]^{+2}$ [Auger et al., 1990].
(c) Butterfly: $[Mn(III)_4O_2(CH_3CO_2)_7(bipy)_2]^{+}$ [Vincent et al., 1987].
(d) Symmetric trimer: $[Mn(III)_3O(C_6H_5CO_2)_6(HIm)_3]$ [G. Christou, personal communication].
(e) Dimer: $[Mn(III)_2O(CH_3CO_2)_2(tacn)_2]^{+2}$ [Wieghardt et al., 1985].

Figure 3.6 Schematics of model compounds containing Mn - Mn distances ≥ 3 Å

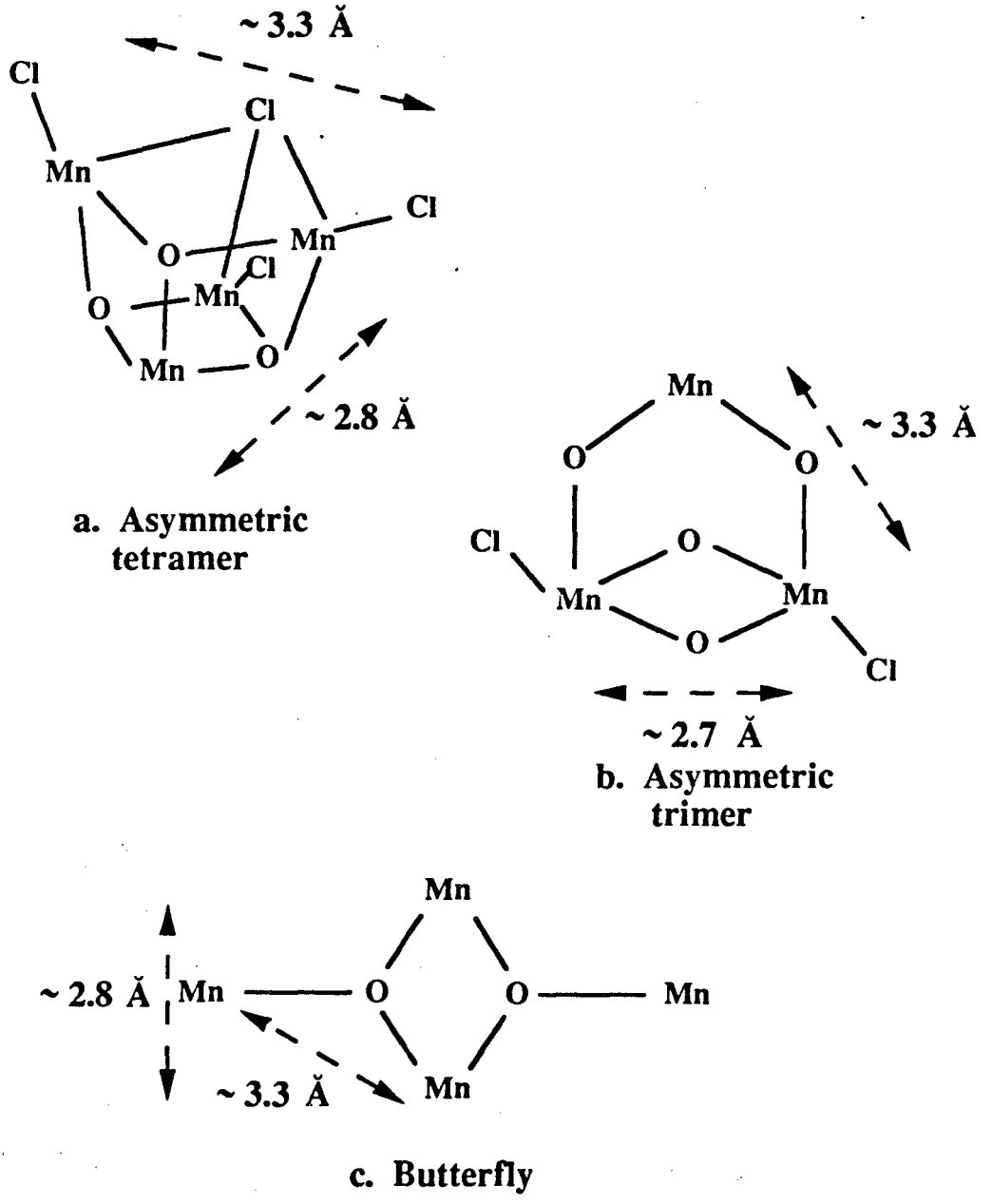

Figure 3.6 (continued)

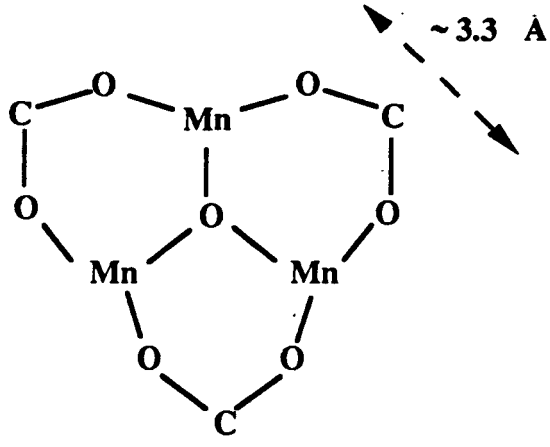

d. Symmetric trimer

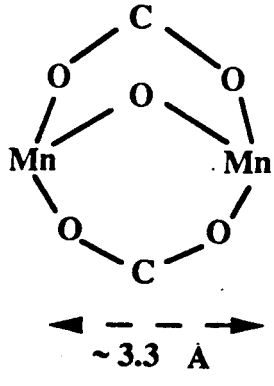

e. Dimer

Figure 3.7. Fourier transforms of Mn EXAFS data taken on the "asymmetric tetramer" at 180 K and at 4 K. The structure of the complex is in Figure 3.6a. Figure 3.7a is the Fourier transform of data taken at a sample temperature of 180 K. In (b) the Fourier transform of data collected at a sample temperature of 4 K is shown. Both Fourier transforms are of k^3-weighted data, k=3.5-11.3 $Å^{-1}$.

Figure 3.7a Asymmetric tetramer, 180 K

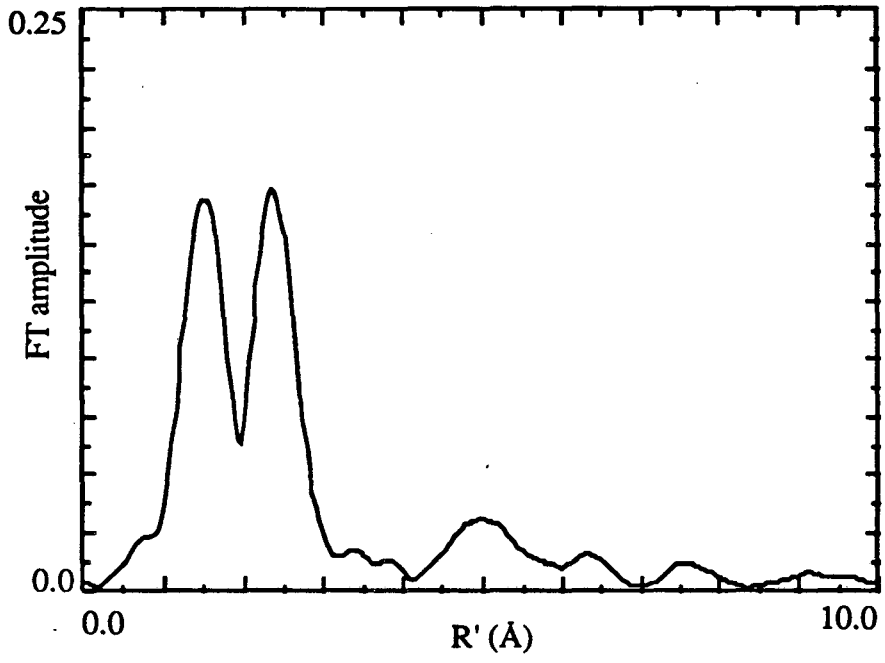

Figure 3.7b Asymmetric tetramer, 4 K

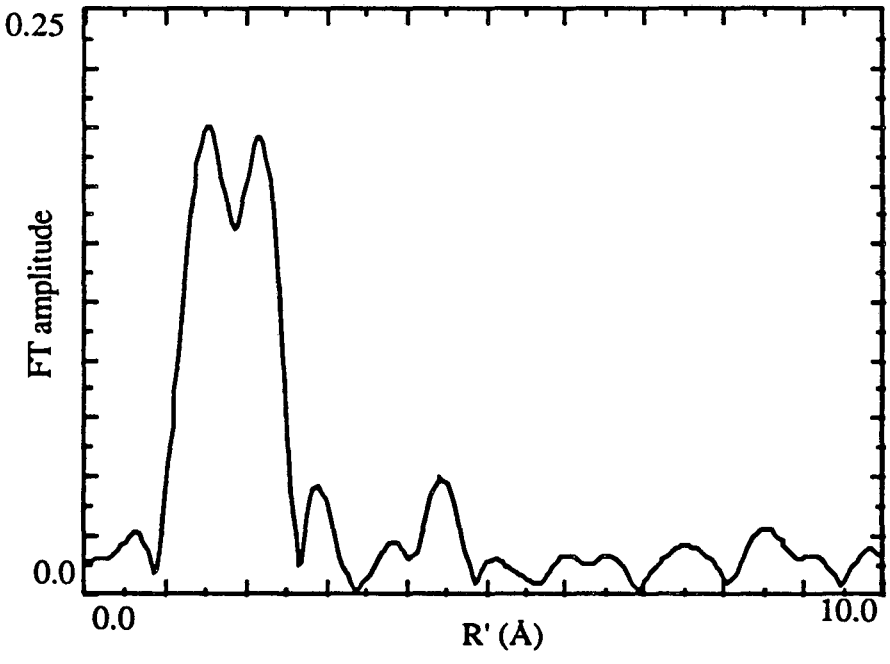

Figure 3.8. Fourier transforms of Mn EXAFS data from several model compounds containing Mn-Mn distances of >3 Å. The compounds are as listed in Figure 3.6. In each case the Fourier transform is of k^3-weighted data, k=3.5-11.8 $Å^{-1}$. The data for the "asymmetric trimer" was collected at 10 K; all others were collected at 170 K.

Figure 3.8
Fourier transforms of model compounds
containing 3.3 Å distances

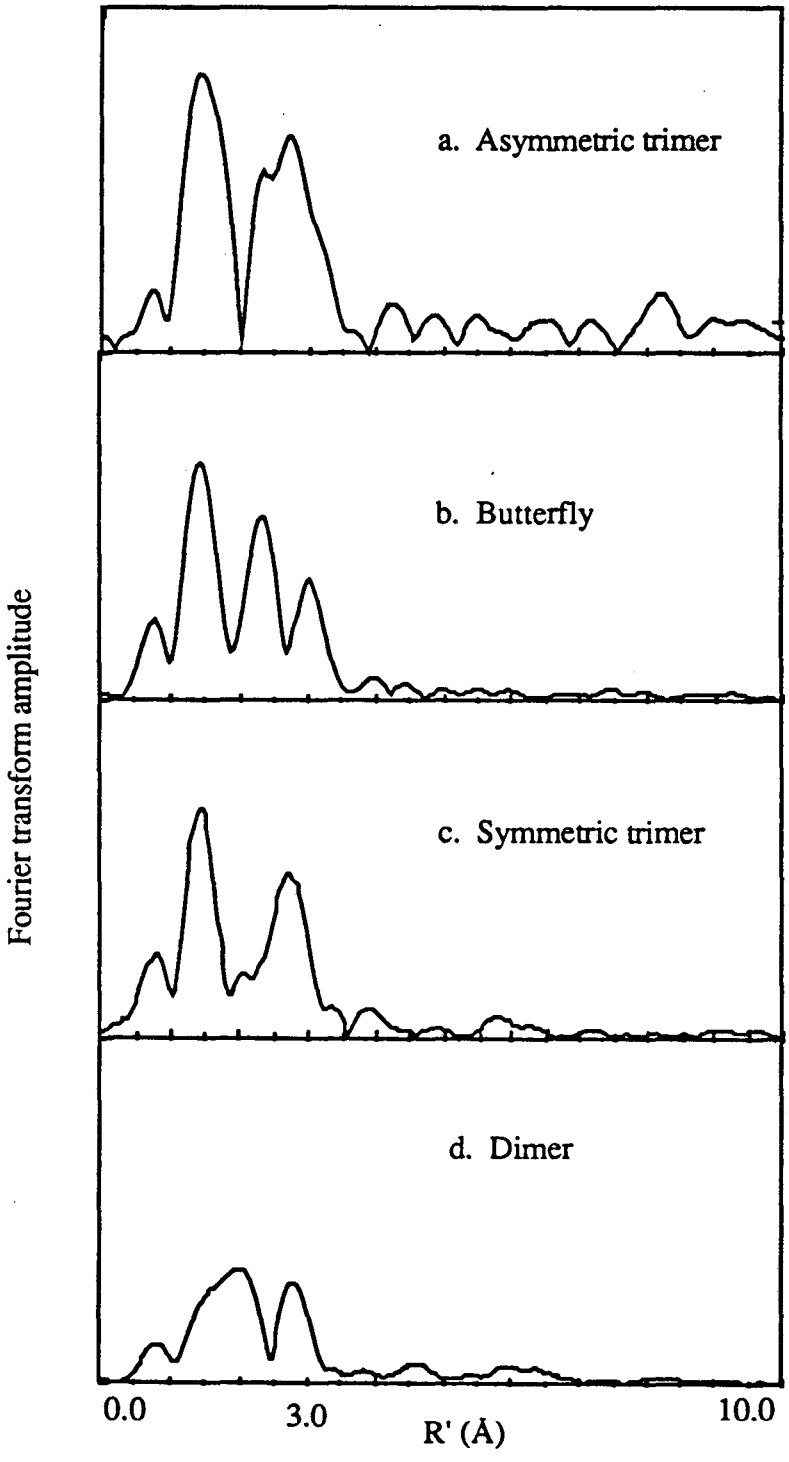

Figure 3.9. Analytical fits to the isolated Fourier transform peaks due to Mn-Mn interactions at 3.3 Å. For each of the model compounds described in Figures 3.6 and 3.7, the Fourier transform peaks at R(apparent)~3 Å were isolated and back-transformed. Data taken at 4 K were used for the "asymmetric tetramer." In the case of the "asymmetric trimer," the filtered data also contain the Fourier transform peak at R(apparent)=2.4 Å. Fits (dotted lines) are plotted over the Fourier filtered data (solid lines). In each case the best "justified" fit is shown. The criteria for a "justified" fit are discussed in the text, and the parameters for each fit are in Table 3.3. The fit error in each case is < 1.0.

Figure 3.9 Fits of 3rd peak isolates from model compounds

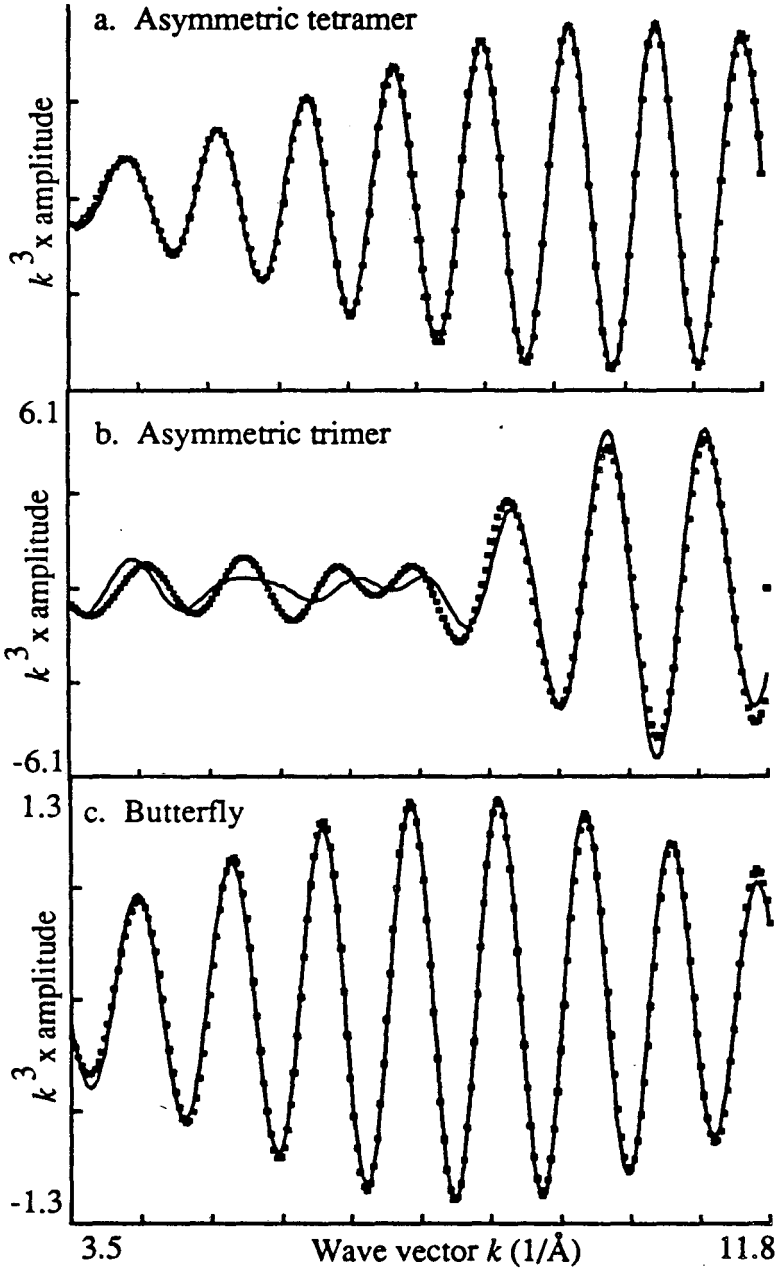

Figure 3.9 (continued)

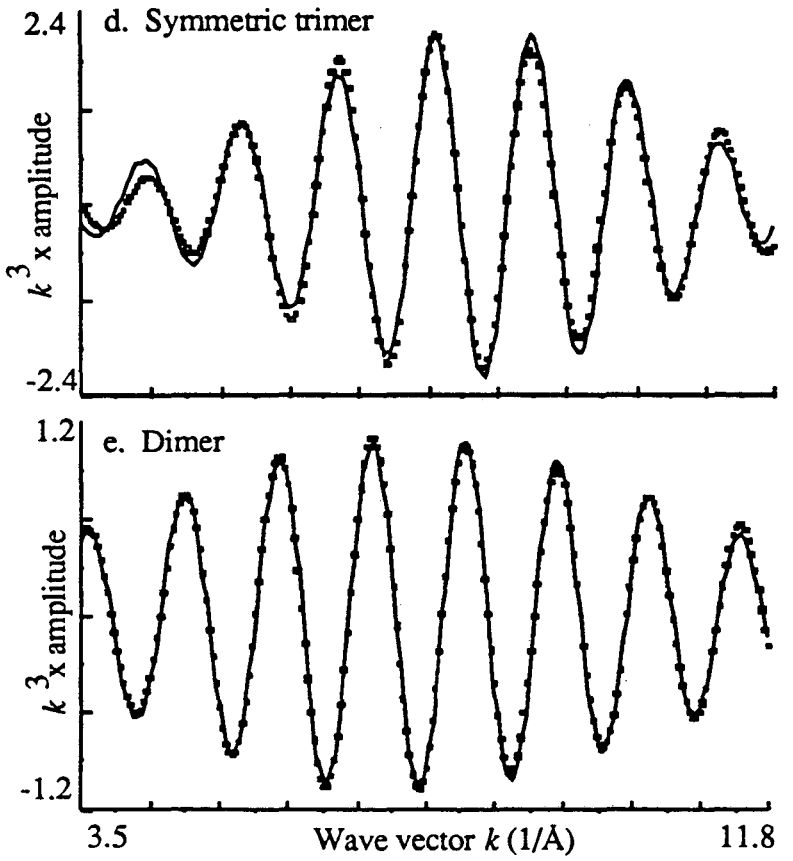

"justified" if it reduced the fit error by at factor of at least 2. In each case the best "justified" fit to the data is presented. In general the best justified fit agrees well with crystallographic data. The fit to the photosystem peak III is also shown in Table 3.3. This peak fits to ~0.5 Mn at 3.3 Å.

Comparison of the EXAFS from the S_1 and S_2 states. The Fourier transforms of EXAFS data from spinach and *Synechococcus* PSII preparations poised in the S_1 and S_2 states are compared in Figure 3.10. The samples were poised in the S_2 state by prior illumination at 200 K. Upon advancement to the S_2 state, the relative amplitude of Fourier transform peak I decreases, while the relative amplitude of peak II increases. These changes are reflected in subtle differences in the phases of the *k*-space isolates of peaks (I and II), which are shown in Figure 3.11. The analytical fits of peaks (I and II) (Table 3.2) from the S_2-state samples give parameters almost identical to parameters derived for the S_1 samples. The subtle differences in *k*-space data shown in Figure 3.11 are accomodated in these multi-shell fits by a slight increase in the Debye Waller factor for the Mn shell at 2.7 Å in data taken on the S_2 state, as well as small changes in other parameters.

Discussion

The structural parameters obtained from from previous EXAFS experiments performed at higher temperatures (180 K) are summarized in Table 3.1 for both spinach [Guiles et al., 1990a] and *Synechococcus* [McDermott et al., 1988]. Recently the results of low temperature X-ray absorption experiments on spinach PSII core preparations [Penner-Hahn et al., 1990] and on preparations of oriented chloroplasts [George et al., 1989] have been reported. The parameters reported from the analyses of these data are also summarized in Table 3.1. Finally, the data presented here for the analyses of spinach and *Synechococcus* PSII data collected at 10 K are summarized in Table 3.2.

The data in Tables 3.1 and 3.2 are generally similar. A first coordination sphere containing O or N and a second shell of Mn at 2.7 Å are found in the analyses of EXAFS data obtained from the four different PSII preparations listed in the Tables. There are some differences in the reported distances for oxygen or nitrogen scatterers in the first coordination sphere of the Mn. The data acquired from spinach core and spinach chloroplast preparations contain a first-shell Mn-O distance of 1.9 Å, in contrast to the shorter 1.8 Å distance reported for spinach BBY preparations and for preparations

Figure 3.10 Fourier transforms of PSII preparations in the S_1 and S_2 states. The Fourier transforms of Mn EXAFS data collected on PSII samples from *Synechococcus* (a) and spinach (b) are shown. Data were collected at a sample temperature of 10 K. In each case the solid lines are from samples poised in the S_1 state and the dotted lines are the Fourier transforms of data collected on samples poised in the S_2 state. Fourier transforms are of k^3-weighted data, k=3.5-11.8 Å.

Figure 3.10 Fourier transforms of PSII preparations in the S_1 and S_2 states

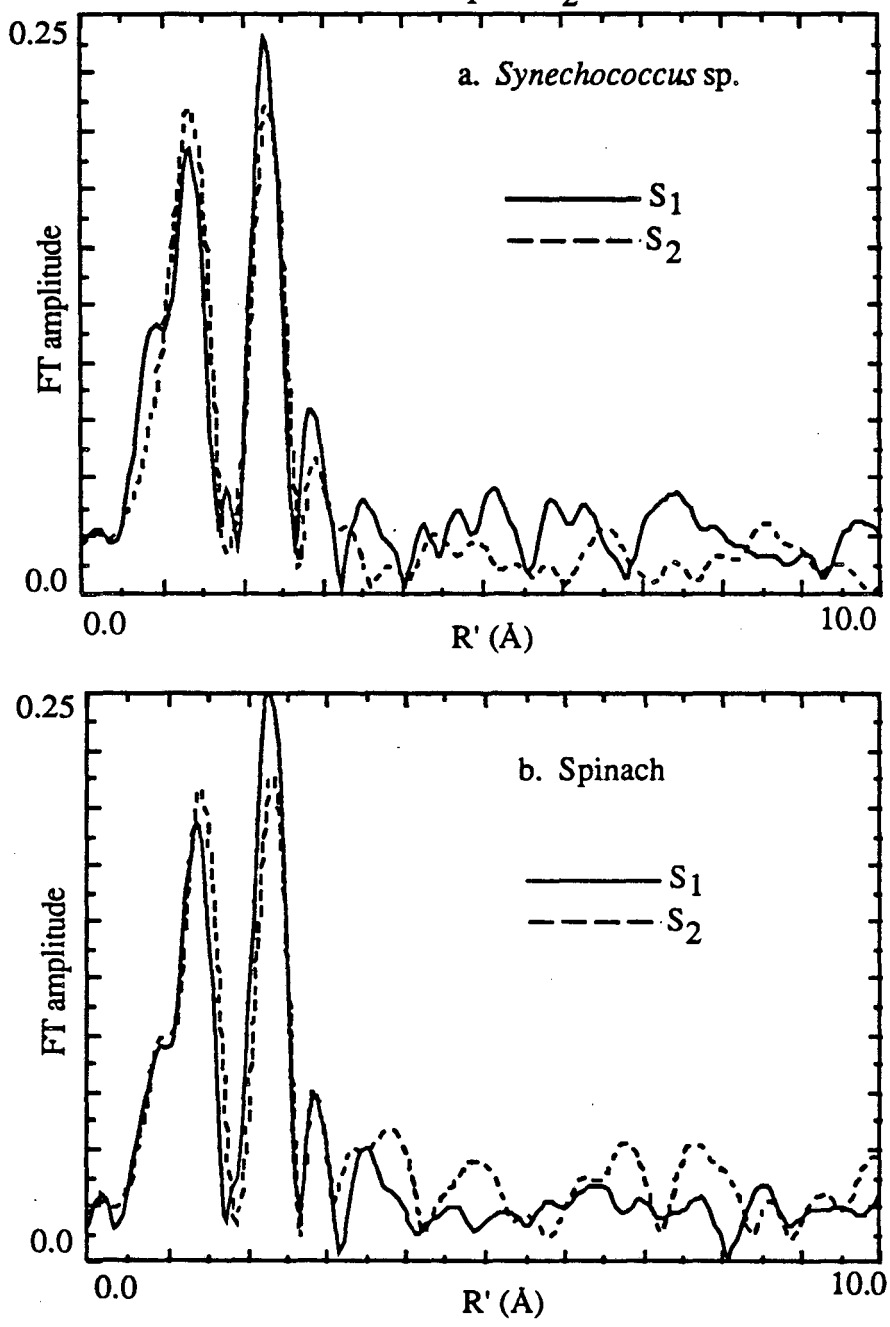

Figure 3.11 Fourier-filtered *k*-space data from PSII preparations poised in the S_1 and S_2 states. A window function was applied to the Fourier transforms shown in Figure 3.10, R(apparent)=0-4 Å. The back-transformed data are shown for (a) *Synechococcus* and (b) spinach samples. In each case the solid line is the Fourier filtered data from the sample poised in the S_1 state and the dotted line is from the sample poised in the S_2 state.

Figure 3.11
Comparison of Fourier isolates of photosystem II samples poised in the S_1 and S_2 states

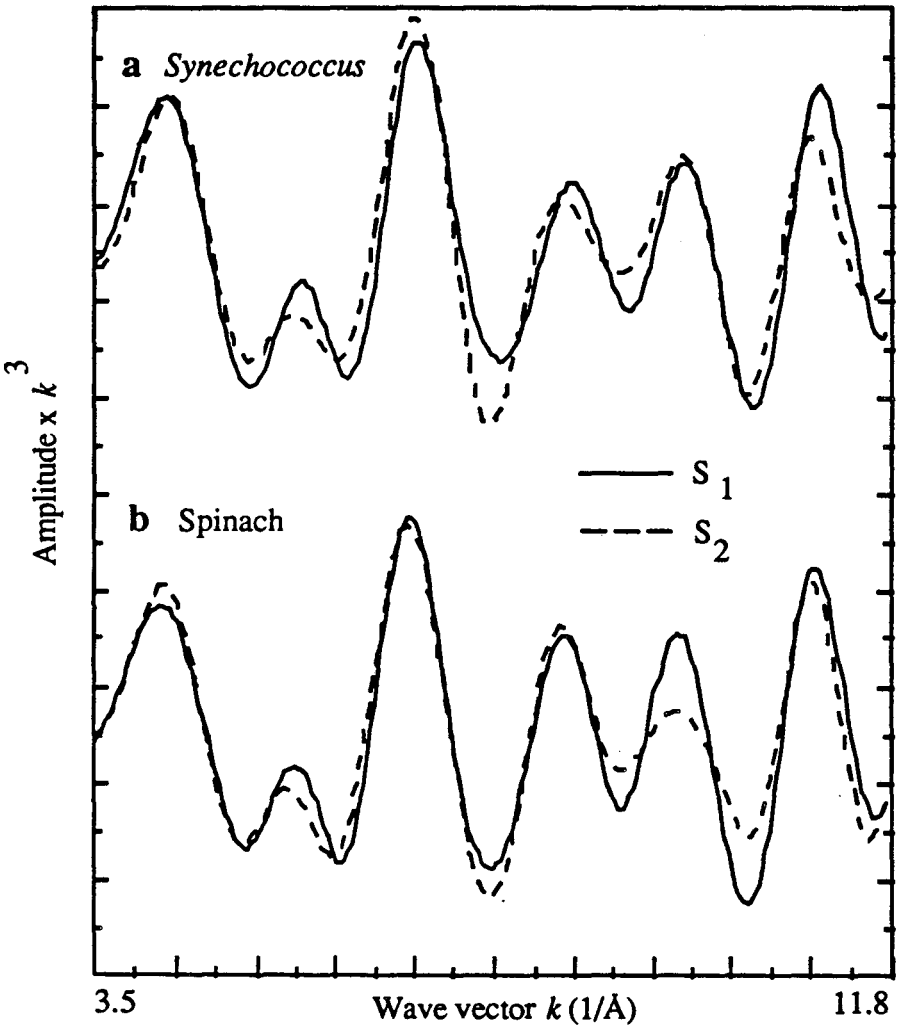

from *Synechococcus*. This discrepancy is most likely due to the presence of adventitious Mn^{+2} which contributed to the spectra from spinach core and chloroplast preparations (J. Penner-Hahn, S. Cramer, personal communication). This Mn^{+2} contribution will increase the deduced average bond length for Mn ligands in the preparation. The analysis of equivalent data taken on spinach BBY preparations does show a short Mn-O shell at 1.83 Å (S. Cramer, personal communication). A second difference is that slightly longer Mn-O distances (~1.83 Å) are reported in Table 3.2 for the recent data on both spinach and *Synechococcus* preparations, compared with the 1.74-1.77 Å distances previously reported for the same preparations (Table 3.1). This difference is most likely due to the use of theoretical parameters derived from curved wave approximations [McKale et al., 1988] in fitting the recent data, as opposed to theoretical parameters from plane wave approximation [Teo & Lee, 1979] which were used previously. Use of the curved wave theoretical parameters give distances which are slightly longer (~.05 Å) than the distances derived by use of the plane wave approximation (data not shown).

The results from data taken at low temperature contain information about atoms at distances greater than 3 Å from the Mn. A Mn-Mn distance of 3.3 Å is reported by both Penner-Hahn et al. (1990a) and George et al. (1989). This Mn-Mn interaction is now evident in the data presented here on PSII preparations from both *Synechococcus* and spinach. Penner-Hahn et al. (1990a) also report an interaction due to a scatterer at 4.35 Å. The data presented here do not contain a clear Fourier transform peak, which is above the noise, at R(apparent)>3 Å. There is, however, a consistency in the appearance of Fourier transform peaks at R(apparent)=3.5 Å between the data from spinach and from *Synechococcus* poised in the S_1 states (for example, in Figure 3.10). The assignment of this peak to a scatterer such as calcium is under investigation using samples in which calcium has been replaced with strontium [M.J. Latimer, personal communication].

The fits to EXAFS data of model compounds containing Mn-Mn distances at ~3 Å (Table 3.3) in general give good agreement with crystallographic values. This is encouraging, given the propensity for the shells of carbon (from terminal ligands) at ~3 Å to interfere with information about metal scatterers at this distance [Scott & Eidsness, 1988]. In most cases the number of scatterers are within 30% of the correct value, and the Mn-Mn distances are within 0.1 Å. An exception is the "butterfly" compound. This compound contains four long Mn-Mn distances, which can be grouped into two shells at average distances of 3.3 and 3.4 Å. Despite this, the isolated Fourier transform peak

Table 3.1

Structural parameters derived from EXAFS of the oxygen evolving complex in the S_1 state

Shell	O (bridging)		O,N (terminal)		Mn		Mn		
Preparation	R[a]	N[b]	R	N	R	N	R	N	T (K)[c]
Spinach[d]	1.75	1-2	2.24	1.5-3.0	2.72	1.0-1.5			170
Synechococcus[e]	1.74	1-2	2.21	1.0-1.5	2.76	1.0-1.5			"
Spinach[f]	1.79	1.6-2.4	1.96, 2.15	2, 1	2.70	0.5-1.5			77
Spinach cores[g]	1.92	2	2.13	2	2.72	1.0-1.5	3.31	0.5-1.0	10
Chloroplasts[h]	1.90	0.9-1.2	2.23	0.6-1.0	2.72	2.0-2.2	3.28	0.5-1.1	4
Synechococcus[i]	1.82	1.5-2.2	1.92-2.05	0.5-5.0	2.73	1.0-1.5	3.29	0.5-1.0	10
Spinach[i]	1.83	"	1.93-2.06	"	2.73	1.0-1.5	"	"	"

(a) Distance R (Å)
(b) Coordination number N, in atoms per manganese. The range of N allowed by the reported errors is shown.
(c) Temperature of data collection
(d) Guiles et al. (1990). Distribution in R reported as .02 Å; errors in N reported as 30%.
(e) McDermott et al.(1988). Mn distance taken from fit of isolated second Fourier peak; O distances taken from fits of combined first and second Fourier peaks. Errors reported as in (d).
(f) Corrie et al. (1990). Errors in R reported to be .03 Å; distribution in N of shorter and longer terminal ligand shells is $\pm$ 1 and $\pm$ 0.5, respectively.
(g) Penner-Hahn et al. (1990). N is fixed at integer values for these fits. These results may be affected by adventitious Mn^{+2}, which has probably increased the distance in the short Mn-O shell relative to the values determined for other preparations. A fourth shell due to Mn or Ca at 4.35 Å is also reported.
(h) George et al. (1989). Preparation is oriented chloroplasts.. N and R are the reported range for fits of the data taken at various orientations. As in (g), these samples contain some Mn^{+2}.
(i) This work. Distribution in R for the bridging O shell is .02 Å; distribution in R for Mn shells is .01 Å; distribution of N is 30%. The variability in the terminal ligand shell is shown. "Distribution" is range of values which give fit errors within 10%.

Table 3.2
Structural parameters for peaks I and II in the oxygen evolving complex from spinach and *Synechococcus*

Preparation	Atom	R(Å)[a]	N	σ^2(Å)^2
Synechococcus, S_1	O	1.82[b]	1.6[c]	.002
	O	1.92-2.05[d]	0.6[e]	.002
	Mn	2.73	1.2[f]	.005
S_2	O	1.82	1.6	.002
	O	1.91-2.02	0.6	.002
	Mn	2.74	1.2	.006
Spinach BBY, S_1	O	1.83	1.6	.002
	O	1.93-2.06	0.6	.002
	Mn	2.73	1.2	.004
S_2	O	1.84	1.6	.002
	N,O	1.93-2.02	0.6	.002
	Mn	2.74	1.2	.006

(a) R is the Mn-scatterer distance in Å; N is the average number of scatterers per Mn; σ^2 is the Debye Waller disorder parameter, in Å^2.
(b) The value for R varied by $\pm$ .02 Å between equivalent fits.
(c) Coordination numbers are derived by multiplication of the fit values by a factor of 2 (Teo & Lee, 1979). The value for N in this shell varied by $\pm$ 0.2 between equivalent fits.
(d,e) Equivalent fits could be obtained with a range of R values for this shell. The small number of scatterers here reflects the disorder in the shell, as a range of equivalent fits could be obtained with N as high as 2.5 and σ^2 increased to .02.
(f) The number of scatterers at 2.7 Å was determined from the best fit of an S_1 data set and then held constant for subsequent fits of data in the S_1 and S_2 states.

Table 3.3
Structural parameters derived from EXAFS for ~3 Å Mn-Mn distances in model compounds and the oxygen-evolving complex

Compound	Atom	R(Å)	N[a]	σ^2(Å)^2
Asymmetric tetramer	Mn	3.18 (3.27)[b]	0.6(1.5)[c]	.007
(Mn(III)$_3$Mn(IV)	C	3.02	0.6	.010
Butterfly[d]	Mn	3.42 (3.31,3.30) (3.39,3.37)	1.0(2.0)	.007
Mn(III)$_4$	C	2.86	0.3	.020
Asymmetric trimer	Mn	3.24(3.24)	1.7(1.3)	.003
Mn(IV)$_3$	Mn	2.78(2.68)	1.0(0.7)	.002
	C	3.70	1.8	.002
Symmetric trimer[d]	Mn	3.28(3.26,3.27)	1.7(2.0)	.012
Mn(III)$_3$	C	2.92	1.6(4)	.002
Dimer[d]	Mn	3.19(3.08)	1.2(1.0)	.012
Mn(III)$_2$	C	2.99	1.0	.020
Photosystem II	Mn	3.29	0.4	.002
	C	3.22	1.3	.013
	Mn	3.29	0.6	.004
	C	3.14	1.0	.007

a) Fit parameters are described in Table 3.1. Coordination numbers N are derived by multiplying the number of scatterers from the analytical fit by a factor of 2 (Teo, 1987).
(b,c) The crystallographic distances (or average distances) and coordination numbers are in parentheses.
(d) These data collected at a sample temperature of 180 K. Asymmetric tetramer data was collected at 4 K. Others collected at 10 K.

at R(apparent)=3 Å fits well to a single shell of Mn at an average 3.4 Å distance. Since the data on this compound were collected at 180 K, it could be that one shell of Mn scatterers is too disordered to be detected. A second exception is the "asymmetric tetramer," which contains an average of 1.5 Mn-Mn scatterers at 3.3 Å. The data collected (at 4 K) on this complex also fit to substantially fewer Mn scatterers (0.6) than expected at this distance. In this complex, each of the three Mn which are separated by 3.3 Å has a pyridine ligand. Multiple scattering effects from the pyridine ring carbons at ~3 Å might be interfering with the accurate determination of the number of Mn scatterers at around 3 Å in this compound. It is of note that the Fourier transform of this compound shown in Figure 3.7b contains an additional peak at ~4 Å, consistent with multiple scattering contributions from a planar ring ligand [i.e., Strange et al., 1987].

Peak III from the PSII samples fits well to a single shell of Mn at 3.3 Å. A good fit is obtained with 0.5 scatterers at 3.3 Å, indicating a model with a single Mn-Mn distance at 3.3 Å per four Mn. The value for σ^2 and thus the value for N can be raised slightly without changing the fit error, and the parameters for this alternative fit are the second entry in Table 3.3 for the OEC . Since the determination of N has an associated error of 30%, the combination of this range for N and the 30% error gives limits for N of 0.4-0.8. There is good agreement between the results reported in Table 3.1 and the results reported here for *Synechococcus* and spinach in this range for the number of scatterers at 3.3 Å. These values for N accommodate models with either 1 or 2 Mn-Mn interactions at 3.3 Å. In comparison with other data taken at 10 K on model compounds, however, the lower value for σ^2 and thus the lower value of 0.5 for N seem more reasonable. Given this, and the stoichiometry of 4 Mn per photosystem II, the data favor a model for the OEC with a single Mn-Mn interaction at 3.3 Å.

A model which is consistent with the data reported here is depicted in Figure 3.12. This model consists of a pair of di-μ-oxo bridged Mn dimers linked by a mono-μ-oxo, carboxylato bridge. The model predicts an average of 2.2 O at 1.8 Å, 1.0 Mn at 2.7 Å, and 0.5 Mn at 3.3 Å. These numbers are in good agreement with numbers derived from the EXAFS studies. Recent reports of EXAFS data from oriented preparations of spinach chloroplasts [George et al., 1989] and of oriented spinach BBY preparations [I. Mukerji, unpublished results] indicate that the 3.3 Å Mn-Mn vector is highly dichroic, resulting in a maximum scattering amplitude when the preparations are oriented with the normal of the membrane parallel to the incoming X-ray *e*-vector. For this reason the 3.3 Å distance in Figure 3.12 is depicted as oriented parallel to the membrane normal. The 2.7 Å Mn-Mn vector is less dichroic, with an orientation

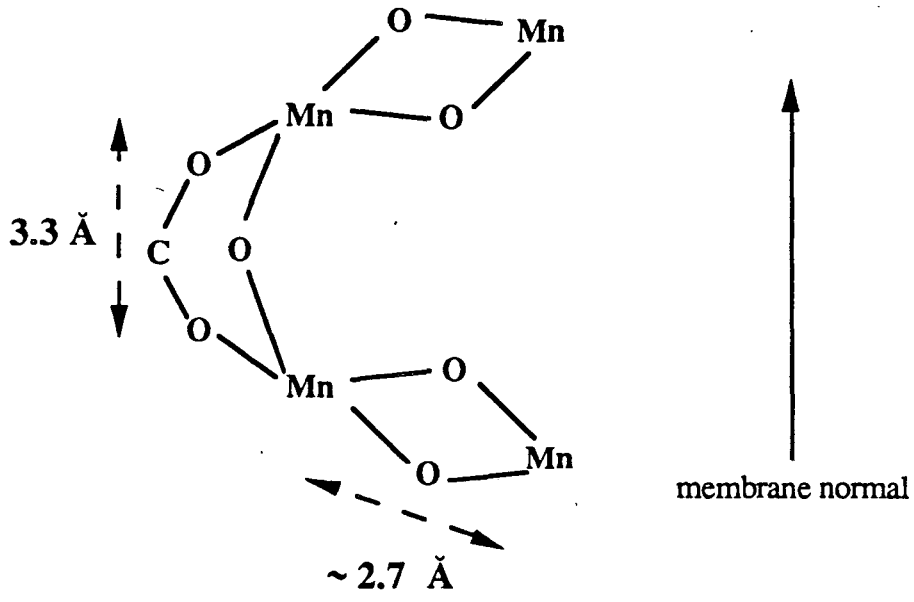

Figure 3.12 Proposed model for the oxygen evolving complex in photosystem II. For simplicity only bridging ligands are shown. The Mn-Mn distance of 3.3 Å is aligned with the normal to the membrane.

dependence indicating an angle of ~60° to the membrane normal [George et al., 1989; I. Mukerji, unpublished results]. The model in Figure 3.12 is also consistent with this orientation of the 2.7 Å vector.

Since the EXAFS data from *Synechococcus* are nearly identical to those from spinach, the same model is predicted for the oxygen evolving complex from both organisms. It is of note, however, that the preparation from *Synechococcus* shows different EPR characteristics. A light-induced g=4.1 EPR signal which is evident in spinach preparations has not been detected in PSII preparations from *Synechococcus* [McDermott et al., 1988]. The results here and in previous work [McDermott et al., 1988] show that this difference between the organisms is not caused by a large structural difference. A possible origin for the g=4.1 EPR signal is from the S=3/2 ground state of a tetrameric Mn spin exchange-coupled system. Evidence against a monomeric origin of the g=4 signal is in Kim et al. (1990). An S=3/2 ground state could arise from weak ferromagnetic coupling between two dimers; a Mn(III,IV) antiferromagnetically coupled pair with an S=1/2 ground state, and the first excited S=1 state of a Mn(IV,IV) antiferromagnetically coupled pair. In this scenario the EPR g=2 multiline spectrum would arise from the same system, but with *antiferromagnetic* coupling between the S=1/2 Mn(III,IV) pair and the ground S=0 state of the Mn(IV,IV) pair [i.e., Brudvig, 1989]. Since the g=4 and g=2 forms of the oxygen-evolving complex from spinach are interconvertible upon warming the system from 140 K to 200 K, the difference between conformations which give rise to either ferromagnetic or antiferromagnetic exchange couplings between the pairs of Mn must be quite small. For example, it has been shown that protonation of an oxo bridge can cause a switch between ferro- and antiferromagnetic exchange coupling [Hagen et al., 1989]. Such small conformational differences might be too small to detect using EXAFS (although see the following discussion).

In the data presented here, small changes are detected in the EXAFS of the oxygen-evolving complex upon advancement from the S_1 to the S_2 (200 K illuminated, "multiline") state. Because these differences in the EXAFS of PSII in the S_1 and S_2 states are slight, they are difficult to characterize using curve fitting techniques. The results from curve fitting indicate that the parameters derived from analysis of the S_2 data differ from the parameters derived for S_1 in two ways: (1) in the shell due to Mn at R~2.7 Å the average Mn-Mn separation increases by .01 Å and the average Debye Waller value increases by .001-.002 $Å^2$ in the S_2 data; (2) the average distance in the terminal ligand shell (O or N at R~2 Å) decreases by .03-.04 Å in data taken on the S_2

preparations. These differences in the parameters for R and σ^2 are within the uncertainties that we report for the EXAFS technique. However, they are worthy of mention both because the differences are consistently seen between data sets in the S_1 and S_2 states, in preparations from two organisms, and because the differences follow the trend expected for the complex as it undergoes oxidation, as explained below. The results from X-ray absorption edge [summarized in Sauer et al., 1987] and EPR [i.e., Hansson et al.,1982] experiments indicate that the advance of the oxygen evolving complex from S_1 to S_2 is accompanied by the oxidation of a Mn(III) to Mn(IV). A comparison of model compounds containing Mn(III) and Mn(IV) centers shows that the average bond lengths of terminal ligands to Mn(IV) are decreased by ~0.05-0.08 Å relative to those for Mn(III). In homologous di-μ-oxo bridged binuclear complexes, oxidation from Mn(III,IV) to Mn(IV,IV) is accompanied by an increase in Mn-Mn distance of .01-.05 Å [summarized in Wieghardt, 1989]. The trends of these changes are reflected in the EXAFS results reported here.

Summary

1. Mn EXAFS data have been collected at low temperatures (10 K) for PSII preparations from both spinach and *Synechococcus* sp.

2. The data give evidence for a Mn-Mn interaction at 3.3 Å. By comparison with parameters determined from model compounds, the average number of scatterers at 3.3 Å is most likely 0.5, indicating a single Mn-Mn vector at this distance in the complex. A model for the oxygen evolving complex is proposed which incorporates the structural parameters derived from EXAFS.

3. The data show small changes upon advancement from the S_1 to the S_2 state. The changes can be characterized as an increase in the average Mn-Mn distance at 2.7 Å and an increase in the disorder of that shell, as well as a decrease in the average bond length of the terminal ligands. These changes are consistent with the oxidation of a Mn(III) to Mn(IV) in a di-μ-oxo bridged complex.

Chapter 4

The Effect of Fluoride Inhibition on the Oxygen Evolving Complex: EPR and EXAFS Studies

Introduction

The necessity of chloride for oxygen evolution was first discovered when Warburg and Lüttgens (1946) found that chloride reactivated oxygen evolution activity in water-washed chloroplasts. Subsequent studies with spinach photosystem II particles have established a pH dependence of chloride activation, the ability of bromide to substitute for chloride in activating oxygen evolution, and that fluoride, acetate, and several amines are inhibitors of oxygen evolution activity (reviewed in Chritchley, 1985, and Babcock, 1987). Some of the effects of these substitutes for chloride are outlined in Table 4.1, and described below.

Two classes of inhibitors compete with chloride to affect oxygen evolution. Sandusky and Yocum (1986) have interpreted the results of steady-state kinetic studies on oxygen evolution activity to indicate that various amines behave as competitive inhibitors of the chloride activation of oxygen evolution. For amines other than ammonia, the potency of inhibition is correlated with the nucleophilicity of the amine, where increasing nucleophilicity is indicated by an increasing pKa. This dependence on nucleophilicity was taken as an indication that the amine binding site could be a high valent metal center. From these results the authors propose that chloride has a binding site on the manganese of the oxygen evolving complex, and that the amines inhibit oxygen evolution by displacing chloride at this site on the manganese. Unlike the other amines tested, the kinetics of ammonia inhibition indicate two modes of inhibition, only one of which is competetive with chloride. Thus the authors propose two sites of ammonia binding.

The second class of inhibitors is the anions such as fluoride and acetate. Both fluoride and acetate were also shown to compete with chloride to inhibit oxygen evolution. Fluoride was also shown to compete with amines in inhibiting oxygen evolution. Therefore the authors conclude that both fluoride and amines bind to the same site in the oxygen evolving complex. The authors propose that the site is a ligand to the manganese, potentially bridging between two manganese atoms [Sandusky & Yocum, 1986].

Table 4.1

Effects of anions and amines on oxygen evolution activity and S_2-state EPR signals in spinach PSII preparations[a]

Substituting species[b]	O_2 activity[c]	Competes with Cl^-?[d]	Multiline (rel. amp.)[e]	g=4 (rel. amp.)[f]
Anion				
Cl^-	100%		100%	100%
Br^-	NC	Y	NC	↓ (≥ 70%)
F^-	↓ (≤ 10%)	Y	↓ (≤ 10%)	↑(≥250%, narrowed)
CH_3COO^-	↓ (≤ 10%)	Y	↓ (≤ 10%)	NC
NO_3^-	↓ (≤ 65%)	-	↓(≤ 10%)	↑(≥140%)
I^-	↓ (≤ 31%)	-	↓ (≤ 15%)	NC
SO_4^{-2} [g]	↓ (≤ 10%)	N	↓ (≤ 20%)	NC
Amine[h]				
NH_3 (Site 1)	↓	N	(altered)	-
NH_3 (Site 2)	↓	Y	↓	↑ (narrowed)
CH_3NH_2	↓	Y	↓	↑

(a) References for each category are listed separately.
(b) Preparations and anion concentrations vary.
(c) A downwards pointing arrow indicates reduced activity. The number in parentheses indicates the reported remaining activity as a percentage of the control (Cl^--treated) sample activity. "NC" indicates a change of <20%. Percentages as reported in: Kelley & Izawa (1978) [broken chloroplasts]; Yachandra et al. (1986) ["exchanged and Triton-washed" BBY preparations]; Ono et al. (1987) [BBY preparations].
(d) Information taken from Sandusky & Yocum (1986). "Y" indicates that the species was determined to compete with chloride to activate or inhibit oxygen evolution activity. "N" indicates that the action of the species was determined to be noncompetetive with chloride.
(e) Arrows and parentheses as in (c). Relative amplitudes were determined by measuring the height of the individual lines in the multiline EPR signal. Information taken from Yachandra et al. (1986), Ono et al. (1987, 1986a).
(f) Arrows and parentheses as in (c). Information taken from Ono et al. (1987, 1986a). Relative amplitudes were determined by measuring the peak-to-peak amplitude of the EPR signal. "Narrowed" refers to a lesser peak-to-peak linewidth, reported for fluoride-treated samples in Cole (1988) and in this work.
(g) Values for "chloride-depleted" preparations were used in this category when sulfate was present in the "chloride-depleted" assay media.
(h) Values for amine-treated preparations were obtained from Beck & Brudvig (1986, 1988). Competition behavior reported by Sandusky & Yocum (1986). The "altered" multiline was first reported by Beck & Brudvig (1986). The "narrowed" g=4 EPR signal in the presence of ammonia has been reported by Andréasson & Hansson (1987).

Spectroscopic studies have given more specific information concerning the functional role of halide in the oxygen evolving complex. In the absence of chloride, the OEC can be advanced from S_1 to a stable "S_2-like" state, but is blocked from advancing from the S_2 to the S_3 state [Ono et al., 1986a, 1986b; Vass et al., 1987]. By monitoring the kinetics of the reduction of Z^+, Ono et al. (1986b) found that a series of flashes removes only two equivalents from the chloride-depleted OEC, advancing it from the state S_1Z to S_2Z^+. The oxidation of S_2 by Z^+ seems to be blocked in the absence of chloride [Ono et al., 1986b]. Additionally, conclusions reached from both thermoluminescence [Vass et al., 1987] and single flash illumination experiments [Ono et al., 1986a,1987] indicate that the S_2 state is stabilized in chloride-depleted samples relative to untreated preparations with respect to charge recombination.

Chloride has a direct effect on the EPR signals associated with S_2 state of the oxygen evolving complex. In the absence of chloride, the multiline EPR signal is not formed upon advance to the S_2 state [Yachandra et al., 1986; Ono et al., 1986a,b]. Yachandra et al. (1986) showed that the yield of multiline signal and the level of oxygen evolution activity were directly correlated with the concentration of chloride added back to chloride depleted samples. Ono et al. (1986a) concluded that single-flash illumination of chloride-depleted samples generates an "EPR silent" S_2 state. The multiline signal can be restored by addition of chloride directly into this EPR silent state. Ono et al. (1986a) also concluded that the species giving rise to the g=4 EPR signal was unaffected by the chloride depletion, because the yield of that signal was only slightly diminished in samples illuminated in the absence of chloride.

Fluoride and ammonia have been determined to influence the yield and shape of the S_2 state g=4 EPR signal. Under conditions of fluoride inhibition, the yield of the multiline EPR signal is decreased and the yield of the g=4 signal is increased [Casey & Sauer, 1984; Yachandra et al., 1986; Ono et al., 1987]. Low-temperature illumination (200 K) of ammonia-treated samples also gives rise to a large g=4 EPR signal [Beck & Brudvig, 1986; Andréasson & Hansson, 1987]. At higher temperatures (274 K), enhanced ligand exchange allows competition between this site for ammonia and the second, chloride-independent ammonia site [Beck & Brudvig, 1986] which was predicted from steady-state oxygen evolution studies [Sandusky & Yocum, 1984]. This second, chloride-independent site has been shown to be a direct ligand to the Mn [Beck & Brudvig, 1986; Britt et al., 1989]. Beck & Brudvig (1988) also report an

enhanced yield of the g=4 EPR signal in the presence of methylamine under conditions of low chloride concentration.

In the presence of sucrose as a cryoprotectant, the light-induced g=4 signal formed in fluoride-treated preparations has been reported to have a narrower linewidth than that formed in chloride-treated controls [Casey & Sauer, 1984; Cole, 1988]. In addition, the apparent g-value of the signal is slightly increased from 4.1 in untreated preparations to 4.2 after exposure to fluoride [Casey & Sauer, 1984]. These same effects on the g=4 signal have been reported in ammonia-treated samples under conditions of low chloride concentration [Andréasson & Hansson, 1987]. Under these conditions it is thought that the chloride-sensitive ammonia binding site is populated [Beck & Brudvig, 1986; Andréasson & Hansson, 1987]. The narrowing of the g=4 signal in fluoride and ammonia-treated samples has only been seen in samples in which sucrose was the cryoprotectant. In particular, Beck and Brudvig (1986, 1988) report no change in the lineshape of the g=4 signal formed in the presence of ammonia or methylamine when ethylene glycol is used as the cryoprotectant. This, and their observation that the other amines reported to inhibit oxygen evolution had no effect on the EPR signals from the S_2 state of the oxygen evolving complex, led them to conclude that the putative amine/fluoride binding site was nearby, but not a direct ligand, to the manganese [Beck & Brudvig, 1986, 1988].

In this study, we report the results of EPR and Mn K-edge X-ray absorption experiments performed on PSII samples which have been inhibited with fluoride. The structural information gained about the fluoride-inhibited oxygen-evolving complex is used to construct a model of halide and amine binding to the oxygen evolving complex.

Materials and Methods

Spinach BBY particles were prepared as in Chapter 2. Fluoride-inhibited PSII samples for X-ray spectroscopy were prepared by first washing the PSII particles at 1 mg/ml Chl in 50 mM MES/0.5 M sucrose/1 mM $CaCl_2$, pH 6, and then washing the particles twice at a concentration of 0.5 mg Chl/ml in 50 mM MES/0.5 M sucrose/50 mM NaF. Control samples were prepared by washing PSII particles under the same conditions, but using 50 mM NaCl in place of NaF. After a final centrifugation of 1 hr (17000 rpm, SS-34 rotor) the pellets were loaded directly into Lucite sample holders

and frozen at 77 K until use. All treatments after the wash in 1 mM $CaCl_2$ were performed under dim green light.

EPR and X-ray absorption spectroscopies were performed directly on the same samples, as described in Chapter 2. Mn K-edge EXAFS data were collected on beamline X19A at the NSLS using a solid state Ge detector and liquid He cryostat. A Si<111> monochromator was used. Mn XANES data were collected on beamline IV-2 at SSRL using a solid state Si/Li detector and liquid He cryostat. A Si<220> crystal monochromator was used, and the energy resolution of the experiment was $\leq$ 1.5 eV. The EXAFS analysis is described in Chapter 2.

To perform EPR and oxygen evolution measurements on samples which had been treated with fluoride at the same ratio of fluoride to reaction center, the following procedure was used. Spinach BBY particles were washed once in 50 mM MES/0.5 M sucrose/1 mM $CaCl_2$, pH 6.0, and then resuspended to 1 mg Chl/ml in 50 mM MES/0.5 M sucrose, pH 6.0. Two ml aliquots of this suspension were diluted into 38 ml of measuring buffer which contained the desired concentration of NaF. This gave a concentration of 50 μg Chl/ml. From this mixture 1.5 ml were removed and immediately assayed for oxygen evolution activity (described below) after addition of DCBQ (to ~0.7 mM from a stock solution of DCBQ in DMSO). The remaining fluoride-inhibited PSII membranes were pelleted by centrifugation at 17,000 rpm in an SS-34 rotor (10,000xg) for 20 min. Each pellet was resuspended in 400 ml buffer/50% glycerol and loaded into an EPR tube, giving a final concentration of 5 mg Chl/ml in the EPR sample. The samples were frozen at 77K until EPR spectra were taken (less than 24 hr later). All of the above treatments with fluoride were performed under a dim green safety light.

To investigate fluoride inhibition in PSII particles from *Synechococcus* sp., particles were prepared as described in Chapter 2. Oxygen evolution activity was performed at 24 °C as in Chapter 2. The assay mixture consisted of 1.5 ml of 50 mM MES/0.5 M sucrose, pH 6.0. NaF was added from a stock solution in water to the required final concentration. DCBQ was added from a stock solution in DMSO to a concentration of ~0.7 mM. Aliquots of the PSII preparation were then added, to a final chlorophyll concentration of 10 μg/ml for preparations from *Synechococcus*. This corresponds to approximately 0.2 μM concentration of PSII for each assay. The assay mixture was stirred for 15 sec before the light was turned on. Oxygen evolution rates were measured as the slope of the straight line between 5 and 20 sec after the light was turned on (the first few seconds contain an artifact due to initial heating by the

light). The conditions of the assay were checked at various points of pH and halide concentration to insure that changes in the oxygen evolution rate were not due to lack of light intensity or amount of electron acceptor DCBQ.

Results

Relation between the fluoride-induced inhibition of oxygen evolution and formation of g=4 EPR signal.

In Figure 4.1 the effect of fluoride on oxygen evolution activity in PSII preparations from spinach and *Synechococcus* is demonstrated. Figure 4.1a is a plot of oxygen evolution as a function of fluoride in spinach PSII preparations. Figure 4.1b is the analogous plot for PSII preparations from *Synechococcus*. It is clear that fluoride is a potent inhibitor of oxygen evolution in both preparations. The concentration of fluoride required to produce 50% inhibition of oxygen evolution activity in spinach samples was found to be dependent on the amount of time that the samples were exposed to fluoride. The spinach PSII samples measured for Figure 4.1 were mixed with the given concentration of fluoride for at least 20 min before activity measurement. The concentration of fluoride which produced 50% inhibition in these samples was 20 mM. In experiments in which samples were exposed to fluoride for 1.5 min prior to being measured for activity, 40 mM fluoride was required to produce 50% inhibition of oxygen evolution activity (data not shown). This indicates the presence of a kinetic barrier to inactivation with fluoride in these membrane-bound preparations. Beyond 15 seconds of mixing at a given concentration of NaF, the percent inhibition in the *Synechococcus* PSII preparations did not change substantially. This could be due to greater accessibility of the oxygen evolving complex to the surrounding media in the *Synechococcus* PSII preparations. Unlike the spinach preparations, the PSII samples from *Synechococcus* are detergent-solubilized particles and lack the extrinsic 24 and 16 kD polypeptides which are thought to shield the halide binding site in spinach PSII preparations [Ghanotakis et al., 1984].

Fluoride-inhibited PSII samples exhibit differences in their EPR spectra relative to untreated samples. In PSII samples from spinach which have been treated with fluoride, the multiline signal from the S_2 state is decreased, while the g=4.1 signal is enhanced. The common fluoride treatment used to make EPR samples is to resuspend spinach PSII preparations, at a Chl concentration of 1-2 mg/mL, in ~50 mM NaF [Casey & Sauer, 1984; Cole, 1988]. Oxygen evolution measurements, however, are

Figure 4.1. Fluoride-induced inhibition of oxygen evolution activity in PSII preparations from spinach and *Synechococcus* sp. Oxygen evolution activity is plotted as the percent of activity in samples resuspended into a buffer containing neither chloride nor fluoride. The activity in this buffer was approximately 75% of the oxygen evolution activity measured in 50 mM NaCl in both spinach and *Synechococcus* preparations. The maximum activity (in 50 mM NaCl) for spinach preparations was ~500 μM O_2/(mg Chl-hr). Maximum activity for *Synechococcus* preparations was ~2000 μM O_2/(mg Chl-hr). The concentration of Chl (50 μg/ml for spinach PSII, 10 μg/ml for *Synechococcus* PSII) was chosen to provide approximately the same concentration of PSII in both measurements. In (a), the results are plotted for two experiments with spinach PSII preparations. In (b), the average of 4-5 measurements are shown for each point. Error bars in (b) are the standard deviation of 4-5 measurements.

Figure 4.1
Oxygen evolution activity vs. [F-] in PSII preparations
from spinach and *Synechococcus* sp.

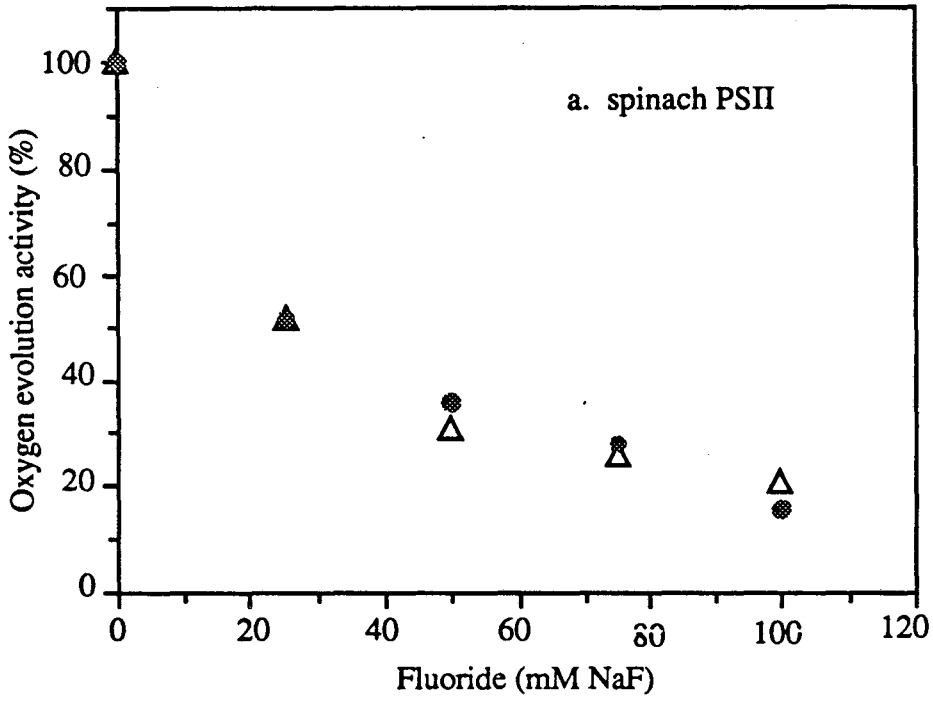

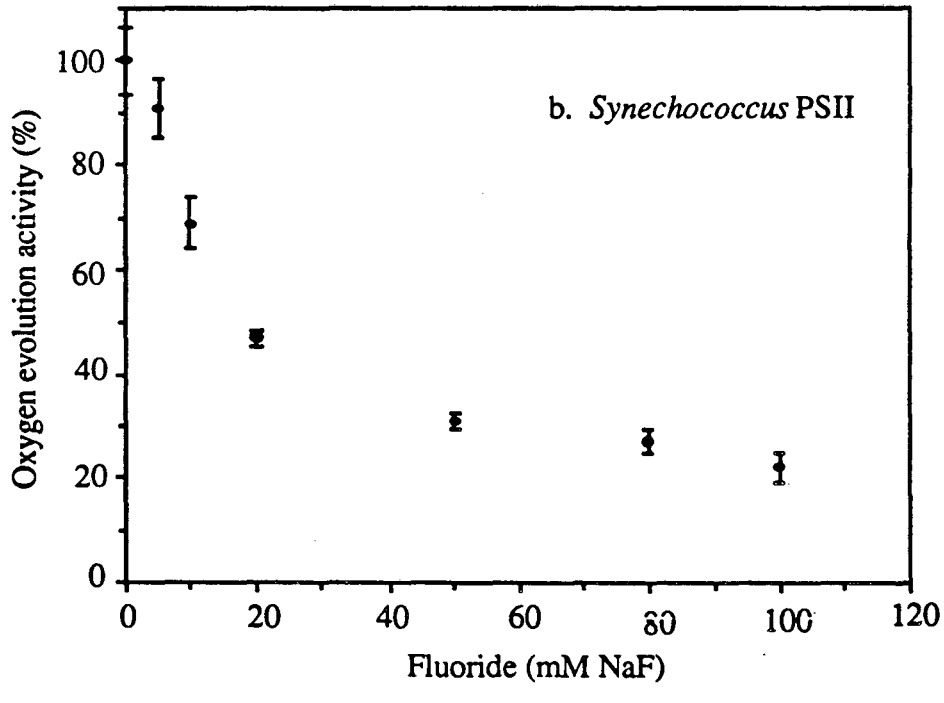

performed on very dilute samples (50 μg Chl/ml for spinach). To relate the results of the steady-state kinetic studies of oxygen evolution activity directly to the results of EPR experiments, samples were treated at the same Chl concentration for both experiments.

Figure 4.2 shows EPR spectra from the S_2 state (200 K illuminated minus dark-adapted spectra) of spinach PSII samples which have been treated at a Chl concentration of 50 μg/ml with 0-100 mM fluoride. The decrease in amplitude of the multiline signal and the increase in g=4 signal appear to be directly correlated (Figure 4.3). In addition, the decrease in multiline signal amplitude parallels the decrease in oxygen evolution activity with increasing concentrations of fluoride. The results of steady-state oxygen evolution studies [Sandusky & Yocum, 1984,1986] indicate that in this range of fluoride concentration, fluoride acts competetively with chloride to inhibit oxygen evolution. Given this competetive behavior, the data in Figures 4.2 and 4.3 indicate that the enhanced g=4 EPR signal is due to fluoride binding at the chloride binding site.

At concentrations above 20 mM NaF, an additional effect on the EPR spectra of spinach PSII samples appears. In Figure 4.4, the spectra of dark adapted samples which have been treated (at 50 μg Chl/ml) with 0-100 mM fluoride are shown. A broad EPR signal around g=2 appears at concentrations greater than 25 mM fluoride. The amplitude of the signal increases with the concentration of fluoride. At these concentrations of fluoride, the samples still give rise to the light-induced EPR signal at g=4 (Figure 4.2). Figure 4.5 is the EPR spectrum of the dark-adapted sample inhibited at 100 mM fluoride after subtraction of the spectrum of the dark-adapted sample treated with 0 mM fluoride. The shape of the g=2 signal can be clearly seen in this subtracted spectrum. The peak-to-peak linewidth of the signal shown in Figure 4.5 is 220 G. At the measuring temperature of 8 K and microwave powers beyond 1 mW, a plot of the amplitude of the EPR signal vs. $(P)^{1/2}$ is not linear, indicating that the EPR signal at g=2 is already saturated at a power of 1 mW (data not shown).

Properties of the g=4 EPR signal produced by inhibition with fluoride. In Figure 4.6 the g=4 EPR signal produced by 200 K illumination of samples inhibited with 50 mM NaF at 0.5 mg Chl/mL is compared with the g=4 EPR signal produced by illumination of samples treated with 50 mM NaCl. The peak-to-peak linewidth of the g=4 spectrum in the fluoride-inhibited samples is 300 G, compared with 350 G in the control (NaCl-treated) samples. In addition, the zero-crossing of the fluoride-induced EPR signal is

Figure 4.2 Amplitude of light-induced g=2 and g=4 EPR signals vs. fluoride concentration. Samples were treated at 50 mg Chl/ml with the indicated concentration of NaF. Samples were then concentrated to 5 mg Chl/ml to make EPR samples. The light-minus-dark subtracted spectra are shown. Spectrometer conditions are: 9.2 GHz microwave frequency, 30 mW microwave power, 100 kHz modulation frequency, 32 G modulation amplitude, 8 K temperature.

Figure 4.2
Amplitudes of light-induced multiline and g=4 EPR signals
as a function of fluoride concentration

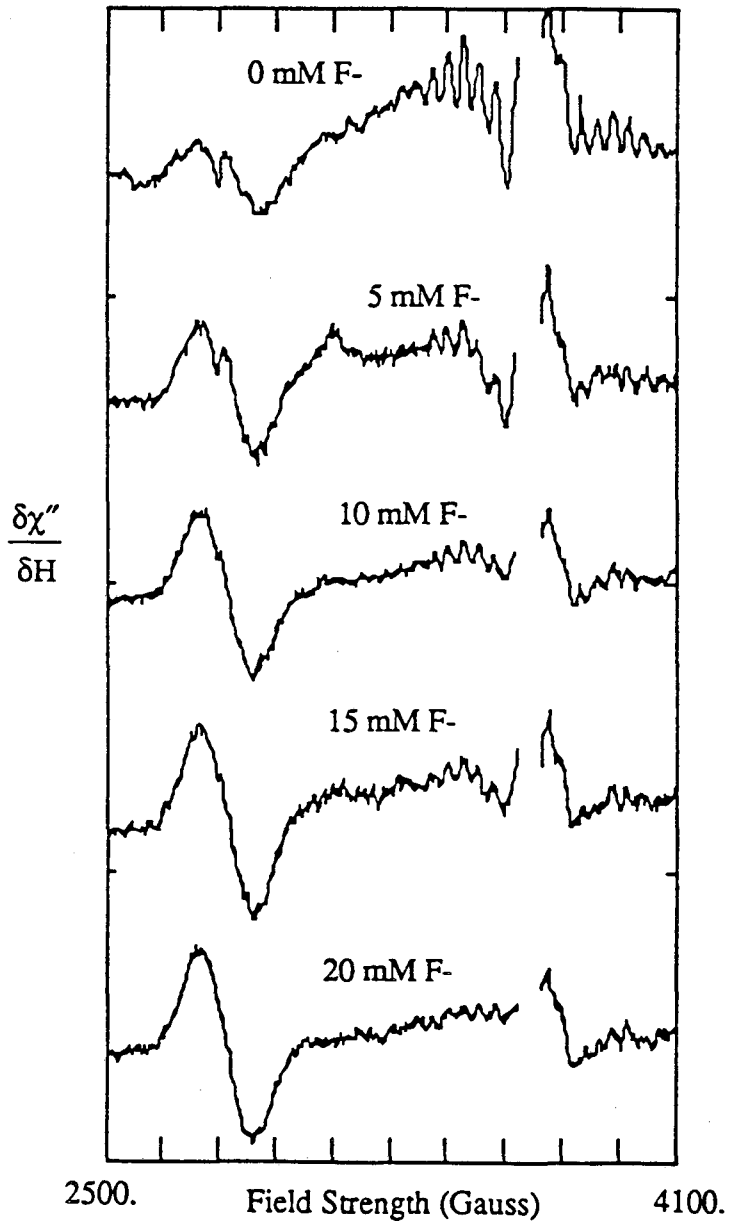

Figure 4.2 (Cont.)

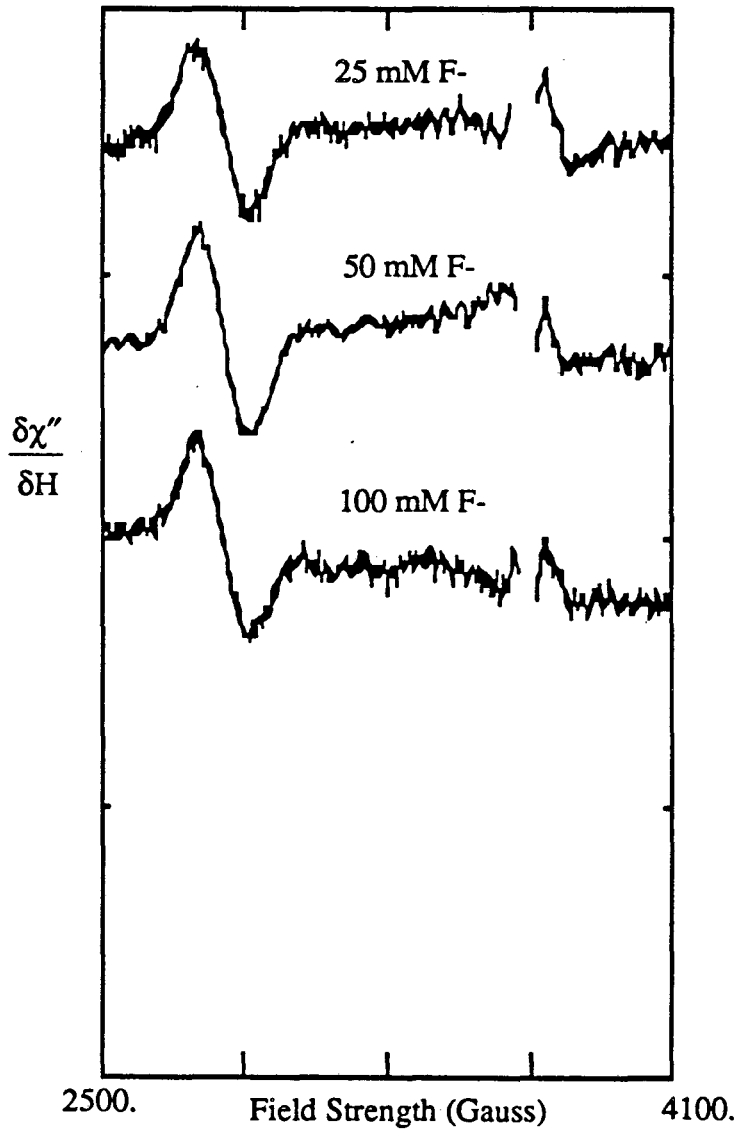

Figure 4.3 EPR signal amplitudes and oxygen evolution activity as a function of fluoride concentration. In (a) the oxygen evolution activity and amplitude of the light-induced multiline EPR signal are plotted against the concentration of NaF. The amplitude of the multiline spectrum is presented as the peak heights of the two hyperfine peaks at ~2700 and 2800 G. The EPR signals were normalized to the amplitude in dark-adapted preparations of the g=4.3 EPR signal due to rhombic Fe^{+3}. The errors of the oxygen evolution activity determination and the normalized EPR signal amplitudes are ~10 %. In (b) the amplitude (peak-to-peak) of the g=4 EPR signal and multiline EPR signals are plotted versus [NaF]. Spectrometer conditions are as in Figure 4.2.

Figure 4.3
EPR signal amplitudes in the oxygen evolving complex as a function of fluoride inhibition

a. Oxygen evolution and multiline EPR signal amplitude vs. mM F-

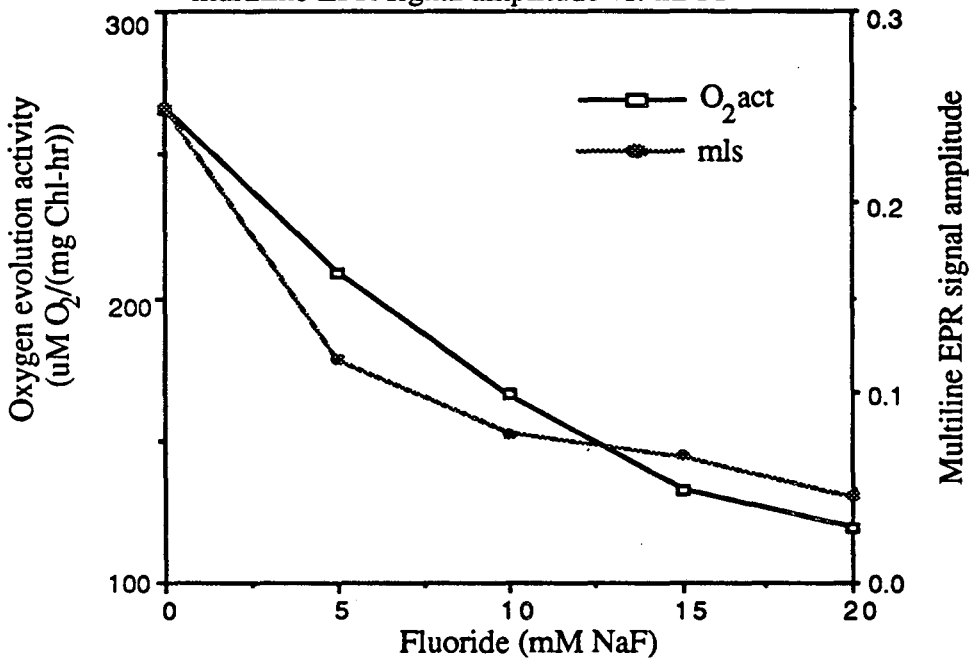

b. Multiline and g=4 EPR signals vs. mM F-

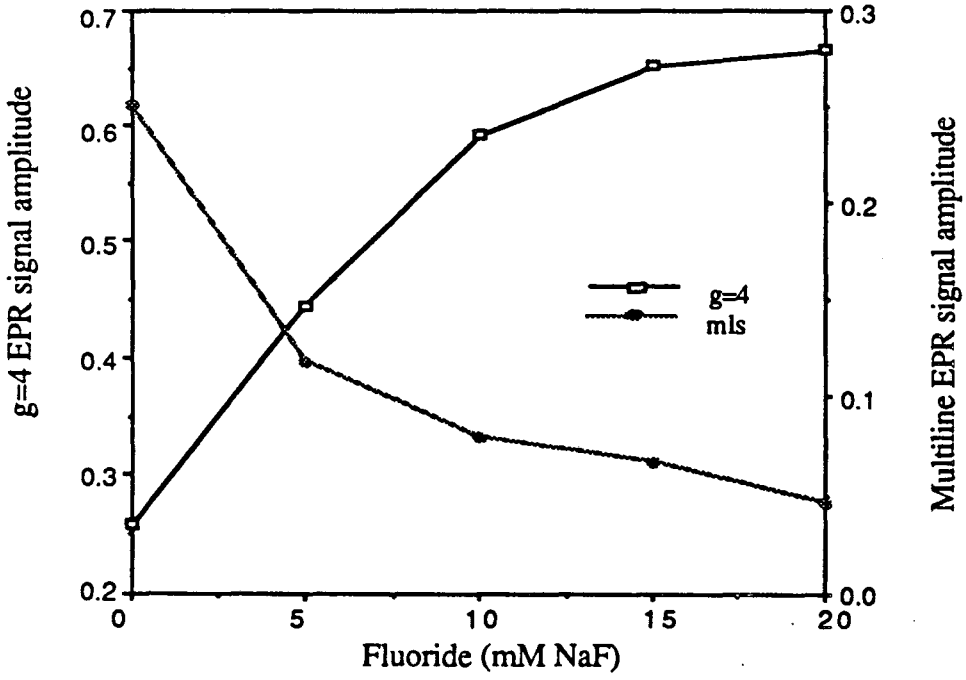

Figure 4.4 EPR spectra of dark-adapted PSII samples following treatment with fluoride. Samples were treated at 50 μg Chl/ml, then concentrated to 5 mg Chl/ml for EPR samples. Spectrometer conditions are as in Figure 4.2. The light-induced signals from these dark-adapted preparations are shown in Figure 4.2.

Figure 4.4
EPR spectra of dark-adapted PSII preparations treated with fluoride

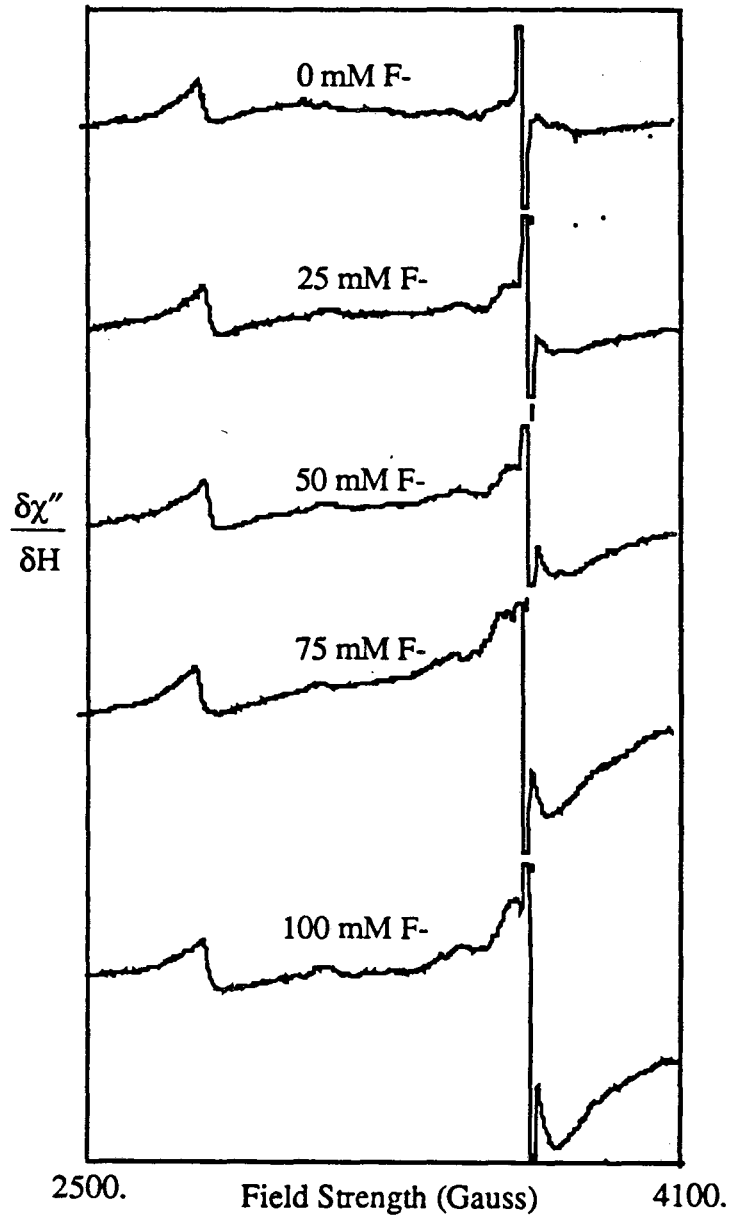

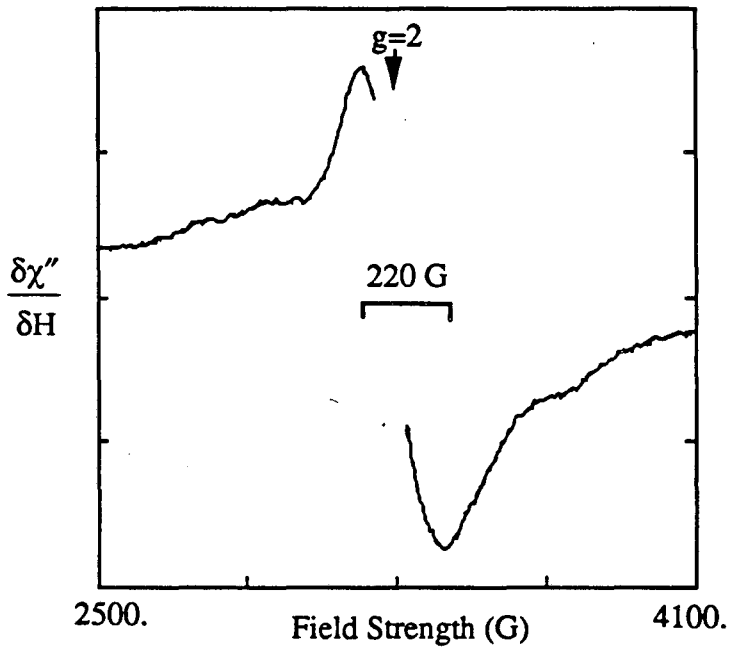

Figure 4.5 EPR signal from dark-adapted PSII sample following treatment with 100 mM NaF. The spectrum of a dark-adapted sample treated with 0 mM fluoride has been subtracted. The subtraction artifact at g=2 has been deleted. Spectrometer conditions are as in Figure 4.2.

decreased slightly to give an effective g-value of 4.2. Since both samples were treated in the same cryoprotectant (sucrose), this reduction in linewidth and increase in g-value is due to the binding of fluoride, and is not a cryoprotectant-induced effect.

The saturation properties at 5 K of the g=4 EPR signals produced in these samples are compared in Figure 4.7. The power saturation behavior of an EPR signal depends on its magnetic environment. Power saturation studies have been used, for example, in distinguishing between EPR signals arising from 2Fe-S or 4Fe-S clusters [Rupp et al., 1978]. The g=4 EPR signals from control and fluoride-treated samples areexpected to have similar saturation properties if they arise from similar species. The peak-to-peak amplitudes of the light-induced signals (after subtraction of the dark background) were measured as a function of microwave power. In both of the samples the linewidth of the g=4 EPR signal did not change between conditions of saturating and non-saturating microwave power (data not shown), indicating that the amplitudes are good measures of total peak intensity. The log of the amplitude of the EPR signal (normalized to the incident microwave power) is plotted against the log of the microwave power. These data were fit to the expression $X''=C/(1 + P/P_{1/2})^{b/2}$ (Castner, 1959), where X'' is represented by the amplitude of the EPR signal divided by the square root of the microwave power, P is the microwave power, $P_{1/2}$ is the power at 1/2 saturation of the signal, C is a constant and b is the "homogeneity" parameter which is expected to be 1 for inhomogeneously broadened spectra. The saturation curves from both samples fit to a value of 1-2 mW for $P_{1/2}$ at the temperature of 5 K (fits not shown). The ability to fit the saturation data more exactly was hampered by the low amplitude of the signal at powers < 1 mW, making it difficult to collect data at nonsaturating powers. The value of 1-2 mW for $P_{1/2}$ is in good agreement with Zimmermann & Rutherford (1984), who report a value of 5 mW for $P_{1/2}$ at 5 K for the g=4 EPR signal.

X-ray absorption spectroscopy of fluoride-inhibited PSII samples. In Figure 4.8 the Mn K-edge inflection point of fluoride-inhibited PSII samples in both dark-adapted (S_1) and illuminated (S_2) states are shown. The inflection point energy of the manganese K-edge, determined by the peak in the first derivative of the edge spectrum, is increased by approximately 1 eV in the illuminated, fluoride-inhibited samples. The inset of Figure 4.8 shows the pre-edge (1s-3d transition) region of the K-edge spectra. In the fluoride-inhibited sample the pre-edge region of the spectrum is more pronounced, and peaks at a lower energy, than in the S_2 state.

Figure 4.6 The g=4 EPR signals from untreated and fluoride-inhibited PSII preparations. The spectrum of an untreated (control) sample (a) is compared with a fluoride-inhibited PSII sample (b). Both samples contain sucrose as cryoprotectant, and both are illuminated at 200 K. Spectrometer conditions as in Figure 4.2.

Figure 4.6
g=4 EPR signals from untreated and
fluoride-inhibited PSII preparations

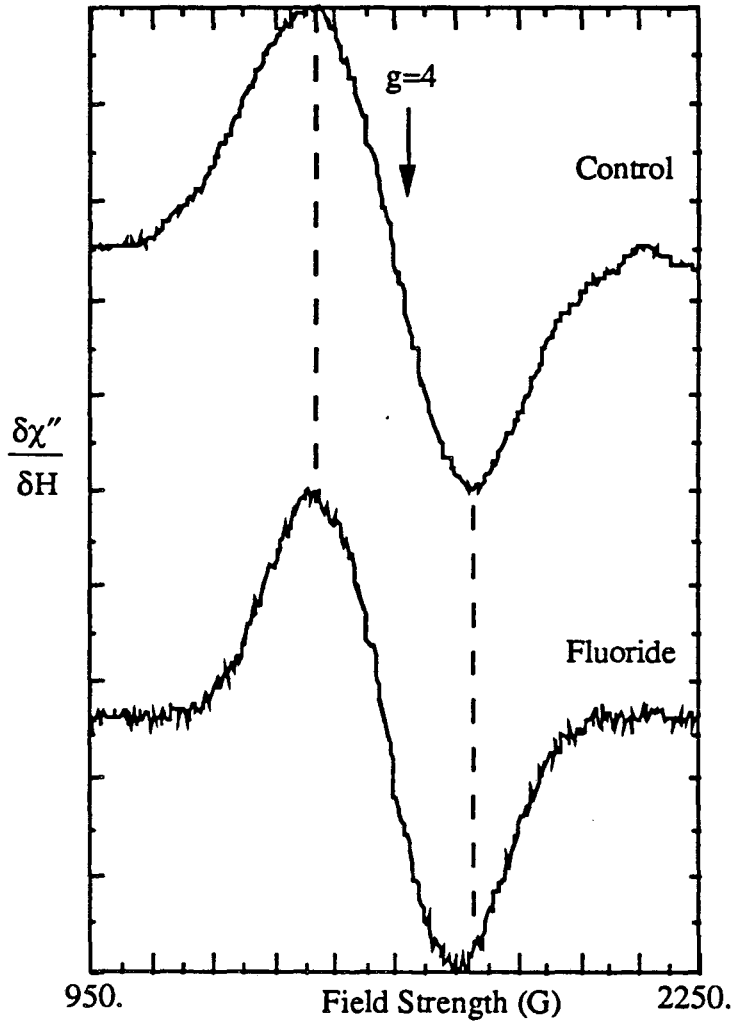

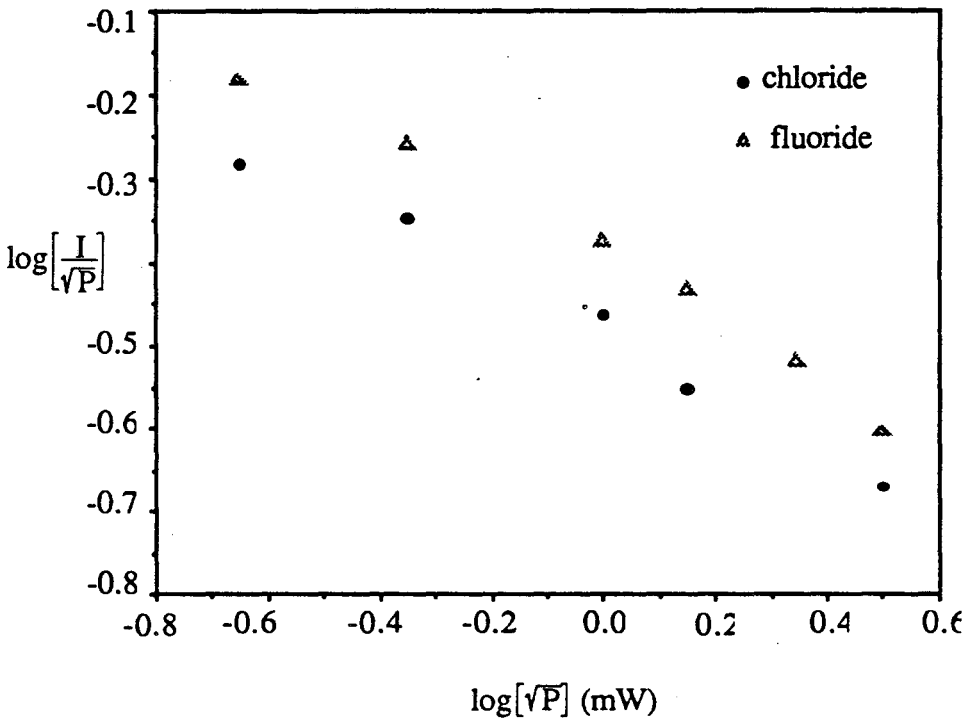

Figure 4.7 Power saturation at 5 K of light-induced g=4 EPR signals from fluoride-treated and control PSII preparations. The log of the peak-to-peak amplitude of the g=4 EPR signals are plotted as a function of log(P). Error in the normalized EPR spectra amplitudes is ~10%. The g=4 EPR signal in control ("chloride") preparations was formed by illumination at 140 K. The g=4 EPR signal in fluoride-inhibited preparations was formed by illumination at 200 K. The amplitudes were measured after subtraction of the spectra of the dark-adapted sample.

The Mn EXAFS spectra of fluoride-inhibited samples are compared with the EXAFS of control (NaCl-treated) samples in Figure 4.9 and 4.10. Small differences are seen in the Fourier transforms in Figure 4.10 of the data from fluoride-treated preparations poised in both the S_1 and S_2 states. The largest difference in the EXAFS between these samples occurs in the S_2 state of the fluoride-treated samples. In these data, the amplitude of the Fourier transform peak II is reduced and less resolved from both peaks I and II as compared with the Fourier transforms of data from control samples.

The curve-fitting analysis of isolated peaks (I and II) in the control samples was discussed in Chapter 3. These results are compared in Table 4.2 with the fits to data from fluoride-inhibited samples. The number of Mn scatterers at 2.7 Å was constrained to be the same in all samples. The principal difference in these three-shell fits to peaks (I and II) is an increase in the magnitude of the Debye Waller value for the Mn scatterers at 2.7 Å in the S_1 and S_2 state fluoride-inhibited samples. This value increases to .007 $Å^2$ in fluoride-inhibited samples in the S_2 state, as compared with .006 $Å^2$ in the control S_2 state samples. The error in the fit to the fluoride-inhibited S_2 state sample is around twice as large as the error in the fit to the control S_2 state sample.

An increase in the apparent disorder of the Mn scatterers at 2.7 Å suggests that the shell could be fit by more than one distance of scatterers. In Figure 4.11, the *k*-space data of the isolated Fourier transform peak II from fluoride and control preparations are compared. The results from fits containing either one or two Mn shells are shown below the figure. The best single-shell fit of control data gives the number of scatterers N=1.2 for the Mn at 2.7 Å. For the two-shell fits, the number of Mn in each shell was constrained to one-half of this value. The fit to two Mn shells decreases the fit error in both the control and the fluoride-treated samples. The second Mn shell (at 2.8 Å) in the control data fit, however, has a Debye Waller value which is higher than that for the single Mn shell fit. This indicates that a two-shell fit of the data from the control sample may not have physical reality. In contrast, the two-shell fits of data from fluoride-inhibited preparations give Debye Waller values for each shell which are less than the value in the single shell fit. This is consistent with the validity of a two-shell fit for this Fourier transform peak in the fluoride-inhibited S_2 state sample.

Figure 4.8 Mn K-edge X-ray absorption edges of control and fluoride-treated spinach PSII preparations in the S_1 and S_2 states. The absorption spectra of dark-adapted S_1 state and 200 K illuminated S_2 state samples are shown. Each trace is the average of data taken on 2 independent samples. The data are smoothed for presentation by a sliding fit to a window of $\pm$ 3 eV. The insets show the pre-edge region of the spectra.

Figure 4.8
Mn K-edge x-ray absorption spectra of control and fluoride-treated spinach PSII preparations in the S_1 and S_2 states

a. Untreated spinach PSII

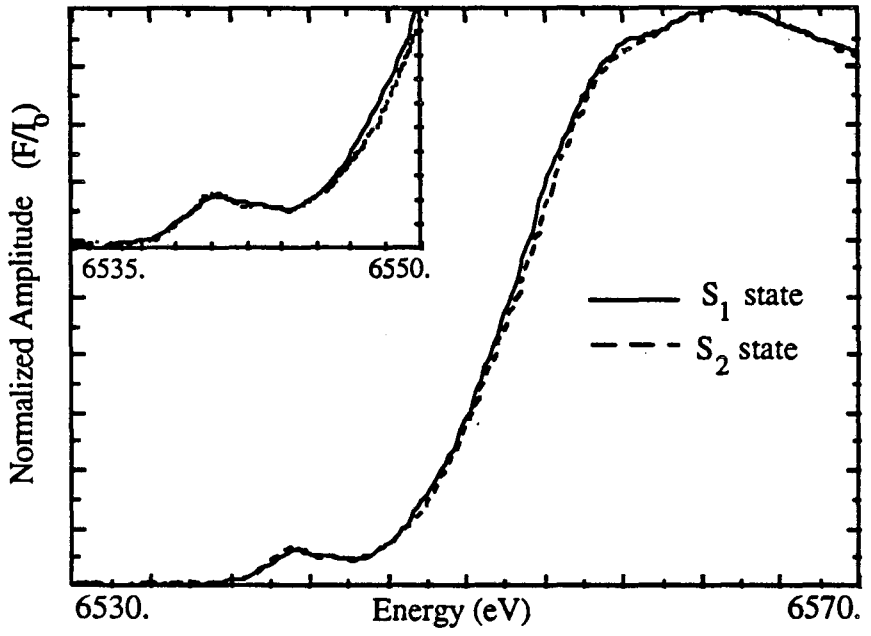

b. Fluoride-inhibited spinach PSII preparations

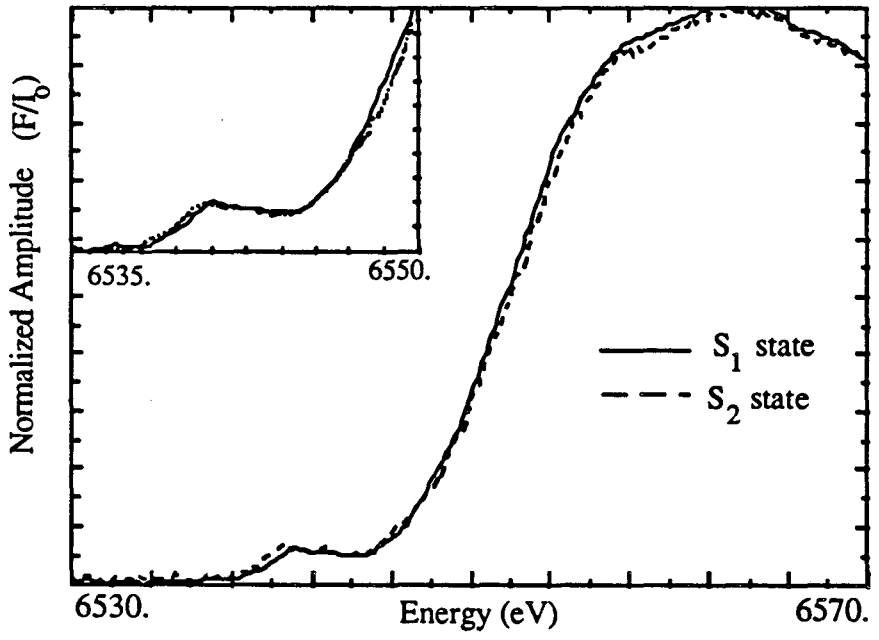

Figure 4.9 *k*-space Mn EXAFS data from spinach PSII control and fluoride-treated preparations. The *k*-space spectra of spinach PSII preparations following inhibition with fluoride are shown for the S_1 (a) and S_2 (c) states. The corresponding data from samples from untreated spinach PSII preparations are in (b) and (d). The data are weighted by k^3, and are the average of approximately 12 scans, 5 seconds per point. The dotted line in each spectrum is the Fourier filtered data set containing peaks I-III shown in Figure 4.10.

Figure 4.9
Mn K-edge EXAFS spectra of control and fluoride-inhibited PSII preparations

a. Fluoride-treated spinach PSII, S_1 state

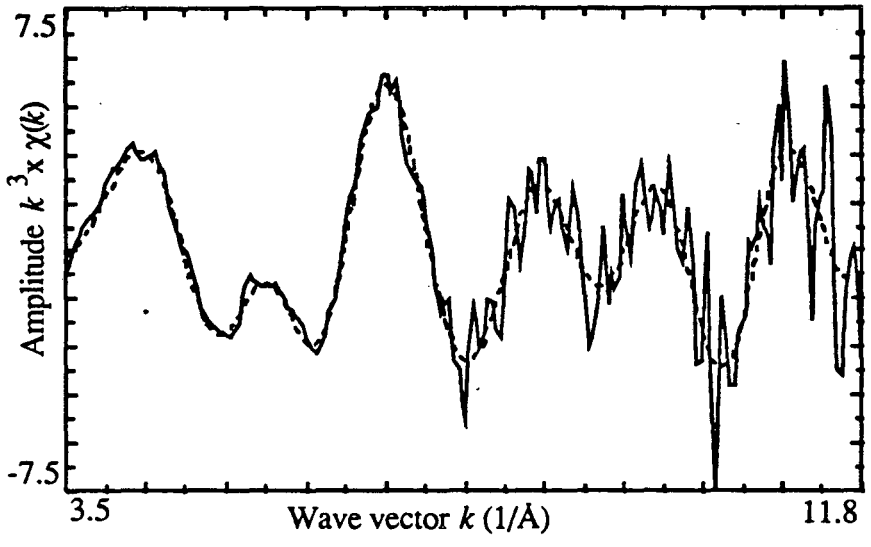

b. Control spinach PSII, S_1 state

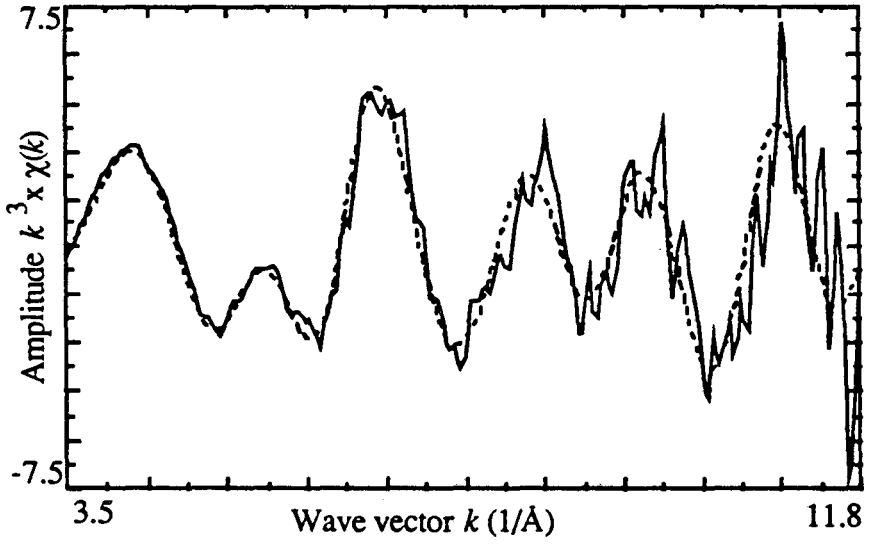

Figure 4.9 (cont.)

c. Fluoride-treated spinach PSII, S_2 state

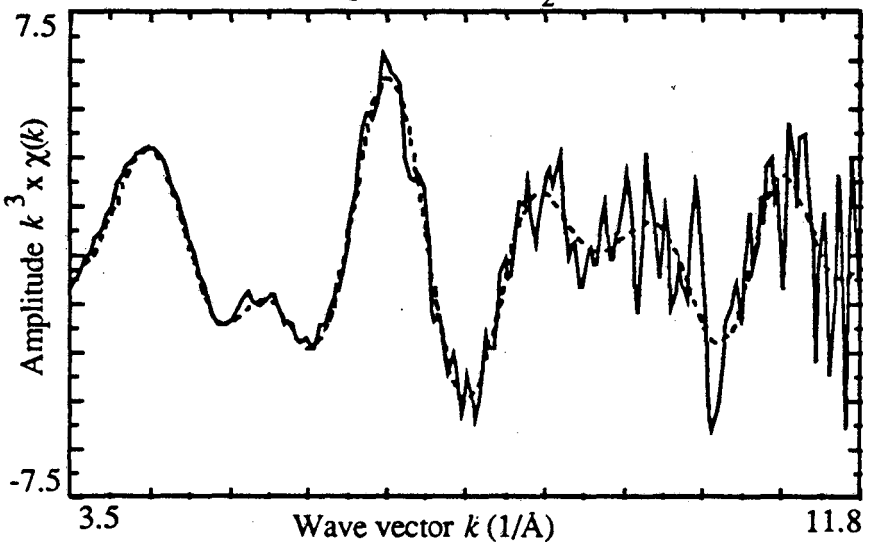

d. Control spinach PSII, S_2 state

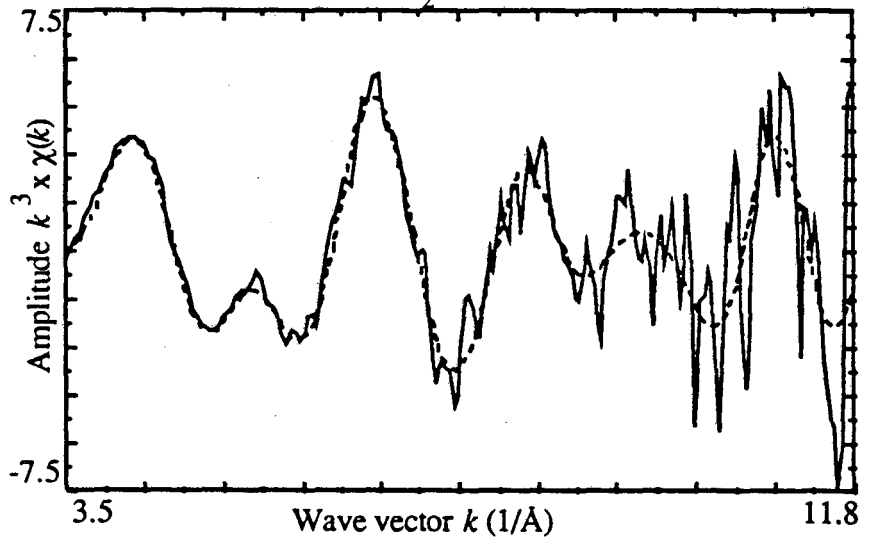

Figure 4.10 Fourier transforms of Mn EXAFS data from control and fluoride-treated spinach PSII preparations. The Fourier transforms of the data in Figure 4.9 are presented. Three main peaks are identified.

Figure 4.10
Fourier transforms of Mn EXAFS from control and fluoride-treated spinach PSII preparations in the S_1 and S_2 states

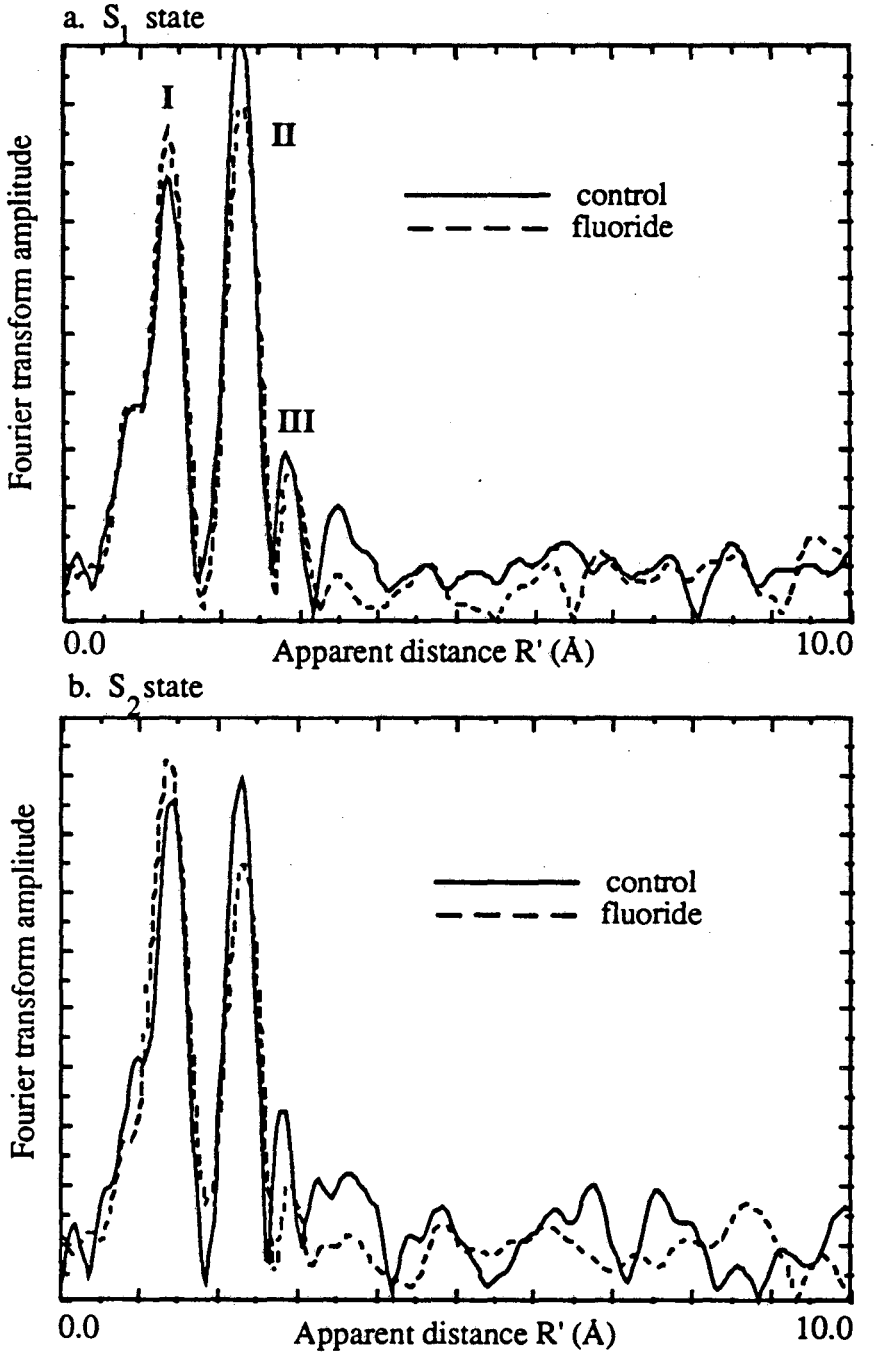

Figure 4.11 Isolates of peak II from control and fluoride-treated spinach PSII preparations poised in the S_2 state. Peak II from the Fourier transforms in Figure 4.10b were isolated and the back-transformed *k*-space data was fit with a single Mn or with two Mn shells. For these fits the number of Mn was constrained to N=1.2 in the single Mn shell fits, and N=0.6 for each shell in the two Mn shell fits. ΔE_0 was held to values between -20 and +10 eV.

Figure 4.11

Isolates of peak II from control and fluoride-treated spinach PSII preparations poised in the S_2 state

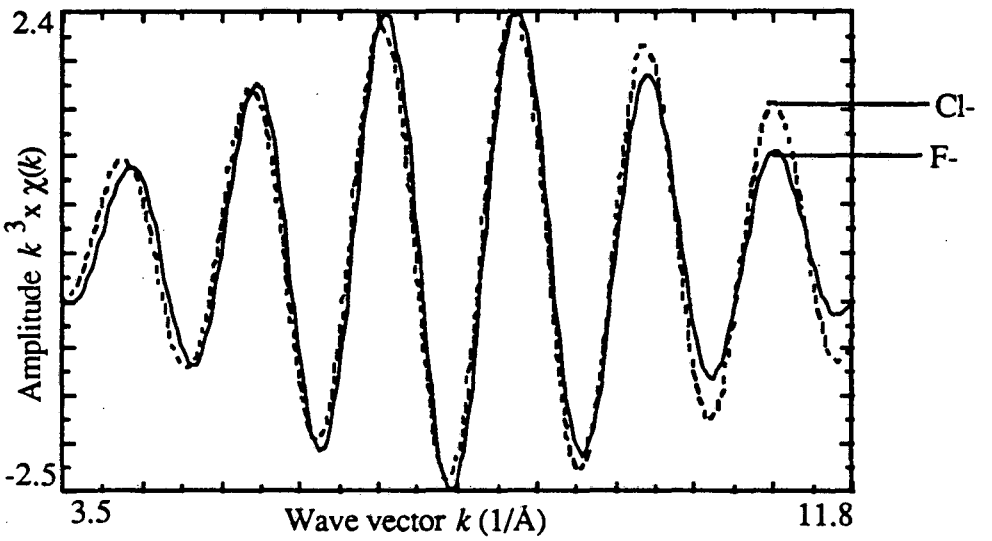

Fit parameters (defined in Table 4.1):

Single Mn shell

		R (Å)	N	σ^2 (Å)^2	ΔE_0(eV)	Fit error
a. F^-	Mn	2.74	1.2	.007	-12.0	23
b. Cl^-	Mn	2.73	1.2	.006	-15.0	15

Two Mn shells

a. F^-	Mn	2.84	0.6	.006	1.0	9
	Mn	2.68	0.6	.002	-20.0	
b. Cl^-	Mn	2.81	0.6	.008	-5.0	9
	Mn	2.70	0.6	.002	-20.0	

Table 4.2

Simulation results for EXAFS data on control and fluoride-treated spinach PSII preparations

Preparation	Atom	R(Å)[a]	N	σ^2 (Å^2)	ΔE (eV)	Fit error
Spinach control S_1	O	1.85	2.2	.002	8	23
	O	1.95[b]	5.0	.010	-15	
	Mn	2.73	1.2[c]	.004	-15	
Fluoride-treated S_1	O	1.82	2.0	.002	9	27
	O	1.91	5.0	.010	-15	
	Mn	2.73	1.2	.006	-13	
Spinach control S_2	O	1.85	2.2	.002	10	18
	O	1.94	5.0	.009	-15	
	Mn	2.74	1.2	.006	-15	
Fluoride-treated S_2	O	1.84	2.2	.002	10	40
	O	1.92	5.0	.008	-15	
	Mn	2.73	1.2	.007	-14	

(a) Parameters are: R, distance to scattering atom in Å; N, average number of scatterers or coordination number; σ^2, the disorder or Debye Waller parameter in Å^2; ΔE, difference between the calculated and assumed edge energy E_0; fit error, sum of residuals between calculated fit and data. The coordination numbers are derived by multiplication of the fit values by a factor of 2 (Teo & Lee, 1979).
(b) Equivalent fits could be obtained in this shell for all samples with a increase of R up to ~2.05 Å. The range of equivalent fits included values for σ^2 and N decreasing to .002 Å^2 and 0.5, respectively.
(c) The number of scatterers at 2.7 Å was held to N=1.2 for all samples.

Discussion

There are many possible roles that halide could take in affecting the catalytic cycle of the oxygen evolving complex. Precedence exists in enzyme catalysis of chloride ions interacting with positively charged amino acid side chains [i.e., Lifshitz & Levitzki, 1973] as well as chloride binding to the metal centers of metalloproteins [i.e., Ikeda-Saito & Prince, 1985]. Spectroscopic studies should help distinguish between these possibilities. The EPR and X-ray absorption spectra of fluoride-inhibited PSII samples presented in this study show that fluoride directly affects the structure of the manganese cluster in the oxygen evolving complex. Since fluoride has been shown to compete with chloride in influencing the steady-state oxygen evolving activity of the complex, this indicates that the action of chloride is also very close to the manganese.

It is important to be able to relate the results of oxygen evolution activity studies, which have shown fluoride, acetate, and amines to compete in inhibiting oxygen evolution, with spectroscopic studies, which address the structure of the Mn complex in a particular S state. The data in Figures 4.2 and 4.3 establish that in fluoride-treated PSII samples the S_2 state g=4 EPR signal arises from an inhibited complex. This agrees with evidence that chloride is necessary for the S_2 to S_3 state transition [Ono et al., 1986a, 1986b, 1987; Vass et al., 1987].

The g=4 signal has been proposed to arise from Mn(IV) in an S=3/2 ground state [Casey & Sauer, 1984; Zimmermann & Rutherford, 1984]. An S=3/2 ground state could originate either from a monomeric Mn(IV) [Hansson et al., 1987], or from three or four exchange coupled Mn [see Brudvig, 1989]. The recent observation of >16 Mn hyperfine lines on the g=4 EPR signal from ammonia treated samples which have been oriented indicates that the signal arises from the coupling of at least 3 Mn ions into an effective S>1 state [Kim et al., 1990]. In control, untreated preparations, the g=4 EPR signal appears upon low temperature (140 K) illumination of the sample. Warming the sample (to 200 K) elicits an the appearance of the multiline EPR signal at the expense of the amplitude of the g=4 EPR signal [Casey & Sauer, 1984; Zimmermann & Rutherford, 1984]. Cryoprotectant and the presence of small molecules such as ethylene glycol or ethanol influence the relative yields of the g=4 and the multiline EPR signals in samples illuminated at 200 K [Zimmermann & Rutherford, 1984]. In contrast, preparations which have been treated with fluoride show the g=4 EPR signal upon illumination at 140 K, but the multiline signal does not

grow in upon warming the sample to 200 K (data not shown). In addition, in fluoride treated samples the g=4 EPR signal is observed upon 200 K illumination even in the presence of glycerol as the cryoprotectant. In untreated preparations, glycerol inhibits the formation of the g=4 EPR signal upon 200 K illumination. Thus, the effect of fluoride is to stabilize the configuration of the oxygen evolving complex which gives rise to the g=4 EPR signal, and this effect is independent of the cryoprotectant and temperature of illumination.

The g=4 EPR signal is narrower by ~50 G in the presence of fluoride. There are several contributions to the linewidth of this EPR signal. The signal is inhomogeneously broadened, meaning that the contributions to its linewidth include g-anisotropy, unresolved hyperfine coupling, and "g-strain" (the influence of microheterogeneities in environment giving rise to a spread in the effective magnetic field seen by the unpaired spin). It has been determined from measurements of the g=4 signal at S (4 GHz) and X (9 GHz) bands that the linewidth contribution due to g-strain, which should decrease with frequency, is very small in this signal [Haddy et al., 1989]. The hyperfine coupling due to Mn is unresolved in the spectra of unoriented samples, and certainly contributes to the linewidth of the signal. This Mn hyperfine coupling is not expected to change, however, through the substitution of fluoride for chloride in the environment of the unpaired spin. If the linewidth of the g=4 EPR signal were dominated by ligand hyperfine coupling, the effect of substituting a fluoride ligand for chloride would be to *increase* the linewidth. For an inhomogeneously broadened line, the expected change *in the component of the linewidth due to the superhyperfine interaction* upon substitution of a ligand nucleus is a function of the ratio of the nuclear magnetic moments and the nuclear spins [Kip et al., 1953]:

$$\frac{\Delta H_{Cl}}{\Delta H_F} = \left(\frac{I_{Cl}(I_{Cl}+1)}{I_F(I_F+1)}\right)^{1/2} \frac{\gamma_{Cl}}{\gamma_F} \qquad [4\text{-}1]$$

Assuming a relatively small quadrupole moment interaction from the Cl nucleus, the relative contributions from Cl ($I=3/2$, $\gamma_n=0.53$) and F ($I=1/2$, $\gamma_n=5.3$) to the linewidth would be increased by a factor of 5 $\Delta H_{p\text{-}p}$ if Cl were replaced by F. Superhyperfine coupling to ligand atoms, however, is expected to be a very minor component of the linewidth in EPR signals from high valent Mn [Britt et al., 1989], and the linewidth

decrease of ~50 G in the g=4 EPR signal upon substitution of fluoride for chloride is not due to a change in superhyperfine interactions.

The g=4 EPR signal (in untreated preparations) does show g-anisotropy (Rutherford, 1985, A. Haddy, personal communication). The effect of g-anisotropy on the linewidth of the EPR signal depends on the zero-field splitting terms D and E:

$$H_{zfs} = D[S_z^2 - 1/3S(S + 1)] + E(S_x^2 - S_y^2) \qquad [4\text{-}2]$$

Here $S_{x,y,z}$ are the components of the spin along the x, y, and z axes, and S is the value of the total spin. In a powder pattern EPR spectrum the transitions due to specific orientations of the magnetic field with respect to the molecular axes may not be resolved. Given axial symmetry (D>>E, E≠0) the EPR spectrum features designed by g_y and g_x may be close together but not resolved. In this case, as the ratio E/D decreases (indicating greater axial symmetry), the linewidth of the (g_x, g_y) powder pattern EPR signal component will also decrease [Hempel et al., 1970; Blumberg & Peisach, 1973]. In a cluster consisting of several metal atoms, the values for D of each individual metal center contribute to the total zero field splitting for the complex [Diril et al., 1989]. Ligand field strength increases as in the "spectrochemical series": $I^- < Cl^- < F^- < H_2O < NH_3$ [i.e., Carrington & McLachlan, 1967]. The substitution of a fluoride ligand for a chloride ligand is expected to decrease the ratio E/D, thus decreasing the linewidth of the g=4 EPR signal. The narrowing of the g=4 EPR signal in the presence of fluoride can be explained, then, by a decrease in the rhombicity of the Mn caused by the binding of a fluoride instead of a chloride ligand. Similar ligand-induced effects upon substitution of fluoride for chloride have been seen in S=3/2 Cr^{+3} (d^3) complexes [Hempel et al., 1970; Pedersen & Toftlund, 1974] and in Fe^{+3} porphyrin systems [Ikeda-Saito & Prince, 1985].

It is of note that a narrower linewidth for the g=4 EPR signal is also reported in samples which have been treated with ammonia under conditions of low chloride concentration [Andréasson & Hansson, 1987]. Under these conditions, the ammonia "type II" site, competetive with both fluoride and chloride in steady-state oxygen evolution measurements, is expected to be filled. These differences in the g=4 EPR signal lineshape between fluoride, ammonia, and chloride-treated samples have also been detected in EPR experiments performed at P band (16 GHz) (A. Haddy, personal communication).

It should also be noted that the narrowing of the g=4 EPR signal in the presence of fluoride and ammonia seems to depend on the croprotectant used. The samples whose EPR spectra are shown in Figures 4.3 and 4.4 were all treated with fluoride when sucrose was present in the media. The EPR samples contained both sucrose and glycerol as cryprotectants (see Methods). In contrast, samples treated with fluoride (W. Beck, unpublished results) in the presence of ethylene glycol show inhibition of the multiline signal, but do not show the narrowing of the g=4 EPR signal. Samples treated with ammonia in the presence of ethylene glycol also do not show the narrowed g=4 EPR signal (Beck & Brudvig, 1986), although the narrowing effect is present in samples treated in sucrose [Andréasson & Hansson, 1987; A. Haddy, personal communication]. The cause for this dependence on cryoprotectant is unknown, but could be related to cryoprotectant-dependent differences in the affinity of chloride and related inhibitors [W. Beck, personal communication].

Fluoride clearly has a second affect on the EPR signals from the oxygen evolving complex. A broad g=2 EPR signal appears in dark-adapted samples which have been treated with high concentrations of fluoride (Figures 4.5 and 4.6). The amplitude of this EPR signal appears to be independent of the amplitude of the light-induced g=4 signal. The amplitude of the g=2 signal increases dramatically with the concentration of fluoride between 25 and 100 mM fluoride. In contrast, the light-induced g=4 EPR signal shows a steep increase in amplitude between 0 and 25 mM fluoride, which is also the region of most dramatic decline of oxygen evolution activity. At concentrations greater than 25 mM fluoride the amplitude of the light-induced g=4 signal does not increase greatly. The appearance of the broad g=2 signal in dark-adapted samples requires a high ratio of fluoride to PSII centers, as it does not appear in the samples prepared for EXAFS studies which were treated with 50 mM NaF at higher chlorophyll concentrations (0.5-1.0 mg Chl, data not shown).

This broad g=2 EPR signal appears very similar to one which has been reported in calcium-depleted PSII preparations. A broad (160 G wide) EPR signal centered at g=2 is seen in spinach PSII samples which have been treated to remove calcium, and then poised in the S_3 state [Boussac et al., 1989; Sivaraja & Dismukes, 1989]. The signal from calcium-depleted samples has a reported linewidth of 160 G, and has been suggested to arise from an oxidized radical species whose EPR signal is broadened through weak exchange coupling with a metal center [Boussac et al., 1989, 1990]. Power saturation studies indicate that, like the signal from calcium-depleted preparations [Boussac et al., 1989], the broad g=2 signal shown in these dark-adapted

fluoride inhibited samples is easily saturated between 1 and 20 mW at 8K (data not shown). Unlike the signal from the calcium-depleted preparations, however, this signal is present in fluoride-treated samples which have not been illuminated.

There are several possibilities for the origin of the g=2 EPR signal detected in the dark-adapted fluoride treated preparations. Broad EPR signals centered around g=2 arise from Mn^{+2} doped into glasses [Nicklin et al., 1973]. The linewidth of the signal varies with the percent of Mn in the glass, can become quite narrow (<200 G) depending on the history of the glass, and may show no resolved hyperfine coupling from the Mn nucleus. It could be the case that under high concentrations of fluoride high valent Mn from the photosystem becomes reduced, but is not released from the protein. Under these conditions, the broad, unresolved spectrum of Mn^{+2} in the glass may appear instead of the familiar six-line EPR spectrum which arises from octahedrally coordinated Mn^{+2}. Arguing against this scenario is the result that the yield of the light-induced g=4 EPR signal is independent of the amount of broad g=2 signal seen in the dark. The g=4 signal arises from manganese in the photosystem (Cole et al., 1987, and see below). While there is no evidence that the g=4 signal arises from all four of the photosystem manganese atoms, analogy with the g=4 signal arising from ammonia-treated preparations indicates that *at least* three manganese atoms contribute to the signal (Kim et al., 1990). The data presented here cannot disprove the theory that the broad g=2 EPR signal comes from the fluoride-induced reduction of manganese which is isolated from the manganese giving rise to the g=4 EPR signal. It seems improbable, however, that such a structural arrangement occurs in the oxygen evolving complex (see, for example, the conclusions from Chapter 3).

A second possibility for the broad g=2 EPR signal seen in the dark-adapted fluoride-inhibited preparations is that it is due to Fe^{+3} which has been altered through the binding of fluoride. Since high spin Fe^{+3} is an S=5/2 system, it could in principle give rise to EPR signals similar to those discussed for Mn^{+2} (S=5/2) species. The oxygen evolving complex contains cytochrome b_{559}, Fe^{+2} in the Fe-quinone acceptor complex, and nonspecifically bound Fe^{+3} which gives rise to an EPR signal at g=4.3. Signals from ferricytochrome species with axially bound fluoride generally occur at g=6, with very small amplitude in the g=2 region [Blumberg & Peisach, 1973]. It is therefore unlikely that the broad g=2 signal from fluoride-inhibited preparations is due to modified, oxidized cytochrome b_{559}. The amplitude of the g=4.3 EPR signal due to nonspecifically bound iron in a rhombic environment does not decrease as the g=2 signal increases, making it unlikely that the signal arises from nonspecific Fe^{+3}.

Finally, samples which show a very large g=2 signal in the dark do not have the comcomittant decrease in amplitude of the light-induced EPR signal at g=1.8 which is due to the reduced Fe-quinone species. These observations make it unlikely that the broad g=2 EPR signal is due to either nonspecifically bound Fe^{+3} or Fe^{+3} from the iron-quinone acceptor complex in the oxygen evolving complex.

The broad g=2 signal in the fluoride-treated samples may be due to the oxidized species proposed to give rise to the broad g=2 signal in calcium depleted samples. The similarity between the two signals is striking. The extremely low solubility of CaF_2 ($K_{sp} \sim 10^{-11}$) suggests that a high concentration of fluoride could result in fluoride replacing ligands to the calcium, creating a "calcium-depleted" enzyme. Exposure to the ambient potential could promote oxidation of the species giving rise to the g=2 EPR signal. Supporting a stabilization of oxidized species is the observation that as the concentration of fluoride is increased, an increase in the amplitude of the EPR signal due to oxidized cytochrome b_{559} is also seen (Figure 4.4). The g-2 EPR signal in calcium-depleted samples has been suggested to arise from an organic radical species broadened by exchange interaction with a nearby spin from manganese in the S_2 state (S=1/2) [Boussac et al., personal communication]. In the case of the dark-adapted fluoride-inhibited preparations, however, the manganese is expected to be in the S_1-state with an even spin configuration. If the broad g=2 EPR signal is due to a radical species interacting with the manganese complex, the difference in spin states of the complex in the S_1 and the S_2 states may contribute to the broader linewidth in the signal from fluoride depleted samples. The linewidth of such signals has been shown to be quite sensitive to environmental effects which govern the exchange coupling parameters of the system [Butler et al., 1984].

From the above observations, the most likely source of the broad g=2 EPR signal in the dark-adapted fluoride treated PSII preparations is the same species that gives rise to the nearly identical signal from the S_3 state of calcium-depleted preparations.

The energy of the manganese K-edge inflection point is an indication of the oxidation state of the manganese, as well as the average distance of the ligands to the manganese. An increase in K-edge inflection point energy has been shown for the advance of the oxygen-evolving complex from S_1 to S_2, both in samples which give rise to the g=4 EPR signal through illumination at 140 K, and in samples illuminated at higher temperatures (200 K, and 274 K in the presence of DCMU). The K-edge inflection point energy also increases upon illumination of fluoride-treated PSII

samples (Figure 4.9). The shape of the K-edge in fluoride treated preparations is very similar to that of control samples in both the S_1 and S_2 states. The pre-edge feature at ~6540 eV also shows the same behavior in the S_1 and S_2 states in fluoride-inhibited preparations, becoming more pronounced in the S_2 state. This small change in the pre-edge feature upon advance to S_2 has been correlated with the oxidation of Mn^{+3} to Mn^{+4} [Sauer et al., 1988].

The EXAFS spectra of fluoride-inhibited preparations show differences relative to the control samples. The amplitudes of the Fourier transform peaks I and II are slightly different in the S_1 preparations of control and fluoride-treated samples. In the S_2 state, the amplitude of peak II in the fluoride-inhibited sample is diminished and the peak appears broader, showing less resolution from peaks I and III. In addition, peak III appears noticeably smaller in the fluoride-treated S_2 preparation. The parameters used to fit these data (Table 4.2) differ only slightly between the fluoride and control preparations. The parameters used to fit peak II in the S_1 and S_2 data from fluoride-treated preparations indicate that a larger value for the Debye Waller parameter for the Mn shell at ~2.7 Å is necessary to fit these data. As indicated in Figure 4.11, the decreased amplitude in peak II for fluoride-treated preparations poised in the S_2 state can be modelled using two Mn shells at distances that differ by >0.1 Å. In control preparations, a fit for this peak which includes two different Mn distances results in an *increase* in the Debye Waller parameter for one of the Mn shells [Figure 4.11]. This type of fit is therefore not justified for data from the control preparations. This does not mean that there is not a spread in Mn-Mn distances in other preparations, but only that the distances cannot be resolved into separate components.

A survey of μ-oxo bridged Mn(III)Mn(IV) compounds indicates that the Mn-Mn distances differ by ~.08 Å depending on the ligands of the complexes [Wieghardt, 1989]. Differences could be larger in a protein environment, which would include amino acid instead of macrocyclic ligands. The Mn-Mn distance in a μ-oxo bridged compound depends both on the bridging Mn-oxo distances and on the Mn-O-Mn bond angle. For example, the oxidation of Mn(III,IV) complex to Mn(IV,IV) is in general accompanied by a decrease (by ~0.1 Å) in the bridging Mn-O bond lengths, but an increase in the Mn-Mn distance of ~0.05 Å [summarized in Christou, 1989, and Wieghardt, 1989]. The increase in Mn-Mn distance is due to an increased Mn-O-Mn bond angle, which is more flexible in the case of spherically symmetric d^3 Mn(IV) ions than in Jahn-Teller distorted d^4 Mn(III) ions [see Goodson et al., 1990]. Replacement of a chloride ligand with a fluoride ligand may affect the Mn-Mn distance in a μ-oxo

bridged system either by exerting a *trans* influence on the bridging Mn-O bond lengths [i.e., Diril et al., 1989], or by changing the Mn-O-Mn bond angle through steric effects.

The Mn-F bond length in Mn^{+3} and Mn^{+4} componds is expected to be < 2 Å [Levason & McAuliffe, 1971], compared with average Mn-Cl bond distances of >2 Å [i.e., Pecoraro & Butler, 1986]. The backscattering amplitude function for fluoride is very similar to that from other light elements such as nitrogen and oxygen. It is therefore not possible to determine the presence of a single fluoride ligand per four Mn using EXAFS. Qualitatively, however, the trends in the Fourier transforms shown in Figure 4.10 are mimicked in simulations which include either a single chloride ligand at 2.3 Å or a single fluoride ligand at 1.9 Å. The comparison of such simulations for the S_1 state are shown in Figure 4.12. The contribution to the Fourier transform from a chloride ligand at 2.3 Å appears as a small peak between peaks I and II. It can be seen that the substitution of a fluoride ligand tends to increase the amplitude of peak I, and increase the apparent resolution between peaks I and II. Similar differences are also seen in the region between peaks I and II in the Fourier transforms of the S_1 states of control and fluoride-treated preparations (Figure 4.12b). While this is by no means proof of the presence of a fluoride ligand, the similarity between the simulated data and the photosystem EXAFS supports the substitution of fluoride for chloride as a ligand to the manganese.

The substitution of fluoride for chloride has a direct effect on both the EPR spectrum and on the manganese EXAFS from PSII samples. Both effects can be interpreted in terms of fluoride replacing chloride as a ligand to the manganese of the oxygen evolving complex. In Chapter 3, a structural model was proposed for the oxygen evolving complex. This model is reproduced in Figure 4.13, and a speculative role for halide in the S_1 and S_2 states is included. The model presented in Chapter 3 includes two di-μ-oxo bridged Mn dimers, linked by a mono μ-oxo, carboxylato bridge. In Figure 4.13, a chloride atom is included as a single ligand of one manganese. The putative histidine ligand and a calcium atom are also included in this model. The oxidation states of the manganese are included. The S_1 state is shown as consisting of a Mn(III,III) and a Mn(IV,IV) dimer. These oxidation states are favored for the S_1 state of the oxygen evolving complex because the X-ray absorption edge inflection point energy of ~6551 eV for the S_1 state can best be accounted for with the presence of at least two Mn(IV) atoms [V.K. Yachandra, unpublished results]. In the

Figure 4.12 Simulated effect of 1 fluoride or 1 chloride ligand per four manganese on the EXAFS data from the oxygen evolving complex. Simulations in (a) were performed as follows. The best 3-shell fit to the *k*-space data from Fourier filtered peaks I and II from a control S_1 state sample was obtained, as in Table 4.2. A shell due to one F at 1.9 Å or one Cl at 2.3 Å was added to the fit, and the simulated data was Fourier transformed. The simulated halide shell included the parameters $\sigma^2 = .005$ Å^2 and ΔE_0=-10 eV. The Fourier transforms in (b) are of fluoride-treated (solid line) and control samples (dotted lines). Data from both spinach and *Synechococcus* PSII S_1 samples (dotted lines) are shown for comparison. Note that the simulated data contain components from the isolated peaks I and II, whereas the data in (b) have not been Fourier filtered.

Figure 4.12
Simulated effect on Mn EXAFS of one fluoride or one chloride ligand per four manganese

a. Simulated spectra

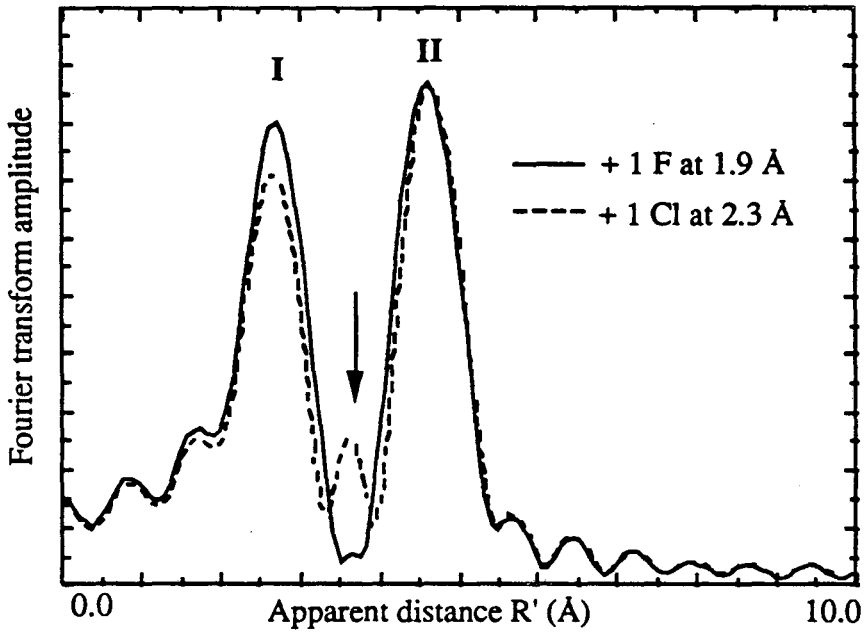

b. Mn EXAFS data of S_1 state fluoride and control PSII preparations

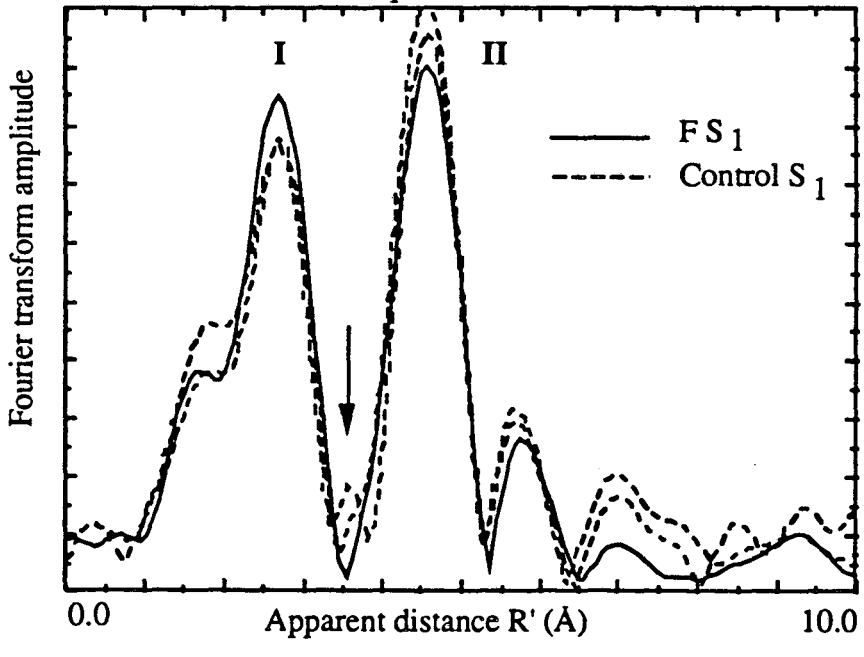

Figure 4.13 Structural model for halide in the oxygen evolving complex. The oxygen evolving complex in the S_1, S_2, and S_3 states is shown. Halide is included as a ligand to one manganese. A putative histidine ligand is also shown, as well as a functional calcium atom.

Figure 4.13
Structural model for the oxygen evolving complex

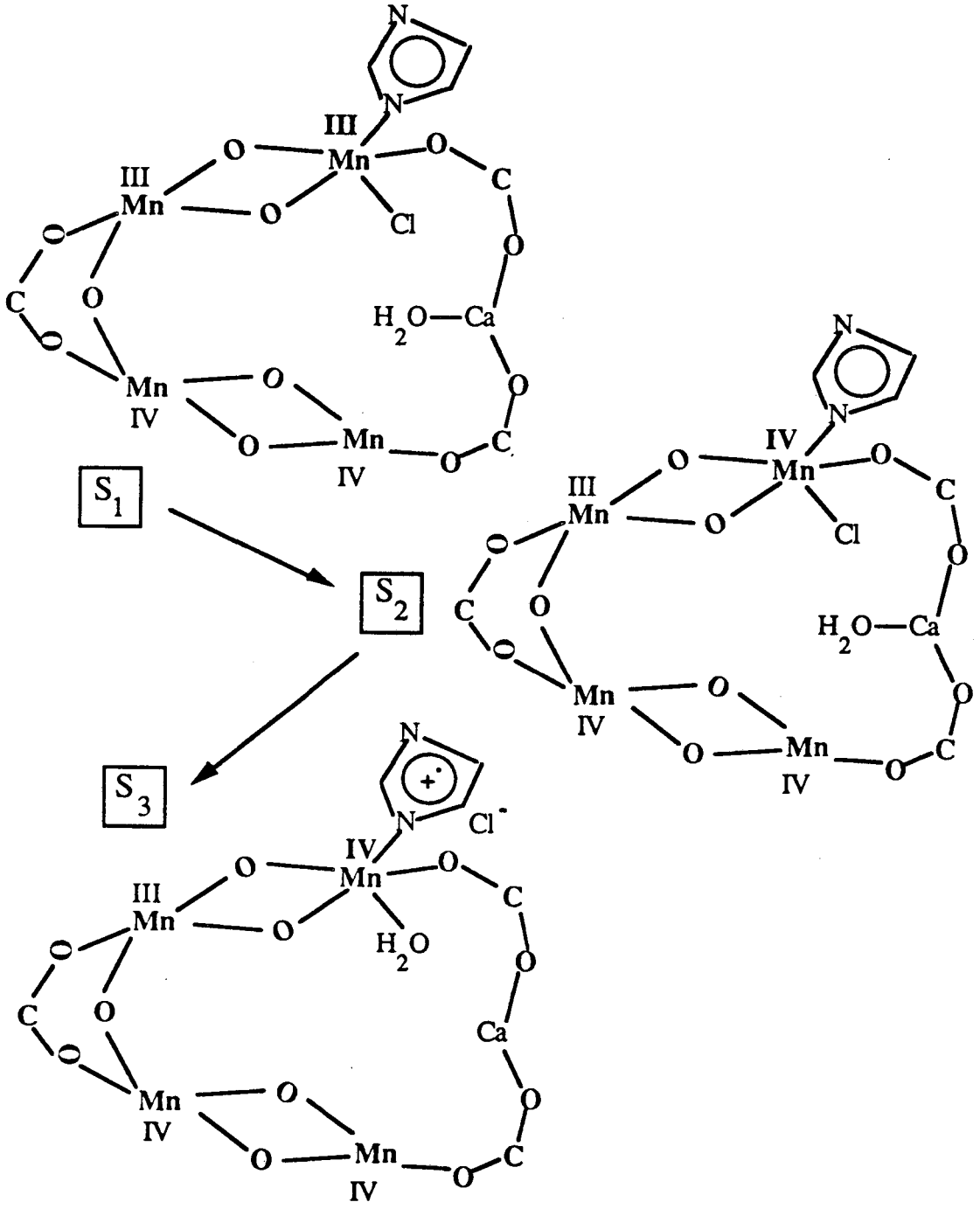

S_2 state, the Mn(III,III) dimer is oxidized to Mn(III,IV). The halide is shown as a ligand to the Mn(IV) species.

In this hypothetical model, the S_2 state g=2 multiline and g=4 EPR signals arise from different electron exchange coupling schemes between the Mn dimers. The multiline EPR signal is thought to arise from a ground state S=1/2 arising from antiferromagnetic coupling between a ground state S_a=1/2 from the Mn(III,IV) and ground state S_b=0 from the Mn(IV,IV) pairs. The g=4 EPR signal could arise from a ground state S=3/2 arising from *ferromagnetic* coupling between the ground state S_a=1/2 and a first excited state S_b=1. Strong antiferromagnetic exchange coupling is generally seen between di-μ-oxo bridged Mn atoms. The value for J depends slightly on the terminal ligands [Wieghardt, 1989, and references therein]. In contrast, the exchange coupling between mono-μ-oxo bridged Mn atoms is generally much weaker, and varies from weakly ferromagnetic to antiferromagnetic depending on the terminal ligands [Wieghardt, 1989]. An exception to this was recently found in an oxo-bridged Mn dimer with a Mn-O-Mn bond angle of nearly 180^0, in which the exchange coupling was found to be strongly antiferromagnetic [Kipke et al., 1990]. This indicates an additional dependence of the exchange coupling on the angle at the bridging oxo group. Thus, in the hypothetical model shown in Figure 4.13 the single oxo bridge allows flexibility in the strength and sign of the exchange coupling *between* the dimers. Relative values for the exchange coupling *within* each dimer may be changed by the substitution of a terminal ligand.

Inhibition with fluoride has the following effects which must be explained in the context of this proposed model. The complex shows only the g=4 EPR signal in the S_2 state. The g=4 EPR signal is narrower in the presence of fluoride. Inhibition with fluoride has an apparent effect on at least one Mn-Mn distance at around 2.7 Å.

One model for the origin of the g=4 EPR signal in control, untreated samples is that it arises from samples which have undergone oxidation of a Mn(III) to Mn(IV), but have not undergone the slight ligand rearrangement expected from the Mn(III) Jahn-Teller distorted ligand environment to the more symmetric Mn(IV) ligand environment [Brudvig, 1989]. This is invoked to explain the appearance of the multiline signal at the expense of the g=4 signal after "annealing" of samples which have been illuminated at low (140 K) temperature. If fluoride replaces chloride as an "equatorial" ligand *trans* to one of the Mn-O bonds, the shorter Mn-F bond could have the effect of stabilizing the complex in a tetragonally distorted arrangement. Illumination at any temperature would then give rise to the g=4 configuration of the

complex. The stronger ligand field of fluoride may decrease the ratio of E/D for the single ion zero-field splitting parameters. As discussed above, a smaller value for the ratio E/D could have the effect of narrowing the linewidth of the g=4 signal. The extremely short Mn-F bond distance may also have the effect of shortening the Mn-O bridging ligand distances, which would then affect the Mn-Mn distance in the complex as well as the value for the exchange coupling parameter.

High concentrations of fluoride promote a broad g=2 EPR signal in dark-adapted samples. The g=2 signal closely resembles that arising from the S_3 state of calcium-depleted samples. According to a current model of the S_3 state, in both untreated and calcium-depleted samples a putative histidine species is oxidized in lieu of Mn upon advance from S_2 to S_3 [Guiles et al., 1990a; Boussac et al., 1990]. The EPR signal from the oxidized radical species is only apparent in calcium depleted samples, however. Fluoride, by replacing ligands to the calcium, may "deprotect" the species giving rise to the broad g=2 signal. This may serve the function both of exposing the putative histidine to oxidation, and of rendering the oxidized species EPR visible. The "deprotected" species might be oxidized by the ambient potential, or by another electron carrier such as the tyrosine D. The species D is known to be capable of oxidizing S_0 to S_1 in the dark over a long (~30 min) period of time [Styring & Rutherford, 1987]. The putative radical species could be stabilized in its oxidized state by the prevalence of negatively charge F^- ions.

If halide actually binds to Mn in the oxygen evolving complex, the question arises as to what its role is in the catalytic cycle of oxygen evolution. One potential purpose for halide binding to the manganese is to protect a binding site for water in higher S-states. It is widely believed that the manganese in the oxygen evolving complex forms a site for water binding and oxidation. It is thought that water does not bind in the advance from S_1 to S_2 [Britt et al., 1990]. If this is the case, there must be a site occupied on the manganese in the S_1 and S_2 states which is either occupied with water or hydroxide in the S_1 and S_2 states, or which becomes replaced with a water molecule in the S_3 or S_4 state. One possibility is that chloride occupies this binding site in the S_1 and S_2 states, but is replaced by water or hydroxide upon advance to S_3. In the model shown in Figure 4.13, the water-chloride ligand exchange is facilitated by the attraction of chloride to the newly oxidized histidine in the S_3 state. In the fluoride-inhibited centers, the relative strength of the Mn(IV)-F bond may inhibit this ligand exchange. This is one possible role for halide in the oxygen evolving complex. Alternatively, the role of chloride may be to tune the redox potential of the complex, or

to act as a structural link between Mn and a positively charged species such as the Ca^{+2}. The smaller size and greater electronegativity of fluoride could be inhibitory in these roles as well.

Summary

1. The loss of multiline and gain of g=4 EPR signals are correlated with loss of oxygen evolution activity in PSII preparations from spinach which have been inhibited with fluoride.

2. The g=4 EPR signal which arises in the presence of fluoride is narrower than in the presence of chloride. The spin relaxation characteristics of the two signals are very similar, indicating that they do not arise from different sources.

3. The Mn K-edge EXAFS spectra of fluoride-inhibited samples show an increase in the apparent disorder of the peak due to Mn at 2.7 Å. The increase in disorder is great enough in the S_2 state of fluoride-inhibited samples to be modelled with two separate Mn-Mn distances at ~2.7 Å.

4. The Mn K-edge inflection point energy in fluoride-inhibited samples shows no change relative to control samples in both the S_1 and S_2 states.

5. Fluoride at high concentrations induces a broad g=2 EPR signal in dark-adapted preparations. The broad g=2 signal is very similar to that reported in calcium-depleted preparations.

6. A model for halide binding to the oxygen evolving complex is proposed.

Chapter 5

X-ray Absorption and Electron Paramagnetic Resonance Experiments on Bromide-Substituted PSII Preparations from *Synechococcus* sp.

In the Mn X-ray absorption experiments presented in this chapter the larger size of bromide over chloride is used as a probe for halide in the oxygen evolving complex. Bromide has been shown to substitute effectively for chloride in activating oxygen evolution in photosystem II [Warburg & Lüttgens, 1944; Kelley & Izawa, 1978] and in reversing many of the specific effects that chloride depletion has on the oxygen evolving complex. For example, bromide replaces chloride in regenerating the multiline EPR signal from the S_2 state [Yachandra et al., 1986; Ono et al., 1987] and reversing the increased temperature required for the recombination of [$Q_b^-S_2$] in chloride-depleted preparations [Ono et al., 1987].

The increased nuclear magnetic moment and nuclear quadrupole moment of bromide prompted Yachandra et al. (1986) to search for differences in the multiline EPR signal from chloride- and bromide-substituted PSII preparations. Such differences would be attributable to superhyperfine coupling from a halide nucleus. While no change was detected in the EPR spectra from bromide-substituted preparations, it is acknowledged that such a hyperfine coupling may be quite small compared with the linewidths of the EPR signal. Similarly no change was detected in the multiline signal from bromide-substituted samples when measured at S-band (4 GHz), despite the decrease in linewidth at the lower frequency [Haddy et al., 1989].

X-ray absorption experiments have provided a great deal of information about the organization of the manganese atoms in the oxygen evolving complex. Information about the ligands of all four manganese are averaged into the photosystem II manganese EXAFS spectrum, however, making the technique somewhat less effective as a probe of the identity of a single manganese ligand atom. In the EXAFS experiment, elements around the central absorbing atom are distinguished on the basis of their effect on the amplitude and phase of the back-scattered photoelectron. The amplitude of the back-scattered photoelectron wave increases with the atomic number Z of the scattering atom. This makes it difficult to distinguish between elements of similar Z, such as Mn and Fe, or O and N. For these reasons, EXAFS investigators

Figure 5.1. Photoelectron scattering amplitude functions for relevant atoms. The amplitude functions are plotted as a function of k for Br, Cl, N, and Mn. Amplitude functions were taken from material described in McKale et al., 1988. Note that the functions will be weighted by k^3 for most of the data analysis.

Figure 5.1

Photoelectron scattering amplitude functions for several elements

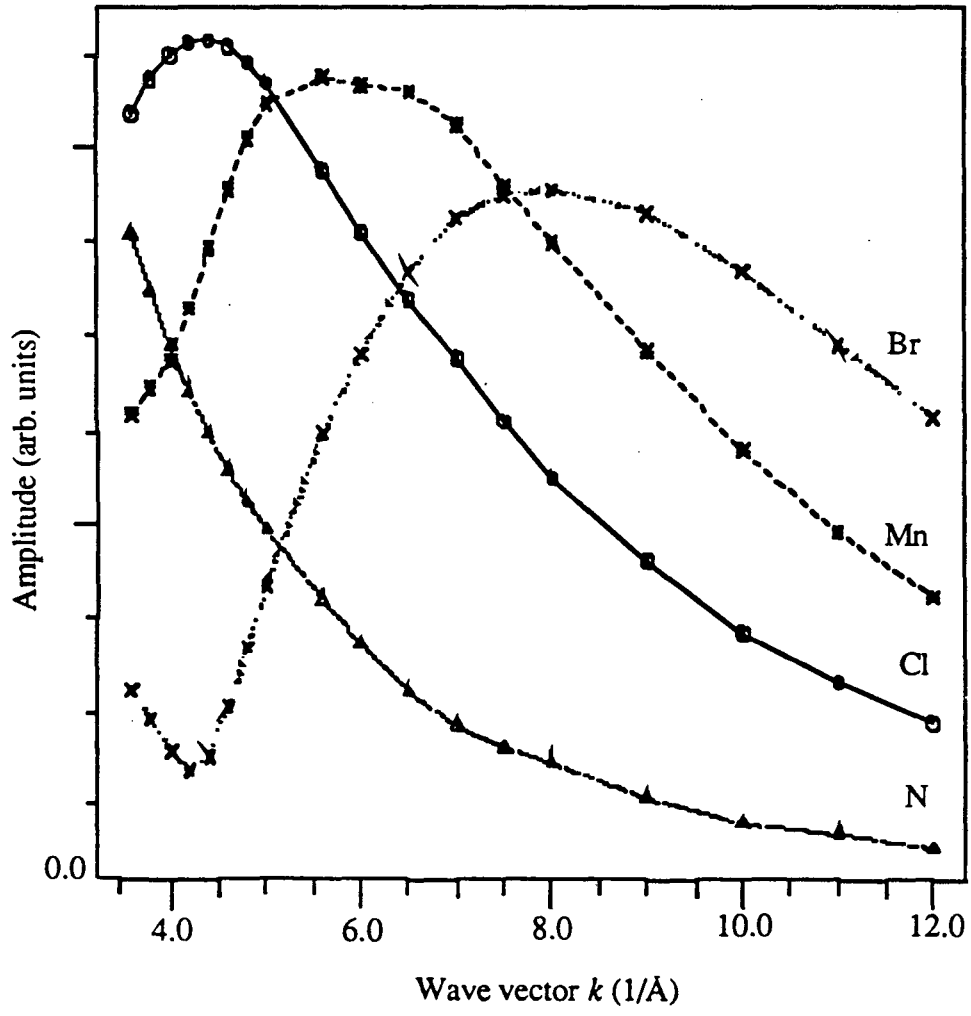

have concluded that a single chloride ligand per four manganese cannot be ruled out on the basis of curve fitting the manganese K-edge EXAFS data from the oxygen evolving complex [McDermott et al., 1989; Penner-Hahn et al., 1990].

The difference in the back-scattering amplitude functions for Cl (Z=17) and Br (Z=35), however, is substantial (see Figure 5.1). The comparison between EXAFS of chloride- and bromide-substituted PSII preparations may therefore give an indication of the type of interaction that halide has with the manganese of the oxygen evolving complex.

To achieve full exchange of bromide for chloride in an oxygen evolving preparation, the cyanobacterium *Synechococcus* was grown in bromide-replaced medium, and PSII particles were isolated in a medium containing only bromide. This method of halide exchange was chosen in order to promote the most extensive replacement of bromide for chloride. Simply washing preparations with bromide instead of chloride does not allow a measurement of the amount of chloride that has been displaced. This is especially a problem in light of evidence that halide exchange may occur quite slowly [Sachar-Hill et al., 1989; Lindberg et al., 1990]. An alternative method of halide replacement would be chloride-depletion of PSII preparations followed by reconstitution with bromide. The maximum depletion of oxygen evolution activity requires exposure of the preparation to high pH in the absence of chloride, which results in a small amount (10-30%) of irreversible loss of activity [Yachandra et al., 1986; Homann, 1985; Ono et al., 1987], accompanied by the release of Mn^{+2} [Ono et al., 1986], and possible loss of the extrinsic 23 kD polypeptide [Homann, 1988a]. These effects would lead to heterogeneity of the sample, which is undesirable for a comparative EXAFS experiment. By growing the cyanobacteria and isolating PSII particles in media which contains only bromide we hope to avoid such effects.

The polypeptide composition of the OEC from spinach has been shown to affect the activity of the enzyme with respect to both Ca^{+2} and Cl^- concentrations [Miyao & Murata, 1985]. Incubation in high ionic strength (1-2 M NaCl) dissociates the 17 and 23 kD polypeptides from the spinach oxygen evolving complex. Homann (1988) has reported that in the absence of these extrinsic polypeptides, the apparent K_m at pH 6 for chloride activation of oxygen evolution is increased from ~100 μM in untreated preparations to ~1 mM in the polypeptide-depleted preparations. A third polypeptide, the 33k D "manganese stabilizing" protein, can be removed from the spinach oxygen evolving complex with incubation in 1 M $CaCl_2$. In the absence of all

three of these "extrinsic" polypeptides, the OEC can attain only 50% of its original oxygen evolution activity, and that only in the presence of 100 mM Cl^- [Miyao & Murata, 1984].

The polypeptide composition in photosystem II preparations from cyanobacteria differs from that of higher plants. No polypeptides have been found in cyanobacteria which cross-react with antibodies raised against the 23 and 17 kD polypeptides in higher plants [Stewart et al., 1985; Phillbrick & Zilinskas, 1988]. The gene for the 33kD extrinsic polypeptide has been shown to have a high level of sequence homology with that of spinach, but the amount of post-translational processing that the protein undergoes in cyanobacteria is in question [Kuwabara et al., 1987; Phillbrick & Zilinskas, 1988]. The high salt treatments which remove the 33 kD polypeptide from spinach thylakoid membranes was found to be much less effective in removing the 33 kD polypeptide from cyanobacterial preparations [Stewart et al., 1985]. Despite these differences, chloride activation of oxygen evolution has been reported in PSII preparations from *Phormidium laminosum* [Stewart et al., 1985] and in membrane fragments from *Nostoc* [McSwain et al., 1976]. In these experiments, we report a K_m for chloride activation in PSII preparations from *Synechococcus* sp.

Materials and Methods

The growth of *Synechococcus* sp. and isolation of PSII particles in both chloride- and bromide-containing media was described in Chapter 2. "Bromide-grown" *Synechococcus* sp. was grown on media in which all chloride salts were replaced with bromide salts. The PSII preparations used in these experiments were grown through at least five generations in bromide-containing media. PSII preparations were isolated from *Synechococcus* sp. with bromide salts replacing chloride in every isolation buffer. Samples were prepared for EPR and X-ray absorption spectroscopy (XAS) as described in Chapter 2. Most of the EPR spectra reported here were taken on samples in the XAS holders.

Spinach PSII particles used for oxygen evolution measurements were prepared as follows. After pelleting out of a buffer containing 50 mM MES, 500 mM sucrose, 0.2 mM PMSF, and 5 mM $CaCl_2$ (or $CaBr_2$) , the preparation was resuspended to 0.1 - 0.2 mg Chl/ml in the same buffer without $CaCl_2$ (or $CaBr_2$). Oxygen evolution measurements were performed at 25 °C. The following components were mixed in the measuring cuvette: 1.5 ml of measuring buffer [500 mM sucrose, 50 mM MES

(pH 5.5, 6.0, 6.5) or HEPES (pH 7.5) or Tricene (pH 8.0)], NaCl (or NaBr) from a stock solution of 1M NaCl in H_2O, and 5 μl of a stock solution of 0.2 M DCBQ in DMSO (to a final concentration of 670 mM DCBQ). Aliquots of the PSII preparation were then added to a final chlorophyll concentration of 10 μg/ml for preparations from *Synechococcus*. This corresponded to approximately 0.2 μM concentration of PSII for each assay. The assay mixture was stirred for 15 sec in darkness before the light was turned on. Oxygen evolution rates were measured as the slope of the straight line between 5 and 20 sec after the light was turned on. The conditions of the assay were checked at various points of pH and halide concentration to insure that changes in the oxygen evolution rate were not due to lack of light intensity or amount of electron acceptor DCBQ.

X-ray absorption spectroscopy was performed on beamline X-19A at the NSLS using a Ge solid state detector and Si[111] crystal monochromator, as described in Chapter 2. The sample temperature was maintained at 10 K with a liquid helium cryostat.

Results

Chloride activation of oxygen evolution in PSII preparations from Synechococcus sp.

In figure 5.2, the rates of oxygen evolution as a function of added chloride are plotted for PSII preparations from *Synechococcus* sp. The data points are the average of 3-7 measurements each. More than one PSII preparation from *Synechococcus* was used. The maximum activity varied from 2500-4000 μM O_2/(mg Chl-hr) between preparations. It was found, however, that the % activity as a function of chloride was reproducible among different preparations. For this reason, the % maximum activity is plotted in Figure 5.2, where the maximum activity for each preparation is that achieved in 10 mM Cl^- at pH 6.0. The traces in Figure 5.2 did not differ with the addition of either NaCl or NaBr, and preparations from chloride- or bromide-grown *Synechococcus* gave similar results and so were used interchangeably.

The influence of chloride on the steady-state kinetics of oxygen evolution in photosystem II has been treated using the formalism for an enzyme-activator complex [Kelley & Izawa, 1978; Homann, 1984]:

Figure 5.2. Oxygen evolution of PSII particles from *Synechococcus* sp. as a function of pH and [Cl^-]. The percent of the "maximum" activity (the activity at pH 6.5 in 10 mM NaCl) is plotted as a function of added NaCl at different pH's. Data points are averages of 3-7 measurements each, with standard devisions of 5-10%. The representative errors are shown as error bars in Figure 5.3.

Figure 5.2
Chloride activation of oxygen evolution
as a function of pH in PSII particles from *Synechococcus* sp.

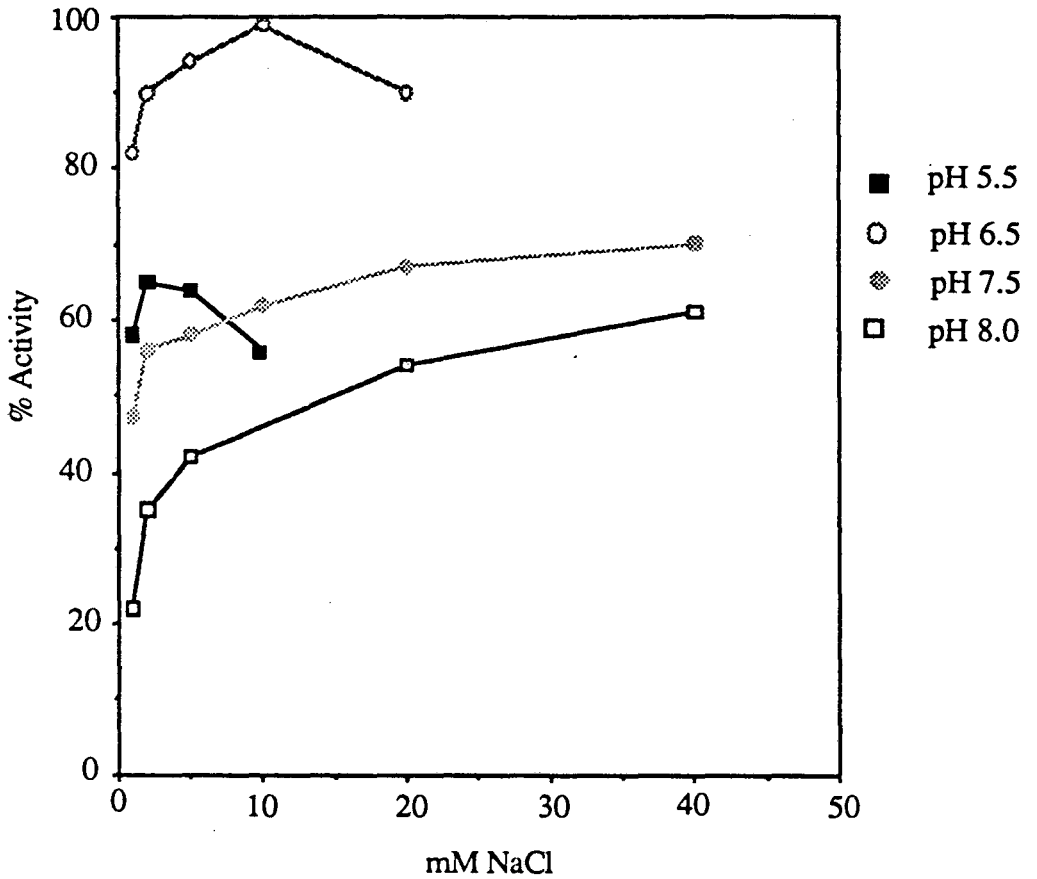

$$E + Cl^- \underset{k_2}{\overset{k_1}{\Leftrightarrow}} ECl \xrightarrow{k_3} ECl + 4H^+ + O_2$$

$$\Uparrow$$

$$2H_2O$$

$$K_m = (k_2+k_3)/k_1$$

The Michaelis-Menton constant K_m describes the dissociation of the activator-enzyme complex. A Lineweaver-Burke plot of 1/rate vs. $1/[Cl^-]$ then gives a line with slope of K_m/V_m, a y-intercept of $1/V_m$ and an x-intercept of $-1/K_m$. This treatment assumes (a) that the substrate concentration (in this case, H_2O) is saturating; and (b) that without the activator (in this case, chloride), the enzyme cannot complete its reaction [Dixon & Webb, 1979]. For the light-induced water oxidation reaction of the oxygen evolving complex in spinach PSII particles, the maximal velocity V_m depends on light intensity, but the K_m for chloride activation is found to be independent of light intensity [Homann, 1985]. The apparent K_m in intact PSII preparations from spinach increases with pH from approximately 0.1 mM at pH 6.0 to 1.8 mM at pH 8.0 [Homann, 1985]. The pH dependence has been interpreted to mean either that chloride binding requires the cooperative protonation of an amino acid group, or that hydroxide ion and chloride compete for binding at the same site. These mechanisms can be treated as either a sequential activation or competetive inhibition of enzyme activity. Both mechanisms predict a linear relationship between the apparent K_m for chloride binding and $[OH^-]$, with an x-intercept of $-K_m$. This extrapolated value for K_m has been found to be 70 μM for spinach PSII preparations [Homann, 1985].

It is clear from Figure 5.2 that for PSII preparations from *Synechococcus*, as the pH is increased from 6.5 to 8.0, the chloride activation of oxygen evolution changes. At pH 8 the maximum oxygen evolution activity is reached with the addition of 40 mM NaCl, whereas at pH 6.5 the maximum activity is attained at 10 mM NaCl. The double reciprocal plots of the data from *Synechococcus* for each pH are shown in Figure 5.3a. Data corresponding to the inhibitory effects of high chloride concentrations are not included in Figure 5.3a [Dixon & Webb, 1979]. From the slopes and intercepts of least-square fits to these data the apparent K_m for chloride activation at each pH can be calculated. These values are plotted against $[OH^-]$ in Figure 5.3b. From the x-intercept of a least-squares fit to these data, a K_m of .08 ± 0.10 μM is obtained for PSII particles from *Synechococcus* sp. This value can be considered the K_m for chloride binding either in the absence of competing hydroxide

Figure 5.3. Determination of the K_m for chloride binding in *Synechococcus* sp. In (a), the points from Figure 5.2 are replotted as the double reciprocal of activity vs. $[Cl^-]$ for each pH. Note that only points due to the activating effects of chloride, and not points due to the inhibitory effects of excess chloride, are used for the double reciprocal plots. A least-squares fit to the points is shown for each pH. The apparent K_m for each pH (-slope/intercept) is replotted in (b) as a function of $[OH^-]$. The least squares fit to these points is shown. The value for K_m determined from this plot is 0.08 mM, and the standard deviation for this value is 0.10 mM [as in Harris, 1982].

Figure 5.3

a. Double reciprocal plot of activity vs. [NaCl] in PSII particles from Synechococcus

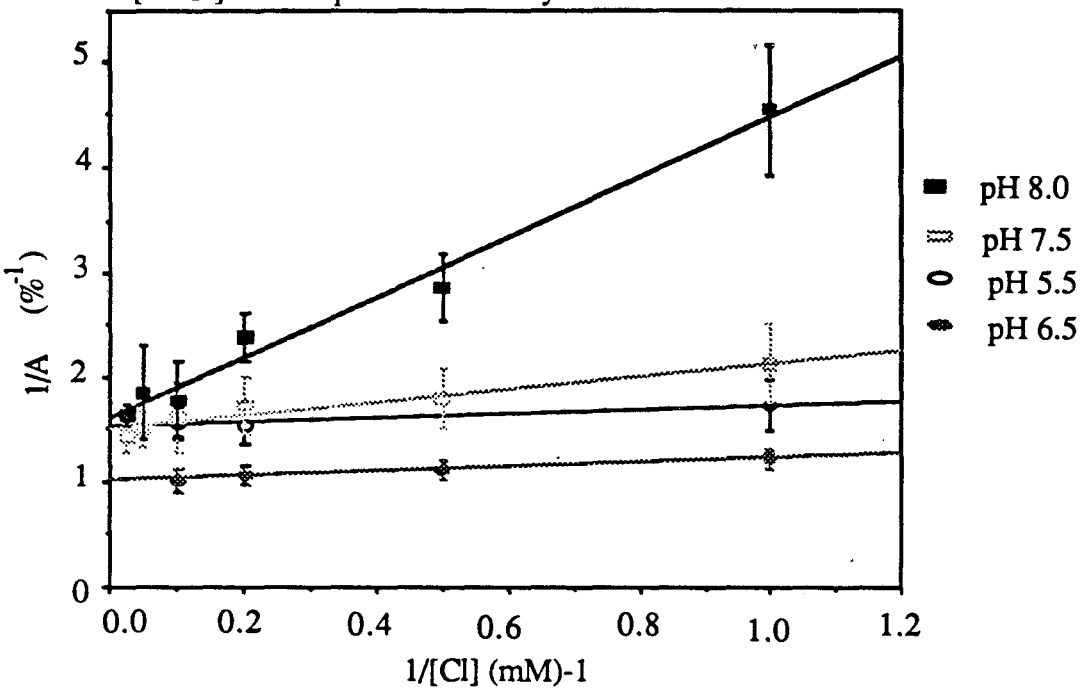

b. Apparent K_m vs. [OH-]

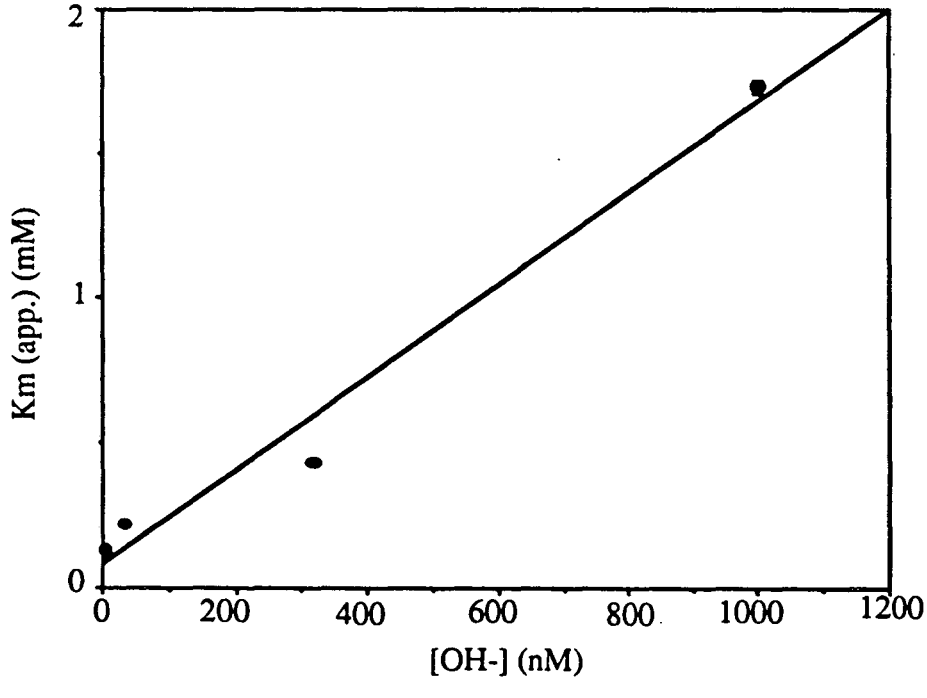

anion, or when the sites of protonation on the group necessary for chloride binding are filled. In spinach preparations containing the extrinsic polypeptides, the analogous value for K_m was determined to be 70 μM, whereas in preparations which were *lacking* the 17 and 23 kD polypeptides this K_m was determined to be ~1 mM at pH 6.0 [Homann, 1988a]. Thus, although the OEC in *Synechococcus* lacks the 17 and 23 kD polypeptides, its chloride binding behavior resembles that of intact spinach PSII preparations.

Calcium and other divalent cations are known to affect the rates of oxygen evolution in spinach and cyanobacteria [Homann, 1984, 1985; Stewart et al., 1985; McSwain et al., 1976]. Since the common salts of Ca^{+2} such as $Ca(OH)_2$, $CaCl_2$, and $Ca(NO_3)_2$ contain counterions which affect halide binding in the oxygen evolving complex, Ca^{+2} was not added to the assay medium. The addition of 5 mM Ca^{+2} raised the maximum oxygen evolution rates (at pH 6.5 and 10 mM Cl^-) by approximately 5%. The functional Ca^{+2} is known to be tightly bound in PSII centers from cyanobacteria [Ohno et al., 1986]. Because the preparations used for these oxygen evolution assays were incubated in 5 mM Ca^{+2} previous to resuspension without halide, it is likely that most of the functional calcium remained bound to the OEC.

EPR studies of bromide-substituted PSII particles from Synechococcus.
In Figure 5.4a, the EPR spectrum from a dark-adapted sample of PSII particles prepared from *Synechococcus* grown on bromide-containing media is shown. There are several signals present in dark-adapted preparations. The large EPR signal at g=6 is most likely due to Fe^{+3} in an axial environment, and is similar to signals previously assigned to oxidized, dissociated cytochrome b_{559} in photosystem II preparations from spinach [i.e. Rutherford, 1985]. The signal at g~4 has been ascribed to nonspecifically bound Fe^{+3} in a rhombic environment. Signals at g~3 and g~2.1 are due to oxidized, intact cytochrome b_{559}. The very sharp, off-scale signal at g=2 arises from the oxidized radical D^+, as well as other radical species such as damaged chlorophyll.

In addition to these EPR signals, which have been seen in other PSII preparations from spinach, a new multiline signal around g=2 is seen in these dark-adapted preparations. This signal consists of eight clearly resolved lines at magnetic field values below g=2, separated by 45-70 G, as well as structure which is less resolved above g=2. The average line separation in the features below g=2 is 62 G.

Figure 5.4. EPR spectra of PSII preparations from *Synechococcus* grown and isolated in bromide-containing media. (a) Spectrum of dark-adapted preparation. The preparation has been maintained in darkness since the PSII was extracted from the thylakoid membrane. (b) Spectrum after illumination for 10 minutes at 200 K. The spectrum from the dark-adapted sample is subtracted. The vertical scale in (b) is twice that of (a). Spectrometer conditions: 9.2 GHz, 30 mW microwave power, 32 G modulation amplitude, 8 K, 100 kHz modulation frequency. The hyperfine lines indicated by vertical bars are those studied in detail in Figure 5.5.

Figure 5.4

EPR spectra of PSII preparations from *Synechococcus* grown and isolated in bromide.

a. Dark-adapted preparations

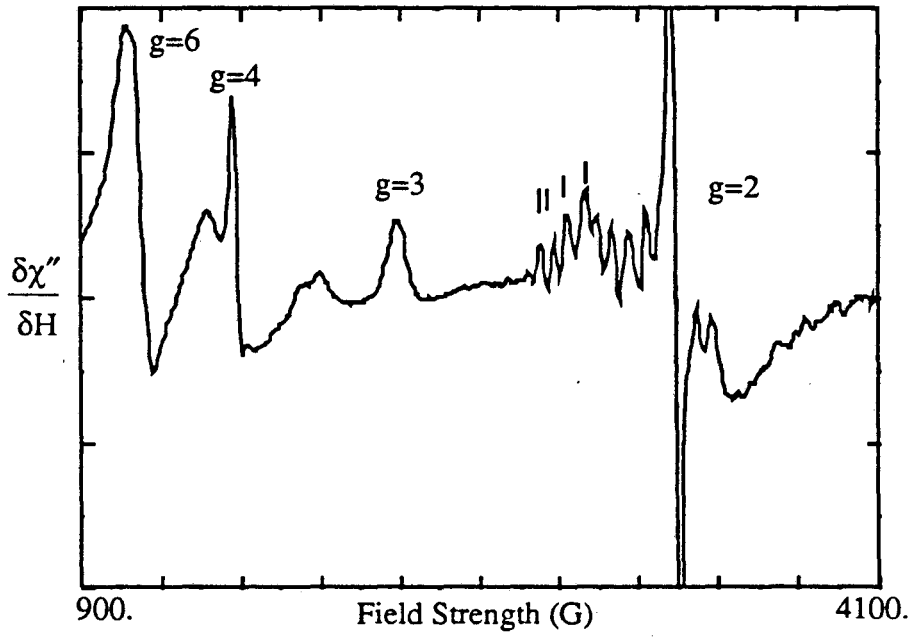

b. Illuminated minus dark

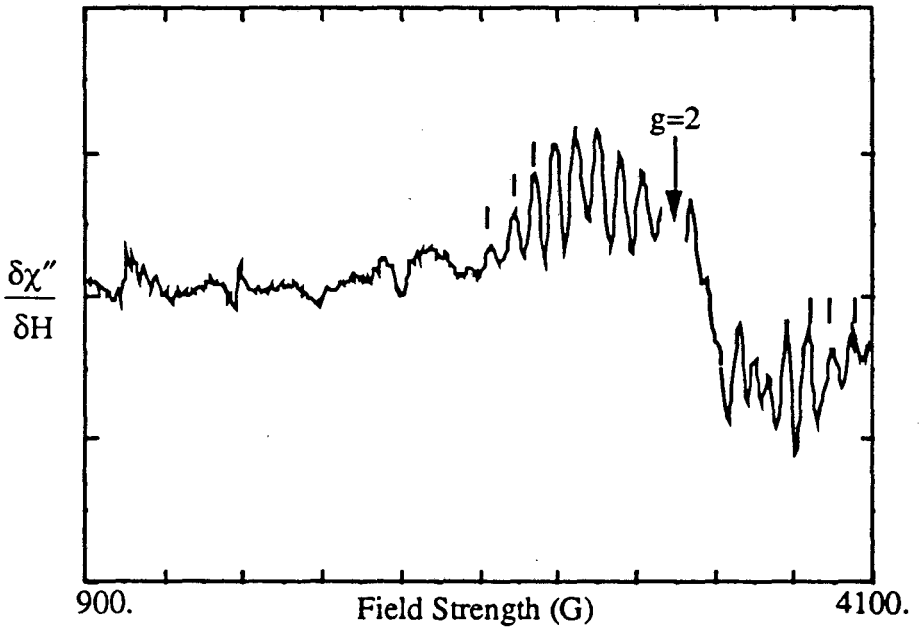

This signal does not disappear upon advance to S_2, as seen in Figure 5.4b in which the EPR spectrum of illuminated samples minus the dark-adapted background spectrum is shown. In this subtracted spectrum, only the familiar S_2 -state EPR multiline signal is evident. The unsubtracted spectrum from illuminated samples contains the superposition of both the dark-adapted multiline signal and the light-induced S_2 multiline signal (data not shown).

This new dark signal is also evident, but in lower amplitude, in PSII preparations which have been grown in chloride-containing media. In Figure 5.5 the spectrum from dark-adapted PSII preparations from bromide-grown *Synechococcus* is compared with the spectrum of preparations from dark-adapted chloride-grown *Synechococcus*. Similar features are seen in both EPR signals.

In a series of preparations exhibiting very high oxygen evolution activities, 3000-4000 μM O_2/(mg Chl-hr), the amplitudes of both the dark-adapted multiline and the light-induced (S_2 -state) multiline signals varied by ~30%. In general, the yield of the S_2-state multiline signal was decreased when the level of the signal from dark-adapted preparations was increased. The total number of lines in the signal from dark-adapted preparations is not evident, and so it is not possible to quantitate the number of spins represented by the new signal. An upper limit can be calculated by assuming that the signal is symmetric about g=2. Then the integrated intensity of the signal at field values below g=2 can be compared with the integrated intensity of the light-induced multiline EPR signal for the same field range. The two signals show similar power saturation characteristics at 8 K. This integration was used to choose samples for X-ray absorption spectroscopy in which the integrated intensity of the signal in dark-adapted samples was less than 20% of the integrated intensity of the light-induced multiline EPR signal.

Several treatments were performed to help identify the origin of the new multiline EPR signal in these dark-adapted preparations. The treatments, and their effects on the signal, are listed in Table 5.1. Protocols affecting the acceptor side of PSII do not affect the yield of the signal, whereas treatments which are known to remove the functional manganese from the oxidizing side of PSII also result in the disappearance of the new signal. The results of these experiments indicate that the signal is not due to nonspecifically bound Mn^{+2} or to Mn^{+2} replacing Fe^{+2} on the acceptor side of the oxygen evolving complex (as in Fee et al., 1986), but is due to some form of the manganese involved in the oxygen evolving complex.

Figure 5.5. Spectra of dark-adapted PSII preparations from *Synechococcus* grown and isolated from bromide- or chloride-containing media. The spectrometer conditions are as in Figure 5.4. The concentrations of the samples are approximately equal, as are the vertical scales in both spectra.

Figure 5.5

EPR signals from dark-adapted PSII preparations from *Synechococcus* sp. grown on bromide- or chloride-replaced media

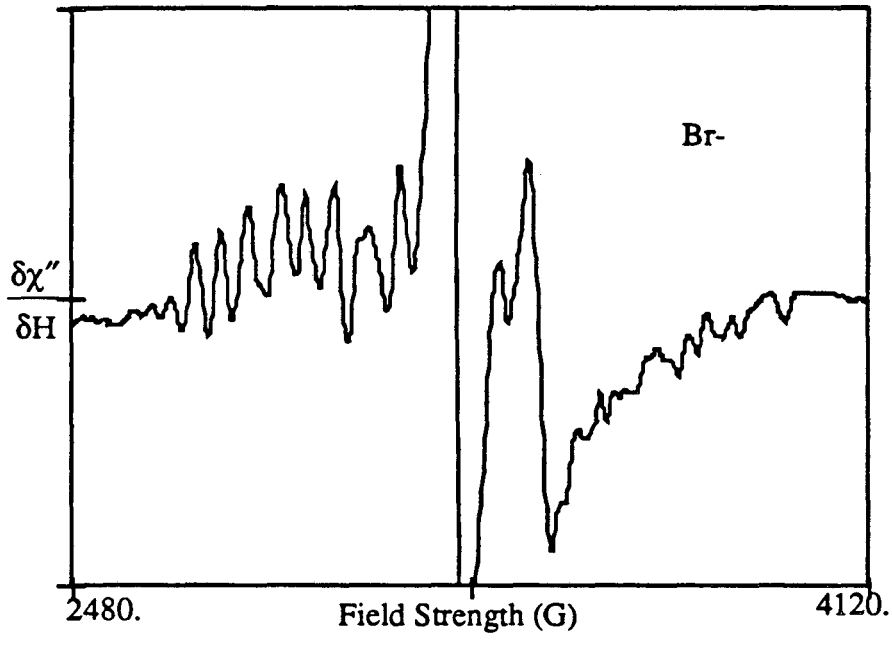

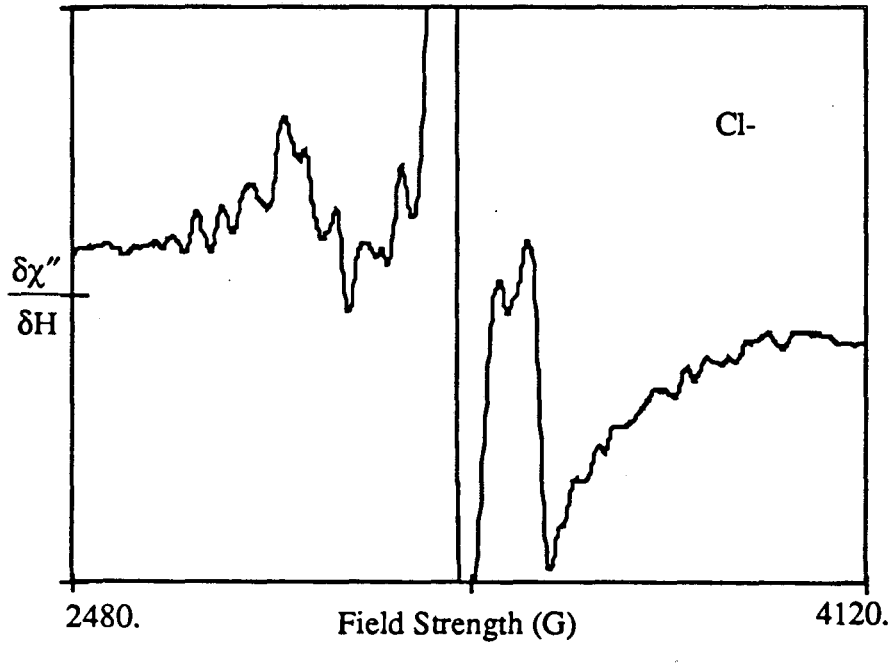

Table 5.1

Effects of various treatments on the EPR signal from dark-adapted PSII preparations in *Synechococcus* sp.

Treatment	Effect	Amplitude of dark signal
Control		100%
1 M Tris	Removes functional manganese from oxygen evolving complex	0
40 mM NH_2OH	"	0
1 mM EDTA	Removes nonspecifically bound Mn^{+2} from preparation	100 %
1 mM Tiron	Removes nonspecifically bound Fe from preparation	90%
50 μM PPBQ	Binds to Q_b site, accepts electrons from Q_a^- or Q_b^-. $PPBQ^-$ oxidizes Fe^{+2} to Fe^{+3} in spinach preparations, generating EPR signals between g=5.5 and g=8. In *Synechococcus*, PPBQ added in the dark split the g=6 EPR signal into three features (data not shown), suggesting that this g=6 signal is due to Fe^{+3} from Fe-quinone centers].	80%
50 μM DCBQ	Binds to Q_b site, oxidizes any Q_a^- or Q_b^- present in the dark	90%

The structure of the individual lines on both the light-induced, S_2-state multiline signal and the signal from dark-adapted preparations are compared in Figure 5.6 between samples from chloride- and bromide-grown *Synechococcus*. Under conditions of higher resolution (lower modulation amplitude in the EPR experiment) the manganese hyperfine lines on the multiline signal from the S_2 state are seen to be asymmetric and to have structure due to unresolved transitions. In Figures 5.6a and 5.6b it is shown that this structure is almost identical in the S_2-state multiline EPR signal from spinach and from *Synechococcus*. Similarly, it is seen from Figure 5.6c that the individual lines in the new signal from dark-adapted samples of *Synechococcus* are also asymmetric and in some cases show unresolved structure. No change in the unresolved structure of either of the multiline EPR signals is seen upon substitution of bromide for chloride. In addition, within an estimated accuracy of 5 G no consistent change in linewidth of the individual lines (determined as the full width at half maximum height) is detected in the different samples.

The structure on the Mn hyperfine lines of the S_2-state multiline EPR signal has been ascribed to additional unresolved transitions due to manganese hyperfine coupling [Haddy et al., 1989]. The lines may be further broadened by effects due to ligand hyperfine interactions. Neglecting nuclear quadrupole interactions, the linewidth component due to unresolved ligand hyperfine interactions is a function of the nuclear spin and nuclear moment of the ligand atom. Substitution of bromide for chloride would be expected to increase this linewidth component by a factor of 2.8 (equation 4-1). The accuracy in linewidth determination in the above experiment is estimated to be 5 G, which means that the change in linewidth due to bromide must be greater than 5 G to be detected in this experiment. This would require a hyperfine coupling interaction of > 2 G for a chloride ligand, which is approximately twice the value of the isotropic hyperfine coupling determined for ^{14}N ligands to Mn in the model compound $Mn(III,IV)(\mu\text{-oxo})_2(bipy)_2$ [Britt, 1988]. Thus, the superhyperfine coupling due to a single halide ligand may remain undetected by this type of high resolution EPR experiment. A bridging ligand would be expected to have a much larger hyperfine interaction than a terminal ligand, however, and so the similarity of the linewidths from the multiline signals in chloride- and bromide-exchanged samples argues against a bridging halide ligand in the oxygen evolving complex.

X-ray absorption experiments on bromide-substituted PSII particles from Synechococcus. The Mn K-edge X-ray absorption spectra of PSII preparations from

Figure 5.6. Structure of the hyperfine lines from the multiline EPR signals. (a) The light-induced multiline signal formed by illumination for 10 minutes at 200 K. The structure of three highest-field lines is compared for PSII samples from spinach, *Synechococcus* grown on chloride, and *Synechococcus* grown on bromide. (b) Structure on the three lowest-field lines of the light-induced multiline signal. The lowest two of these lines should have no contribution from the signal present in dark-adapted preparations. (c) Signal from dark-adapted preparations. Spectrometer conditions: 9.2 GHz, 20 mW microwave power, 4 G modulation amplitude, .128 sec time constant, 8 K, 100 kHz modulation frequency. The average of about 20 2- minute scans for each sample are shown.

Figure 5.6

a. High-field lines of S_2 state multiline signal

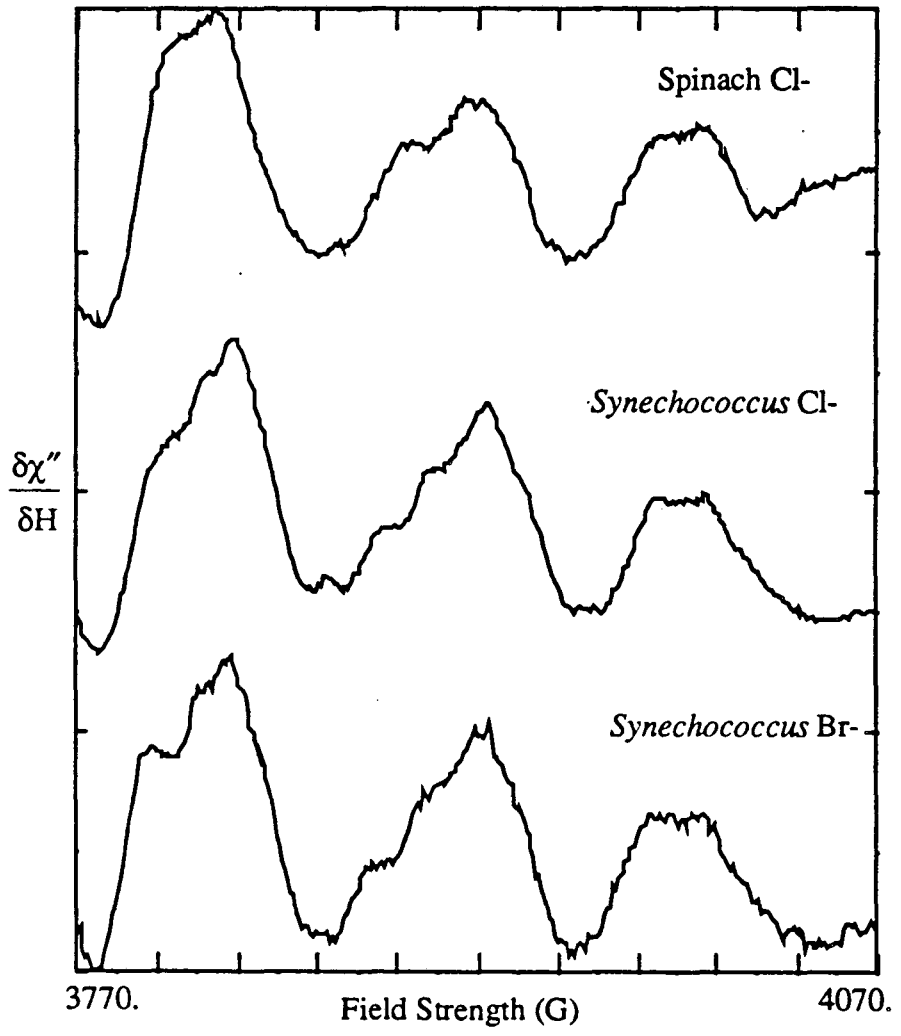

Figure 5.6 continued

b. Low-field lines of light-induced multiline signal

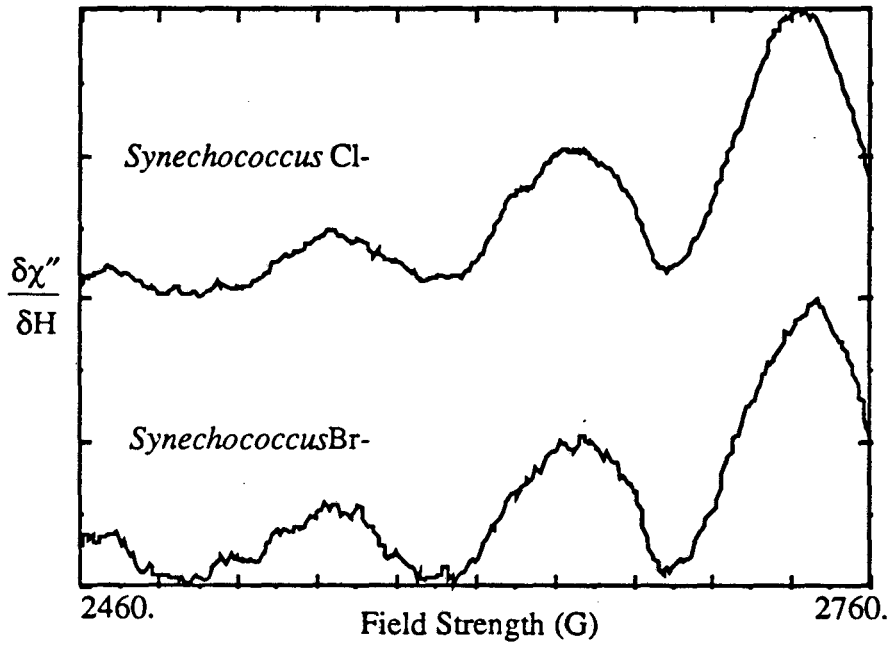

c. Low-field lines of signal from dark-adapted samples

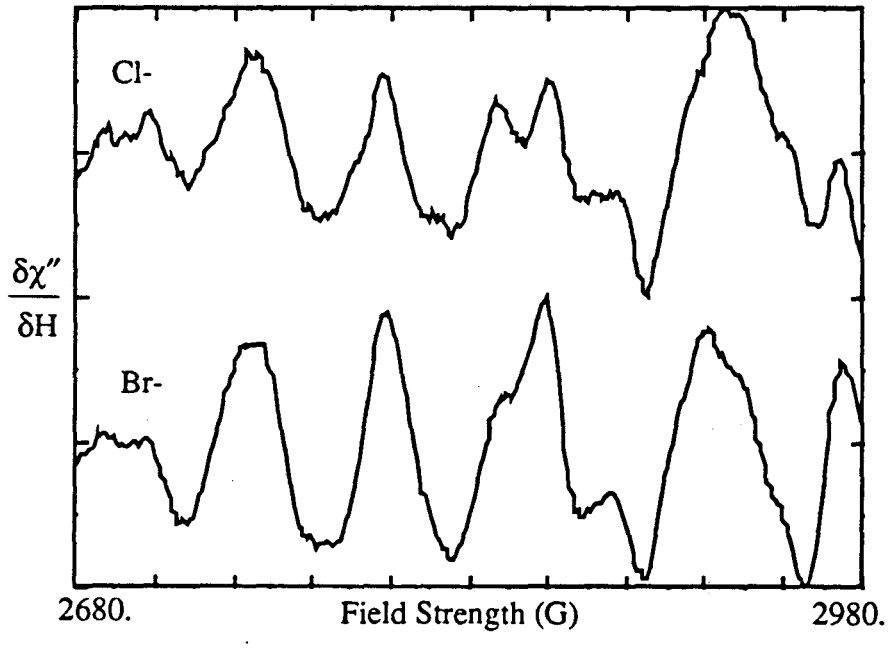

bromide- and chloride-grown *Synechococcus* S_1 samples are displayed in Figure 5.7. In Figure 5.7b the Fourier transforms of k^3-weighted k-space data are shown for the preparations from bromide- and chloride-grown cyanobacteria in the S_1 state. The positions and amplitudes of peaks I-III of the two samples are quite similar. Slightly less resolution is seen between peaks I and II in the bromide-substituted preparations. The back-transformed k-space data from isolated peaks I-III ($0 \leq R' \leq 4$ Å) are shown for the two preparations in Figure 5.7a (upper trace). In the lower trace of Figure 5.7a, the back-transformed k-space data are compared for an S_1 sample from chloride-grown *Synechococcus* and from spinach. The difference between the spinach and *Synechococcus* data is representative of the overall disparity among data from separate experiments on the same type of preparation. The difference between the back-transformed data from the bromide- and chloride-grown *Synechococcus* preparations appears within this level of variance between control preparations.

Several simulations were devised to estimate the changes in the Mn EXAFS spectrum expected upon the substitution of one or two bromide atoms for chloride atoms. In Figure 5.8, the estimated effect of the addition of a single chloride atom to the Mn EXAFS is shown. The calculated scattering envelope from a single chloride atom at a distance of 2.3 Å was added to the isolated k-space data from a *Synechococcus* S_1 preparation. It can be seen that the effect on the k-space data of a single chloride atom appears to be quite small. The effect on the Fourier transform of this small change in the k-space data is to increase the amplitude of a peak which is already present in the Fourier transform of control data, at $R'=1.8$ Å. A similar simulation was discussed by Penner-Hahn et al. (1990), with a demonstration of the effect of adding a single chloride scatterer to the raw k-space data. Fourier filtering, however, is an effective method of removing high frequency noise from this data. Simulations describing the effects of halide substitution on Fourier filtered data seem to be a more useful approach.

In Figure 5.9, the effect of bromide substitution on the isolated k-space data is described for two models of halide ligation to the manganese. In Figure 5.9a, the effect of a single ligand substitution is shown. Average Mn-Cl bond distances in Mn(III) and Mn(IV) compounds are 2.2-2.4 Å [Bashkin et al., 1987; Chang et al., 1988; Auger et al., 1990]. The Mn-Br bond lengths of Mn(II) complexes are found to be ~0.15 Å longer than Mn-Cl distances [Chang et al., 1988; Reedjik et al., 1971 and Gorter et al., 1974] and so Mn-Br bond distances of 2.4-2.6 Å are predicted for higher valent manganese compounds. To simulate the effect of the substitution of a single

Figure 5.7. Mn K-edge X-ray spectroscopy of PSII preparations from *Synechococcus* grown on chloride or bromide. In (a), the *k*-space data from isolates of Fourier transform peaks I-III (shown in (b)) is overplotted for *Synechococcus* grown in chloride media (solid line) and bromide media (dotted line). In the lower trace, the same spectrum from chloride-grown *Synechococcus* is plotted with isolated data from a spinach S_1 preparation. This kind of variation in data is typical for samples in this experiment. The Fourier transforms of data taken on PSII preparations from chloride- (solid line) and bromide- (dotted line) grown cyanobacteria are shown in (b). All data are weighted by k^3.

Figure 5.7
k-space isolates and Fourier transforms of
Mn EXAFS from chloride and bromide grown
Synechococcus sp. PSII preparations

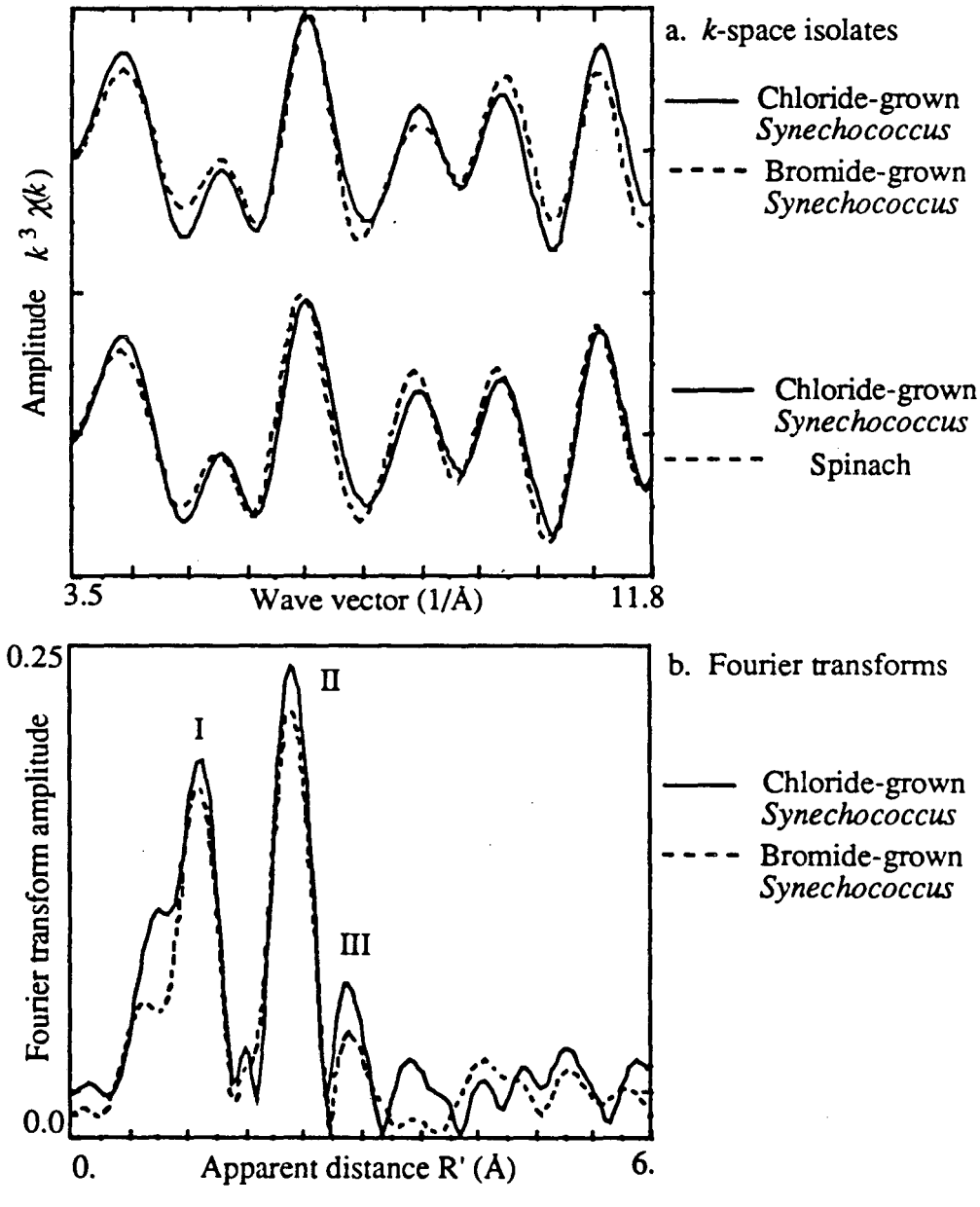

Figure 5.8. Simulated effects due to a single chloride scatterer at 2.3 Å from the Mn in photosystem II. The simulated chloride shell consists of N=0.25, R=2.3 Å, σ^2=.005, and ΔE_0=-10 eV. The data for the chloride-grown *Synechococcus* are plotted (solid line) with the same data set after addition of the chloride shell (dotted line). The Fourier transforms of these data are shown in (b).

Figure 5.8
Simulated effects on the PSII Mn EXAFS of the addition of one chloride per four manganese

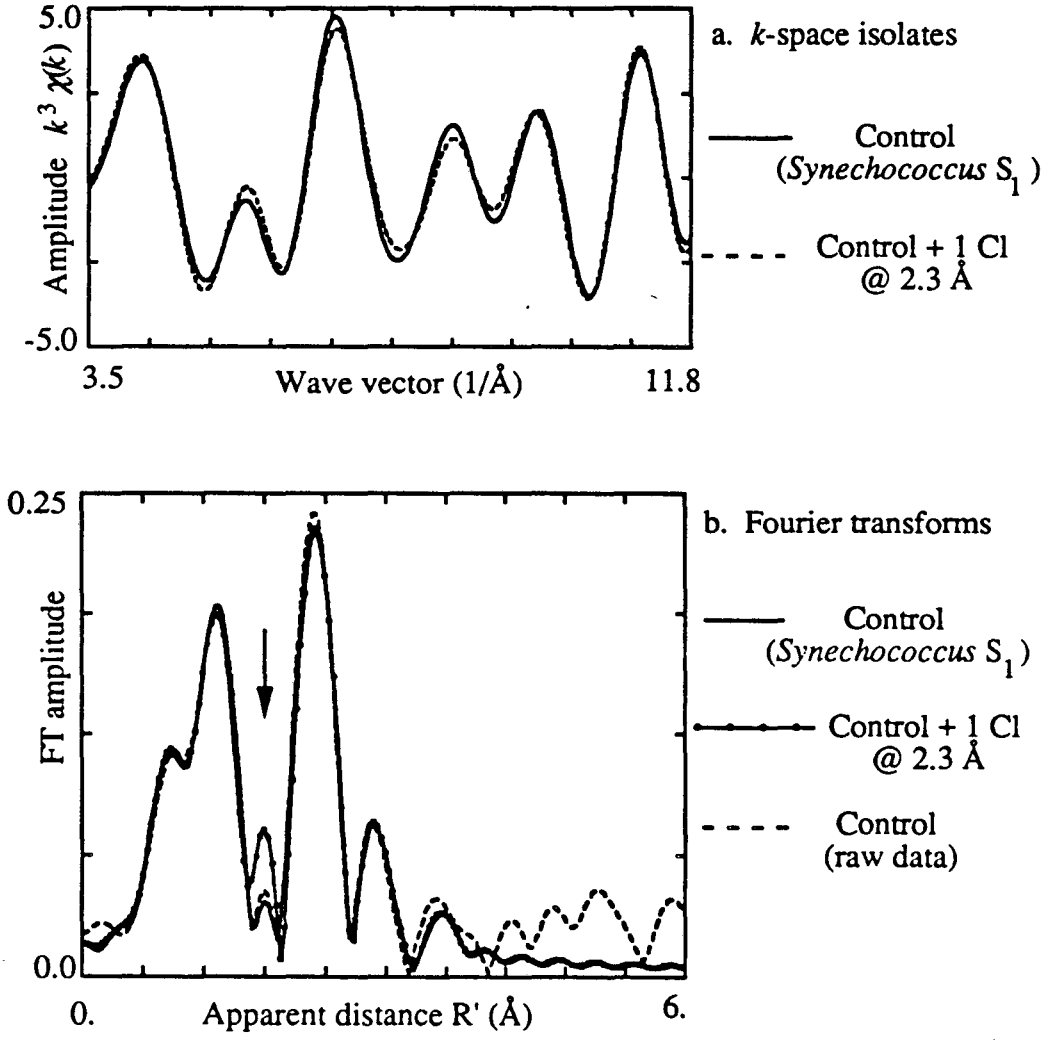

halide ligand in the oxygen evolving complex, the *k*-space function for back-scattering from a single chloride atom at 2.3 Å distance was first subtracted from the (chloride-grown) *Synechococcus* S_1 PSII *k*-space isolated data. The *k*-space function for backscattering from a single bromide atom at 2.5 Å distance was then added to the data. The resulting simulated spectrum is compared in Figure 5.9a (dotted line) with the data from chloride-grown *Synechococcus* (solid line). The Fourier transforms are also shown. The corresponding effect for *two* halide ligands is shown in Figure 5.9b. This second comparison represents both the case of two terminal halide ligands, and the possibility of a single bridging halide ligand which replaces a μ-oxo bridging ligand. It is of note that a final possibility, that of a bridging halide ligand in addition to the di-μ-oxo bridge, would probably contain Mn-halide distances of 2.6-2.7 Å for chloride [Bashkin et al., 1987; Chang et al., 1988], and the difference in the PSII Mn EXAFS between bromide or chloride for ligands at that distance would not be discernible (simulations not shown).

It is evident that the differences in the simulated *k*-space spectra representing a single chloride or a single bromide ligand are small and are within the range of variation in the real data shown in Figure 5.7. The effects simulated for the case of two terminal ligand atoms or a single bridging atom, however, are greater and predict a larger variation in data than that seen between the samples from bromide- and chloride-grown *Synechococcus*. A distinctive damping of the *k*-space oscillations at high *k* occurs in the simulation with two bromide scatterers. This is due to interference effects between the bromide scattering function with R=2.5 Å and the scattering function due to manganese with R=2.7 Å, both of which peak at similar values of *k*.

The data from Figure 5.7 were fit (as described in Chapter 3) to shells of Mn and O or N. The fits were performed on isolated data from peaks I and II of the Fourier transforms shown in Figure 5.7. These fits are listed in Table 5.2. Good fits are obtained for both samples with similar parameters for shells consisting of Mn scatterers at 2.7 Å,(bridging) O at 1.8 Å, and O or N from other ligands near 2 Å. As described earlier (Chapter 3), the number of degrees of freedom available in fitting this two-peak isolate is ~16. In theory, this number supports the use of four shells of scatterers in fitting these data, with four adjustable parameters per shell. It was found, however, that in general the addition of a fourth shell of scatterers did not improve the fit error significantly, where a "significant" improvement is 50 %. In Table 5.2, the results of a series of fits to data from chloride- and bromide-replaced PSII preparations are listed. The data were fit with the three shells mentioned above, plus a fourth shell

Figure 5.9. Simulated effects due to a single bromide scatterer or two bromide scatterers replacing chloride in photosystem II. The simulation parameters are as in Figure 5.6, except that N was allowed to be 0.25 or 0.5. In each figure, the effect of chloride at 2.3 Å was subtracted from the data taken on PSII preparations from chloride-grown *Synechococcus*. Simulated scattering shells from bromide at 2.5 Å were then added to the data.

Figure 5.9
Simulated effects on theMn EXAFS of the substitution of bromide for chloride in photosystem II preparations from *Synechococcus* sp.

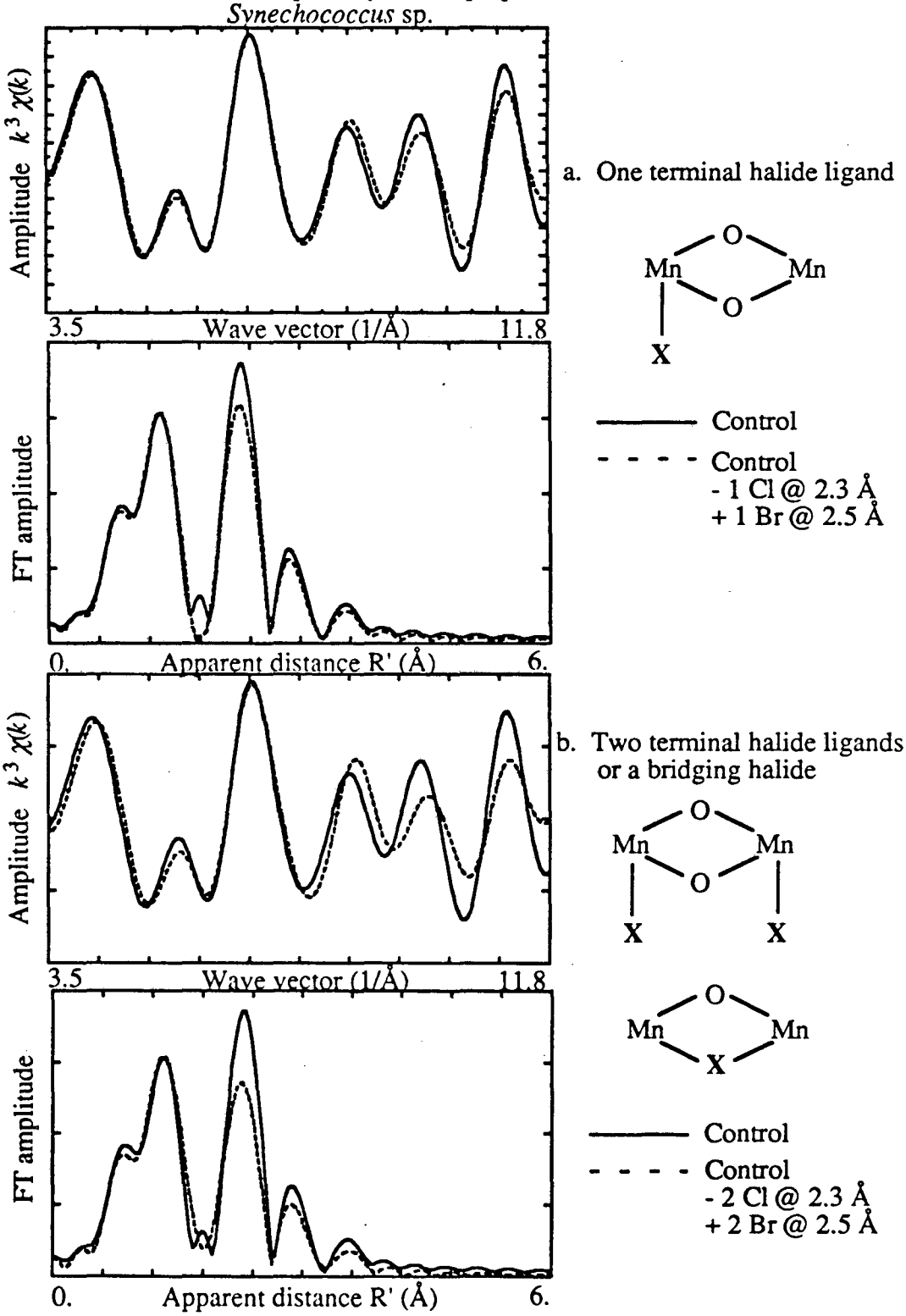

Table 5.2

Fit parameters for Mn EXAFS of PSII preparations from chloride- and bromide- grown *Synechococcus* sp.

Shell		Mn			O				O				X				
	X[a]	R[b]	σ^2	E	R	N	σ^2	E	R	N	σ^2	E	R	N	σ^2	E	Error
(A)	---	2.73	.005	-17	1.83	2.4	.002	1	1.94	5.0	.01	-20					23
	2 C	2.75	.006	-13	1.81	1.8	.004	-20	2.12	1.6	.01	10	2.34	4.0	.02	-8	17
	1 Br	2.73	.007	-16	1.81	1.5	.002	-20	2.04	0.50	.002	5	2.43	0.25	.010	10	19
	2 Br	2.71	.007	-16	1.80	1.5	.002	-20	2.00	0.50	.002	-1	2.45	0.50	.010	10	24
(B)	---	2.73	.005	-11	1.82	2.2	.002	5	1.91	5.0	.01	-20					15
	2 C	2.73	.005	-11	1.80	1.5	.002	-20	2.07	1.5	.01	10	2.23	4.0	.02	-20	12
	1 Cl	2.71	.004	-15	1.82	2.2	.002	6	1.91	5.0	.01	-20	2.36	0.25	.01	8	14
	2 Cl	2.70	.003	-19	1.82	2.4	.002	5	1.91	5.0	.01	-20	2.41	0.50	.01	10	17

(A) PSII preparation from bromide-grown *Synechococcus* sp.
(B) PSII preparation from chloride-grown *Synechococcus* sp.
(a) X corresponds to the type of atom in the additional shell that is included in the fit.
(b) The parameters are as follows: R, distance (Å); σ^2, Debye Waller (Å^2); N, number of scatterers (multiplied by a factor of 2 (Teo & Lee, 1979); E, adjustable parameter ΔE_0 (eV); Fit error, weighted sum of residuals between the data and the calculated fit. The parameters for the Mn-Mn distance were constrained as: $2.70 \leq R \leq 2.73$ Å; $.003 \leq \sigma^2 \leq .007$ Å^2; N = 1.2. The values for σ^2 and ΔE_0 for other shells were held as: $.02 \leq \sigma^2 \leq .002$ Å^2; $-20 \leq \Delta E_0 \leq 10$ eV.

consisting of C, one halide, or two halide atoms. It is seen that the four-shell fits including carbon or one halide slightly decrease the fit error, whereas fits including two halides slightly increase the fit errors. The parameters for the Mn-Mn shell at 2.7 Å were constrained for these fits. When they were not constrained, the effect of two bromide ligands tended to be compensated for by an increase in the Mn-Mn distance for bromide atoms, as well as an increase in the apparent disorder of that shell. Such a difference in Mn-Mn distance in the presence of bromide is not supported by the EPR data, which show that the magnetic couplings between the manganese in bromide- and chloride-substituted samples must be extremely similar. The EXAFS data therefore do not support a bridging halide ligand in the oxygen evolving complex.

Discussion

Suggestions for the interaction of halide with the oxygen evolving complex include both manganese ligation [Sandusky & Yocum, 1986] and interaction with protonated amino acids [Coleman & Govindjee, 1988; Homann, 1988b]. The size and type of ion added to photosystem II preparations have an effect on the manganese of the oxygen evolving complex. Ammonia, which would not be expected to bind to a protonated amino acid, competes with chloride in inhibiting oxygen evolution [Sandusky & Yocum, 1986]. Fluoride has a direct effect on the oxygen evolution activity and the EPR signals arising from manganese. The effects of fluoride are reversed upon the addition of either chloride or bromide [Sandusky & Yocum, 1986]. In these experiments we show that the binding constant for the activating chloride in PSII preparations from *Synechococcus* is indistinguishable from the K_m determined for intact spinach preparations, even though the PSII preparations from *Synechococcus* have a different extrinsic polypeptide composition. This similarity argues that the site of chloride activation is very close to the manganese.

Using EXAFS on bromide-substituted samples, we have attempted to gain evidence for halide ligation to the manganese. If the halide is coordinated to manganese, it could be either as a terminal ligand or as a bridging ligand. There is much precedence for terminal halide ligands in high valent Mn model compounds [i.e., Warren & Bennett, 1976]. The structure of a Mn-Mn complex with an oxo, μ-chloro bridge could be expected to have a Mn-Mn distance of > 3 Å [Mathur et al., 1987]. As such a distance exists in the oxygen evolving complex, it is reasonable to search for evidence for a bridging halide ligand as well.

In these experiments the comparison of EPR and X-ray spectroscopy of photosystem II preparations from cyanobacteria grown in bromide- or chloride-containing media is presented. As discussed in the introduction, this method of halide substitution was chosen to promote a full exchange of bromide for chloride. Chloride quantitation in the PSII preparations from bromide-grown cyanobacteria (for example, by ion-selective electrodes) was not undertaken in these experiments, due to its difficulty in the presence of high levels of bromide ion. There are several reasons to believe, however, that the bromide substitution in these preparations is almost complete. First, the growth medium is expected to contain <10 μM chloride (based on the listed chloride contaminations of the chemicals used), while the concentration of bromide was 3 mM. Cyanobacteria, like chloroplasts [Robinson & Downton, 1984; Harvey et al., 1981], accumulate chloride from the surrounding medium [Dewar & Barber, 1974]. Bromide has been found to mitigate this uptake of chloride in cyanobacteria [Dewar & Barber, 1974]. Since the effects of chloride and bromide on oxygen evolution in PSII preparations as well as in broken and unbroken chloroplasts have been found to be indistinguishable (Kelley & Izawa, 1978 for spinach; this work for *Synechococcus*), it seems unlikely that chloride is retained instead of bromide in the oxygen evolving complex of photosystem II particles which are grown in and isolated from bromide-containing media.

A new EPR signal is found in the dark-adapted PSII preparations from *Synechococcus* grown both in bromide and chloride. This signal consists of at least eight lines separated by an average of 62 G, indicating that it could arise from the S=1/2 state of two or more exchange-coupled manganese atoms. Upon illumination of the samples at 200 K, the S_2-state multiline EPR signal is superimposed upon this signal. The appearance of the signal is not correlated with a decrease in oxygen evolution activity; it is clearly evident in samples with activities of up to 4000 μM O_2/(mg Chl-hr). Since the freeze-thaw cycle of these preparations typically results in the loss of 10-20% activity, it is not possible to rule out the possibility of 10-20% inactive centers in the EPR samples, however. Alternatively, the signal could arise from a manifestation of spin couplings in the S_1 state of the complex which does not allow advance to the S_2 multiline EPR signal state at cryogenic temperatures.

The increased amplitude of the EPR signal in dark-adapted samples from bromide-grown cyanobacteria is not diminished when those samples are then washed in chloride-containing media (data not shown). Thus, the enhancement of the signal is not due to cryoprotectant effects, in which the glass formed at low temperatures is

altered by the presence of bromide instead of chloride ions. Even if the signal represents inactive centers, determining its origin may give new insights into the structure of manganese in the oxygen evolving complex. Some experiments are discussed in Chapter 7 which might help further investigate this EPR signal.

The EXAFS of bromide- and chloride-replaced samples are very similar. The difference between the data sets is smaller than what is expected on the basis of simulations of the replacement of two chloride scatterers with two bromide scatterers per four manganese (Figure 5.9). In addition, fits to the *k*-space data do not support the addition of two halide ligands. This rules out a model for the oxygen evolving complex of the manganese having two terminal halide ligands as well as a model of two manganese bridged by a single μ-oxo and a halide ligand.

As shown by simulations and fits, however, it is very difficult to use the EXAFS experiment to discriminate against a single terminal bromide or chloride ligand in the oxygen evolving complex. With regard to this, it is of interest that the resolution between peaks I and II in control PSII samples is much greater in EXAFS data taken at low (10 K) data than in data taken at 170 K [see, for example, McDermott et al., 1988]. The increased resolution at low temperatures is due to the effect of decreasing Debye Waller values as the temperature is lowered. For a given absorber-scatterer pair, the magnitude of the expected change in the Debye Waller value as the temperature is lowered increases as the magnitude of the vibrational frequency describing the interaction decreases [Teo, 1986]. The vibrational stretching frequencies for Mn-Cl bonds are found to be ~350 cm^{-1} [Warren & Bennet, 1976]. This can be compared with approximately 700 cm^{-1} for the Mn-O-Mn bending mode in di-μ-oxo bridged compounds [Cooper & Calvin, 1977]. Thus, the increased resolution and appearance of the small isolated peak between peaks I and II in the data taken at lower temperatures could be due to the enhancement of back-scattering from a halide ligand as the temperature is lowered.

Summary

1. The K_m for chloride binding in PSII preparations from *Synechococcus* sp. is similar to that from intact spinach PSII preparations, despite the polypeptide differences in the two organisms.
2. There is an EPR signal present in dark-adapted preparations of *Synechococcus* which has an enhanced amplitude in preparations from bromide-grown bacteria. The

signal contains > 8 lines separated by ~ 60 G, and is most likely due to manganese from the oxygen evolving complex. The linewidth and substructure of the signal do not perceptibly change upon substitution of chloride for bromide, but the amplitude of the signal is dependent on the halide.

3. The substructure of the multiline EPR signal from *Synechococccus* is almost identical to that of spinach. The substructure shows no change between preparations from bromide-grown or chloride-grown *Synechococcus*.

4. The Mn EXAFS of PSII preparations from bromide-grown *Synechococcus* is very similar to that from chloride-grown *Synechococcus*. This similarity and the resulting fits to the EXAFS data preclude two halide ligands or a bridging halide ligand, but cannot exclude a single terminal halide ligand in the oxygen evolving complex.

Chapter 6

Continuous Wave EPR and Electron Spin Echo Spectroscopy Studies of ^{14}N- and ^{15}N-Containing Photosystem II Preparations from *Synechococcus* sp.

Introduction

Ligands for the Mn of the oxygen evolving complex have been proposed to come from amino acids in regions of the D_1 and D_2 polypeptides, near the carboxy-termini, which are highly conserved amongst water-oxidizing species (Michel & Deisenhofer, 1988). These conserved sequences contain many carboxylic acid residues as well as several histidines, both of which are common ligands in metalloproteins. As discussed in Chapter 5, techniques such as EXAFS, which sample the average ligand environment of all four manganese, cannot discern between oxygen or nitrogen ligands in the oxygen evolving complex. In this chapter the results of continuous wave (CW) EPR and electron spin echo experiments are reported, in which the differing magnetic moments and nuclear spins of ^{14}N and ^{15}N are used as probes for nitrogen ligation to the manganese of the oxygen evolving complex.

At X-band the multiline EPR signal from the S_2 state of the oxygen evolving complex contains 16 or more Mn hyperfine lines, separated by approximately 80 G, which result from at least 2 exchange-coupled Mn nuclei. Each hyperfine line of the EPR multiline signal exhibits further substructure of three or four partially resolved peaks with 10-30 G separation (Yachandra et al., 1986a; Nugent, 1987; Hansson et al., 1986; Andréasson, 1989). Both additional Mn hyperfine transitions and superhyperfine coupling from ligands with paramagnetic nuclei have been proposed to contribute to the substructure of the multiline signal. Researchers have attempted to gain evidence for superhyperfine interactions from exchangeable Cl^- ligands or from protons by measuring the multiline signal substructure in samples which have been washed with Br^- and ^2H_2O, respectively. A slight increase in resolution of the substructure features following exchange with ^2H_2O was reported by Nugent (1987), but others have found no such effect (Yachandra et al., 1986a; Haddy et al., 1989). No detectable change in linewidth was reported after exchange of Cl^- with Br^- (Yachandra et al., 1986a; Haddy et al., 1989). A comparison between chloroplast preparations from spinach grown hydroponically in ^{15}N and ^{14}N also showed no detectable linewidth changes in the multiline signal (Andréasson, 1989). From this it

was concluded that nitrogen hyperfine coupling to the manganese was very unlikely. A negative result with this kind of experiment does not prove the absence of an interaction, however, as the magnitude of the superhyperfine interaction may be very small compared with the inhomogeneous width of the Mn hyperfine lines.

Electron spin echo envelope modulation (ESEEM) is a more sensitive method of measuring superhyperfine couplings in such systems with large inhomogeneous broadening (Mims & Peisach, 1981; Kosman, 1984). The amplitude of the spin echo induced by a pulse sequence is modulated through the interaction of the electron spin with nearby paramagnetic nuclei. The modulation frequencies can be directly related to the nuclear Zeeman and hyperfine interactions, as well as the electric quadrupole interactions for nuclei with spin $I \geq 1$. Recently, the weak hyperfine coupling of directly ligating nitrogen from the bipyridyl ligands in the model compound di-μ-oxo bridged Mn(III)Mn(IV) bipyridine complex has been measured using ESEEM (Britt, 1988). This binuclear complex presents a 16-line EPR spectrum which is very similar to the multiline signal from the OEC. The ^{14}N isotropic hyperfine coupling of approximately 1 G determined by ESEEM is too small to be detected on the 40 G wide Mn hyperfine lines using continuous wave EPR (Britt et al., 1990a). ESEEM has also been successful in demonstrating the binding of ammonia (an inhibitor and potential substrate analog) to Mn in the OEC from spinach, again with an isotropic hyperfine coupling of approximately 1 G (Britt et al., 1989). No difference in linewidth of the multiline signal was detected by CW EPR between $^{14}NH_3$- and $^{15}NH_3$-substituted samples (Beck et al., 1986).

The ESEEM spectrum of the multiline signal from the native OEC of spinach contains modulation at two frequencies, ca. 14 and 5 MHz (Britt et al., 1989). The modulation at 14 MHz is assigned to weak interactions with nearby matrix protons (Britt et al., 1990b). The 5 MHz peak has remained unassigned but could be due to interaction with a nearby ^{14}N nucleus. This is tested in the present study using PSII OEC preparations from the cyanobacteria *Synechococcus* sp. grown in media containing either $^{15}NO_3^-$ or $^{14}NO_3^-$ as the sole source of nitrogen. The effects of nitrogen isotope substitution on the ESEEM spectrum and the CW EPR spectrum of the multiline from *Synechococcus* are reported.

Materials and Methods

Synechococcus sp. growth and PSII-OEC isolation. Ten-liter cultures of *Synechococcus* sp. were grown as described in Chapter 2. The growth medium was modified from that in (McDermott et al., 1988) such that all added nitrogen was in the form of KNO_3. Oxygen-evolving PSII complexes from *Synechococcus* were isolated from thylakoids having specific O_2 activities of 300-500 μmole O_2(mg Chl-h)$^{-1}$ as described in Chapter 2. The PSII preparations typically exhibited activities of 2500-4000 μmole O_2(mg Chl-h)$^{-1}$. Detergent-extracted PSII complexes were pelleted by centrifugation at 4 ^{o}C, 300000xg for 3-4 h. The pellet was resuspended in sucrose buffer (50 mM Mes pH 6.5, 5 mM $CaCl_2$, 400 mM sucrose, pH 6.5, 2 mM PMSF) and centrifuged as before, then resuspended in the same buffer minus sucrose and containing 1 mM EDTA and centrifuged as above for 2 h. The pellet was then resuspended in a mixture of 50% buffer (with EDTA)/ 50% glycerol to 2-3 mg Chl/ml. Samples were loaded into EPR tubes and dark-adapted on ice for at least 30 min before being stored at 77 K. Typically, four concentrated EPR samples could be made from the yield from a 10 L culture. For illumination at 200 K, samples were immersed in a methanol/solid CO_2 bath and illuminated for 5-10 min with a 400 W tungsten lamp thermally isolated from the sample by a 5 cm water filter containing 5% aqueous $CuSO_4$.

^{15}N enrichment determination. ^{15}N-content was determined from the mass spectrum of Chl a using an AEI MS12 low resolution mass spectrometer following ionization at 10 eV. Comparison of the ratios of the parent and M-1 peaks of Chl a from ^{14}N- and ^{15}N-grown bacteria showed >95% labeling with ^{15}N. Chl a was isolated from *Synechococcus* using a preparation slightly modified from that of Omata and Murata (1983). Chl a was isolated from the pellet which is left after the detergent extraction of PSII. This pellet contains most of the PSI as well as other thylakoid membrane components. Briefly, part of the pellet was resuspended in sucrose buffer to approximately 2 mg Chl/ml. One ml of the suspension was mixed with 9 ml of acetone and centrifuged. The supernatant was evaporated to near dryness (in a rotary evaporator), resuspended in less than 0.5 ml of hexane:isopropanol (20:1), and loaded onto a 12 ml column of Octyl-Sepharose Cl-4B (Pharmacia) which had been prepared as in Omata and Murata (1983). Chlorophyll a was separated from carotenoids during

elution with hexane:isopropanol (20:1) and determined to be >98% pure by optical spectrophometry using the ratio of A_{430}/A_{660} of 1.21.

Electron Paramagnetic Resonance. EPR at X-band was performed using a Varian E-109 spectrometer with a standard TE_{102} cavity. A GaAsFET amplifier (Dexheimer & Klein, 1988) was used for spectra taken at 5 mW power. Individual scans were collected using a signal averager of local design interfaced with a VAX 11/785 computer. The sample temperature was maintained at 8.0 $\pm$ 0.5 K with an Air Products liquid helium cryostat.

Electron Spin Echo Spectroscopy. Two-pulse ESE spectroscopy was performed at 4.2 K using a homebuilt spectrometer with a cryogenic loop-gap resonator probe (Britt & Klein, 1987; Britt et al., 1989). Microwave pulses, 200 W, were of 12 ns duration. The instrument dead time was 120 ns. The two-pulse time domain data were acquired by gated integration of the spin echo signal as a function of interpulse time τ, which was increased in 10 ns increments. The cosine Fourier transforms are presented with short experimental dead times reconstructed using the Fourier backfill technique described by Mims (1984).

Results

Continuous wave EPR of the multiline signal from ^{14}N and ^{15}N-grown Synechococcus.

Figure 6.1 shows an EPR spectrum of a 200 K-illuminated PSII sample from ^{14}N-grown *Synechococcus*, after subtraction of the spectrum of the dark-adapted sample. As previously reported (Aasa et al., 1987; McDermott et al., 1988), the multiline signal is very similar to that from spinach in terms of the number and splittings of the hyperfine lines. A slight difference in lineshape from *Synechococcus* on the high field side of g=2 can be ascribed to a small amount of an underlying signal at g=1.6, which has been assigned as a reduced acceptor species (McDermott et al., 1988). That signal contributes to the spectrum as a broad, featureless absorption from 3700 to 4000 G.

Figures 6.2a and b are signal-averaged spectra of the high-field side of the multiline signal recorded at 4 G modulation amplitude and 5 mW power. Under these conditions, the individual lines can be seen to have asymmetric shapes, which are split or have shoulders with 10-30 G separation. Figure 6.2a is from cyanobacterial

Figure 6.1. Continuous wave EPR spectrum of PSII-OEC preparation from *Synechococcus* sp. (grown on ^{14}N) in the S_2 state. The spectrum was recorded after advancement to the S_2 state following a 4 min illumination at 200 K of a dark-adapted sample, and the spectrum of the dark-adapted sample is subtracted. A narrow region of the spectrum at g=2 is removed due to a sharp feature from the subtraction. Spectra were recorded at 9.2 GHz, 30 mW power, 8 K, 25 G modulation amplitude, 5000 gain, and 100 kHz modulation frequency. Chlorophyll concentration is 2-3 mg/ml. Arrows indicate boundaries of the region which is examined in detail in Figure 6.2.

Figure 6.1

Multiline EPR signal from a photosystem II preparation from *Synechococcus* sp.

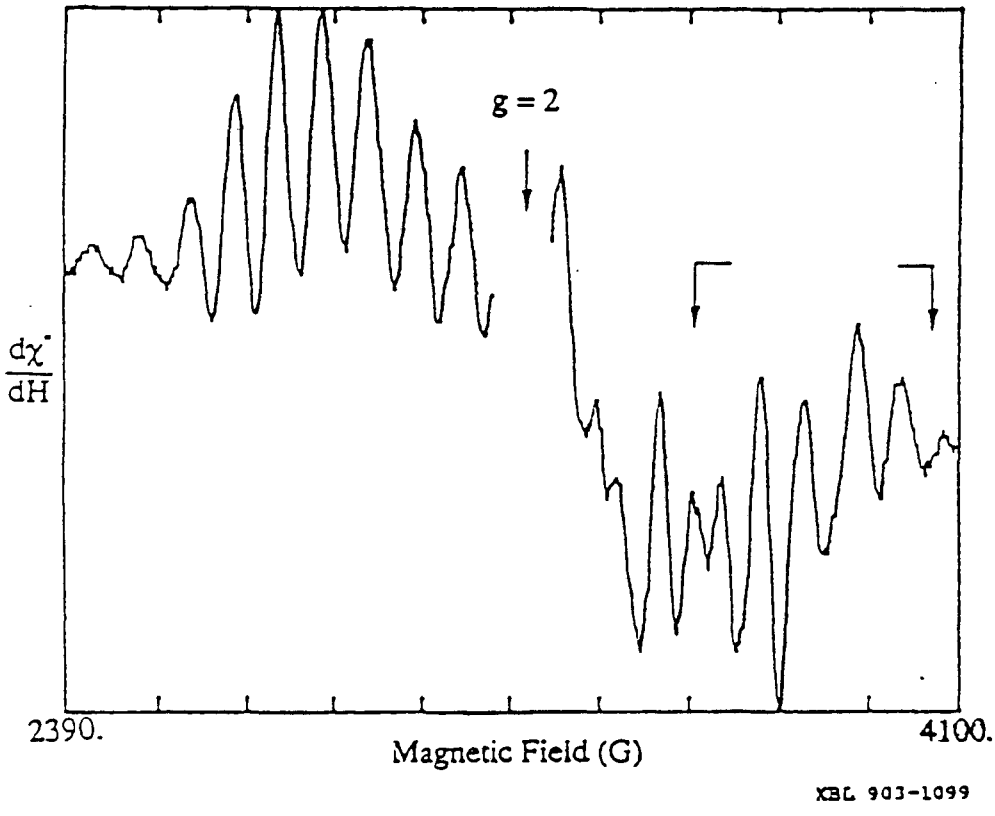

Figure 6.2. Comparison of multiline EPR signals from PSII preparations of ^{14}N- and ^{15}N-grown *Synechococcus*. (a) Continuous wave EPR spectra comparing the multiline substructure in PSII-OEC preparations from *Synechococcus* sp. grown on ^{14}N (upper trace) and ^{15}N (lower trace). Spectra are averages of 50 scans, 2 min each, recorded at 9.2 GHz, 5 mW, 4 G modulation amplitude, 100 kHz modulation frequency, 8.0 $\pm$ 0.5 K, and 1 x 10^5 gain. Samples were illuminated at 200 K for 4 min. (b) Comparison of the first derivatives of the data shown in (a) (second derivatives of the absorption). The upper trace is from *Synechococcus* grown on ^{14}N, and lower trace from *Synechococcus* grown on ^{15}N. The derivatives were calculated from a second-order polynomial fit to a sliding window of 16 G. A comparison of individual peak positions shows them to be indistinguishable within $\pm$ 2 G.

Figure 6.2

Comparison of the multiline signals in PSII preparations from ^{14}N- and ^{15}N-grown *Synechococcus*

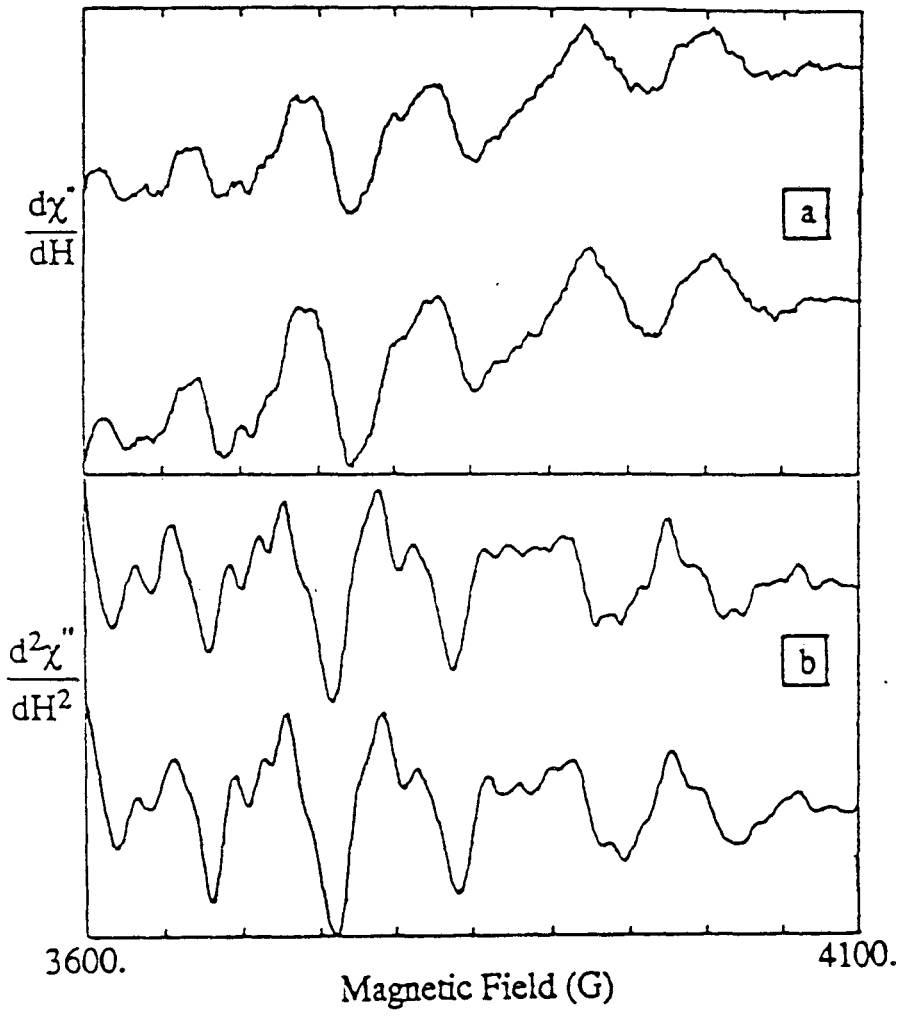

XBL 903-1101

preparations grown on $^{14}NO_3^-$ (upper trace) and $^{15}NO_3^-$ (lower trace). There are no obvious differences between the two preparations in the shapes or splittings of the Mn hyperfine lines. The second derivatives of the absorption line, calculated from the first derivative of a sliding polynomial fit to the spectra, are compared in Figure 6.2b. These second derivative spectra show no systematic changes in peak positions, indicating that at 4 G spectrometer resolution no change in line shape is evident in the multiline EPR signal due to the substitution of ^{15}N for ^{14}N in the cyanobacterial OEC.

ESEEM of ^{15}N and ^{14}N-grown Synechococcus PSII. Figures 6.3a and b display the ESEEM patterns following a two-pulse sequence at a field of 3200 G on the multiline signal from a ^{14}N-grown *Synechococcus* sp. PSII sample. Both the time domain data (Figure 6.3a) and the cosine Fourier transform (Figure 6.3b) are shown. Peaks are observed in the Fourier transform at 4.5 and 13.6 MHz. Comparable features were observed in ESEEM spectra obtained at 3100 G and 3400 G (data not shown). These features are very similar to those observed in PSII preparations from spinach (Britt et al.,1989). The 13.6 MHz peak arises from weak coupling to protons, some of which in spinach are exchanged upon short (4 h) incubation in ^2H_2O-enriched buffer (Britt et al., 1990b).

Figures 6.4a and b show the ESEEM time domain data and Fourier transform of the multiline signal from a ^{15}N *Synechococcus* PSII preparation. The modulation at around 4.5 MHz is absent from these data, which were taken at 3200 G, as well as from data taken at 3100 and 3400 G (data not shown). The absence of the 4.5 MHz peak from the ^{15}N data indicates that the feature arises from coupling of the electron spin to one or more ^{14}N in the vicinity of the manganese cluster. No corresponding feature due to ^{15}N appears in the data taken at 3200 G (Fig. 6.4b), 3100 G or 3400 G (data not shown).

Nitrogen modulation in dark-adapted samples. A comparison of the Fourier transforms of ESEEM at 3200 G of the dark-adapted ^{14}N and ^{15}N samples is shown in Figures 6.5a and b. The ^{15}N sample shows modulation at ~1.3 and ~4.8 MHz, whereas the ^{14}N sample has modulation at ~4 and ~7 MHz. This modulation is most likely due to nitrogen ligation to Fe^{+3} in oxidized cytochrome b_{559}. As described in Chapter 5, the continuous wave EPR spectra of these dark-adapted PSII preparations show large signals at g=3.0 and 2.2 which arise from the oxidized cytochrome, as well as a signal at g=6 which resembles oxidized high-spin ferricytochrome (data not

Figure 6.3. ESEEM of the multiline EPR signal from PSII preparations from ^{14}N-grown *Synechococcus*. Amplitude of the spin echo, as a function of τ after a two-pulse sequence, from the multiline signal from PSII-OEC preparations from *Synechococcus* sp. grown on $^{14}NO_3^-$ (a). The subtracted data (200 K-illuminated samples minus dark-adapted samples) are shown. The cosine Fourier transform shows peaks at ca. 14 and 4.5 MHz in the ^{14}N spectrum (b). The peak at around 14 MHz is due to protons and is centered at the proton larmor frequency. Spectrometer conditions were 9.2 GHz microwave frequency, 4.2 K, 3200 G field position. The spectra are the average of 15 scans. The intervals τ between pulses in the two-pulse sequence were increased by 10 ns increments, with a 2.5 ms interval between each two-pulse sequence.

Figure 6.3

ESEEM of the multiline signal
in a PSII preparation from ^{14}N-grown *Synechococcus* sp.

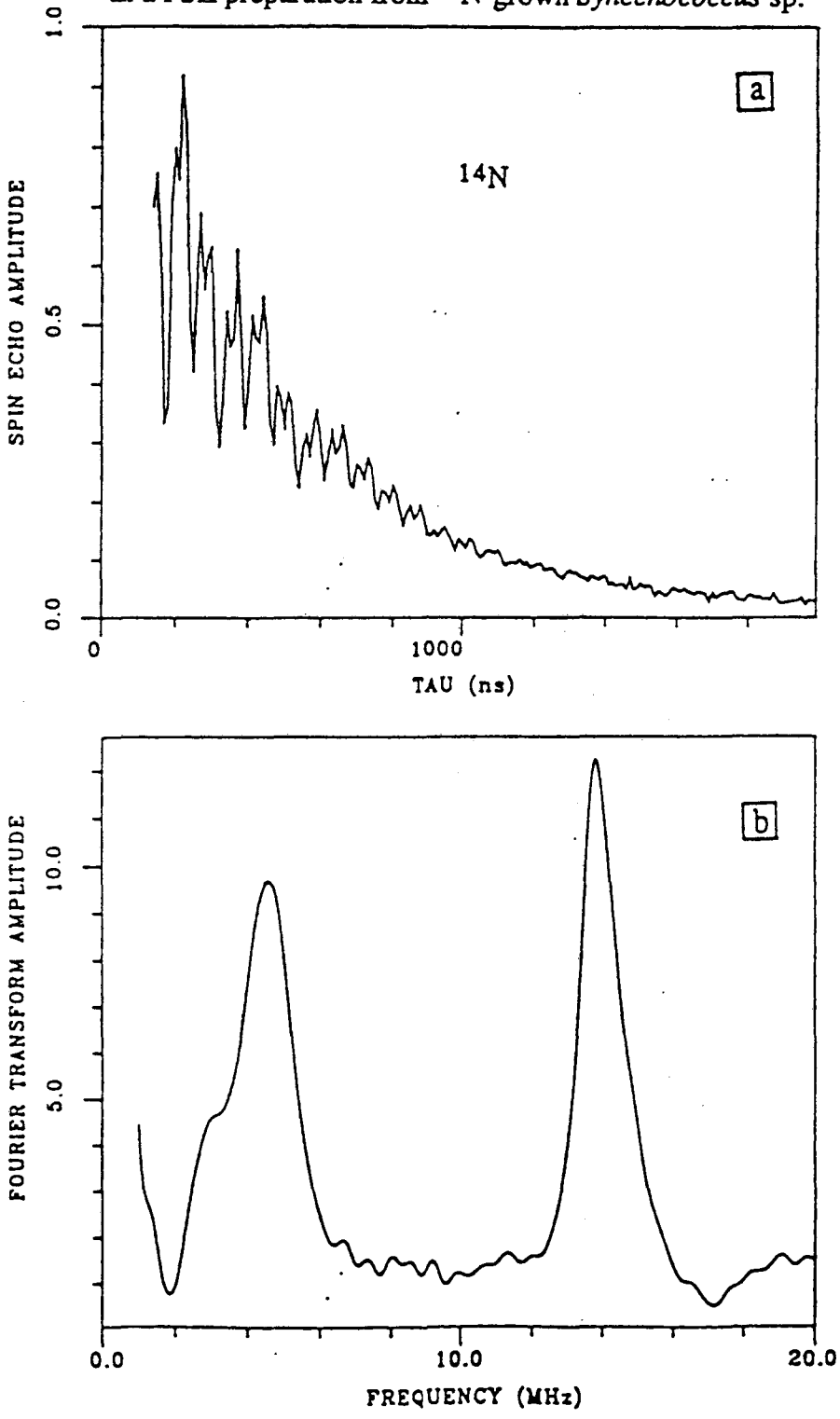

XBL 903-1100

Figure 6.4. ESEEM of the multiline EPR signal from PSII preparations from ^{15}N-grown *Synechococcus*. Amplitude of the spin echo (a) and the cosine Fourier transform (b) from the multiline signal from PSII-OEC preparations from *Synechococcus* sp. grown on $^{15}NO_3^-$. In contrast to the spectra for the ^{14}N-enriched samples (Figure 6.3), the ^{15}N Fourier transform shows only the peak centered at the proton larmor frequency of ~14 MHz. Spectrometer conditions were as in Figure 6.3.

Figure 6.4

ESEEM of the multiline signal
in a PSII preparation from ^{15}N-grown *Synechococcus* sp.

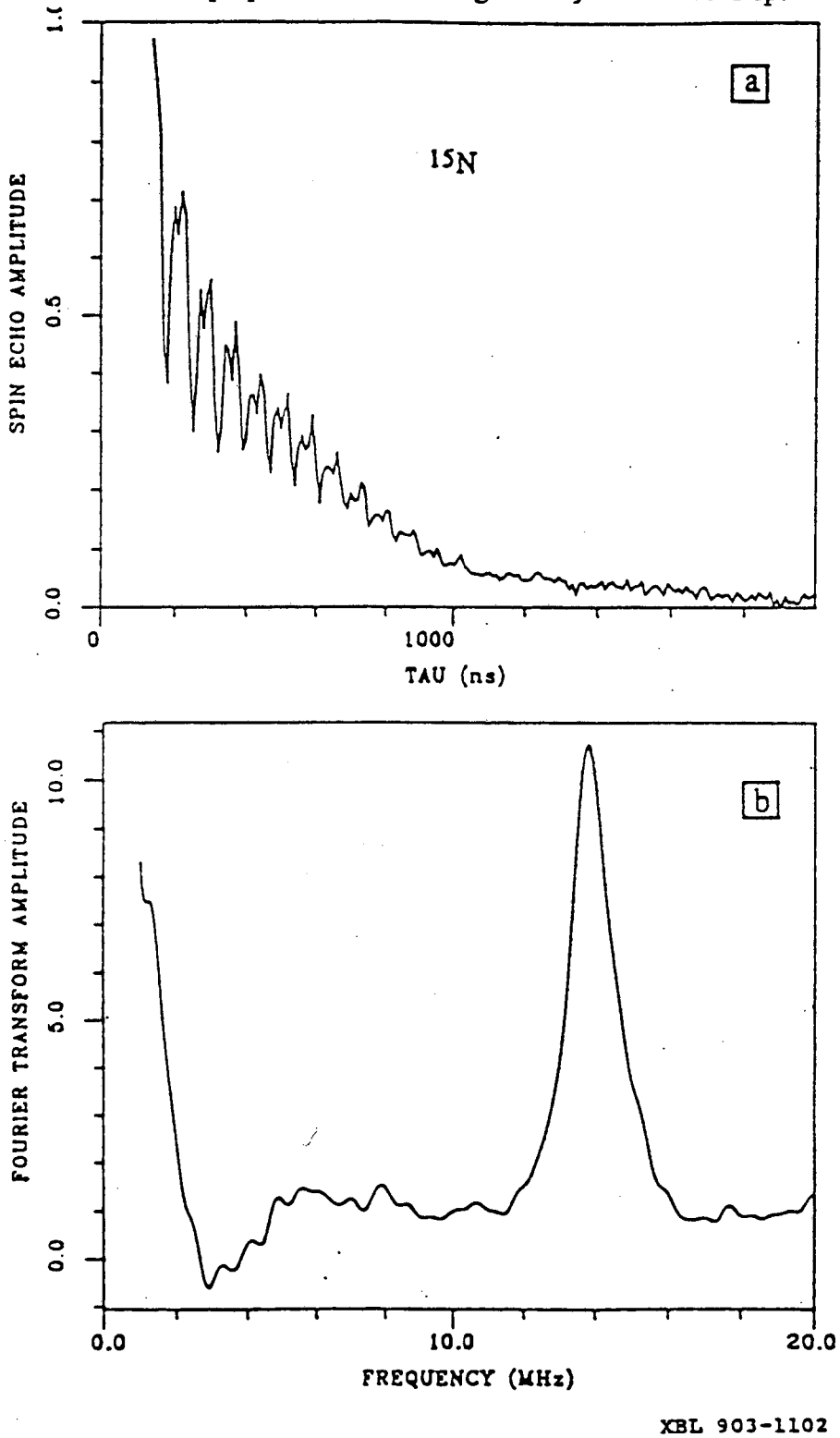

Figure 6.5. Comparison of the Fourier transform spectra of dark-adapted PSII-OEC preparations from ^{14}N- and ^{15}N-grown *Synechococcus* sp. The cosine Fourier transforms of the time-domain ESEEM pattern are shown. Peaks at ca. 4 and 7 MHz are found for the ^{14}N sample (a), and 1.2 and 4.8 MHz for the ^{15}N sample (b). Experimental conditions were as in Figure 6.4.

Figure 6.5

ESEEM in dark-adapted PSII preparations from ^{14}N- and ^{15}N-grown *Synechococcus* sp.

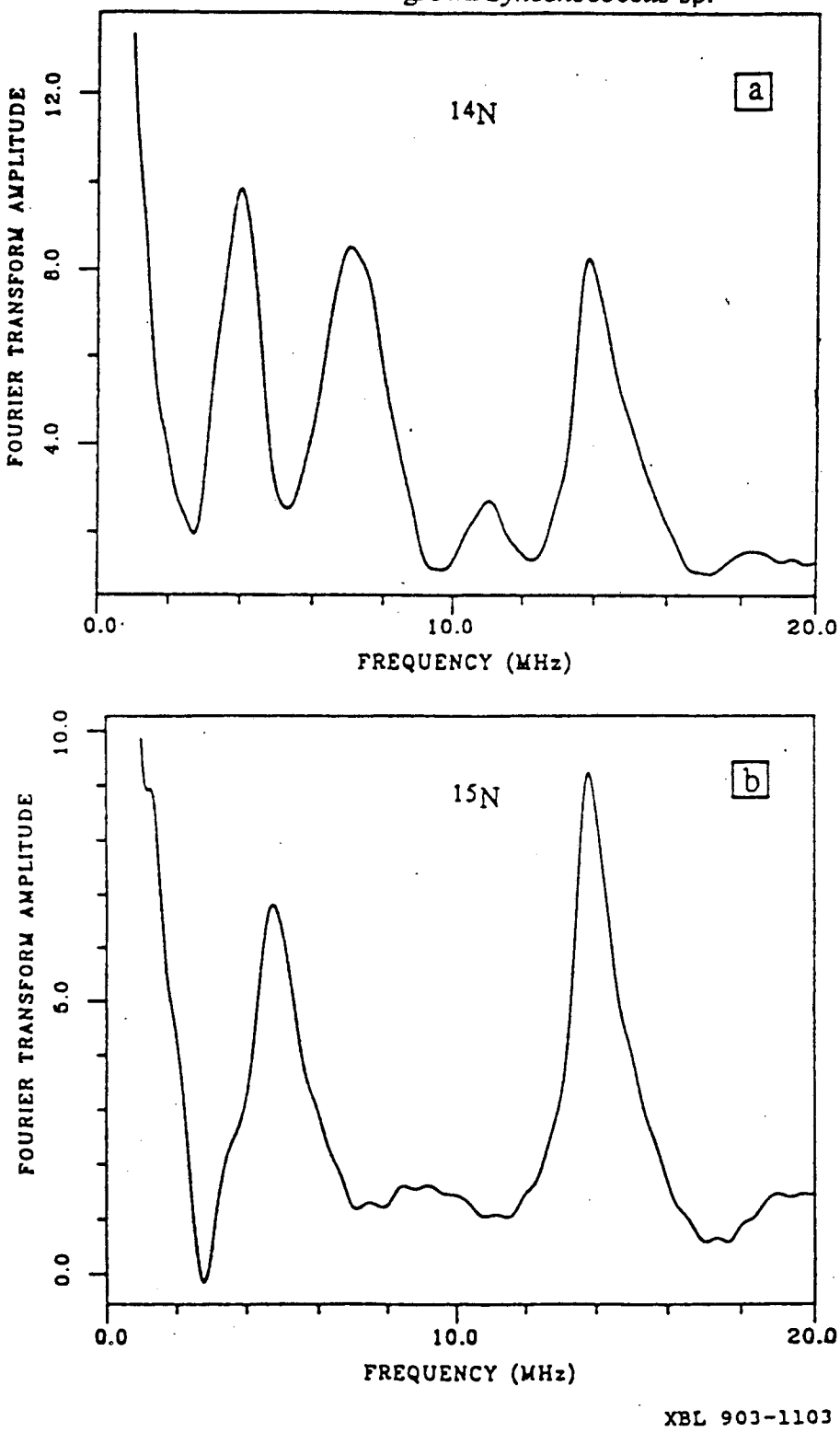

shown). In these dark-adapted samples the >8-line EPR signal reported in Chapter 5 is barely evident.

In its reduced form, cytochrome b_{559} is an alternative electron donor to P_{680}^+ at temperatures below 200 K (dePaula et al., 1985). For the ESEEM experiments on the multiline signal from *Synechococcus*, the amplitude of the signals at g=3.0 and g=6.0 were monitored with CW EPR before and after the 200 K-illumination to show that no additional oxidized cytochrome b_{559} was formed during the illumination. Thus, the frequencies in the light-minus-dark ESEEM data are due only to the multiline species.

Discussion

In this study, the question of nitrogen ligation to the Mn in the PSII oxygen evolving complex was addressed using both pulsed and continuous wave EPR on ^{15}N-substituted samples from the thermophilic cyanobacterium *Synechococcus* sp. The ESEEM of the multiline signal from the *Synechococcus* OEC was found to have the same frequency components as the OEC from spinach. The ESEEM frequency at ~4.5 MHz disappeared upon total isotopic substitution with ^{15}N, giving unambiguous evidence for weak hyperfine interaction of nitrogen with the Mn of the OEC.

In the Mn(III)Mn(IV) di-μ-oxo bridged bipyridine compound, the magnitude of the isotropic hyperfine coupling of the *directly ligating* N has been determined by ESEEM to be less than 1 G (Britt et al., 1990a). By contrast, in Cu-histidine or Cu-imidazole complexes the coupling between Cu and the ligating imino N of >30 MHz (>10 G) is greater than can be observed with conventional ESEEM (Mims & Peisach, 1978). We expect the hyperfine interactions to ligands in the OEC to resemble those in the Mn(III)(IV) model compound, whose EPR spectrum is very similar to the OEC multiline EPR signal. However, we have also used continuous wave EPR to show that in the OEC strong hyperfine interactions with nitrogen could not be detected by comparing the substructure on the multiline EPR signals from ^{14}N- and ^{15}N-substituted PSII samples.

What is the origin of the weak ^{14}N hyperfine interaction in the OEC? In some cases, the ESEEM frequencies of both ^{14}N and ^{15}N-substituted samples allow an analysis of the nitrogen hyperfine and quadrupole coupling parameters (see, for example, Mims & Peisach, 1978; McCracken et al., 1988). These parameters can be used to describe the interacting species. Unfortunately, in this experiment modulation

due to ^{15}N was not detected over the magnetic field range of the multiline signal at 9 GHz. Additionally, only one frequency due to ^{14}N is detected in both 2-pulse and 3-pulse (stimulated echo) experiments (Britt et al., 1990a). It may therefore be necessary to extend the ESEEM measurements to microwave frequencies beyond the range of the X-band spectrometer to gain information about the specific parameters of nitrogen hyperfine coupling in the OEC. For both ^{15}N and ^{14}N nuclei, the ESEEM amplitudes will be maximal at a field position where the nuclear Zeeman frequency is one half the magnitude of the hyperfine coupling constant (Astashkin et al., 1984; DeGroot et al., 1986; Flanagan & Singel, 1987; Lai et al., 1988). For the I=1/2 ^{15}N nucleus, the field range over which significant modulation is observed is determined by the magnitude of the anisotropic component of the hyperfine interactions (Lai et al., 1988), whereas the electric quadrupole interaction of the I=1 ^{14}N nucleus enhances the modulation amplitude and increases the field range over which modulation from ^{14}N may be observed (Flanagan & Singel, 1987).

The high value of the ^{14}N ESEEM frequency (4.5 MHz at 3200 G) indicates that it is due to interactions with specific nitrogen nuclei in the immediate vicinity of the OEC Mn. It is unlikely that ^{14}N nuclei in a protein environment would have transitions at a frequency as high as 4.5 MHz without magnetic contributions from hyperfine contact interactions. Such a contact interaction could result from either ligation of a nitrogen directly to the Mn cluster, or possibly through hydrogen-bonding to a bridging oxygen of the Mn complex. Without such a contact interaction, the only magnetic contributions would be from the 3200 G applied field and a weaker dipolar field arising from the electronic spin. We estimate by numerical simulations (peformed as described in Britt et al., 1989) that in the absence of a contact interaction, the value of the electric quadrupolar coupling parameter e^2qQ would have to exceed 4.0 MHz in order to generate a transition at 4.5 MHz. A quadrupolar coupling value of greater than 4.0 MHz is larger than expected for peptide nitrogens (e^2qQ between 3.0 and 3.4 MHz), amide nitrogens (e^2qQ approximately 2.5 MHz), or nitrogens in the imidazole sidechain of histidine (e^2qQ or 3.4 MHz for the imino nitrogen, 1.4 MHz for the amino nitrogen) (Edmonds, 1976). We therefore consider it unlikely that the ^{14}N ESEEM transition observed at 4.5 MHz arises from one or more distant nitrogens.

A more likely source of the nitrogen interaction detected by ESEEM is through superhyperfine coupling between a nitrogen ligand from an amino acid and the unpaired spin on the manganese. The multiline EPR signal from the OEC shows very shallow nitrogen modulation in comparison with the model compound di-μ-oxo

bridged Mn(III)Mn(IV) bipyridine complex (Britt, 1988, 1990a). This qualitative comparison would indicate few, perhaps only 1 or 2, nitrogen ligands in the OEC. It is important here to note that the nitrogen interaction detected in this study applies only to the manganese in the OEC which contribute to the multiline EPR signal, which may include only 2 or 3 of the 4 Mn in the complex.

The proposed Mn-binding regions on the *c*-termini of the D_1 and D_2 polypeptides (Trebst, 1986; Michel & Deisenhofer, 1988) contain a lysine (K_{318} on D_2) and several histidine (H_{337}, H_{332} on D_1 and H_{337} on D_2) and arginine (R_{334}, R_{323}, R_{312} on D_1 and R_{349}, R_{305} on D_2) residues which are conserved among both cyanobacteria and higher plants (summarized in Gingrich et al., 1988, 1990). Additional conserved nitrogen-containing residues are found in regions which are predicted to be on the lumenal side of the membrane between the alpha-helices A and B (H_{92} and R_{64} on D_1, H_{62} and R_{104} on D_2) and C and D (H_{191} on D_1, H_{190} and R_{181} on D_2) (Gingrich et al., 1990). Figure 6.6 is a composite of the D_1 and D_2 polypeptides. In the Figure both nitrogen- and oxygen-donating potential ligands which are conserved among cyanobacteria and higher plants are emphasized. It is not possible to distinguish among these possibilities for an amino acid ligand from the results of this experiment (vide supra). In all known structures of manganese-containing proteins, however, there is no nitrogen coordination other than that arising from histidine (Brookhaven Protein Data Bank). In recent work Guiles et al. (1990) proposed a redox-active ligand in the OEC which becomes oxidized in the S_2- to S_3-state transition, and suggested an aromatic amino acid such as a histidine for the identity of this ligand. Supporting this is the discovery of a broad, featureless EPR signal centered at g=2, reported to arise from the S_3 state in samples which have been depleted of Ca^{+2} (Sivaraja et al., 1989; Boussac et al., 1989). This signal has tentatively been assigned to a histidine radical (Boussac et al., 1990). The involvement of histidine in binding Mn is also supported by chemical modification experiments, in which the use of a histidine-specific modifying agent was reported to inhibit the photoactivation of Mn-depleted PSII particles (Tamura et al., 1989).

An alternate possibility for the interaction of nitrogen with the Mn complex is through a hydrogen bond between an amino acid side chain or peptide amide and a Mn-Mn μ-oxo-bridge or oxo or hydroxo ligand. Hydrogen bonding to metal bridging ligands is seen, for example, in Fe-S centers (Mino et al., 1987) and oxyhemerythrin (Shiemke et al., 1986). While it is not possible to rule out this type of interaction in the OEC, isotope exchange experiments using ^2H_2O may provide some information.

Figure 6.6. Amino acid sequences of the D_1 and D_2 peptides. The folding pattern predicted from hydropathy plots is shown [Trebst, 1986; as depicted in Michel & Deisenhofer, 1988]. Amino acids which are conserved amongst sequences from higher plants and cyanobacteria are in boldface, and the sequence numbers for possible nitrogen ligands are given [Gingrich et al., 1988, 1990].

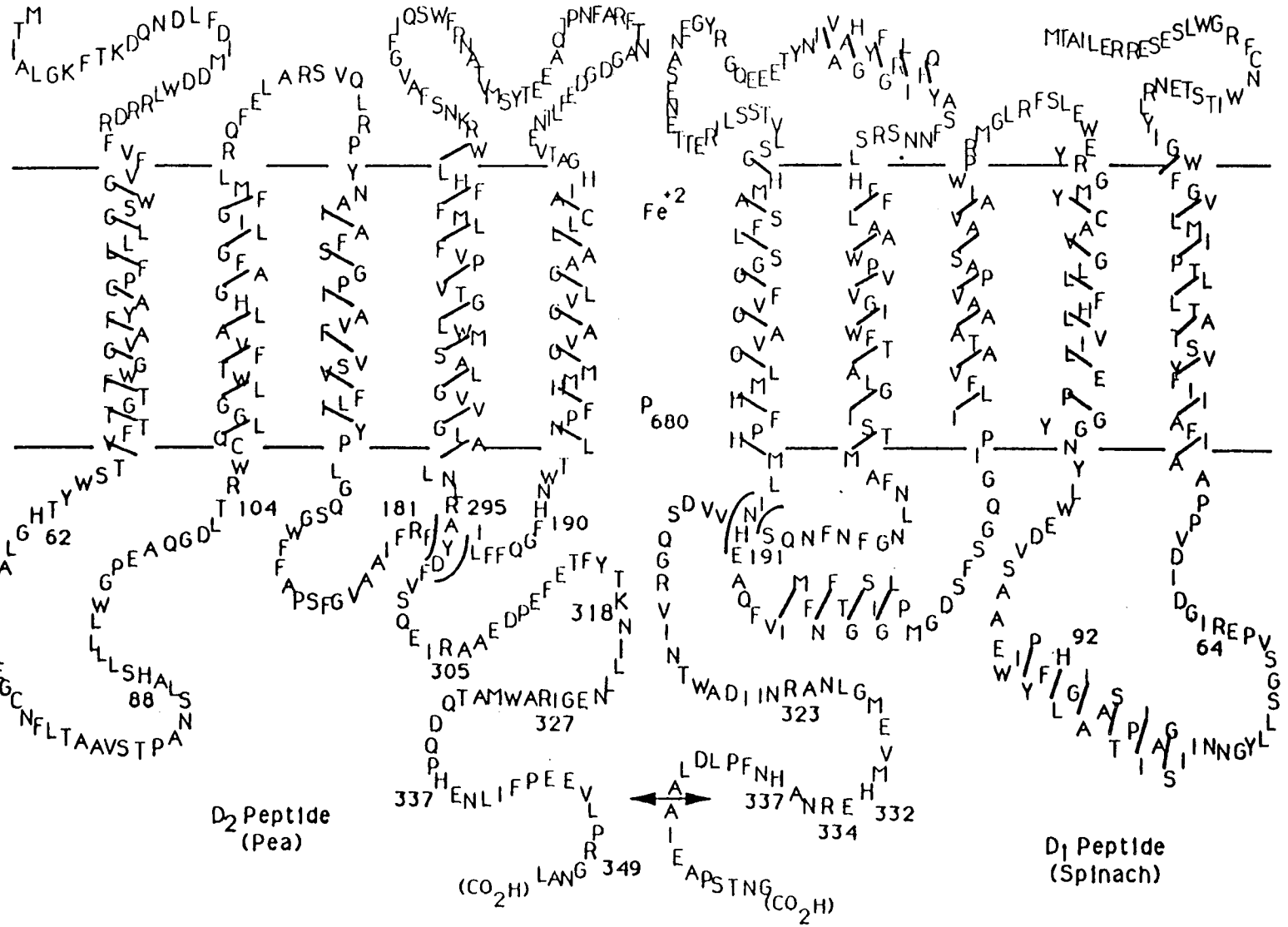
D2 Peptide
(Pea)
D1 Peptide
(Spinach)
Fe+2
P680
(CO2H)
(CO2H)

The isotropic hyperfine coupling through a hydrogen bond would be expected to change significantly upon exchange in ^2H_2O, as ^2H in general forms weaker hydrogen bonds. The ^{14}N ESEEM peak in the OEC remains unchanged upon a 4 hour exchange in ^2H_2O-enriched buffer, although approximately half of the protons contributing to the 15 MHz modulation component are replaced by deuterons (Britt, 1988; Britt et al., 1990b). Because acidic protons are expected to exchange readily, this would indicate that the nitrogen modulation does not arise from an amide or amino group which is hydrogen-bonded to the Mn complex. For this test to be conclusive, however, it may be necessary to have prolonged exposure to ^2H_2O for complete exchange, especially if the site is buried in the interior of the protein.

To address the possibility of nitrogen hyperfine interactions in the OEC which are larger than could be observed by ESEEM we have compared the continuous wave EPR spectra of the ^{15}N- and ^{14}N-substituted PSII samples. It has been suggested that the substructure on the multiline EPR signal is due to partially resolved superhyperfine interactions from nitrogen ligands. Substitution of ^{15}N for ^{14}N produced no detectable change in the positions of the substructure features on the multiline EPR signal. For the simple case of resolved splitting due to an isotropic hyperfine interaction from a single N nucleus, substitution of ^{15}N (I=1/2) for ^{14}N (I=1), where the nuclear moment ratio $g_n(^{15}N)/g_n(^{14}N)$ is 1.4, would collapse three peaks into two with the separation between the outermost peaks reduced by approximately 17%. With a modulation amplitude of 4 G, the narrowest features on the multiline signal which we could reliably resolve were positive peaks (in the first derivative) separated by approximately 10 G. Lowering the modulation amplitude to 2 G resolved no new features in the spectrum (data not shown). We thus estimate that the inability to detect consistent changes on the substructure of the multiline EPR signal upon substitution of ^{14}N with ^{15}N indicates the absence of nitrogen hyperfine coupling of magnitude $\geq$ 10 G. The substructure is most likely due to partially resolved Mn hyperfine interactions, as has been suggested from the results of previous experiments with spinach chloroplasts (Andréasson, 1989), and experiments at S-band (Haddy et al., 1989).

The dark-adapted samples of PSII from ^{14}N-grown *Synechococcus* show ESEEM at frequencies of 4 and 7 MHz. The predominant features in the continuous wave EPR spectrum of these dark-adapted samples are signals at g=3.0 and g=2.2 from oxidized cytochrome b_{559}. The ^{14}N ESEEM is very similar to that reported for porphyrin ^{14}N in low-spin Fe^{+3} complexes (Peisach et al., 1979), and is consistent with an assignment as hyperfine interactions from the porphyrin nitrogens in oxidized

cytochrome b_{559}. The Fourier transform of ESEEM in dark-adapted PSII samples from ^{15}N-grown *Synechococcus* is shown in Figure 6.4b. Modulation occurs at 1.3 MHz, which is the ^{15}N Zeeman frequency at 3200 G. A shoulder is present on this Fourier transform peak at ~2 MHz, and the higher frequency modulation is at 4.8 MHz. Since ESEEM occurs at frequencies $|\nu_I \pm A/2|$ for I=1/2 species, the frequencies in the dark-adapted samples from ^{15}N-grown *Synechococcus* are consistent with arising from a species with A_{iso} (for ^{15}N) of 7 MHz. This scales (by the ratio of the $^{14}N/^{15}N$ magnetic moments) to A_{iso} of 5 MHz for ^{14}N. This ^{15}N ESEEM could be due to hyperfine interactions from the porphyrin nitrogens, which were found to have an A_{iso} of 5 MHz for ^{14}N (Peisach et al., 1979). Alternatively, the ^{15}N ESEEM may arise from the postulated *bis*-imidazole coordination in cytochrome b_{559} (Babcock et al., 1985). ENDOR experiments on *bis*-imidazole Fe^{+3} porphyrin model complex have determined a hyperfine coupling of 5 MHz for the directly coordinating ^{14}N of the imidazoles (Scholes et al., 1986). We note, however, that the continuous wave EPR spectra of dark-adapted samples from *Synechococcus* also show a signal at g=6, which potentially arises from high-spin Fe^{+3} from damaged cytochrome b_{559} (Rutherford, 1985). Since this signal may have counterparts in the g=2 region, it is not possible to rule out contributions from damaged cytochrome to the ESEEM of the dark-adapted samples.

Summary

1. Weak hyperfine coupling to one or more ^{14}N nuclei has been detected on the multiline EPR signal.
2. Simulations indicate that a contact interaction must exist between the unpaired spin on the manganese and the nitrogen nucleus. This favors assignment of the nitrogen as a ligand from an amino acid, such as a histidine. It is not possible at this time to rule out an interaction with nitrogen which is hydrogen bonded to the Mn complex.
3. Continuous wave EPR detected no change in the substructure of the multiline EPR signal upon substitution of ^{14}N with ^{15}N. This indicates that no strong coupling ($a_{iso} \geq 10$ G) to nitrogen is present.
4. Modulation due to nitrogen present in dark-adapted preparations is consistent with assignment as either porphyrin or imidazole nitrogen from oxidized cytochrome b_{559}.

Chapter 7

Summary and Suggested Future Work

The goal of current research on the photosystem II oxygen evolving complex is to elucidate the mechanism of biological water oxidation. To deduce such a mechanism, structural information concerning the manganese in the complex is necessary on both a broad and detailed level. The following questions concerning the structure of the complex in its successive S-states must be answered:

1) What is the three-dimensional arrangement of the manganese atoms, and what are their oxidation states?

2) What are the identities of the manganese ligands, and what is the arrangement of the necessary cofactors of oxygen evolution?

Structure of the oxygen evolution complex

Recent information obtained from X-ray absorption spectroscopy has increased our ability to successfully address question (1). Past results from manganese K-edge EXAFS have established the presence of di-μ-oxo bridged structural units for the manganese in the oxygen evolving complex [Yachandra et al., 1987; McDermott et al., 1988; Penner-Hahn et al., 1990; Corrie et al., 1990]. Recent, low-temperature data collection [as described in Chapter 3; see also George et al., 1989; Penner-Hahn et al., 1990] has allowed observation of a longer Mn-Mn distance at 3.3 Å. These combined structural parameters support the model of two di-μ-oxo bridged binuclear manganese units joined by a mono-μ-oxo bridge. This model is supported by EXAFS data taken on preparations from both higher plants (spinach) and cyanobacteria (*Synechococcus* sp.). New data from oriented studies indicate that the 3.3 Å vector is aligned parallel to the membrane normal, whereas the 2.7 Å vectors show substantially less dichroism [George et al., 1989; I. Mukerji, unpublished results]. Taken together, this information provides a good working model for the three-dimensional structure of the oxygen evolving complex.

In addition, X-ray absorption edge spectroscopy provides information about the oxidation states of the manganese. The relatively high values of the K-edge inflection points of the manganese in the oxygen evolving complex poised in the S_1 and S_2 states indicate the presence of a combination of Mn(III) and Mn(IV) atoms [Yachandra et al., 1987]. The shape of the absorption edge, represented by the second

derivative of the spectrum, is fit well with a combination of $(III)_2(IV)_2$ oxidation states in the S_1 state, and $(III)(IV)_3$ oxidation states in the S_2 state (V.K. Yachandra, unpublished results). Thus, a good model of the oxygen evolution complex in the S_1 and S_2 states is a pair of di-μ-oxo bridged binuclear complexes linked by a mono-μ-oxo bridge, with oxidation states of $(III)_2(IV)_2$ in the S_1 state and $(III)(IV)_3$ in the S_2 state.

The recent success in using second derivatives to emphasize and fit the shape of the K-edge spectra of samples poised in the S_1 and S_2 states invites application of this method to the S_3 and S_0 states. The lack of change in the manganese K-edge spectrum between samples poised in the S_2 state and the S_3 state has been explained as oxidation of a species ("L") other than manganese at this S-state transition [Guiles et al., 1990a]. This obviates the need to invoke a Mn(V) species in the S_4 state, which could then have oxidation states $Mn(IV)_4L^+$. A concerted four-electron oxidation of two bound oxygen atoms to form molecular oxygen in the S_4 to S_0 transition would allow a combination of $Mn(II)Mn(III)Mn(IV)_2$ oxidation states for S_0, as favored by Guiles et al. (1990b). Additional evidence for this sequence of oxidation states could be gained through analysis of the Mn K-edge shape of samples poised in the S_3 state.

The "dimer of dimers" model described above is the simplest structure which incorporates the parameters derived from EXAFS spectroscopy for the numbers and distances of manganese scatterers in the oxygen evolving complex. The number of scatterers determined by EXAFS, however, is subject to relatively large error (~30%). The numbers of scatterers predicted for both the 2.7 Å (1.0-1.5 per manganese) and the 3.3 Å (0.5-1.0 per manganese) distances depend on a restricted range of disorder parameters taken from model compounds. It is important to note that other structures, such as the "asymmetric tetramer" described in Chapter 3 [Bashkin et al., 1987], also contain manganese scatterers at distances of both ~2.7 Å (1.5 per manganese) and ~3.3 Å (1.5 per manganese). Such a tetrameric model for the oxygen evolving complex could be valid if restrictions on the disorder parameter were lifted. The Debye Waller (disorder) parameter has contributions from both static and thermal effects which complicate the transferability of the parameter between known and unknown systems. A comparative temperature-dependent study of >3 Å scattering distances in model compounds and the oxygen evolving complex would supply additional information about the thermal parameters contributing to the disorder of scatterers at this distance. This information would allow a firmer assignment of the number of scatterers at >3 Å, and the ability to discriminate between the models discussed above.

Amino acid ligands

Attempts to chelate and extrude the oxygen evolving complex as an intact structure, as has been accomplished for example in iron sulfur centers and the molybdenum-iron cofactor in nitrogenase, have not yet been successful. Clearly the protein environment plays an irreplaceable (to date) role in stabilizing the manganese complex. Aside from structural stability, as discussed above a role for an amino acid as a redox-active ligand has been invoked in the S_2 to S_3 state transition [Guiles et al., 1990; Boussac et al., 1990]. Evidence for a nitrogen species close to the manganese of the oxygen evolving complex, described in Chapter 6, supports the assignment of this species as a histidine. Other than this interaction no evidence has been found for nitrogen ligation to the manganese [i.e. Andréasson, 1989, and see Chapter 6], strengthening the view that carboxyl groups make up most of the ligands [Pecoraro, 1988].

Cofactor arrangement

There is evidence for a specific, reversible interaction of halide with the oxygen evolving complex [see Chapters 4 and 5]. A role has been advanced for a halide ligand in the mechanism of oxygen evolution. This role is to protect a site on the manganese against water binding and subsequent premature oxidation in the lower S states [Wydrzynski & Sauer, 1980; Christou & Vincent, 1987; Rutherford, 1989]. Gaining evidence to verify or discount this action of halide is essential to understanding the full mechanism of water oxidation. Physical evidence for such a ligand, however, is still lacking. The negative results of experiments designed to find evidence for halide binding are often inconclusive, due to the complexity of studying a single ligand amidst a potential twenty-four manganese ligands in the complex. In Chapter 4, EPR signals are found to be affected by the presence of fluoride. In particular, the shape of the g=4 EPR signal arising from the S_2-state of the oxygen evolving complex is found to narrow in the presence of fluoride. This result is positive evidence for, but not proof of, halide binding to the manganese. In Chapter 5, the similarity of EPR and EXAFS data from bromide- and chloride-replaced samples strongly strongly against a bridging halide interaction. Again, however, the complexity of the system does not allow the similarity between the samples to be proof against a *single* terminal halide ligand. Further experiments (described below) are required for more definitive information.

An equally important role for calcium, another cofactor essential for oxygen evolution, has been proposed. Both calcium depletion of photosystem II preparations, and their repletion with strontium, have drastic effects on the EPR signals from the oxygen evolving complex [Boussac & Rutherford, 1989; Sivaraja & Dismukes, 1989]. This has led to the proposal that calcium provides a water binding site in close proximity to the manganese [Rutherford, 1989]. Further, it is suggested that the calcium provides an alternative to manganese as a binding site for chloride, for example when water replaces chloride as a ligand to the manganese [Rutherford, 1989]. EXAFS experiments on calcium-depleted and strontium-reconstituted photosystem II preparations are in progress [M.J. Latimer, unpublished results] and their results may give evidence for the proximity of calcium to the manganese in the oxygen evolving complex.

Mechanisms for water oxidation

At this time two models have been put forward which contain explicit proposals regarding the structural basis of water oxidation in the oxygen evolving complex. Both models describe water binding to form a bridging ligand in a tetrameric manganese complex, followed by formation of a peroxo bridge and the release of molecular oxygen. These models predict intermediate structures of the manganese complex which can be compared with the predictions obtained from EXAFS spectroscopy.

Brudvig and Crabtree (1986) hypothesize a cubane-like tetrameric manganese cluster with μ_3-oxo bridges for the oxygen evolving complex in the S_1 and S_2 states. In this hypothesis, two molecules of water are added (as O^{2-} or OH^-) during the S_2 to S_3 state transition to form a μ_2-oxo bridged adamantane-like structure. Further oxidation of the complex to S_4 results in the oxidation of two of the oxo bridges which then form a peroxo group. Oxygen is released upon nucleophilic displacement of the peroxo group by the remaining oxo bridges, regenerating the cubane-like complex. Although the authors suggest that a transition from a cubane-like to an adamantane-like structure need not result in the movement of the manganese atoms, model compounds with adamantane structures contain manganese-manganese distances of >3 Å exclusively [Wieghardt et al., 1983; Hagen et al., 1989]. The available evidence from EXAFS does not allow a regular cubane structure for the S_1 and S_2 states [Yachandra et al., 1987; McDermott et al., 1988; Penner-Hahn et al., 1990] although as discussed above a highly distorted tetramer is more difficult to rule out. No evidence for an

adamantane-like structure in the S_3 state, however, has been found by EXAFS [Guiles et al., 1990]. This makes the model proposed by Brudvig and Crabtree unlikely.

A second model has been proposed by Christou and Vincent (1987). The authors suggest a "butterfly" arrangement of manganese in the S_1 state, based on their successful syntheses of several tetrameric "butterfly" compounds in various oxidation states. These models consist of a pair of Mn atoms separated by ~2.7 Å (the "body") and a pair of manganese ~3.3 Å from them (the "wings"). Two μ_3-oxo bridges connect the body to the wings. The authors suggest that the addition of two water molecules to the "wingtip" manganese atoms takes place in the S_1 to S_2 transition, and that deprotonation of the water molecules and a slight rearrangement of the manganese atoms result in the water molecules becoming new μ_3-hydroxo bridges in the tetrameric complex. Further deprotonation of the hydroxo bridges and subsequent bond formation between them results in the release of O_2 and regeneration of the "butterfly" compound. Unfortunately, the "butterfly" compound contains only one Mn-Mn distance of 2.7 Å. Formation of an additional μ_3-oxo or hydroxo bridge would invoke an increase in the number of scatterers at ~2.7 Å. The EXAFS data of the oxygen evolving complex in the S_1, S_2, and S_3 states all require at least two such distances, and show no increase in the 2.7 Å coordination number upon changing the S-state. This mechanism of water binding and oxidation, therefore, is not supported by the EXAFS data.

The dimer-of-dimers model discussed above allows for a mechanism of water oxidation which is consistent with the observed structure, as derived from EXAFS, of the manganese in the S_1, S_2, and S_3 states. A scheme for water oxidation and oxygen formation in a di-μ-oxo bridged manganese complex is reproduced in Figure 7.1. In the general mechanism, water molecules are bound as terminal ligands to the two manganese, and are deprotonated in two oxidation steps. Two further oxidation steps allow formation of a peroxodimanganese complex, which then releases oxygen and binds two new water molecules. In applying this mechanism to the the oxygen evolving complex it can be envisioned that intermediate (2) in Figure 7.1 corresponds to the S_2 state. Advances to S_3 and S_4 store two more oxidizing equivalents which are then reduced by peroxo formation in S_4 (intermediate (3) in Figure 7.1). Following the transfer of two more reducing equivalents to the complex, oxygen is released and the complex is returned to S_0 (intermediate (1)). It is not necessary that two water molecules be bound at the S_0 state; for example, chloride could bind at S_0 and be replaced by hydroxide in a higher S-state. The intermediates predicted by this

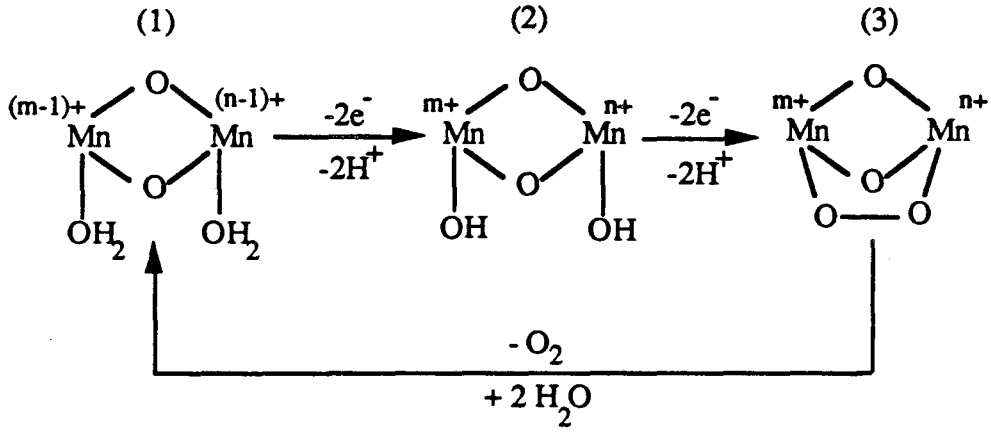

Figure 7.1. Mechanism for water oxidation in a di-μ-oxo bridged manganese complex. Adapted from Wieghardt (1989). The oxidation states of the manganese are depicted as m and n. See text for details. As described in the text, intermediate (1) could correspond to the S_0 state of the oxygen evolving complex, intermediate (2) would be the S_2 state, and intermediate (3) represents the S_4 state.

mechanism agree with the current results from X-ray absorption experiments. Importantly, the 2.7 Å Mn-Mn distance would not change significantly until formation of the peroxo bridge in the S_4 state. The recently described structure of a binuclear μ-peroxo bridged complex ([1,4,7-trimethyl-1,4,7-triazocyclononane]$_2$Mn(IV)$_2$(μ-O)$_2$(μ-O$_2$)](ClO$_4$)$_2$) (Bossek et al., 1990) shows a Mn-Mn distance of 2.5 Å. Alternatively, water oxidation could occur between the two dimers. A peroxo bridge between mono-μ-oxo bridged manganese would be expected to shorten the Mn-Mn distance from 3.3 Å to 3.1 Å (Bhula et al., 1988). Consistent with the addition of water molecules as terminal ligands, the terminal ligand shell as determined by EXAFS does show slight variation as the complex advances from S_1 to S_2 (Chapter 3), and from S_2 to S_3 [Guiles et al., 1990].

The above mechanism for water oxidation is quite attractive in terms of simplicity and agreement with current results from EXAFS spectroscopy. In pursuing proof of this or any mechanism, two missing pieces of information present a challenge for future experimenters. First, as described above, a peroxo intermediate is expected to force a change in Mn-Mn distances in the complex. The challenge is to trap this intermediate, possibly through experiments in which the preparation is advanced by laser flashes and immediately quenched. The EXAFS spectrum of the intermediate would be sensitive to a change either in the 2.7 Å Mn-Mn distance, indicating bond formation between two manganese atoms in a binuclear complex, or in the 3.3 Å distance, indicating bond formation between the binuclear clusters.

The second and potentially more difficult challenge is to determine at what step, and in what form, water binds to the manganese. Magnetic resonance experiments are suited to this experiment. The ubiquitous nature of water, however, while advantageous for photosynthetic organisms, makes it difficult to observe a specifically bound water molecule. High-resolution EPR measurements of the multiline signal generated in the presence of $H_2{}^{17}O$ has shown broadening of the hyperfine lines due to the ^{17}O (I=5/2) nucleus [Hansson et al., 1986], as expected if the oxygen is ligated to the manganese. It is not possible to rule out ^{17}O exchange of an oxo bridge, however. Similarly, while ESEEM measurements of ^2H_2O-labelled photosystem II preparations show some exchangeable "inner sphere" protons [Britt et al., 1990b], it is difficult to uniquely identify these as being due to bound water or hydroxide.

In theory, an ESEEM investigation using ^{17}O could give detailed information about the form of bound water. The ^{17}O quadrupole coupling parameters are expected to be sensitive to the electronic environment, but the analysis would be more

complicated than, for example, analysis of an ^{14}N interaction [[Mims & Peisach, 1989]. One experiment that may be successful would be to first measure the ESEEM of a di-μ-oxo bridged manganese complex in which the bridges have been purposefully exchanged with ^{17}O. The ESEEM from the ^{17}O oxo bridge would provide background information for further investigations. Water binding in the S_1 state could then be investigated by dilution into $H_2{}^{17}O$ buffer followed by fast freezing, for example, and higher S-states could be trapped using laser flashes, as discussed above. Preliminary results from this sort of experiment have revealed a great deal of modulation due to the ^{17}O nucleus [R. D. Britt, unpublished results].

Future Work

The first part of this section discusses experiments designed to further address the question of halide ligation to the manganese of the oxygen evolving complex. The other two parts outline some experiments to further address the origin and significance of the EPR signals present in dark-adapted preparations which were described in Chapters 4 and 5.

Halide ligation to the manganese

The results of the experiments described in Chapters 4 and 5, which show specific effects of halide on the EPR as well as oxygen evolution activity, emphasize the proximity of the halide binding site and the manganese of the oxygen evolving complex. None of the experiments described in this thesis, however, prove that halide is ligated to manganese in the oxygen evolving complex. The best physical evidence for halide ligation is the narrowing effect that fluoride has on the g=4 EPR signal from the S_2 state. In the experiments described in Chapter 4 it is shown that this narrowing, and the loss of multiline signal, are directly due to the addition of fluoride. The EXAFS experiments described in Chapter 5 show very little difference between the EXAFS of bromide- and chloride-substituted photosystem II preparations. It is argued that this is evidence against a bridging halide ligand, but it is shown that a single terminal halide ligand may not be detected in such experiments.

More sensitive types of experiments will be necessary to detect a single halide ligand in the oxygen evolving complex. Electron spin echo envelope modulation (ESEEM) is one method of detecting small changes in the environment of the manganese. Table 7.1 lists some relevant nuclei, their nuclear moments, nuclear

Table 7.1

Magnetic resonance parameters for selected nuclei

Isotope	Natural abundance (%)	I	g_n	ν_n(MHz) (at 3300 G)	Q (10^{-24} cm^2)
^{55}Mn	100	5/2	1.38	3.5	0.55
^{1}H	100	1/2	5.58	14.1	--
^{2}D	.015	1	.857	2.1	.0027
^{14}N	99.6	1	.403	1.0	.016
^{15}N	.37	1/2	-.566	1.4	--
^{16}O	100	0			
^{17}O	.037	5/2	-.756	1.9	-.026
^{35}Cl	75.5	3/2	.547	1.4	-.079
^{37}Cl	24.5	3/2	.455	1.1	-.062
^{79}Br	50.5	3/2	1.40	3.5	0.33
^{81}Br	45.5	3/2	1.51	3.8	0.28
^{19}F	100	1/2	5.26	13.2	--
^{40}Ca	100	0			
^{88}Sr	93.0	0			
^{87}Sr	7.0	9/2	-0.242	0.6	0.2
^{23}Na	100	3/2	1.48	3.7	0.14
^{39}K	93.1	3/2	0.261	0.7	0.11

quadrupole moments, and their Zeeman frequencies at 3300 G. The use of ESEEM in determining hyperfine coupling from chloride or bromide is complicated by the nuclear spin I=3/2 and the expected large quadrupolar moments [Köhler et al., 1990]. Although ESEEM of the multiline signal from the oxygen evolving complex has shown no resonances that could be attributed to halide nuclei, such resonances could be broadened beyond detection. ^{19}F, however, might be an ideal candidate for such experiments as it is I=1/2 with no quadrupole moment and a relatively large nuclear magnetic moment. The effects of fluoride on oxygen evolution and the EPR of the oxygen evolving complex are clearly defined. The g=4 EPR signal formed in the presence of fluoride or chloride is easily saturated at 8 K, and in the presence of fluoride the signal is formed in high yield, independent of cryoprotectant. There is a background signal at g=4.3, due to nonspecifically bound Fe^{+3} in a rhombic environment, which is typically 50% of the amplitude of light-induced g=4 signal. The amplitude of this background signal might be reduced by washing or incubating the PSII preparations in a Fe chelator such as Tiron (4,5-dihydroxy-1,3-benzene disulfonic acid). The identification of ESEEM due to ^{19}F would be a clear indication that halide is bound to the manganese.

Manganese EXAFS experiments on the oxygen evolving complex are greatly complicated by the averaging of information due to all four manganese. For this reason, the reverse experiment of performing halide EXAFS spectroscopy on the appropriate samples might provide more specific information about the proximity of manganese and halide in the oxygen evolving complex. Both bromide and chloride x-ray absorption experiments are feasible, and they would give complementary information. Bromine, with a K-edge absorption energy of 13.5 keV, has a very high fluorescence yield which will increase the sensitivity of the experiment. Data could be collected to high values of *k*, as there would be no atoms with higher atomic number in the sample. Bromine EXAFS should be able to detect a Mn scatterer at 2.4 - 3 Å distance. Chloride, on the other hand, absorbs at much lower energies (the chlorine K absorption energy is 2.6 keV). X-rays of this energy are attenuated by air, but chlorine x-ray absorption experiments in a helium atmosphere have been shown to be quite feasible [Hedman et al., 1988]. The reduced intrinsic linewidth at the lower energies gives much greater energy resolution (~0.1 eV, compared with ~1 eV at the manganese K edge). Preliminary work (Figure 7.2) has shown that the features of the chlorine K-edge spectrum in high valent manganese complexes are very sensitive to the oxidation state of the manganese. Despite the fact that the data shown in Figure 7.2

Figure 7.2 Chlorine X-ray K-edge absorption spectra of two manganese-chloride model compounds. (a) Mn(III)Cl(salen): N,N'-ethylenebis(salicylideneiminato)Mn(III)chloride (Pecoraro & Butler, 1986). A distinct pre-edge feature at 2821.7 eV, which is separated from the main edge feature by ~7 eV, is seen on this and other Mn(III) compounds (data not shown). (b) $Mn(II)Cl_2(mim)_2$: dichlorotris-(2-methylimidazole) Mn(II) (Phillips et al., 1976). This and other Mn(II) compounds do not show a separated pre-edge feature. Fluorescence data were collected on powder samples at room temperature from beamline VI-2 at SSRL.

Figure 7.2

Chlorine K-edge spectra of manganese model compounds

a. Mn(III)Cl (salen)

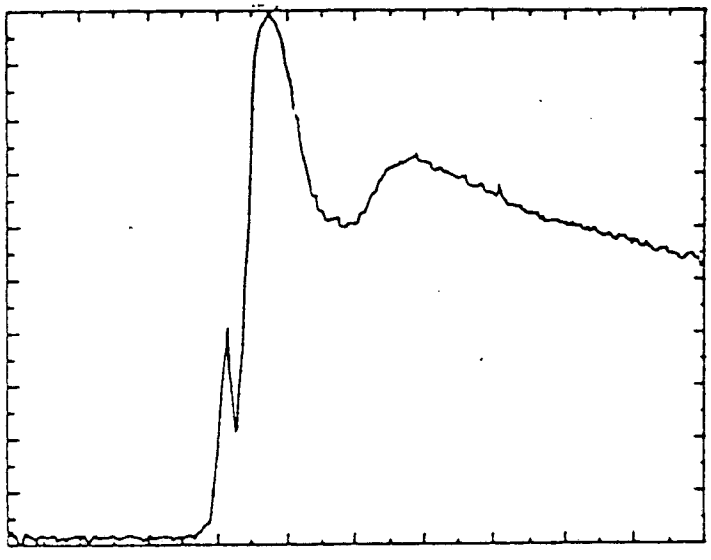

2765. X-ray energy (eV) 2880.

b. $Mn(II)Cl_2(mim)_2$

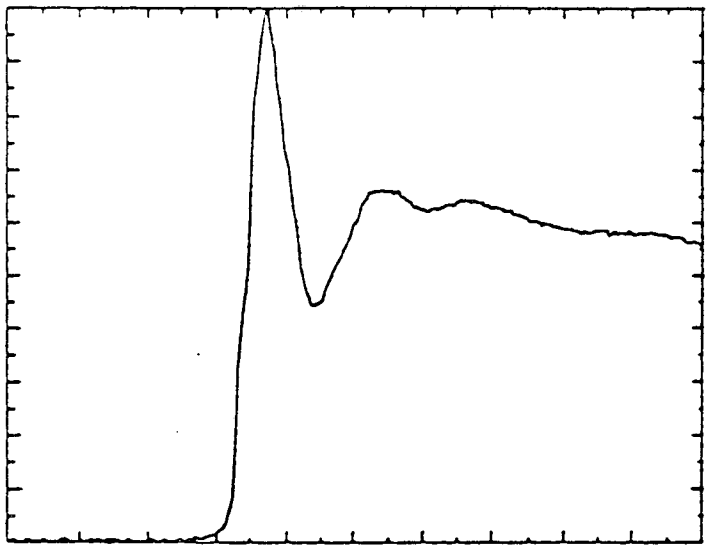

2765. X-ray energy (eV) 2880.

were taken with minimal effort to optimize the resolution of the spectra, a well-resolved pre-edge transition is observed in the Mn(III) complex. The amplitude of this transition is at least twice that of the corresponding pre-edge transition in the Mn K-edge absorption spectrum (data not shown). It is expected that the chloride edge spectrum in the oxygen evolving complex would be quite sensitive, for example, to whether chloride was bound to Mn(III) or Mn(IV).

The "reverse" EXAFS experiments require the preparation of a sample which contains, optimally, one functional halide bound per PSII. There are many indications that the functional halide is tightly bound in photosystem II preparations [Homann, 1985; Lindberg et al., 1990; Sachar-Hill et al., 1990]. Recently, Lindberg et al. (1990) have measured the release of ^{36}Cl in PSII preparations isolated from spinach grown in ^{36}Cl media. They found that 50% of the ^{36}Cl was released from PSII preparations over a two-hour period during which the preparations were incubated in 5 mM NaCl and stirred, in the light, at 0°C. In contrast, wash steps in which samples were resuspended in the dark and then centrifuged resulted in no measurable loss of ^{36}Cl from the membranes. Lindberg et al. conclude that, at pH 6, chloride in PSII exchanges very slowly with anions in the medium. This slow exchange at pH 6 is in agreement with the results of several other experiments [Homann, 1985; Wydrzynski et al., 1990; Sacher-Hill, 1990] and indicates that PSII samples may be prepared in which nonspecific halide has been washed away. Samples for chloride XAS could be made with one or two washes in bromide-containing medium. Samples for bromide EXAFS could be made from PSII preparations from *Synechococcus,* grown and isolated in bromide, after one or two washes in or dialysis against a chloride-containing medium. Atomic absorption spectroscopy could be used to monitor the bromide content per photosystem II as a function of wash number, for example, or as a function of dialysis time.

An alternative experiment which may give positive results concerning halide ligation is to use oriented, bromide-replaced samples to look for effects on the Mn K-edge EXAFS spectra. The use of an oriented preparation provides a partial selection against some of the potential twenty-four manganese ligands, therefore improving the sensitivity of the experiment to the exchange of a single halide ligand. Further motivation for this experiment comes from the observation that the small, isolated peak *between* Fourier transform peaks I and II, referred to in chapters 4 and 5 as a possible indication of a chloride ligand, is resolved in oriented S_1 control samples only when the incoming *e*-vector is parallel to the membrane normal [I. Mukerji, unpublished results].

It would be interesting to see the effect of bromide replacement on the EXAFS spectra of samples in this orientation.

The broad g=2 EPR signal from fluoride-inhibited PSII preparations

In the experiments described in Chapter 4 it was found that a broad g=2 EPR signal could be induced in dark-adapted PSII preparations which had been treated with a high concentration of fluoride. The EPR signal is very similar to the signal proposed to arise from the S_3 state of the oxygen evolving complex in the absence of calcium. It is proposed in Chapter 4 that high levels of fluoride replace the ligands to calcium, creating a calcium-depleted preparation. The implication is that the broad g=2 EPR signal in fluoride-treated preparations and the "S_3-state" signal in calcium-depleted preparations arise from the same species. Since this species may be a manifestation of a real S-state intermediate, it is important to determine its properties.

A key question is whether the broad g=2 and the light-induced g=4 signals can occur in the same PSII center. The amplitudes of the respective signals, as shown in Figures 4.2 and 4.4, are both very high in a preparation which has been treated with 100 mM NaF. Accurate quantitation of both signals along with the EPR signal due to the FeQ_a^- center in the illuminated samples is necessary, however. Additionally, if indeed the broad g=2 EPR signal is formed in centers from which calcium has been released, the addition of calcium to the medium (in the form of $Ca(OH)_2$) should attenuate the amplitude of the signal. Finally, the question of whether the ambient potential is able to oxidize the species giving rise to the broad signal in dark-adapted preparations could be addressed by investigating the effect of redox mediators such as ascorbic acid or ferrocyanide on the amplitude of the signal.

The dark "multiline" signal from bromide-grown Synechococcus preparations

This EPR signal has a distinctly enhanced amplitude in preparations from bromide-grown *Synechococcus*. Centers that show this signal do not show a g=2 multiline signal with low temperature illumination. The new signal arises from either (1) PSII centers in the S_1 state which do not advance at low temperature; (2) centers in S-states other than S_1; (3) manganese centers which have been somehow uncoupled from the reaction center. It is not obvious how bromide would increase any of these effects. The composition of cryoprotectant, however, is critical in observing some of the low temperature EPR signals in *Synechococcus*. For example, only very low levels of the S_2-state multiline signal are formed by low temperature illumination in the

presence of sucrose. While bromide supports high levels of oxygen evolution activity at 24°C, the larger size of the bromide ion might influence the microstructure of some manganese centers when the sample is brought to cryogenic temperatures.

An exciting possibility is that the new EPR signal is due to centers in the S_0 or S_3 state. Poising PSII preparations from *Synechococcus* in these S-states, as has been accomplished for spinach preparations, might help answer the question. Procedures have not yet been developed to poise PSII preparations from *Synechococcus* into the S_0 and S_3 states. The threshold temperature for maximum formation of the multiline signal by illumination at low temperatures is increased in preparations from *Synechococcus*by ~20 K over the threshold temperature in spinach preparations. Other temperature thresholds, such as for the advance from S_0 to S_1, may also be different in the cyanobacteria.

Such procedures would be fruitful not only to help identify this signal, but to take advantage of the ability of isotopic labelling in cyanobacteria. For example, it has been proposed that the aforementioned broad g=2 signal from calcium-depleted spinach preparations arises from a histidine species which is oxidized instead of manganese upon advance to S_3 [Boussac et al., 1990]. This signal has not yet been seen in *Synechococcus*. If the EPR signal is due to histidine, its linewidth should be influenced by ^{15}N. If the signal is due to another organic radical, its linewidth might be narrowed in samples from bacteria grown in D_2O, but not by ^{15}N. These type of experiments would help identify the species that gives rise to this "S_3"-state EPR signal.

References

Aasa, R., Andréasson, L.-E., Lagenfelt, G. & Vänngard, T. (1987) *FEBS Lett. 221*, 245-248.

Andréasson, L.-E. (1989) *Biochim. Biophys. Acta 973*, 465-467.

Arnon, D.I. (1949) *Plant Physiol. 24*, 1-15.

Astashkin, A. V., Dikanov, S. A. & Tsvetkov, Y. D. (1984) *J. Struct. Chem. 25*, 45-55.

Auger, N., Girerd, J.-J., Corbella, M., Gleizes, A. & Zimmermann, J.-L. (1990) *J. Am. Chem. Soc.* (submitted).

Babcock, G. T. (1987) in *New Comprehensive Biochemistry: Photosynthesis 15,* (Amesz, J., Ed.) pp. 125-158, Elsevier, Amsterdam.

Babcock, G. T., Widger, W. R., Cramer, W. A., Oertling, W. A. & Metz, J. G. (1985) *Biochemistry 24*, 3638-3645.

Barber, J. (1987) *Trends Biochem. Sci. 12*, 321-326.

Barry, B.A., & Babcock, G. (1987) *Proc. Natl. Acad. Sci. USA 84*, 7099-7103.

Bashkin, J.S., Chang, H.-R., Streib, W.E., Huffman, J.C., Hendrickson, D.N. & Christou, G. (1987) *J. Am. Chem. Soc. 109*, 6502.

Beck, W. F., de Paula, J. C. & Brudvig, G. W. (1986) *J. Am. Chem. Soc. 108*, 4018-4022.

Beck, W.F. & Brudvig, G.W. (1986) *Biochemistry 25*, 6479-6486.

Beck, W.F. & Brudvig, G.W. (1988) *J. Am. Chem. Soc. 110*, 1517-1523.

Berthold, D.A., Babcock, G.T. & Yocum, C.F. (1981) *FEBS Lett. 134*, 231-234.

Bhula, R., Gainsford, G.J. & Weatherburn, D.C. (1988) *J. Am. Chem. Soc. 110*, 7550-7552.

Blankenship, R.E. & Prince, R.C. (1985) *Trends Biol. Sci. 10*, 383-383.

Blumberg, W.E. & Peisach, J. (1973) *Ann. New York Acad. Sci. 222*, 539-560.

Bossek, U., Weyhermüller, T., Wieghardt, K., Nuber, B. & Weiss, J. (1990) *J. Am. Chem. Soc. 112*, 6387-6388.

Boussac, A. & Rutherford, A.W. (1988) *Biochemistry 27*, 3476-3483.

Boussac, A., Zimmermann, J.-L. & Rutherford, A.W. (1989) *Biochem. 28*, 8984-8989.

Boussac, A., Zimmermann, J.-L., Rutherford, A.W. & Lavergne, J. (1990) *Nature*, (in press).

Britt, R D. & Klein, M. P. (1987) *J. Mag. Res. 74*, 535-540.

Britt, R.D. (1988) *Ph.D. Thesis, Lawrence Berkeley Laboratory, University of California* LBL 25042.

Britt, R.D., Zimmermann, J.-L., Sauer, K. & Klein, M. P. (1989) *J. Amer. Chem. Soc. 111*, 3522-3532.

Britt, R D., DeRose, V.J., Chan, M., Armstrong, W.H., Sauer, K. & Klein, M.P. (1990a) *J. Amer. Chem. Soc.* (submitted).

Britt, R.D., DeRose, V.J., Yachandra, V.K., Kim, D H., Sauer, K. & Klein, M.P. (1990b) in *Current Research in Photosynthesis* (M. Baltscheffsky, Ed.) I.3.769, Kluwer Academic Publishers, The Netherlands.

Brock, T.D. (1973) in *Biology of Blue-Green Algae* (Carr, N.G. & Whitton, B.A., Eds.) University of California Press, Berkeley, 487-500.

Brudvig, G.W. (1989) *Advanced EPR, Applications in Biology and Biochemistry;* (Hoff, A.J., Ed.) Elsevier, Amsterdam, 839-865.

Brudvig, G.W. & Crabtree, R.H. (1986) *Proc. Natl. Acad. Sci. USA 83*, 4586-4588.

Bryant, D. (1986) in *Photosynthetic Picoplankton* (Platt, T. & Li, W.K.W., Eds.) Canadian Bulletin of Fisheries and Aquatic Sciences 214, 423-500.

Butler, W.F., Calvo, R. Fredkin, D.R., Isaacson, R.A., Okamura, M.Y. & Feher, G. (1984) *Biophys. J. 45*, 947-973.

Carrington, A., & McLachlan, A.D. (1967) *Introduction to Magnetic Resonance* Harper & Row, New York.

Casey, J.L. & Sauer, K. (1984) *Biochim. Biophys. Acta 767*, 21-28.

Castner, T.G. (1959) *Phys. Rev. 115*, 1506-1515.

Chang, H.-R., Larsen, S.K., Boyd, P.D.W., Pierpont, C.G. & Hendrickson, D.N. (1988) *J. Am. Chem. Soc. 110*, 4565-4576.

Cheniae, G.M. & Martin, I.F. (1970) *Biochim. Biophys. Acta 197*, 219-239.

Christou, G. & Vincent, J.B. (1987) *Biochim. Biophys. Acta 895*, 259-274.

Christou, G. & Vincent, J.B. (1988) *Metal Clusters in Proteins* (Quet, L., Ed.).

Cole, J.C. (1988) *PhD Dissertation,* University of California-Berkeley, CA-Lawrence Berkeley Laboratory Report LBL-24123.

Cole, J.C., Yachandra, V.K., Guiles, R.D., McDermott, A.E., Britt, R.D., Dexheimer, S.L., Sauer, K. & Klein, M.P. (1987) *Biochim. Biophys. Acta 890*, 395-398.

Coleman, W.J. & Govindjee (1988) *Photos. Res.* 199-223.

Cooper, S.R. & Calvin, M. (1977) *J. Am. Chem. Soc. 99*, 6623-6630.

Cooper, S.R., Dismukes, G.c., Klein, M.P. & Calvin, M.C. (1978) *J. Am. Chem. Soc. 100*, 7248-7252.

Corrie, A.R., Evans, M.C.W, Hubbard, J.A.M., Strange, R.W. & Hasnain, S.S. 1990) in *Current Research in Photosynthesis Vol. I*, (Baltscheffsky, M., Ed.) Kluwer Academic Publishers, the Netherlands, 793-796.

Cramer, S.P. & Scott, R.A. (1981) *Rev. Sci. Instrum. 52*, 395-399.

Critchley, C. (1985) *Biochim. Biophys. Acta 811*, 33-46.

dePaula, J. C., Innes, J. B. & Brudvig, G. W. (1985) *Biochemistry 24*, 8114-8120.

DeGroot, A., Evelo, R. & Hoff, A. J. (1986) *J. Mag. Res. 66*, 331-343.

Dewar, M.A. & Barber, J. (1974) *Planta 117*, 163-172.

Dexheimer, S. L. & Klein, M. P. (1988) *Rev. Sci. Instrum. 59*, 764-766.

Dexheimer, S.L., Sauer, K. & Klein, M.P. (1990) in *Current Research in Photosynthesis* (Baltscheffsky, W., Ed.) Kluwer Academic Publishers, The Netherlands.

Diril, H., Chang, H.-R., Nilges, M.J., Zhang, X., Potenza, J.A., Schugar, H.J., Isied, S.S. & Hendrickson, D.N. (1989) *J. Am. Chem. Soc. 111*, 5102-5114.

Dismukes, G. C. & Siderer, Y. (1981) *Proc. Natl. Acad. Sci. USA 78*, 274-278.

Dixon, M. & Webb, E.C. (1979) *Enzymes* ,Longman Grp. Ltd., London.

Dyer, D.L. & Gafford, R.D. (1961) *Science 134*, 616-617.

Edmonds, D. T., (1976) *Phys. Rep. 29*, 233-290.

Fahrenbruch, A.L. & Bube, R.H. (1983) *Fundamentals of Solar Cells: Photovoltaic Solar Energy Conversion* Academic Press, New York.

Fee, J.A., Kuila, D., Mather, M.W., Yoshida, T. (1986) *Biochim. Biophys. Acta 853*, 153-185.

Flanagan, H. L. & Singel, D. J. (1987) *J. Chem. Phys. 87*, 5606-5616.

Joliot, P., Barbieri, G. & Chabaud, R. (1969) *Photochem. Photobiol. 10*, 309-329.

George, G.N., Prince, R.C. & Cramer, S.P. (1988) *Science 243*, 789-791.

Ghanotakis, D.F., Babcock, G.T. & Yocum, C.F. (1984) *FEBS Lett. 167*, 127-130.

Gherlach, T.M. & Graeber, S.J. (1985) *Nature 313*, 273-277.

Gingrich, J. C., Buzby, J. S., Stirewalt, V. L. & Bryant, D. A. (1988) *Photo. Res. 16*, 83-99.

Gingrich, J. C., Gasparich, G. E., Sauer, K. & Bryant, D. A. (1990) *Photo. Res. 24*, 137-150.

Gmür, N.F,, Thomlinson, W. & White-DePace, S.M. (1989) *User's Manual: Guide to the VUV and X-ray Beamlines* (3rd Ed.) National Synchrotron Light Source-Brookhaven National Laboratory Report BNL-42276.

Goodin, D. (1983) *Ph.D. Dissertation,* University of California-Berkeley, CA Lawrence Berkeley Laboratory Report LBL-16901.

Goodin, DB., Yachandra, V.K., Britt, R.D., Sauer, K. & Klein, M.P. (1984) *Biochim. Biophys. Acta 767*, 209-216.

Goodson, P.A. & Hodgson, D.J. (1989) *Inorg. Chem. 28*, 3606-3608.

Goodson, P., Glerup, J., Hodgson, K.J., Michelsen, K. & Pedersen, E. (1990) *Inorg. Chem. 29*, 503-508.

Gorter, S., van Ingen Schenau, A.D. & Verschoor, G.C. (1974) *Acta Cryst.* 1867-1871.

Guiles, R.D. (1988) *Ph.D. Dissertation*, University of California, Berkeley, CA Lawrence Berkeley Laboratory Report LBL-25186

Guiles, R.D., Yachandra, V.K., McDermott, A.E., Cole, J L., Dexheimer, S.L., Britt, R.D., Sauer, K. & Klein, M.P. (1990a) *Biochemistry, 29,* 486-495.

Guiles, R D., Zimmermann, J.-L., McDermott, A.E., Yachandra, V.K., Cole, J.L., Dexheimer, S.L., Britt, R.D., Wieghardt, K., Bossek, U., Sauer, K. & Klein, M.P. (1990b) *Biochemistry 29*, 471-485 .

Haddy, A., Aasa, R. & Andréasson, L.-E. (1989) *Biochemistry 28*, 6954-6959.

Hagen, K.S., Westmoreland, T.D., Scott, M.J. & Armstrong, W.H. (1989) *J. Am. Chem. Soc. 111*, 1907-1909.

Hansson, Ö. & Andréasson, L.-E. (1982) *Biochim. Biophys. Acta 679*, 261-268.

Hansson, Ö., Andréasson, L.-E. & Vänngard, T. (1986) *FEBS Lett. 195*, 151-154.

Hansson, Ö, Aasa, R., Vänngård, T. (1987) *Biophys. J. 51*, 825-832.

Harris, D.C. (1982) *Quantitative Chemical Analysis*, W.H. Freeman and Co., U.S., pp. 53-58.

Harvey, D.M.R., Hall, J.L., Flowers, T.J. & Kent, B. (1981) *Planta 151*, 555-560.

Hedman, B., Frank, P., Penner-Hahn, J.E., Roe, A.L., Hodgson, K.O., Carlson, R.M.K., Brown, G., Cerino, J., Hettel, R., Troxel, T., Winick, H. & Yang, J.(1986) *Nuclear Instruments and Methods in Physics Research A246*, 797-800.

Hedman, B., Frank, P., Gheller, S.F., Roe, A.L., Newton, W.E. & Hodgson, K.O. (1988) *J. Am. Chem. Soc. 110*, 3789-3805.

Hempel, J.C., Morgan, L.O. & Lewis, W.B. (1970) *Inorganic Chem. 9*, 2064-2072.

Homann, P. (1984) *Biochim. Biophys. Acta 764*, 247-252.

Homann, P. (1985) *Biochim. Biophys. Acta 809*, 311-319.

Homann, P. (1988a) *Biochim. Biophys. Acta 934*, 1-13.

Homann, P. (1988b) *Plant Physiol. 88*, 194-199.

Kelley, P.M. & Izawa, S. (1978) *Biochim. Biophys. Acta 502*, 198-210.

Kuwabara, T., Reddy, K.J. & Sherman, L.A. (1987) *Proc. Natl. Acad. Sci. 84*, 8230-8234.

Huber, R. (1989) *Agnew. Chem. Int. Ed. Engl. 18*, 848-869.

Ikeda-Saito, M. & Prince, R.C. (1985) *J. Biol. Chem. 260*, 8301-8305.

Johnson, F.S. (1970) in *Global Effects of Environmental Pollution* (Singer, S.F., Ed.) Springer-Verlag, New York, 4-11.

Kim, D.H., Britt, R.D., Klein, M.P., Sauer, K. (1990) *J. Amer. Chem. Soc. Comm.* (submitted).

Kim, K.-J. (1986) in *Center for X-ray Optics X-ray Data Booklet* (Vaughan, D., Ed.) Lawrence Berkeley Laboratory-University of California, Berkeley PUB-490.

Kip, A.F., Kittel, C., Levy, R.A. & Portis, A.M. (1953) *Phys. Rev. 91*, 1066-1071.

Kipke, C.A., Scott, M.J., Gohdes, J.W. & Armstrong, W.H. (1990) *Inorg. Chem. 29*, 2193-2194.

Köhler, K., Kirmse, R., Böttcher, R., Abram, U., Gribnau, M.C.M., Keijzers, C.P. & De Boer, E. (1990) *Chemical Physics 143*, 83-95.

Kok, B., Forbush, B., and McGloin, M. (1970) *Photochem. Photobiol. 11*, 457-476.

Kosman, D. J. (1984) in *Structural and Resonance Techniques in Biological Research* (Rousseau, D. J., Ed) pp. 183-222, Academic Press.

Joliot, P., Barbieri, G. & Chabaud, R. (1969) *Photochem. Photobiol. 10*, 309-329.

Lai, A., Flanagan, H. L., & Singel, D. J. (1988) *J. Chem. Phys. 12*, 7161-7166.

Lawrence Berkeley Laboratory-University of California (1988) *An ALS Handbook* (PUB-653).

Levason, W. & McAuliffe, C.A. (1972) *Coord. Chem. Rev. 7*, 353-384.

Li, Q., Vincent, J.B., Libby, E., Chang, H.-R., Huffman, J.C., Boyd, P.D.W., Christou, G. & Hendrickson, D.N. (1988) *Angew. Chem. Int. Ed. Engl. 27*, 1731-1733.

Lifshitz, R. & Levitzki, A. (1976) *Biochem. 15*, 1987-1993.

Lindberg, K., Wydrzynski, T., Vanngard, T. & Andréasson, L.-E. (1990) *FEBS Lett. 264*, 153-155.

Mathur, P., Crowder, M. & Dismukes, G.C. (1987) *J. Am. Chem. Soc. 109*, 5227-5233.

McCracken, J., Pember, S., Benkovic, S.J., Villafranca, J.J., Miller, R.J. & Peisach, J. (1988) *J. Amer. Chem. Soc. 110*, 1069-1074.

McDermott, A.E. (1987) *Ph.D. Dissertation*, University of California, Berkeley, CA Lawrence Berkeley Laboratory Report LBL-24474

McDermott, A.E., Yachandra, V. K., Guiles, R. D., Cole, J. L., Dexheimer, S.L., Britt, R. D., Sauer, K., & Klein, M. P. (1988) *Biochemistry 27*, 4021-4031.

McKale, A.G., Veal, B.W., Paulikas, A.P., Chan, S.-K, Knapp, G.S. (1988) *J. Amer. Chem. Soc. 110*, 3763-3768.

McMaster, W.H., Kerr Del Grande, N., Mallet, J.H. & Hubbel, J.H. (1969) *Compilation of X-ray Cross Sections* Lawrence Berkeley Laboratory.

McSwain, B.D., Tsujimoto, H.Y., Arnon, D.I. (1976) *Biochim. Biophys. Acta 423*, 313-322.

Michel, H. & Deisenöfer, J. (1988) *Biochemistry 27*, 1-7.

Mims, W.B. (1984) *J. Mag. Res. 59*, 291-306.

Mims, W.B. & Peisach, J. (1978) *J. Chem. Phys. 69*, 4921-4930.

Mims, W.B. & Peisach, J. (1981) in *Biological Magnetic Resonance 3* (Berliner, L. J. & Reuben, J., Eds) pp. 213-263, Plenum Press, New York.

Mims, W.B. & Peisach, J. (1989) in *Advanced EPR in Biology and Biochemistry* (A.Hoff, Ed.) Elsevier, Amsterdam.

Mino, Y., Loehr, T. M., Wada, K., Matsubara, H. & Sanders-Loehr, J. (1987)*Biochemistry 26*, 8059-8065.

Miyao, M. & Murata, M. (1985) *FEBS 180*, 303-308.

Miyao, M. & Murata, M. (1984) *FEBS 170*, 350-354.

Miyazaki, A., Shina, T., Toyoshima, Y., Gounaris, K. & Barber, J. (1989) *Biochim. Biophys. Acta 975*, 142-147.

Norris, J.R. & Schiffer, M. (1990) *Chem. & Eng. News 68*, 22-37.

Nicklin, R.c., Poole, C.P. Jr. & Farach, H.A. (1973) *J. Chem. Phys. 58*, 2579-2584.

Nugent, J. H. A. (1987) *Biochim. Biophys. Acta 893*, 184-189.

Ohno, T., Satoh, K. & Katoh, S. (1986) *Biochim. Biophys. Acta 852*, 1-8.

Omata, T. & Murata, N. (1983) *Plant & Cell Physiol. 24*, 1093-1100.

Ono, T., Conjeaud, H., Gleiter, H., Inoue, Y., Mathis, P. (1986) *FEBS Lett.203*, 215.

Ono, T., Zimmermann, J.-L., Inoue, Y. & Rutherford, A.W. (1986) *Biochim. Biophys. Acta 851*, 193-201.

Ono, T., Nakayama, H. Gleiter, H. Inoue, Y. Kawamori, A. (1987) *Arch. Bioch. Biophys. 256*, 618-624.

Pecoraro, V. L. (1988) *Photochem. Photobiol. 48*, 249-264.

Pecoraro, V.L. & Butler, W.M. (1986) *Acta Crys. C42*, 1151-1154.

Pedersen, E. & Toftlund, H. (1974) *Inorganic Chemistry 13*, 1603-1612.

Peisach, J., Mims, W. B. & Davis, J. L. (1979) *J. Biol. Chem. 254*, 12379-12389.

Penner-Hahn, J.E., Fronko, R.M., Pecoraro, V.L., Yocum, C.F., Betts, S.D. & Bowlby, N.R. (1990) *J. Amer. Chem. Soc. 112*, 2549-2557.

Philbrick, J.B. & Zilinskas, B.A. (1988) *Mol. Gen. Genet. 212*, 418-425.

Phillips, F.L., Shreeve, F.M. & Skapski, A.C. (1976) *Acta Cryst. B32*, 687-692.

Reedjik, J., Stork-Blaisse, B.A. & Verschoor, G.C. (1971) *Inorg. Chem. 10*, 2594-2599.

Robinson, S.P. & Downton, W.J.S. (1984) *Arch. Bioch. Biophys. 228*, 197-206.

Rupp, H., Rao, K.K., Hall, D.O. & Cammack, R. (1978) *Biochim. Biophys. Acta 537*, 255-269.

Rutherford, A.W. (1985) *Biochim. Biophys. Acta 807*, 189-201.

Shachar-Hill, Y., Beck, W.F. & Brudvig, G.W. (1989) *FEBS 254*, 184-188.

Sandusky, P.O., Yocum, C.F. (1983) *FEBS Lett. 162*, 339-343.

Sandusky, P.O., Yocum, C.F. (1984) *Biochim. Biophys. Acta 766*, 603-611.

Sandusky, P.O., Yocum, C.F. (1986) *Biochim. Biophys. Acta 849*, 85-93.

Sauer, K. (1986) *Encyclopedia of Plant Physiology New Series, Vol. 19 (Photosynthesis III)*, (Staehlein, L.A. & Arntzen, C.J., Eds.) Springer-Verlag, Berlin, 85-97.

Sauer, K., Guiles, R.D., McDermott, A.E., Cole, J.L., Yachandra, V.K., Zimmermann, J.-L., Klein, M.P., Dexheimer, S.L. & Britt, R.D. (1988) *Chem. Scr. 28A*,87-91.

Sauer, K., Yachandra, V.K., Britt, R.D. & Klein, M.P. (1990) in *Manganese Redox Enzymes*, (Pecoraro, V. L., Ed.) VCH Publishers, New York, in press.

Scholes, C.P., Falkowski, K.M., Chen, S. & Bank, J. (1986) *J. Amer. Chem. Soc. 108,* 1660-1671.

Scott, R.A., Eidsness, M.K. (1988) *Comments Inorg. Chem. 7*, 235-267.

Shiemke, A.K., Loehr, T. M. & Sanders-Loehr, J. (1986) *J. Amer. Chem. Soc.108*, 2437-2443.

Sivaraja, M., Tso, J., &Dismukes, G. C. (1989) *Biochem. 28*, 9459-9464.

Stanier, R.Y. (1972) in *Biology of the Blue-Green Algae* (Carr, N.G. & Whitton, B.A., Eds.) University of California Press, Berkeley, 501-518.

Stern, E.A. & Heald, S.M. (1979) *Rev. Sci. Instrum. 50*, 1579-1582.

Stebler, M., Ludi, A. & H.-B. Bürgi (1986) *Inorg. Chem. 25*, 4743-4750.

Stewart, A., Ljungberg, U., Akerlund, H.-E. & Andersson, B. (1985) *Biochim. Biophys. Acta 808*, 353-362.

Strange, R.W., Blackburn, N.J., Knowles, P.F. & Hasnain, S.S. (1987) *J. Am. Chem. Soc. 109*, 7157-7162.

Styring, S. & Rutherford, A.W. (1987) *Biochemistry 26*, 2401-2405.

Tae, G.-S., Black, M.T., Cramer, W.A., Vallon, O. & Bogorad, L. (1988) *Biochemistry 27*, 9075-9080.

Tamura, N., Ikeuchi, M. & Inoue, Y. (1989) *Biochim. Biophys. Acta 973*, 281-289.

Teo, B.-K., Lee, P.A. (1979) *J. Amer. Chem. Soc. 101*, 2815-2832.

Teo, B.K. (1986) in *EXAFS: Basic Principles and Data Analysis* Springer-Verlag, New York.

Theg, S.M., Jursinic, P. & Homann, P.H. (1984) *Biochim. Biophys. Acta 766*, 636-646.

Thompson, L.K. & Brudvig, G.W. (1988) *Biophys. J. 53*, 269.

Trebst, A. (1986) *Z. Naturforsch 41*, 240-245.

Trebst, A. & Depka, B. (1985) in *Antennas and Reaction Centers of Photosynthetic Bacteria* (Michel-Beyerle, M.E., Ed.) Springer Verlag, Berlin, 216-224.

Vass, I., Ono, T., Inoue, Y. (1987) *Biochim. Biophys. Acta 892*, 224-235.

Vincent, J.B., Christmas, C., Huffman, J.C., Christou, G., Chang, H.-R. & Hendrickson, D.N. (1987) *J. Chem. Soc. Chem. Commun.*, 236.

Waggoner, C.M. & Yocum, C.F. (1990) *Current Research in Photosynthesis* (Baltscheffsky, W., Ed.) Kluwer Academic Publishers, The Netherlands, I.3.733.

Warburg, O. & Lüttgens, W. (1946) *Naturwissenschaften 32*, 301.

Warren, L.F. & Bennett, M.A. (1976) *Inorg. Chem. 15*, 3126-3140.

Wieghardt, K., Bossek, U. & Gebert, W. (1983) *Angew. Chem. Int. Ed. Eng. 22*, 328-329.

Wieghardt, K. (1989) *Angew. Chem. Int. Ed. Engl. 28*, 1153-1172.

Wieghardt, K., Bossek, U., Ventur, D., Weiss, J. (1985) *J. Chem. Soc., Chem. Commun.*, 347-349.

Wieghardt, K., Bossek, U., Nuber, B., Weiss, J., Bonvoisin, J., Corbella, M., Vitols, S.E., Girerd, J.J. (1988) *J. Am. chem. Soc. 110*, 7398-7411.

Winick, H. (1987) *Sci. Amer. 257*, 88-102.

Winick, H. & Watson, R.E. (1984) *Nucl. Instrum. Methods Phys. Res. 222*, 373.

Wydrzynski, T. & Sauer, K. (1980) *Biochim. Biohys. Acta 589*, 56-70.

Wydrzynski, T., Baumgart, F., MacMillan, F. & Renger, G. (1990) *Photos. Res. 25*, 59-72.

Yachandra, V.K., Guiles, R.D., Sauer, K. & Klein, M.P. (1986) *Biochim.Biophys. Acta 850*, 333-342.

Yachandra, V.K., Guiles, R.D., McDermott, A.E., Cole, J. L., Britt, R.D., Dexheimer, S.L., Sauer, K. & Klein, M.P. (1987) *Biochemistry 26*, 5974-5981.

Yachandra, V.K., DeRose, V.J., Mukerji, I., Latimer, M.J., Sauer, K. & Klein, M.P. (1990) manuscript in preparation.

Yamagishi, A. & Katoh, S. (1983) *Arch. Biochem. Biophys. 225*, 836-846.

Yocum, C.F., Yerkes, C.T., Blankenship, R.E., Sharp, R.R & Babcock, G.T. (1981) *Proc. Nat. Acad. Sci. USA 78*, 7507-7511.

Zhang, K., Stern, E.A., Ellis, F. (1988) *Biochemistry 27*, 7470-7479.

Zimmermann, J.-L. & Rutherford, A.W. (1984) *Biochim. Biophys. Acta 767*, 160-167.

LAWRENCE BERKELEY LABORATORY
TECHNICAL INFORMATION DEPARTMENT
1 CYCLOTRON ROAD
BERKELEY, CALIFORNIA 94720